UNIVERSITY OF CALIFORNIA SAN DIEGO
SAN DIEGO STATE UNIVERSITY

# Liouville and cloud models of randomly forced particle-laden flow

A dissertation submitted in partial satisfaction of the
requirements for the degree Doctor of Philosophy

in

Engineering Science (Mechanical and Aerospace)

by

Daniel Domínguez-Vázquez

Committee in charge:

University of California, San Diego

Professor Carlos F. Coimbra, Co-Chair
Professor Jiun-Shyan Chen
Professor Oliver T. Schmidt

San Diego State University

Professor Gustaaf B. Jacobs, Co-Chair
Professor Pavel Popov

2024

The Dissertation of Daniel Domínguez-Vázquez is approved, and it is acceptable in quality and form for publication on microfilm and electronically.

_____

_____

_____

_____

Co-Chair

_____

Co-Chair

University of California San Diego

San Diego State University

2024

DEDICATION

To my brother.

# EPIGRAPH

Imagination is more important than knowledge. For knowledge is limited, whereas imagination encircles the world.

*Albert Einstein*

Todo tonto está convencido; y todos convencidos son tontos. Cuanto más defectuoso es el juicio de una persona, más firmes son sus convicciones.

*Baltasar Garcián y Morales*

TABLE OF CONTENTS

LIST OF FIGURES

LIST OF TABLES

ACKNOWLEDGEMENTS

I would like to express my gratitude to Prof. Jacobs, for his support as an advisor. Special thanks are dedicated to Prof. Tartakovsky for his insights on the development of probability methods, and Prof. Wang for his contributions to the development of the adjoint formulation and learning framework.

I would like to express my appreciation to my committee members for their contribution: Prof. Schmidt, Prof. Chen, Prof. Popov, and to my co-advisor Prof. Coimbra.

I expresses here also my gratitude to my labmates, who made my experience through the program much richer from a personal and scientific point of view.

Finally, I want to thank my parents, brother, girlfriend and friends for their unconditional love and support through this journey.

I also acknowledge the financial support from a university fellowship at San Diego State University and the Air Force Office of Scientific Research under award numbers FA9550-19-1-0387 and FA9550-21-1-0381.

Sections 2.1 through 2.6.3 and Section 2.7, are a reprint of the material as it appears in Ref. [2], "Lagrangian models of particle-laden flows with stochastic forcing: Monte Carlo, moment equations, and method of distributions analyses", D. Domínguez-Vázquez, G. B. Jacobs and D. M. Tartakovsky, *Physics of Fluids* 33, 033326, 2021. D. Domínguez-Vázquez: conceptualization, investigation, original draft preparation, visualization. G. B. Jacobs: conceptualization, supervision, review & editing. D. M. Tartakovsky: conceptualization, supervision, review & editing.

Sections 3.1 through 3.5, are a reprint of the material as it appears in Ref. [3], "Closed SPARSE—A predictive particle cloud tracer", D. Domínguez-Vázquez, B. F. Klose and G. B. Jacobs, *International Journal of Multiphase Flow*, 161, 104375, 2023. D. Domínguez-Vázquez: conceptualization, investigation, original draft preparation, visualization. B.F. Klose: data generation, supervision. G. B. Jacobs: conceptualization, supervision, review

& editing.

Sections 4.1 through 4.4, are a reprint of the material as it appears in Ref. [4], "SPARSE-R: A point-cloud tracer with random forcing", D. Domínguez-Vázquez and G. B. Jacobs, *International Journal of Multiphase Flow*, 170, 104653, 2024. D. Domínguez-Vázquez: conceptualization, investigation, original draft preparation, visualization. G. B. Jacobs: conceptualization, supervision, review & editing.

Sections 5.1 through 5.6, are a reprint of the material as it appears in Ref. [5], "Lagrangian Liouville models of multiphase flows with randomly forced inertial particles", D. Domínguez-Vázquez, S. A. Castiblanco-Ballesteros, G. B. Jacobs and D. M. Tartakovsky. D. Domínguez-Vázquez: conceptualization, investigation, methodology, original draft preparation, visualization. S.A. Castiblanco-Ballesteros: methodology. G. B. Jacobs: conceptualization, supervision, review & editing. D. M. Tartakovsky: conceptualization, supervision, review & editing.

Sections 6.1 through 6.4, are a reprint of the material as it appears in "Adjoint-based particle forcing reconstruction and uncertainty quantification", D. Domínnguez-Vázquez, Q. Wang and G. B. Jacobs, in Ref. [6]. D. Domínguez-Vázquez: conceptualization, investigation, methodology, visualization, review & editing. Q. Wang: conceptualization, investigation, methodology, visualization, original draft preparation. G. B. Jacobs: conceptualization, supervision, review & editing.

Sections 7.1 through 7.6 are a reprint of the material as it appears in Ref. [7], "Liouville models of particle-laden flow", D. Domínguez-Vázquez, G. B. Jacobs and D. M. Tartakovsky. D. Domínguez-Vázquez: conceptualization, investigation, methodology, visualization, original draft preparation. G. B. Jacobs: conceptualization, supervision, review & editing. D. M. Tartakovsky: conceptualization, supervision, review & editing.

## VITA

| | |
|---|---|
| 2016 | Bachelor of Science in Mechanical Engineering, University of Málaga |
| 2019 | Master of Science in Mechanical Engineering, University of Málaga |
| 2019 | Master of Science in Environmental Engineering, University of Málaga, University of Granada and University of Córdoba |
| 2024 | Doctor of Philosophy in Engineering Sciences (Mechanical and Aerospace Engineering), Joint Doctoral Program, San Diego State University and University of California San Diego |

## PUBLICATIONS

**D. Domínguez-Vázquez**, G. B. Jacobs and D. M. Tartakovsky, "Liouville models of particle-laden flow", Accepted in *Physics of Fluids*, 2024.

**D. Domínguez-Vázquez**, S. A. Castiblanco-Ballesteros, G. B. Jacobs and D. M. Tartakovsky, "Lagrangian Liouville models of multiphase flows with randomly forced inertial particles", Accepted in *Journal of Computational Physics*, 2024.

**D. Domínguez-Vázquez**, Q. Wang and G. B. Jacobs, "Adjoint-based Particle Forcing Reconstruction and Uncertainty Quantification", In Preparation, 2024.

**D. Domínguez-Vázquez** and G. B. Jacobs, "SPARSE-R: A point-cloud tracer with random forcing". *International Journal of Multiphase Flow*, 170, 104653, 2024.

**D. Domínguez-Vázquez**, B. F. Klose and G. B. Jacobs, "Closed SPARSE—A predictive particle cloud tracer", *International Journal of Multiphase Flow*, 161, 104375, 2023.

**D. Domínguez-Vázquez**, G. B. Jacobs and D. M. Tartakovsky, "Lagrangian models of particle-laden flows with stochastic forcing: Monte Carlo, moment equations, and method of distributions analyses", *Physics of Fluids* 33, 033326, 2021.

**D. Domínguez-Vázquez** and R. Fernández-Feria, "On analytical approximations for the structure of a shock wave in a fully ionized plasma", *Physics of Plasmas* 26, 082118, 2019.

## PRSENTATIONS

**D. Domínguez-Vázquez**, S. A. Castiblanco-Ballesteros, D. M. Tartakovsky and G. B. Jacobs, "Determination of the probability of randomly forced point-particle tracers", *APS*

*Division of Fluid Dynamics*, Washington DC, 2023.

G. B. Jacobs and **D. Domínguez-Vázquez**, "Closure of a point-cloud model with random forcing", *Mechanistic Machine Learning and Digital Twins for Computational Science, Engineering & Technology*, El Paso, TX, 2023.

**D. Domínguez-Vázquez**, Q. Wang and and G. B. Jacobs, "Adjoint-based particle forcing reconstruction from sparse measurements with uncertainty quantification", *APS Division of Fluid Dynamics*, Indianapolis, IN, 2022.

**D. Domínguez-Vázquez** and G. B. Jacobs, "Point-cloud Subgrid Particle-Averaged Reynolds Stress Equivalent (SPARSE) method for particle-laden flows with stochastic forcing", *APS Division of Fluid Dynamics*, Indianapolis, IN, 2022.

**D. Domínguez-Vázquez** and G. B. Jacobs, "High-order approximation of deterministic initial conditions for distributional partial differential equations", *North American High-Order Methods Conference*, San Diego, CA, 2022.

**D. Domínguez-Vázquez** and G. B. Jacobs (2021), "SPARSE Model: Closed!", *APS Division of Fluid Dynamics*, Phoenix, AZ, 2021.

**D. Domínguez-Vázquez**, G. B. Jacobs and D. M. Tartakovsky, "Uncertainty quantification analysis of point-particle Eulerian-Lagrangian systems with stochastic forcing", *APS Division of Fluid Dynamics*, Phoenix, AZ, 2021.

**D. Domínguez-Vázquez**, G. B. Jacobs and D. M. Tartakovsky, "Uncertainty quantification analysis of point-particle Eulerian-Lagrangian systems with stochastic forcing", *Mechanistic Machine Learning and Digital Twins for Computational Science, Engineering & Technology*, San Diego, CA, 2021.

ABSTRACT OF THE DISSERTATION

**Liouville and cloud models of randomly forced particle-laden flow**

by

Daniel Domínguez-Vázquez

Doctor of Philosophy in Engineering Science (Mechanical and Aerospace)

University of California San Diego, 2024
San Diego State University, 2024

Professor Carlos F. Coimbra, Co-Chair
Professor Gustaaf B. Jacobs, Co-Chair

Eulerian-Lagrangian (EL) models are developed that account for stochasticity and randomness in tracers of inertial particles forced by a carrier flow phase. Central to the novelty of the models is a forcing formulation that uses a series expansion with random coefficients to account for epistemic and aleatoric uncertainties, in lieu of commonly used stochastic, random-walk processes.

Starting from randomly forced ordinary differential equations that govern the Lagrangian inertial point-particle tracer dynamics, Lagrangian cloud and Liouville models are derived. Both cloud and Liouville models are closed and are shown to more accurately

and computationally efficiently predict the propagation of the forcing randomness into confidence intervals of the particle phase solution as compared to Monte Carlo sampling methods.

The closed and predictive particle cloud tracer models the mean motion and deformation of a cloud of inertial particles at a singular point in space and along its Lagrangian trajectory in time. The tracer builds upon the Subgrid Particle-Averaged Reynolds Stress Equivalent (SPARSE) formulation first introduced in Davis *et al.* (2017) for the tracing of particle clouds. Using a combination of the forcing models, averaging and a truncated Taylor series expansion to estimate the statistical correlations in the cloud region, the SPARSE model is closed and achieves a third convergence for the confidence interval with respect the number of samples.

The Liouville models are rigorously derived with the method of distributions and do not require truncation or ad-hoc assumptions. The deterministic PDF models are described by hyperbolic partial differential equations (PDEs). In Eulerian form, the PDEs are solved with grid-based spectral methods. To recover the Lagrangian character of the disperse phase, the method of characteristics is employed to derive a PDF formulation based on the computation of flow maps, circumventing difficulties of solving high-dimensional PDE equations. This formulation is local, does not require grid based methods nor sampling, and offers a complete statistical description. It is shown that the Liouville PDF models may generalize Langevin and Fokker-Planck descriptions of particle statistics to non-Gaussian noise of the random walk.

An inverse model to infer stochastic descriptions of particle forcings from noisy trajectory data using an adjoint formulation is also introduced using a point-particle approach.

# Chapter 1

# Introduction

## 1.1 Background and motivation

Multiphase flows in which a dispersed phase composed of particles, droplet or bubbles interacts with a carrier flow are present in many natural and industrial processes. Examples of applications of these flows are gas and liquid fluidized beds [8, 9], aerosol and spray flows in combustion engines [10, 11] and medical devices [12], dispersion of snowflakes in the atmosphere [13], transport and mixing phenomena in oceans [14], sea search and rescue algorithms [15], volcanic eruptions [16, 17, 18], cavitation in turbomachinery [19] or kidney stone fragmentation [20] and sedimentation [21].

The Eulerian-Lagrangian (EL) method provides a natural framework for the modeling of such flows. It uses Eulerian continuum models to describe the dynamics of the ambient flow, and tracks individual particles along their Lagrangian paths. The computational simulation of gas and liquid flows laden with liquid or solid particles using an EL approach can be categorized based on the fidelity of the model into firstly a high–resolution particle–resolved (PR) approach, secondly a point–particle approach and thirdly a point–cloud approach. The highest fidelity approach models and resolves the flow near a particle's surface at scales smaller than the particles' size. The coupling of the two phases is carried out by imposing no–slip boundary conditions on the particle's surface. The hydrodynamic force on a particle can be computed by directly integrating the pressure and shear stress

distribution along the boundary. Examples of various implementations include the arbitrary Eulerian–Lagrangian technique [22, 23], the deformable–spatial–domain/stabilized space–time technique [24], the overset grid technique [25], the constrained interpolation profile method [26, 27], immersed boundary methods [28, 29, 30, 31, 32], lattice Boltzmann equations [33, 34] or the smoothed profile method [35]. The high computational cost limits the number of particles that can be simulated. With the current computational resources, most studies compute hundreds to thousands of particles [1, 31].

In process–scale problems millions of particles must be simulated [36] which for PR methods are not feasible with current day computer infrastructure. For this problem size, the reduced point–particle approach that models a particle as a volumeless singular point has to be the de facto choice. The so–called Particle–Source–In–Cell (PSIC) method [37, 38] accounts for the particle's influence introduced in the Eulerian equations that govern the carrier phase through singular source terms. This model is valid if the smallest hydrodynamical scale of the flow is several orders of magnitudes larger than the particles' size. The PSIC method requires modeling for the terms in the governing equations that couple the mass (if evaporation and condensation are considered), momentum and heat transfer exchanged between the two phases. For spherical particles in a steady incompressible, uniform, creeping flow, the drag force is analytically described by the Stokes' law [39]. If the flow or the particle motion is unsteady, additional forcing terms have to be considered including the unsteady added–mass and viscous–history forcing effects, which through Newton's second law results in a governing equation for the particle's acceleration known as the Boussinesq–Basset–Oseen (BBO) equation [40, 41, 42]. The BBO relation was later modified to include the effects of non–uniform transient ambient flow leading to the widely used Maxey–Riley–Gatignol (MRG) equation [43, 44]. If compressibility effects are considered, additional Faxén forces complete the particle equations [45, 46, 47]. Many physical situations of interest however, lead to particle forcings that can not be described analytically. The default modus operandi to compute these flows relies on the use of

empirical and/or data–driven correlations to correct the MRG equation. Examples of parameters for which empirical correlations are developed include arbitrary Reynolds and Mach numbers [48, 49, 50, 51], particle density and slip coefficients [52] viscosity rations for droplets [53] and inhomogeneities in the particle configurations [54] among others. For the mass and energy exchange, the use empirical correlations is also the most common practice.

Even with the point-particle approach, the degrees of freedom in a given problem may exceed the available computational resources. A further problem size reduction is hence desirable, specially if one is interested in computing on desktop computers for design purposes. The Cloud-In-Cell (CIC) method [55] addresses the computational cost problem by amalgamating groups of particles. Unfortunately, the CIC usually does not account for the second-moment cloud dynamics and statistics but rather just scales a computational point or parcel with the number of particles within the physical cloud, i.e., a zeroth order model [56, 57, 58]. A zeroth order model does not account for velocity distribution of both the carrier phase and the particle phase within the cloud [57, 58, 59, 60, 61, 62]. As investigated in Ref. [60], the pseudo-turbulent kinetic energy (associated with the velocity fluctuations) can be as high as 40% for certain conditions in flow over fluidized beds. These effects can yield rather inaccurate predictions with the zeroth cloud method that does not account for velocity fluctuations. These also called *point-cloud* methods [57, 58, 3, 4] have been less investigated in the literature than classical point-particle methods. Additional difficulty related to a closure problem that arises from a statistical averaging process appears.

### 1.1.1 Computational challenges in particle-laden flows

Despite the broad usage of the point–particle approach, the accuracy, convergence and stability of the method are affected by its numerical treatment. The computational approximation of point–particles requires interpolation between the Lagrangian point

tracer and what is usually a grid based approximation of the Eulerian carrier phase model [63, 64, 65, 66, 67, 68]. Particles move freely through the domain in locations different from the computational grid points of the flow, whose tractability in parallel computing is involved and requires the use of interpolation [69, 70, 71]. Special attention has to be paid to the treatment of pointwise forcing into the numerical grid to regularize the coupling source terms and its numerical representation in the computational grid [72, 73, 74, 75, 76, 77, 78]. Another known approximation challenge is a nonphysical numerical self–forcing that is connected with this interpolation. The point–particle description relies on the knowledge of the unperturbed flow velocity which is in principle unknown. The use of the flow velocity interpolated at the particle location instead of the velocity of the unperturbed flow at that location produces self–motion as a result of a self–induced force that is not physical [79]. Some of the earliest work to tackle this issue led to the forcing–coupling method (FCM) [80, 79, 81], while several corrections to the point–particle method have been recently proposed [82, 75, 77, 83]. The point–particle assumption leads also to convergence issues related to a strong grid dependence because the forcing is modeled by averaging in the volume of the computational cell unless the number of particles per cell exceeds a threshold [76]. These drawbacks have inspired the development of different alternative approaches for the simulation of particle–laden flows [84, 65]. Some of the recent research includes the volume averaged method [85, 86, 87, 88, 89, 19], the modeling of interparticle forcing by the pairwise interaction extended point–particle (PIEP) model [90, 91, 92, 93], the microstructure–informed probability–driven point–particle (MPP) model [94], the exact regularized point particle (ERPP) method [76, 95] to tackle convergence issues, the use of discrete Green's functions to find the undisturbed velocity and correct the particle's self–force [77], and machine learning (ML) models to find closures to reduced descriptions [96, 97].

### 1.1.2 Non-deterministic point-particle forcing laws

If a forcing function is fit empirically to experimental or computational data, the resulting expression is analytical. Then the function and its related trace do not account for quantifiable measures of uncertainty such as confidence intervals defined by plus/minus a standard deviation around the average [98] or confidence intervals defined within a probability range of the samples. We say that methods that trace (tracers) point–particles based on these analytical models are *deterministic*. In an ongoing effort to account for the confidence interval, several formulations of the disperse phase are presented here, that assume the point–particles to be randomly forced (rF), i.e., the forcing is considered *non–deterministic*. These probabilistic models propagate the confidence intervals of the forcing into the kinematics, dynamics and heat transfer of the disperse phase [98, 99, 2, 4, 6, 5, 7]. The randomness may originate from confidence intervals, i.e., the fitting error of empirical or data–driven forcing functions reconstructed from PR simulations [100, 101, 102] as shown in Fig. 1.1 (left). The randomness can also be stochastic in nature for the subgrid scale model, in which the forcing function is described by a probability density function (PDF) according to the dynamics of the subgrid scale [103, 104]. The probabilistic models enable an assessment of sensitivity to uncertain/unknown forcing models in flows where the point–particle assumption is used but analytical descriptions for the particle forcing are not available. The probabilistic macro–model is a natural complement to the multi–scale data–driven framework proposed in Refs. [100, 101, 102], that connects accurate high-resolution simulations with the reduced point-particle method through surrogate models. The latter approximates the interphase force and heat flux with a surrogate model in a wide parameter space using high-resolution simulations in a data-driven manner. In regions of the parameter space with a large uncertainty, additional high-resolution simulations are conducted to improve the accuracy and/or validity range of the surrogate model. As more high-resolution simulations become available, the multi-scale method is

updated via a Bayesian procedure. This procedure yields an approximate forcing function with a computable probability density function. The probabilistic forcing thus propagates into a PDF solution based on the random point–particle dynamics. The development of forward models to propagate it becomes crucial, as discussed in Jacobs and Udaykumar (2019) [98]. This task has motivated this work, where several point–particle models with random forcing based on different approaches such as Monte Carlo (MC), the method of moments (MoM) and the method of distributions (MoD) have been introduced.

### 1.1.3 Stochastic PDF models for particle-laden flow

Stochastic processes are mathematical objects usually defined as a sequence of random variables in a probability space, where the index of the sequence often has the interpretation of time. Stochastic processes are used to model systems and phenomena that appear to vary in a random manner. Stochastic descriptions of particle statistics of positions and velocities in multiphase flows have its origins in the landmark work of Buyevich [105, 106, 107]. The derivation of this type of kinetic PDF equation is analogous to the Maxwell–Boltzmann equation of classical kinetic theory and leads to unclosed PDF models. Since then, a significant body of literature addresses closure analytically [108, 109, 110, 111, 112, 113, 114, 115, 116, 117, 118, 103, 119]. A closure may also be accomplished with numerical approximation. Quadrature–based moment methods, for example, have been derived by describing finite moment sets of the joint PDF by an optimal set of quadrature nodes and weights [120, 121, 122, 123, 124, 125, 126, 127, 128].

To reduce the dimensionality of the PDF formulation, the generalized Langevin model [119] uses stochastic processes, mostly Wiener increments, in the point-particle equations. This approach stems from their usage in modeling subgrid-scale stochasticity on passive tracers in turbulent flows [129, 130]. Stochastic models of the disperse phase based on the use of Wiener increments have also been used in recent years [131, 132, 133, 134, 135, 136, 137, 36, 138, 139, 1, 140, 141, 142, 143, 144, 145, 146].

A drawback of Langevin models is that determination of accurate statistics requires significant sampling, making the approach computationally prohibitively expensive. An alternative is to use the corresponding Fokker–Planck equation [140, 146] making use of the Itô calculus which requires closure and its advection–diffusion character makes its numerical solution a computational challenge that continues inspiring new research [147, 148]. Only under simplified considerations, the Fokker–Planck equation allows constructive analytical solutions to be found [141], where the temporal evolution of the particle statistics is described analytically. Because of the complexity of the numerical solution of the Fokker–Planck equation to compute the joint PDF of the particle phase, most studies are restricted to finding the first and second moments of the joint PDF [141]. The moment equations also require the development of closures that can be based on gradient models or learned correlations from PR simulations [143]. None of these models consider the forcing random, i.e., the consideration of epistemic uncertainty on the point-particle model itself is not accounted for. The stochastic models consider the particle statistics as the result of a stochastic process, without including randomness in the forcing, and as such, they can be considered a subset of randomness. In particular, stochastic models do not treat uncertainties originated from empiricism in the model used to describe the particles' dynamics, related to the impossibility of deterministically describe the particles' force without fully resolving the near flow. Considering a random forcing model implies the model itself may be incomplete, as a result of the use of a reduced description not based on first principles.

A new class of PDF model that starts from an approximation of the random forcing function based on series expansions involving proper sets of random variables [149, 150] was introduced in Ref. [99] for the Eulerian phase in EL systems. The model is then dependent on basis functions, for example Chebyshev polynomials, and random coefficients. The confidence intervals of the forcing so defined are general and can be caused by either empiricism or stochasticity of the problem. Following the method of distributions, the

randomly forced Lagrangian point–particle model is governed by a closed hyperbolic PDE for the joint PDF of the particle solution in physical and phase space. The resulting equation governs a joint PDF that has an augmented dimensionality to include the particle phase variables and the random coefficients. The moment equations follow naturally from the PDF approach, but they require closure of the higher moments. The numerical approximation of the moment model that admits singularities is not trivial [98].

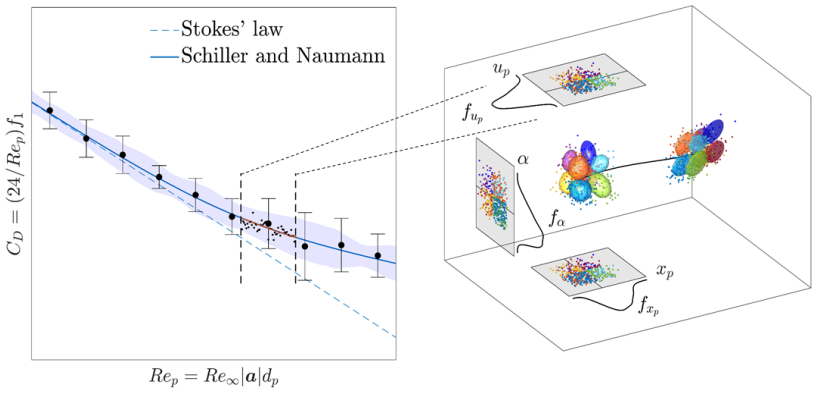


**Figure 1.1.** Scheme of a randomly forced cloud described by the SPARSE–R method. On the left, the drag coefficient $C_D$ as a function of the particle Reynolds number $Re_p = Re_\infty|\boldsymbol{a}|d_p$ with uncertainty bounds where $\boldsymbol{a}$ is the relative velocity, $Re_\infty$ the reference Reynolds number of the flow and $d_p$ the non–dimensional particle diameter. On the right, the representation of a one–dimensional particle cloud in the domain $\alpha - x_p - u_p$. The dots are the point–particles (computed with the PSIC equations) and the ellipsoids the subclouds or point–clouds (computed with the SPARSE–R equations). The PDFs of the particle phase variables are also represented where the point–particles and point–clouds are linked by colors according to a division of the domain in two subclouds per dimension in $\alpha - x_p - u_p$.

## 1.2 Contributions and outline

The primary objective of this thesis is the development of models that propagate a quantified measure of uncertainty in randomly forced particle-laden systems of single tracers and groups of tracers. The central novelty to this development is a random forcing

law based on a series expansion with random coefficients, in lieu of Langevin models. Probability density function models in both Eulerian and Lagrangian form are derived. Lagrangian cloud models are derived in closed-form using a method of moments. The hyperbolic PDF model is shown to be equivalent to classic Langevin and Fokker-Planck models. Additionally the PDF model can be used for non-Gaussian noise. The predictive models are intended to be used for inference of non-deterministic forcing descriptions from sparse and noisy trajectory observations. In ongoing work, an inverse model was developed that is based on the random forcing formulation that infers a forcing law.

Specific contributions that were made towards these objectives, and where they are described in the document, include:

- Derivation of a PDF model for a randomly forced particle phase based on the method of distributions that leads to a high-dimensional hyperbolic PDE. Development of high-order spectral numerical methods to accurately solve this equation in Eulerian frame. Chapter 2.

- Implementation and assessment of a regularized Dirac delta functions with vanishing moments to prescribe deterministic initial conditions to the Eulerian PDF model. Chapter 2.

- Development of a closure of the point-cloud method SPARSE and its extension to include second order moments of the particle phase. Derivation of the expected convergence, which is of the third order of standard deviation of the initial condition, ensuring computational savings with respect to Monte Carlo based methods. Chapter 3.

- Derivation of a point-cloud method for the particle phase considering non-deterministic forcing laws, according to the proposed random forcing model in the first contribution. This closed method of moments shows also third order convergence rate and can

provide approximations of moments higher than second as well as the PDFs of the particle variables. Chapter 4.

- Development of a Lagrangian formulation to solve the hyperbolic PDF equation from the first contribution by using high-dimensional flow maps, discretized with spectral methods, compatibles with discontinuous Galerkin fluid solvers. This formulation recovers the Lagrangian character of the particle phase, and does not require grid based solvers nor sampling, by virtue of the method of characteristic. Chapter 5.

- Development of an inverse model to infer stochastic descriptions of particle forcings from noisy trajectory data using an adjoint formulation. A Monte Carlo point-particle approach is adopted to quantify uncertainty. Chapter 6.

- A generalized hyperbolic PDF model, based on the Liouville theorem, or equivalently the MoD, is proposed as an alternative to the Fokker-Planck and Langevin approaches for describing particle statistics in particle-laden flows. This model allows the use of the method of characteristics, leading to the computational advantages investigated in previous contributions. Analytical models from the literature are reproduced and a model for a FHHS is proposed. Chapter 7.

A significant finding presented here, is related to the connection between the PDF model based on the hyperbolic governing equation, by virtue of the MoD, and classical alternatives based on the Fokker-Planck and Langevin models. In particular, analytical descriptions of canonical stochastic processes used in the literature [141], as well as a model for fluidized homogeneous heating systems (FHHS) [1, 143] are analyzed here with the hyperbolic model. Because of its hyperbolic character, computational advantages are also exploited in this work.

Another approach to account for the kinetic effects of a particle phase in a spatial region, i.e., the stochastic dynamics of the particle phase, is to take a *point-cloud* perspective

as initially proposed in Ref. [57]. By ensemble averaging a group of point–particles within a cloud region and combining that with a Taylor expansion of the forcing function and carrier phase variables around the average values of the particle phase (particle position and relative velocity), one–way and two–way coupled point–cloud tracers were presented in Refs. [57, 58]. This point-cloud method was coined Subgrid Particle–Averaged Reynolds Stress–Equivalent (SPARSE), as it naturally accounts for stochasticity in the subcloud scales. However, these formulations are closed *a priori*, i.e., lacking a closure independent of previously performed Monte Carlo simulations. This has motivated the extension of SPARSE to a closed-form formulation [3], where significant computational savings can be achieved. In SPARSE, the forcing is described analytically and the particle cloud is said to be *deterministically forced* (dF). To account for epistemic effects, i.e., randomness in the forcing, one can assume a random forcing of a single trace that determines the particle's path within a confidence interval. This randomness affects the cloud motion as compared to the deterministic cloud. Notably, the a random forcing can cause the forcing for two particle that have the same relative velocity to be different. In a stochastic environment these two forcings have to be the same. Extension of the SPARSE method to consider randomness in the forcing function in closed-form has also been proposed here. Furthermore, approximation of higher order moments and the PDFs of the particle phase can be provided with the proposed SPARSE-R method [4].

# Chapter 2

# A Probability density function formulation for randomly forced dispersed phases

## 2.1 Introduction

The empirical corrections employed to describe forcing laws of point-particles outside of the range of the Stokes drag, depend of plethora of parameters, such as particle shape and the Reynolds and Mach numbers, that have nonlinear effects on the flow around a particle. This naturally translates into a prediction error of a point-particle model, as the momentum and energy exchange are only known within certain bounds. The presence of such a stochastic forcing in both the empirical and data-driven approaches renders solutions to the corresponding PSIC model random as well. These solutions are given in terms of a joint PDF of system states or their ensemble moments. Monte Carlo (MC) simulations are often used to obtain such solutions. They are easy to implement, "embarassingly" parallel, and free of distributional assumptions; their only approximation stems from the practical need to rely on a finite number of MC realizations, $N_s$, to compute the sample statistics. A drawback of the MC method is its slow convergence: its sampling error decays as $1/\sqrt{N_s}$. This can make MC simulations prohibitively expensive if each realization takes a long time to compute. Various modifications of the standard MC,

e.g., multilevel MC, pseudo-MC, or combinations thereof, can significantly accelerate this convergence rate, but their performance is not guaranteed especially when the goal is to compute the full PDF rather than its moments [151, 152]. Other sampling-based methods, such as stochastic collocation, require nontrivial modifications [153] in order to handle hyperbolic problems with discontinuities. When the stochastic dimension and/or the noise strength become large, such methods might become slower than the standard MC even for problems with smooth solutions [154].

Direct numerical alternatives to sampling techniques include methods based on (generalized) polynomial chaos expansions. These methods represent uncertain inputs and state variables by orthogonal polynomials of standard random variables, and often exhibit spectral accuracy. Of direct relevance to high-speed compressible flows described by the Euler equations with shocks is the multi-element generalized polynomial chaos method [155, 156, 157], which accommodates the presence of discontinuities in the stochastic space. Its computational cost might become comparable to sampling methods [158], especially when the stochastic dimension is large. Like their sampling-based counterparts, the direct simulation methods do not provide physical insight into the probabilistic behavior of a system, e.g., the spatiotemporal nonlocality of the statistical moments [159] and PDFs [160] of the system states.

The method of moments (MoM) alleviates some of these disadvantages by deriving deterministic equations for the statistical moments of a system state. Since the MoM is free of polynomial expansions, it does not suffer from the "curse of dimensionality", but it often requires closure approximations to be computable. It has been used to derive moment equations for high-speed flows interacting with a particle phase [98]; the closure terms were learned from the MC simulations. Practical considerations limit the MoM to the derivation and solution of equations for the first two moments —mean and (co)variance— of a system state, which limits its usefulness for highly non-Gaussian phenomena. Specifically, the MoM cannot capture rare events occurring in such problems, which are characterized by

fat-tailed PDFs.

The method of distributions (MoD) overcomes this limitation by deriving a deterministic equation for either the joint PDF or the joint cumulative density function (CDF) of the system states. Having its origins in the statistical theory of turbulence [161], the MoD has since been used as an efficient uncertainty quantification technique [162]. It retains all the advantages of the MoM, but might require closure approximations. The MoD yields a closed-form PDF/CDF equation for nonlinear flows in the absence of a shock, e.g., those described by the inviscid Burgers equation [99] and the shallow-water equations [163]. Within the MoD framework, shocks and discontinuities can be treated either analytically, as was done for the Buckley-Leverett equation [164] and water hammer equations [165], or by adding the PDF/CDF equation a kinetic defect-like source term that generally has to be learned from Monte Carlo runs [166]. Numerical solutions of PDF/CDF equations admit high-order spectral accuracy [99] and can be up to two orders of magnitude faster than the standard MC [167].

Here we deploy the MoD to describe isothermal particle-laden flows driven by stochastic forcings [2]. The underlying flow model relies on the Lagrangian point-particle formulation with one-way coupling between fluid flow and particle transport. The drag on a particle is modeled as a random variable with a prescribed PDF. The MoD yields a closed-form partial differential equation for the joint PDF of a particle's position and velocity. We consider two canonical flow scenarios, both in one spatial dimension: a uniform carrier flow and a stagnation carrier flow. These are important in their own right and can be used as building blocks of more general and multi-dimensional flows; for example, the stagnation flow is a central component to the dynamic description of attractors and repellers in dynamic systems [168]. Our PDF solutions are validated against high-fidelity MC simulations and compared with solutions of the moment equations [98]. The hyperbolic PDF equation is solved via the Chebyshev collocation method [99]. Discontinuities in its solution are captured using the filtering techniques [74, 169]. An important contribution

of this work is the numerical analysis of the use of regularized Dirac delta functions in the context of deterministic initial conditions for the PDF model. The vanishing moment condition then governs the accuracy of the description of the joint PDF in a statistical sense. The number of moments than can be computed (marginalizing the joint PDF) accurately are directly related to the amount of vanishing moments of the regularized Dirac delta. A key result of our analysis is also the derivation of analytical expressions for the position and velocity of a particle moving in deterministic uniform and stagnation flows. These expressions allow us to generate sufficiently large numbers of MC realizations. In both flow regimes, the PDF solutions are non-Gaussian and their moments can increase or decrease depending largely on the time-dependent increase or decrease of the inter-phase velocity. Moreover, the stochastic solution can develop discontinuities at inflection points of the inter-phase velocity.

## 2.2 Lagrangian Problem Formulation

Dynamics of an isothermal collisionless particle phase in a one-way coupled unidimensional Eulerian-Lagrangian system with the point-particle approximation is governed by[38, 170]

$$\frac{\mathrm{d}x_p}{\mathrm{d}t} = u_p, \tag{2.1a}$$

$$\frac{\mathrm{d}u_p}{\mathrm{d}t} = \phi\frac{u - u_p}{\tau_p}. \tag{2.1b}$$

Here, $t$ is the non-dimensional time, $x_p$ is the non-dimensional particle position, and $u_p$ is the non-dimensional particle velocity. The non-dimensional particle response time $\tau_p$ is a measure of the response of the particle to a change in the carrier velocity $u$. It is expressed as $\tau_p = d_p^2 Re/(18\epsilon)$, where $d_p = d_p^*/L$ is the non-dimensional particle diameter, $Re = U_\infty L/\nu$ is the Reynolds number, $L$ is a characteristic length, $U_\infty$ is the reference velocity, and $\epsilon = \rho/\rho_p$ is the relative density ratio of the two phases.

The function $\phi$ is used to correct the Stokes drag force for flow conditions outside of Stokes assumptions. Such models for the corrected drag coefficient $\phi$ are empirical and, therefore, can only be determined within an uncertainty bound [100, 101, 57]. For the sake of generality, we postulate [57, 99], that $\phi$ depends on the relative velocity $u - u_p$,

$$\phi = ag(u - u_p), \tag{2.2}$$

without specifying the functional dependence of the function $g(\cdot)$. This function can be expanded in terms of several random modes. Here, we consider the first of those random modes, and take $\phi = a$. The random coefficient $a$, with a given PDF $f_a(A)$ accounts for the uncertainty in $\phi$ stemming from a broad range of sources such as uncertainty in the particle size, shape or inexactness/empiricism of the drag force, and renders the system of ordinary differential equations (2.1) stochastic. Its solution is given in terms of the joint PDF $f_{ax_pu_p}(A, X_p, U_p; t)$.

Our model formulation ignores inter-particle collisions. This is justified if the particle phase is dilute, especially in one spatial dimension [171].

## 2.3 Solution Strategies

### 2.3.1 Method of Distributions

When applied to (2.1), the MoD yields an exact PDF equation (see Appendix A)

$$\frac{\partial f_{ax_pu_p}}{\partial t} + \frac{\partial}{\partial X_p}\left[U_p f_{ax_pu_p}\right] + \frac{\partial}{\partial U_p}\left[\frac{Ag(U - U_p)}{\tau_p}(U - U_p) f_{ax_pu_p}\right] = 0, \tag{2.3}$$

with $A$, $X_p$ and $U_p$ the deterministic versions of the stochastic variables $a$, $x_p$ and $u_p$. Equation (2.3) describes the evolution of the joint PDF of the particle phase and drag coefficient, $f_{ax_pu_p}(A, X_p, U_p; t)$, in the phase space $\Omega$ spanned by coordinates $(X_p, U_p, A)$. This space can be either infinite or bounded, $\Omega = [X_p^0, X_p^1] \times [U_p^0, U_p^1] \times [A^0, A^1]$. In the

latter case, (2.3) is subject to boundary conditions for the independent variables $X_p$ and $U_p$

$$f_{ax_pu_p}(A, X_p^b, U_p; t) = f^{X_p}_{ax_pu_p}(A, U_p; t), \tag{2.4}$$

$$f_{ax_pu_p}(A, X_p, U_p^b; t) = f^{U_p}_{ax_pu_p}(A, X_p; t). \tag{2.5}$$

The boundary functions on the right hand side of these expressions are specified according to the corresponding marginal distributions; and using the characteristic velocities of (2.3) defined as in (2.14) and (2.15), $X_p^b = X_p^0$ or $X_p^b = X_p^1$ for $C_X(X_p^0) > 0$ and $C_X(X_p^1) < 0$, respectively. Similarly, $U_p^b = U_p^0$ or $U_p^b = U_p^1$ for $C_U(U_p^0) > 0$ and $C_U(U_p^1) < 0$, respectively. The PDF equation (2.3) is also subject to the initial condition,

$$f_{ax_pu_p}(A, X_p, U_p; 0) = f^0_{ax_pu_p}(A, X_p, U_p). \tag{2.6}$$

The function form of $f^0_{ax_pu_p}(A, X_p, U_p)$ is determined by the degree of certainty in the initial state of the system, $(x_{p_0}, u_{p_0})$. If it is known with certainty, i.e., deterministic, then

$$f_{ax_pu_p}(A, X_p, U_p; 0) = f_a(A)\delta(X_p - x_{p_0})\delta(U_p - u_{p_0}), \tag{2.7}$$

where $\delta(\cdot)$ is the Dirac delta function. We will refer to this as a deterministic initial condition (dIC). If the initial condition is not know with certainty, then we refer to it as stochastic (sIC). Once $f_{ax_pu_p}(A, X_p, U_p; t)$ is computed from (2.3)–(2.6), the PDFs $f_{x_pu_p}(X_p, U_p; t)$, $f_{x_p}(X_p; t)$, and $f_{u_p}(U_p; t)$ are computed as its marginals via numerical integration over the respective variables (see appendix A).

### 2.3.2 Method of Moments

Solutions of the moment equations have been used to elucidate many salient features of stochastically forced particle-laden flows [98]. We summarize that analysis and extend

it to derive third-moment equations in order to understand the degree of non-Gaussianity. The derivation starts by using the Reynolds decomposition to represent all parameters and state variables as the sums of their respective ensemble means (denoted by the overbar) and zero-mean fluctuations (denoted by the prime), e.g., $x_p = \overline{x}_p + x'_p$ with $\overline{x'_p} = 0$. Substituting these decompositions into (2.1) and take the ensemble average, we obtain equations for the means

$$\frac{\mathrm{d}\overline{x}_p}{\mathrm{d}t} = \overline{u}_p, \tag{2.8}$$

$$\tau_p \frac{\mathrm{d}\overline{u}_p}{\mathrm{d}t} = \overline{\phi}(\overline{u} - \overline{u}_p) + \overline{\phi' u'} - \overline{\phi' u'_p}, \tag{2.9}$$

for the variances, $\sigma^2_{x_p} = \overline{{x'_p}^2}$ and $\sigma^2_{u_p} = \overline{{u'_p}^2}$,

$$\frac{\mathrm{d}\sigma^2_{x_p}}{\mathrm{d}t} = 2\overline{x'_p u'_p}, \tag{2.10}$$

$$\frac{\tau_p}{2}\frac{\mathrm{d}\sigma^2_{u_p}}{\mathrm{d}t} = \overline{\phi}(\overline{u' u'_p} - \sigma^2_{u_p}) + \overline{\phi' u'_p}(\overline{u} - \overline{u}_p) + \overline{\phi' u' u'_p} - \overline{\phi' {u'_p}^2}, \tag{2.11}$$

and for the third central moments, $s_{x_p} = \overline{{x'_p}^3}$ and $s_{u_p} = \overline{{u'_p}^3}$,

$$\frac{\mathrm{d}s_{x_p}}{\mathrm{d}t} = 3\overline{{x'_p}^2 u'_p}, \tag{2.12}$$

$$\frac{\tau_p}{3}\frac{\mathrm{d}s_{u_p}}{\mathrm{d}t} = \overline{\phi}(\overline{u' {u'_p}^2} - s_{u_p}) + \overline{\phi' {u'_p}^2}(\overline{u} - \overline{u}_p) - \sigma^2_{u_p}(\overline{\phi' u'} - \overline{\phi' u'_p}) + \overline{\phi' u' {u'_p}^2} - \overline{\phi' {u'_p}^3}. \tag{2.13}$$

As opposed to the exact PDF equation (2.3), these moment equations are not closed since they contain unknown mixed, higher-order moments. To render them computable, one has to introduce closure approximations such as the a priori closure [170, 57] used to analyze the first two statistical moments or a posteriori closure as used in Eulerian formulations [171, 172].

The moment equations (2.9)–(2.13) provide insight into the deviation of the stochastic solution from its deterministic counterpart and/or general dynamics of the moments.

For example, the mean dynamics, described by (2.8) and (2.9), differs from the solution of the deterministic problem (2.1) with the mean value of the random parameter $\overline{a}$. The difference between the deterministic equation and the averaged equation is the correlation $\overline{\phi' u'}$ and $\overline{\phi' u'_p}$. In some special cases, e.g., when the carrier flow is constant and the relative velocity is zero ($u = u_p$), the mean of the solution is the same as the deterministic solution for $\overline{a}$; and the velocity deviation decreases since the right hand side of (2.11) contains only the damping term.

Finally, we note that the moment equations (2.9)–(2.13) are related to the PDF equation (2.3) as they represent the evolution of the first three moments of $f_{x_p}$ and $f_{u_p}$.

### 2.3.3 Singularities in the Stochastic Solution

The characteristic velocities which can be directly inferred from (2.3),

$$C_X = \frac{\mathrm{d}X_p}{\mathrm{d}t} = U_p, \tag{2.14}$$

$$C_U = \frac{\mathrm{d}U_p}{\mathrm{d}t} = \frac{Ag(U - U_p)}{\tau_p}(U - U_p), \tag{2.15}$$

can be different which can lead to a cross-over of the characteristics' paths at certain values of $A$. In general hyperbolic systems when characteristics cross, a discontinuity is expected to appear in the solution. Depending on the sign of the relative velocity, $U - U_p$, we identify two settings in which the resulting discontinuities appear in the joint PDF, $f_{ax_pu_p}$ and its marginals. First, for a positive (and constant) relative velocity (Fig. 2.1a), we consider a cloud of $N_a$ particles with uniformly spaced different drag coefficients $A_i$ ($i = 1...N_a$) such that $A_{i+1} > A_i$. The particle with the greatest forcing, $A_{N_a}$ (rightmost particles), moves fastest, whereas the leftmost particle with a slower response is left behind. As a result the cloud expands. For a nonlinear relative velocity, the characteristics could steepen and cross in the expansion, yielding discontinuities (not exhibited in the graph).

For a second setting the same initial cloud is considered but for a negative (and

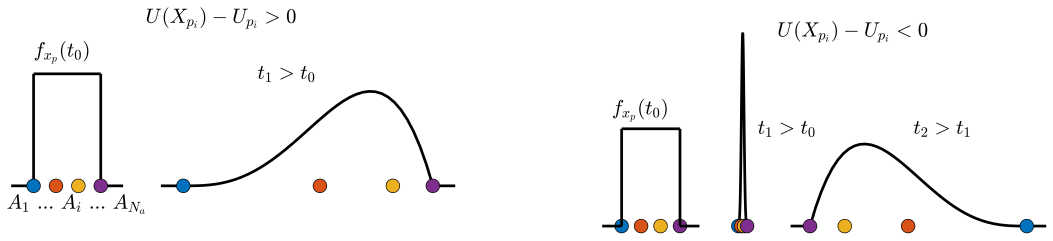


**(a)** **(b)**

**Figure 2.1.** Evolution of the PDF of $x_p$ of a cloud of particles initially distributed uniformly in space and traveling at the same initial velocity (from left to right) with different drag coefficients $A_i$ such that $A_{i+1} > A_i$. Under the influence of positive relative velocity in (a) and negative relative velocity in (b).

constant) relative velocity, which causes the cloud of particles to compress. At some point, the leftmost particles overtake the rightmost particles and the cloud concentrates in a reduced region or even in a singular point. At that instant, the characteristics of the hyperbolic system (2.3) cross. If all of them cross in a single point, then the PDF solution becomes the Dirac delta distribution. After this singular event, the cloud expands and asymmetry can reemerge resulting in steepening of the left side of the PDF $f_{x_p}$ and in its discontinuity, as it did for the positive relative velocity.

Consistent with the formation of discontinuities in the marginal PDF, $f_{x_p}$, discontinuities also arise in the marginal PDF of the particle velocity, $f_{u_p}$. In Section 2.5, we illustrate these phenomena by analyzing the uniform and stagnation carrier flows with stochastically forced particle dynamics.

## 2.4 Numerical Implementation

The discontinuities and sharp gradients that can appear in the solution of the PDF equation (2.3) require special numerical treatment. We use a low-dispersive/diffusive

Chebyshev collocation method to approximate the derivatives with respect to $X_p$ and $U_p$. Such spectral treatment was shown to be effective or even necessary to solve similar moment equations in [98]. We also deploy the filtering and regularization techniques designed to capture discontinuities and regularize singularities in a spectral solution while preserving accuracy [73, 98, 169, 36].

### 2.4.1 Chebyshev collocation method and time integration

The Chebyshev collocation method, extensively described in textbooks [173, 174], is briefly summarized below for the sake of completeness. We do so for one spatial dimension; the multi-dimensional formulation builds upon that, as it is defined along lines on a tensorial grid. In the Chebyshev collocation method, a function $y(x)$ is approximated by a Chebyshev interpolant as

$$y_{N_x}(x) = \sum_{j=0}^{N_x} y(x_j) l_j(x), \quad l_j(x) = \prod_{k=0,\ k\neq j}^{N_x} \frac{x - x_k}{x_j - x_k}. \tag{2.16}$$

Here $j = 0, \ldots, N_x$; and $l_j(x)$ is the Lagrange polynomial of degree $N_x$. The collocation points are chosen as the Gauss-Lobatto quadrature points,

$$\xi_i = -\cos(i\pi/N_x), \quad i = 0, \ldots, N_x \tag{2.17}$$

such that the $L_\infty$ norm of the interpolant is minimized on the interval $[-1, 1]$.

The derivative of the function $y(x)$ at points $x_i$ is approximated by

$$\frac{\partial y}{\partial x}(x_i) \approx \sum_{j=0}^{N_x} y(x_j) l_j'(x_i), \tag{2.18}$$

with $l_j'$ the derivative of the corresponding Lagrange polynomial. This approximated

derivative is recast in the matrix-vector form,

$$\mathbf{y}' = \mathbf{D}\mathbf{y}, \tag{2.19}$$

where the differentiation matrix $\mathbf{D}$ has components $D_{i,j} = l'_j(x_i)$.

The multi-dimensional PDF equation (2.3) is discretized on a tensorial grid that spans $X_p$, $U_p$ and $A$ in the domain $\Omega$. The spectral approximation of the distribution function $\tilde{\mathbf{f}} = \tilde{f}_{N_A N_{X_p} N_{U_p}}(A, X_p, U_p)$ on this grid is governed by the semi-discrete equation

$$\frac{\mathrm{d}\tilde{\mathbf{f}}}{\mathrm{d}t} + \mathbf{D}^{X_p}\mathbf{F}^{X_p} + \mathbf{D}^{U_p}\mathbf{F}^{U_p} = 0, \tag{2.20}$$

where the entries of the flux arrays are given by

$$F^{X_p}_{i,j,k} = U_{p_{i,j,k}} \tilde{f}_{i,j,k}, \tag{2.21}$$

$$F^{U_p}_{i,j,k} = \frac{A_{i,j,k} g(U_{i,j,k} - U_{p_{i,j,k}})}{\tau_p} (U_{i,j,k} - U_{p_{i,j,k}}) \tilde{f}_{i,j,k}, \tag{2.22}$$

with counters $i, j, k$ along the tensors. The matrices $\mathbf{D}^{X_p}$ and $\mathbf{D}^{U_p}$ are the scaled versions of the matrix $\mathbf{D}$ with the following entries

$$\left(D^{X_p}\right)_{m,j} = \frac{\partial \xi}{\partial X_p} \left(D_{m,j}\right), \quad \left(D^{U_p}\right)_{m,k} = \frac{\partial \xi}{\partial U_p} \left(D\right)_{k,m} \tag{2.23}$$

with $\partial\xi/\partial X_p$=$2/(X_p^{\max} - X_p^{\min})$ and $\partial\xi/\partial U_p$=$2/(U_p^{\max} - U_p^{\min})$ for the one-dimensional case. The matrix-vector multiplication $\mathbf{D}^{X_p}\mathbf{F}^{X_p}$ and $\mathbf{D}^{U_p}\mathbf{F}^{U_p}$ is performed along grid lines with the counters $j$ and $k$, respectively, in (2.21) and (2.22). The carrier flow velocity $\mathbf{U}$ is specified at the particle locations. The semi-discrete system is integrated in time with the total variation diminishing (TVD) Runge-Kutta scheme [175].

The marginals $f_{x_p}$ and $f_{u_p}$, are obtained via the numerical integration of $f_{ax_pu_p}$ along $A$ and either $U_p$ or $X_p$, respectively. This is done via Clenshaw-Curtis quadrature in

$U_p$ and $X_p$, and via the trapezoidal rule in $A$. Because the distribution equation does not have terms with derivatives respect to $A$, the spectral approximation is not necessary in this direction.

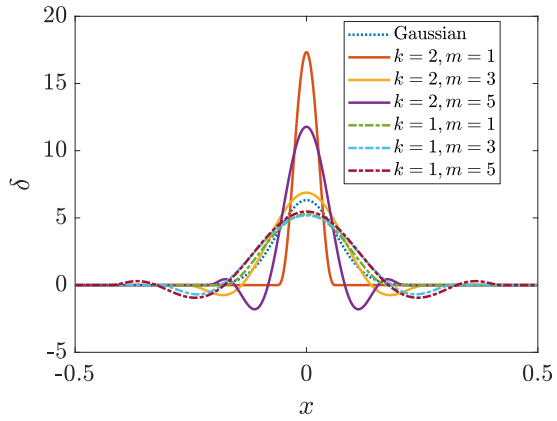


**Figure 2.2.** Regularization of the Dirac delta function, $\delta_\epsilon^{m,k}$, in comparison with a Gaussian PDF.

### 2.4.2 Regularization of Dirac delta function

The numerical solution of the PDF equation (2.3) with the deterministic initial state (2.7) requires an approximation of the Dirac delta function $\delta(\cdot)$. We rely on the kernel that regularizes $\delta(\cdot)$ with a class of high-order, compactly supported polynomials [73],

$$\delta_\epsilon^{m,k}(x) = \begin{cases} \epsilon^{-1} P^{m,k}(x/\epsilon), & x \in [-\epsilon, \epsilon] \\ 0, & \text{otherwise}, \end{cases} \tag{2.24}$$

where $\epsilon > 0$ is the support width or scaling parameter. On the compactly supported interval the regularized delta function integrates to unity (i.e., the zeroth moment is one). The polynomial $P^{m,k}$ is designed to have the first up to the $m^{th}$ moment vanished and to have $k$ continuous derivatives at the endpoints of the compact support. For it to be possible for the moments to vanish the regularized delta is permitted to have negative values on its supported interval. The vanishing moments ensure that the regularized Dirac

delta kernel (a so-called delta sequence) converges to the exact Dirac delta function at a rate of $\mathcal{O}(\epsilon^{m+1})$. This moment property is necessary for the construction of high-order approximations of singular Dirac delta source terms in spectral approximations of PDEs as was shown in Ref. [73]. To preserve high-order spatial accuracy it was further shown that the optimal value for the compact support must be $\epsilon = N_x^{-k/(m+k+2)}$. The compact kernel $\delta_\epsilon^{m,k}(x)$ in (2.24) has a maximum at its center. To achieve high-order accuracy, one has to relax positivity of the kernel, leading to the undershoots in Fig. 2.2.

For the approximation of the initial Dirac delta distribution function in (2.7), the vanishing moments of the regularized delta function yield an accurate representation of the zero moments of the deterministic initial state. Thus, in that case the regularized Dirac delta provides both spatial accuracy and the correct statistical properties of the distribution function at the initial time.

A naive alternative is to approximate $\delta(x)$ via a Gaussian PDF

$$\delta(x) \approx \frac{1}{\sqrt{2\pi}\sigma_x} \exp\left[-\frac{x^2}{2\sigma_x^2}\right], \tag{2.25}$$

with small variance $\sigma_x^2$. The Gaussian PDF, however, has no vanishing moments and can thus not yield high-order approximations to the Dirac delta. If the initial state is random, than the Gaussian distribution does correctly represent uncertainty in the initial state of the system.

### 2.4.3 Filtering for capturing discontinuities

Since (2.3) admits singularities we have to regularize these singularities in numerical approximations to avoid numerical instabilities. To this end, we once again resort to the regularized Dirac delta kernel (2.24). This time the kernel serves as a convolution filter

kernel as discussed in Ref. [169] to smoothen a function $y(x)$ as follows

$$\tilde{y}(x) = \int_{x-\epsilon}^{x+\epsilon} y(\tau)\delta_{\epsilon}^{m,k}(x-\tau)\mathrm{d}\tau. \tag{2.26}$$

Using a quadrature rule for approximation of the convolution integral, the interpolant $y_{N_x}$ is filtered as

$$\tilde{y}_{N_x}(x) = \int_{x-\epsilon}^{x+\epsilon} \delta_{\epsilon}^{m,k}(x-\tau)\sum_{i=0}^{N_x} y(x_i)l_i(\tau)\mathrm{d}\tau = \sum_{i=0}^{N_x} y(x_i)S_i(x). \tag{2.27}$$

The discrete filter $S_i$ is defined as

$$S_i(x) = \int_{x-\epsilon}^{x+\epsilon} l_i(\tau)\delta_{\epsilon}^{m,k}(x-\tau)\mathrm{d}\tau. \tag{2.28}$$

In vector notation, (2.27) and (2.28) take the form

$$\tilde{\mathbf{y}} = S\mathbf{y}. \tag{2.29}$$

The extension to tensorial form is straightforward. This convolution filter was shown in Ref. [169] to smoothen shock discontinuities while providing high-order accurate resolution away from shocks. In some cases a weak exponential filter [99] is needed to remove high-frequency numerical noise that appears in regions near the boundaries.

### 2.4.4 Monte Carlo simulations

The PDF and the moments of the PDF can be computed with a MC approach. In MC, realizations of $x_p$ and $u_p$ are computed by solving (2.1) with random coefficients $a$ drawn from a given PDF $f_a(A)$. Here, we use analytical solutions that will be discussed in the next section and that allow for a computationally efficient determination of a significant number of MC realizations, $N_s$. In all the tests considered, we found $N_s = 10^5$

realizations to be sufficiently accurate yielding a normalized error of the third moment less than 0.1%. The kernel density estimation, implemented in the MATLAB 2019b subroutine `kdensity`, determines the PDFs $f_{x_p}(X_p;t)$, $f_{u_p}(U_p;t)$, and $f_{x_pu_p}(X_p,U_p;t)$. The unknown correlation terms in the moment equations (2.8)–(2.13) are closed using MC realizations. The resulting a priori closed moment equations are integrated in time via the fourth-order Runge-Kutta (RK4) scheme.

## 2.5 Two Canonical Particle-Laden Flows

We consider two one-way coupled particle-laden flows—a uniform flow and an inviscid stagnation flow—for which the carrier phase velocity is described by analytical expressions. These are both important in their own right and serve as building blocks for more complex flows. Both flows admit analytical solutions for the corresponding particle-laden flow with constant deterministic forcing, $\phi$=constant. While this particle solution for the uniform carrier flow is well known, we are not aware of an analytical solution to the particle-laden stagnation flow. Analytical solutions are derived for both flows in the two following sections.

### 2.5.1 Uniform flow

By its definition, a uniform carrier flow is characterized by a constant velocity field $u$. To derive the analytical solution, we cast the particle transport equations (2.1) with the constant $u$ and the initial conditions $x_p(0) = x_{p_0}$ and $u_p(0) = u_{p_0}$ into a the following linear system of ODEs,

$$\frac{\mathrm{d}}{\mathrm{d}t}\begin{bmatrix} x_p \\ u_p \end{bmatrix} = \begin{bmatrix} 0 & 1 \\ 0 & -b \end{bmatrix}\begin{bmatrix} x_p \\ u_p \end{bmatrix} + \begin{bmatrix} 0 \\ bu \end{bmatrix}, \qquad b \equiv \frac{a}{\tau_p}. \tag{2.30}$$

The analytical solution of this system is

$$x_p(t) = x_{p_0} + ut + \frac{1}{b}(u - u_{p_0})\left(e^{-bt} - 1\right), \tag{2.31}$$

$$u_p(t) = u + (u_{p_0} - u)e^{-bt}. \tag{2.32}$$

Details of the derivation are provided in Appendix B.

The solution is plotted in Fig. 2.3 and shows that the response of the particle initially at rest to a fluid velocity is slower with increasing $b$, i.e., with increasing effective inertia. Hence, for a given $\tau_p$, higher values of the correction parameter $a$ decrease the particle's time response. At long times on the order of $\mathcal{O}(1/b)$ the particle velocity becomes equal to the carrier flow velocity $u$. When the relative velocity between the particle and the carrier phase (also called interphase velocity) becomes zero, then the particle position increases linearly at its constant advection rate $u$.

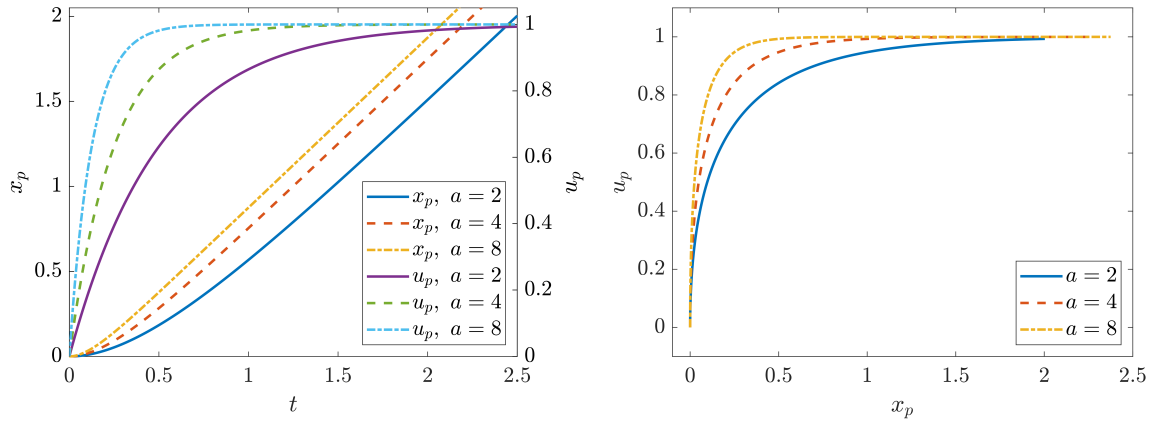


**(a)** **(b)**

**Figure 2.3.** Time dependence (a) and phase space (b) of the particle dynamics in the constant uniform carrier flow.

### 2.5.2 Stagnation flow

The stagnation carrier velocity field, $\mathbf{u} = (u, v)^\top$, is given by the Hiemenz analytical solution for an inviscid, irrotational flow [176] in the domain $x \in [-\infty, 0]$ as follows,

$$u = -kx, \qquad v = ky$$

where $y$ is the coordinate perpendicular to the flow direction, and $k$ is a constant. The viscous boundary layer solution near a wall at $x = 0$ is available as well [177]. It predicts the boundary layer thickness of $\delta = \sqrt{\nu/k}$, too thin to affect the particle dynamics.

Along the center line $y = 0$, the flow is one-dimensional with a stagnation point at $x = 0$ and velocity

$$u = -kx. \tag{2.33}$$

With the carrier velocity at the particle location $x_p$ is $u = -kx_p$ (2.1) can be cast into a linear dynamic system,

$$\frac{\mathrm{d}}{\mathrm{d}t}\begin{bmatrix} x_p \\ u_p \end{bmatrix} = \begin{bmatrix} 0 & 1 \\ -kb & -b \end{bmatrix}\begin{bmatrix} x_p \\ u_p \end{bmatrix}. \tag{2.34}$$

The analytical solution to this system is derived in Appendix B and is characterized by the eigenvalues of the $2 \times 2$ matrix in (2.34)

$$\lambda_1 = \frac{-b - \sqrt{b(b-4k)}}{2}, \quad \lambda_2 = \frac{-b + \sqrt{b(b-4k)}}{2}. \tag{2.35}$$

Their real and imaginary parts are plotted in Fig. 2.4, for $b \in [0, 8]$ and $k = 1$. For $0 < b < 4k$, the eigenvalues are imaginary with negative real part. In that case, the solution of the system (2.34), i.e.,the particle phase solution, is well-known to tend towards

an inward spiral in the phase plane as plotted in Fig. 2.5c. Before it reaches the spiral singularity, however, the particle will have crossed the $x = 0$ line where the wall is located. This is, of course, not possible and the particle trace has to terminate at $x = 0$. Alternatively, we can interpret the solution as a physical solution of a particle trajectory in an opposed jet carrier flow. For $b > 4k$, both eigenvalues are real and negative, in which case the particle moves towards an inward node in the phase space $x_p - v_p$. A bifurcation in particle dynamics from a spiral to a node occurs at $b = 4k$. Figure 2.5c shows the particle phase when the stagnation point is an inward node and an inward spiral, for two different initial conditions.

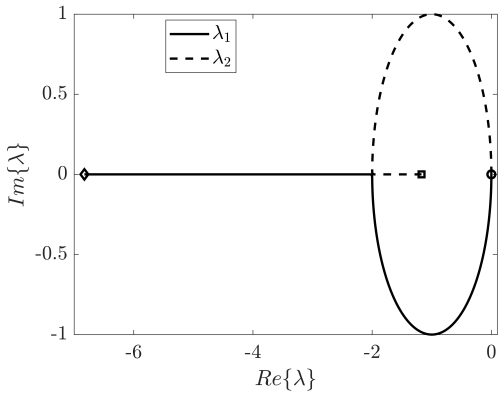


**Figure 2.4.** Imaginary and real part of the eigenvalues $\lambda_1$ and $\lambda_2$ in (2.35), for $b \in [0, 8]$. The circle corresponds to $b = 0$, and the diamond and square to $b = 8$ for $\lambda_1$ and $\lambda_2$, respectively.

The analytical solutions for the particle's position and velocity, $x_p(t)$ and $u_p(t)$, versus time are plotted in Figs. 2.5a and 2.5b. The particle reaches the stagnation point for any forcing $b = a/\tau_p$. The collision of the particle with the wall for the stagnation flow case is indicated by the red dot in the graphs 2.5a, 2.5b and 2.5c.

### 2.5.3 Impact of stochastic forcing

The effect of a stochastic forcing on the particle-laden uniform and stagnation flows is studied for the cases and parameters collated in Table 2.1. For both flow regimes, we

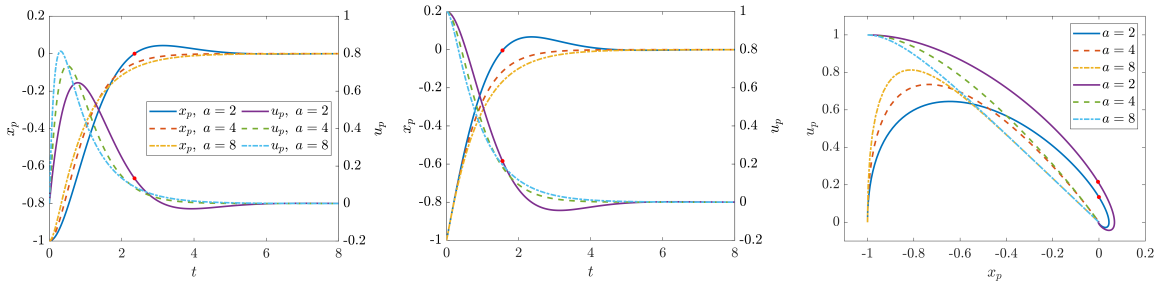


**(a)** **(b)** **(c)**

**Figure 2.5.** Solutions for particles released at rest (a) and at flow condition (b) in a stagnation flow with $k = 1$ for different values of the parameter $b$. The phase space plot in (c).

consider particles initialized at rest. For the stagnation flow, we also consider the particles initialized according to the carrier flow velocity.

**Table 2.1.** Flow regimes and parameter values considered in the simulations.

| **Test case** | $x_{p_0}$ | $u_{p_0}$ | $u$ | $\tau_p$ |
|---|---|---|---|---|
| Uniform flow, particle launched at rest (UF) | 0 | 0 | 1 | 0.25 |
| Stagnation flow, particle launched at rest (SFR) | $-1$ | 0 | $-x_p$ | 1 |
| Stagnation flow, particle launched at flow conditions (SFF) | $-1$ | 1 | $-x_p$ | 1 |

For each of these cases, we consider three PDFs, $f_a(A)$, for the random variable $a$ in the drag correction factor defined in (2.2) including a uniform, normal and beta distribution, all with the same mean $\mu_a$ and standard deviation $\sigma_a$ (Fig. 2.6). For the stagnation flow, $f_a(A)$ is selected to have a non-zero probability in the interval $0 < a/\tau_p < 4k$ to ensure that all particles reach the wall at a finite time (according to the deterministic solution). Also investigated is the effect of deterministic versus stochastic initial conditions.

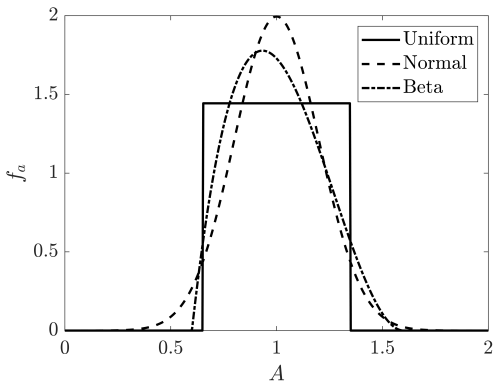


**Figure 2.6.** Uniform, normal and beta ($\mathcal{U}$ , $\mathcal{N}$ , $\mathcal{B}$) PDFs selected for the random parameter $a$. All three PDFs have the same mean $\mu_a = 1$ and standard deviation $\sigma_a = 0.2$, i.e., $a \sim \mathcal{U}[1 - \sqrt{12}/2, 1 + \sqrt{12}/2]$, $a \sim \mathcal{N}[1, 0.2]$, and $a \sim \mathcal{B}[2, 3] + 0.6$.

## 2.6 Simulation Results and Discussion

### 2.6.1 Uniform flow: Monte Carlo results

The PDFs $f_{x_p}(X_p; t)$ and $f_{u_p}(U_p; t)$ obtained via MC solution of (2.1) for the uniform flow with the uniform forcing distribution $f_a(A)$ and deterministic initial conditions are depicted in Fig. 2.7. Starting from the deterministic Dirac delta initial distribution, both $f_{x_p}(X_p; t)$ and $f_{u_p}(U_p; t)$ first widen over time, while showing a skewness, i.e., a bias, towards the upper range of the $X_p$ and $U_p$ values, where more particles accumulate. This bias reflects the particles' asymptotic behavior in the limit of an infinite response time, $\tau_p \to \infty$, in which case all the particles congregate on a step function in time. After the initial widening, the velocity distribution narrows with time as the particles' velocity settles to the uniform carrier flow velocity. The temporal evolution of the PDFs has a characteristic time scale on the order $\mathcal{O}(\tau_p/\overline{a})$. At later times, the velocity distribution returns to the Dirac delta and the corresponding position distribution is advected at constant velocity $u$ without changes in time.

The means $\bar{x}_p(t)$ and $\bar{u}_p(t)$, plotted with their corresponding two standard deviation bandwidths in Fig. 2.8, tell a similar story. The mean particle velocity $\bar{u}_p(t)$ increases

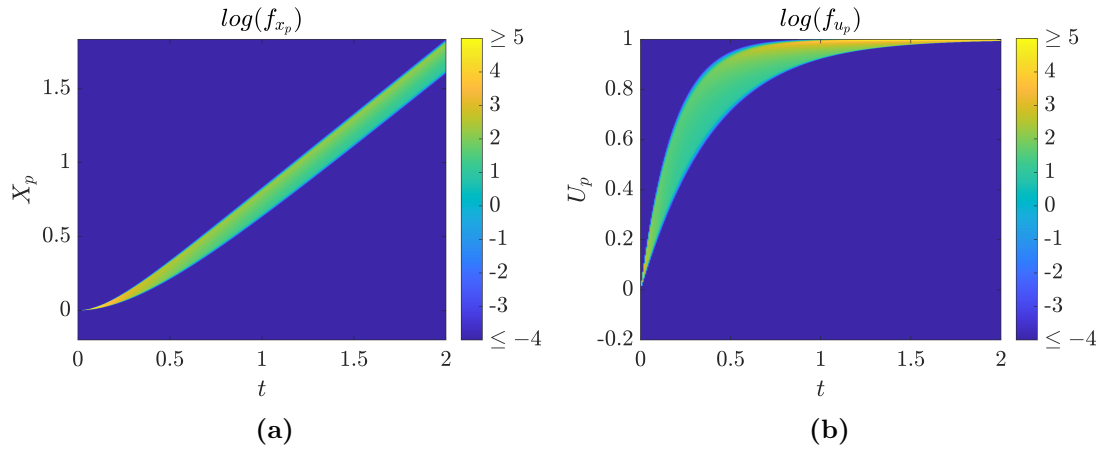


**Figure 2.7.** PDF of particle position (a) and velocity (b) for the UF test case carried out with MC with a uniform forcing distribution.

from its zero initial state and settles to the constant carrier velocity at $t \to \infty$. Associated with the acceleration and settling is an initial increase in the velocity bandwidth that then returns to zero at later times. Consistent with the velocity bandwidth, the position bandwidth grows initially and then remains constant when the particles settle.

Per definition, and as confirmed by Fig. 2.8, the mean of the solution must be contained in the interval of deterministic limit trajectories. Moreover, because $x_p(a)$ and $u_p(a)$ are monotonically increasing with $a$ it follows that

$$\overline{x}_p \in \left[\min_a \{x_p(a_{\min}), x_p(a_{\max})\}, \max_a \{x_p(a_{\min}), x_p(a_{\max})\}\right],$$
$$\overline{u}_p \in \left[\min_a \{u_p(a_{\min}), u_p(a_{\max})\}, \max_a \{u_p(a_{\min}), u_p(a_{\max})\}\right],$$

where $a_{\min} > 0$ and $a_{\max}$ denote a minimum and maximum value of $a$. This suggests that $\overline{x}_p \approx x_p(\overline{a})$ and $\overline{u}_p \approx u_p(\overline{a})$, i.e., that the mean solution is equal to the deterministic solution at the mean stochastic forcing.

The moment equations provide further insight. Because of the correlation terms $\overline{\phi' u'}$ and $\overline{\phi' u'_p}$, the governing equations for the mean position and velocity in (2.8) and (2.9), respectively, are different from the deterministic equations (2.1) with $a = \overline{a}$. But the term

$\overline{\phi' u'}$ is zero for the uniform flow case because $u' = 0$. Moreover, the correlation term $\overline{\phi' u'_p}$ in (2.9) is negligible, but not zero. Thus, to a first approximation $\overline{x}_p \approx x_p(\overline{a})$ and $\overline{u}_p \approx u_p(\overline{a})$. For a random solution with a uniform stochastic forcing distribution, the root mean square difference over the time interval is 0.0073 for the position and 0.0062 for the velocity.

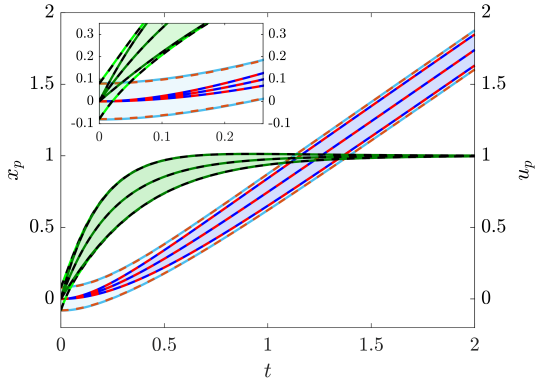


**Figure 2.8.** Two standard deviation interval along the mean for the test case UF with a uniform forcing distribution. In dashed green the particle velocity computed with MoD and in black with MC. In dashed red the particle position computed with MoD and in blue with MC. Dark colors indicate dIC whereas light ones sIC.

With a zero carrier phase velocity perturbation, $u' = 0$, many of the correlation terms in the second central moment or variance of the velocity are also zero or negligible. Significant terms that remain are a damping term $-\overline{\phi}\sigma^2_{u_p}$ and the source term, $\overline{\phi' u'_p}(\overline{u} - \overline{u}_p)$. The latter is positive because the relative velocity is positive, $(\overline{u} - \overline{u}_p) > 0$, and because $\phi' = a'$ and $u'_p$ have the same sign since the particle velocity $u_p$ is monotonically increasing with respect to the forcing $\phi = a$. The positive source term is maximum initially and decreases as the particle velocity settles to the flow conditions. The damping term reduces the velocity variance to zero in the limit $t \to \infty$. Correspondingly, the PDF $f_{u_p}$ tends to the Dirac delta distribution (Fig. 2.7b). The combination of the temporal damping and forcing by the positive source leads to a maximum variance at times that are on the order of $\mathcal{O}(\tau_p/\overline{a})$. The particle position variance depicted in Fig. 2.9a shows an initial increase consistent with the increasing velocity variance and an increased spreading of random

particle trajectories. When the particles settle to the constant carrier flow condition, then all trajectories are advected at constant velocity. After that time the particle variance no longer changes.

In Fig. 2.9a, the variance of the particle velocity and position are plotted versus time for three different forcing distributions $f_a$ (uniform, normal and beta). The temporal trends for the different stochastic forcing are very similar because the mean forcing and its variance are chosen to be the same for the three forcing distributions. The damping term in the velocity variance equation, which depends on the mean forcing and velocity variance only, is therefore not affected by the shape of the forcing distribution. The source correlation term, however, is directly dependent the forcing fluctuations, $\phi'$, which leads to differences in the velocity and position variances for different shapes of the forcing distribution of up to 15%.

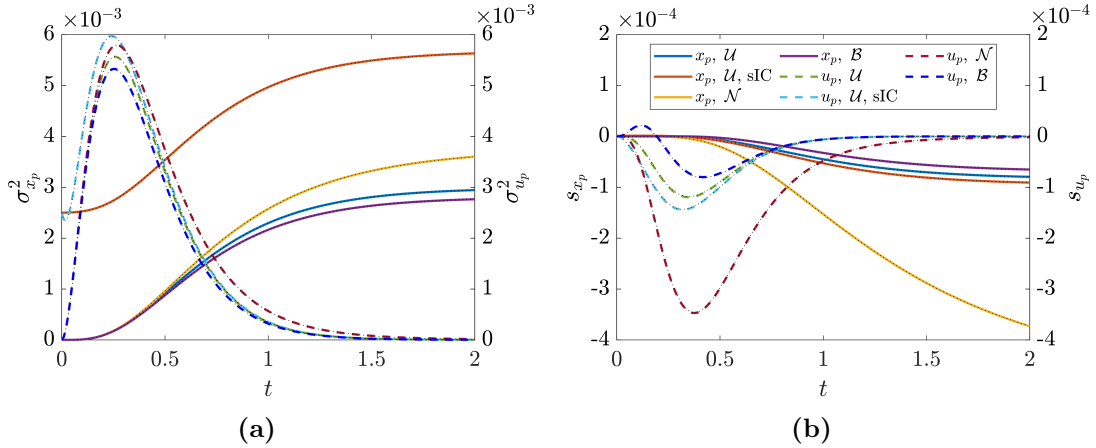


**Figure 2.9.** Computations for the UF case with MC in color lines and with the MoM in black dots of the (a) second and (b) third central moments for the particle position and velocity and the three PDFs considered for $a$ (see Fig. 2.6) and dIC. It is included the case of sIC for the uniform distribution. The legend in (b) is valid for (a) as well.

The third central particle position and velocity moments evolve in a similar way as the variances (Fig. 2.9b). The third velocity moment, $s_{u_p}$, experiences a negative growth followed by an asymptotic decay to zero (or the Dirac delta in the PDF sense as observed

above). The third position moment, $s_{x_p}$, first decreases and then asymptotically evolves to a constant value. Both the minimum in $s_{u_p}$ and the plateau in $s_{x_p}$ occur at slightly later times as compared to the minimum in $\sigma_{u_p}$ and $\sigma_{x_p}$. The difference in the factors $2\phi/\tau_p$ and $3\phi/\tau_p$ in equations (2.11) and (2.13) are assumed to be at least partially responsible for causing this shift in the maximum. The similarity in variance and skewness trends would suggest that the third moment dynamics might also be primarily affected by a positive sourcing and a damping. To verify this, the correlation terms in (2.13) are plotted versus time in Fig. 2.10. Clearly, the damping term $-\overline{\phi} s_{u_p}$ has a major influence on the long term response. However, there is no single dominant source term. While the term $\overline{\phi' {u'_p}^2}(\overline{u} - \overline{u}_p)$ plays a similar role as the positive source term in the variance equation, the other correlation terms are not negligible and contribute also. Surprisingly perhaps is that the term with fourth order correlations, $-\overline{\phi' {u'_p}^3}$, is dominant, an indication that the tail behavior of the solution PDF and tail behavior of the forcing function has a considerable impact on the higher central moment solution of the solution. This is confirmed by the deviation in the third central moment evolution of up to 200% for different forcing distributions. We plan to report further on the tail behavior of the PDF in the near future.

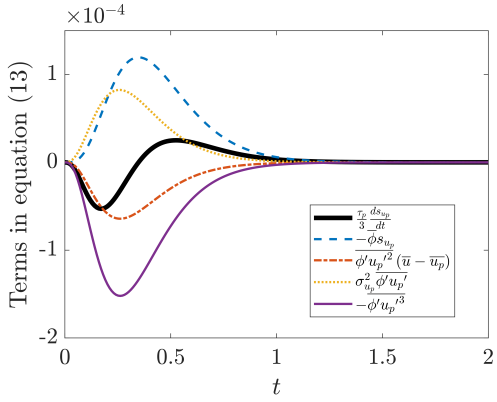


**Figure 2.10.** Terms in equation (2.13) versus time $t$ for the UF case with dIC.

The solution with stochastic initial condition (sIC) is plotted in Figs. 2.8 and 2.9. It shows that while the trends in the position and velocity mean and variance are similar

to those determined with a deterministic initial condition (dIC), the sIC solution is offset as compared to the dIC solution. The offset is according to the initial position deviation of $\sigma_x = 0.05$. Time integration of (2.10) from time zero to a time $t$ confirms that exactly this term $\sigma_x(t = 0)$ appears at the initial time, $t = 0$. The offset in Fig. 2.9 does not change significantly over the time interval $[0, t]$, which implies that the term $\overline{x_p' u_p'}$ in (2.10) is small. MC simulations confirm this and show that the term has a maximum value of 0.002 over the time interval. Because of the damping term the velocity variance and third central moment goes to zero in the asymptotic time limit for both deterministic and stochastic initial conditions.

### 2.6.2 Uniform flow: Method of Distributions

The solution of the governing equation for the PDF in (2.3) is grid-resolved for the uniform flow case using a spectral grid with $N_{X_p} \times N_{U_p} = 300 \times 300$ collocation points and a uniform grid in $A$ direction with $N_A = 200$. The CFL condition is set to 0.8. The Dirac delta distribution function for dIC is regularized according to $\delta_\epsilon^{k,m}$ in (2.24) with an optimal scaling $\epsilon = 0.05$, and $m = 5$ zero vanishing moments and smoothness $k = 2$.

Figure 2.11 shows snapshots of $f_{x_p u_p}$ (contours), $f_{x_p}$ (left and bottom axes) and $f_{u_p}$ (right and top axes) at three consecutive times. For reference, the mean of the particle phase solution (black line) is superposed in the contour plot. At time $t = 0$, the marginals are initialized according to the regularized Dirac delta as shown in Fig. 2.11a. At a later time, $t = 0.54$, the joint PDF $f_{x_p u_p}$ has traveled along the mean in the $X_p - U_p$ coordinate system and has widened and deformed (contours in Fig. 2.11b). The marginal $f_{x_p}$ and $f_{u_p}$ show that the particles have a bias towards the larger values of the position and the velocity. That is consistent with the observations in the moments discussed previously; because the particles with smaller response time, $\tau_p/A$, travel a distance greater than the slower responding particles, they cluster at large $X_p$. Those fast particles furthermore reach their terminal settling velocity faster and thus there is a similar clustering in $f_{u_p}$.

The convexity of the PDFs is an indication that the clustering is more pronounced towards larger values. The schematic in Fig. 2.12 underscores this and shows how the characteristic paths with non-constant advection velocity for different $A_i$ leads to a convex probability density.

At time $t = 1.6$, the velocity PDF has evolved towards a Dirac delta function represented by a narrowly supported distribution centered at $U_p = 1$. The numerical solution successfully captures this PDF behavior despite showing some minor fluctuations caused by Gibbs oscillations. The accuracy of the MoD solution at this time relies largely on the number of vanishing moments $m$ of the regularization of the Dirac delta function at $t = 0$. Because the number of vanishing moments are specified to be greater than five, the first up to the fifth moment are accurately preserved even at times when the distribution function tends to the singular Dirac delta distribution. This accuracy preservation is confirmed by the results in Fig. 2.8 that compares the time evolution of the mean and variance determined with the MoD and MC approach and that shows no discernible difference between the solutions of the two approaches.

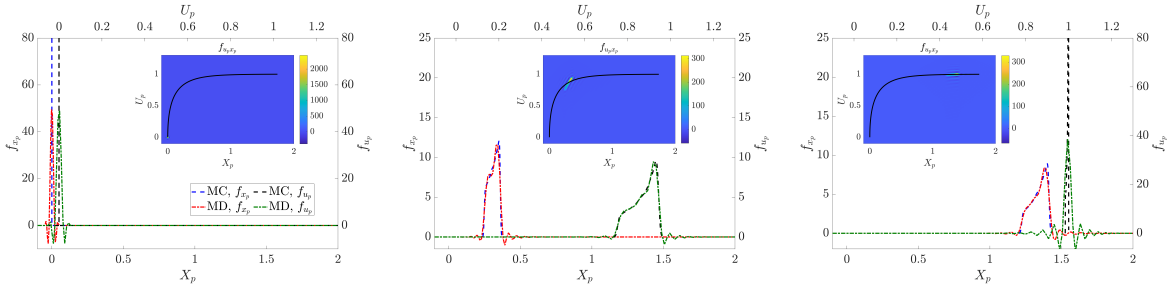


**Figure 2.11.** Marginals $f_{x_p}$ and $f_{u_p}$ at $t = [0, 0.54, 1.6]$ in $(a)$, $(b)$ and $(c)$ respectively for the UF test case with dIC and the uniform distribution for $f_a$. Contour plots of the joint PDF $f_{x_p u_p}$ superposed with the mean of the particle phase solution.

A few remarks on the accuracy of the numerical solution of the equation (2.3):

*Remark 1*: Consistent with the findings in [98], the use of high order methods is necessary to compute an accurate solution of the joint PDF $f_{ax_pu_p}$ such that the marginals

determined according to (A.12)-(A.14), are in good comparison with MC results. To underscore the importance of numerical discretization, we compare the Chebyshev spectral discretization with a first and a second order upwind finite difference (FD) schemes. Fig. 2.13a shows that the FD schemes are overly dissipative as compared to the spectral method if the same number of grid points are used. The root mean square error (RMSE) between resolved MC results and the spectral solution is 0.064, whereas the RMSE for the first and second order FD method is significantly larger at 0.280 and 0.180, respectively. To mitigate the dissipation and inaccuracy, FD requires an excessive resolution for the computation of the PDF after marginalization.

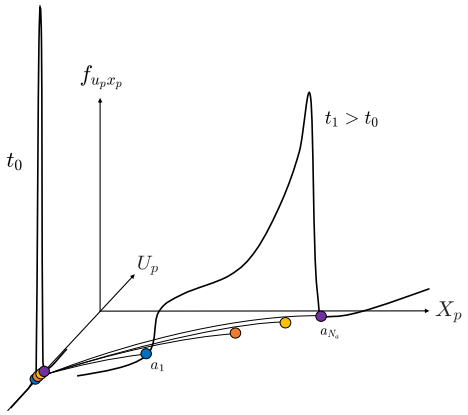


**Figure 2.12.** Schematic evolution in time of the particle phase PDF $f_{x_p u_p}$ for the UF test case.

*Remark 2*: The spectral solution shows dispersion errors in the form of high-frequency oscillations in the distribution function. These are induced by the high-order approximation of the steep gradients in the PDF that in turn are a result of the steep gradient in the uniform forcing distribution $f_a$. These dispersion errors, however, average out and turn out to have no significant effect on the numerical accuracy of the first three moments (see Fig. 2.13b for the third central moment). The second order FD scheme also exhibits dispersion errors, but the FD's oscillations do not average out and the moments are not accurately captured using this discretization.

*Remark 3*: For deterministic initial conditions, the regularization of the Dirac delta

is necessary to accurately compute the moments of the evolving distribution function. Particularly, the vanishing moment condition ensures that the evolution of the third moment (Fig. 2.13b) is not affected by the numerical approximation as compared to Dirac delta regularization with only two vanishing moment $m = 2$ in (2.24), or a Gaussian distribution function.

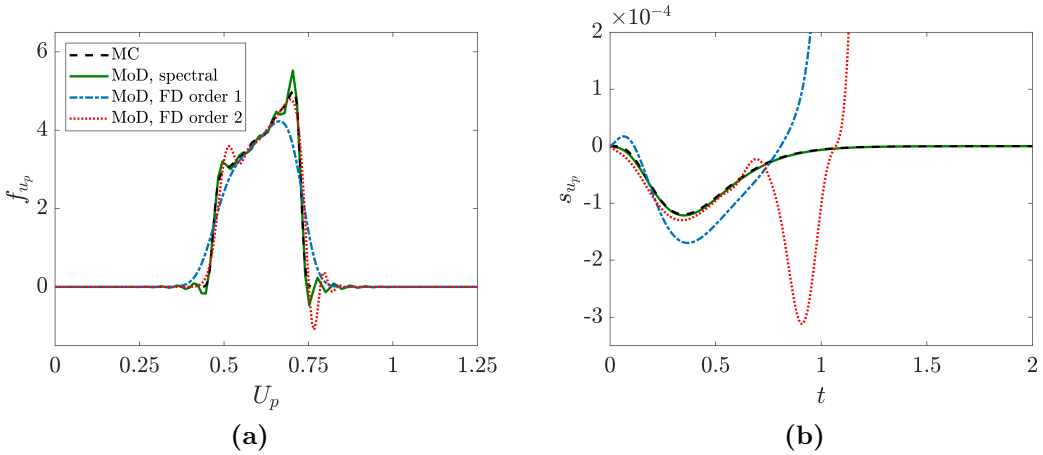


**(a)** **(b)**

**Figure 2.13.** Comparison between the spectral discretization and finite difference upwind discretization with first and second order for (a) $f_{u_p}$ at $t = 0.24$ and (b) $s_{u_p}$. Both figures are for the UF test case with dIC with a uniform forcing distribution.

### 2.6.3 Stagnation flow

In the particle-laden stagnation flow, the relative (interphase) velocity is not only affected by the evolution of the particle phase as is the case in the uniform flow but also by the evolution of the carrier phase velocity along the particle's path. The temporal development of the random particle position and velocity therefore displays a considerably more complex behavior as compared to the uniform flow. Because of the spatial dependence of the carrier flow, the particle solution is furthermore non-trivially dependent on its initial condition. We consider two initial conditions described in section 2.1, one with the particles starting at rest (Case SFR) and another with the initial particle velocity specified at the carrier flow's velocity conditions (Case SFF). We discuss the MC and MoD solutions for

each case below.

**SFR case: Monte Carlo results**

The mean trends with two standard deviation bandwidth determined with the MC approach for a uniform forcing distribution are plotted in Fig. 2.14. To discuss the SFR case three stages of development are identified. In the first stage ($t < 0.6$) each particle identified with a counter $i$ accelerates in positive $x$-direction at a rate $a_i(-kx_{p_i} - ku_{p_i})/\tau_p$. Similar to the uniform flow case, the velocity and position variance both increase in this stage with varying acceleration of the stochastically forced particles. The second central moment plotted versus time in Fig. 2.15a confirms the growth of the particle variance in this stage.

In a second stage ($0.6 < t < 1.6$), the particle with the smallest response time $\tau_p/a_{max}$ –the fastest responding particle with acceleration rate $a_{max}(-kx_{p_{max}} - ku_{p_{max}})/\tau_p$– has accelerated to the carrier velocity ($t = 0.6$). After that, the flow velocity continues to decrease (stagnates) along this particle's path. Because of the particle's inertial response, the particle's velocity, however, does not decrease equally fast along the particle's path. Effectively, the relative velocity of this particle therefor becomes negative. In other words, the particle starts to decelerate. As more particles with larger response time reach the carrier flow conditions, more particles start to decelerate until all particles have a negative relative velocity. During this second stage the velocity variance of the particle phase decreases to a minimum at $t \sim 1.6$, ( Fig. 2.15a).

In a third stage $t > 1.6$, when the relative particle velocity is smaller than zero ($u_p > u(x_p)$) for all the particles, the cloud decelerates to a decreasing carrier velocity and the particle velocity variance increases. The variance increase mechanism is similar to the first stage and the uniform flow, in which a time varying carrier velocity in combination with a random forcing leads to a variance increase in the particle velocity. In the stagnating flow, the random particle cloud compresses with a decreasing position variance before the

wall is reached.

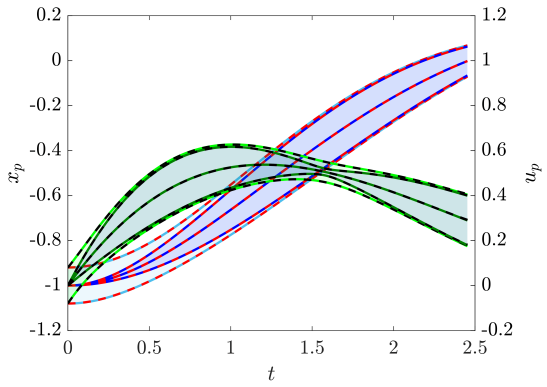


**Figure 2.14.** Two standard deviation interval along the mean for the test case SFR with a uniform forcing distribution. In dashed green the particle velocity computed with the MoD and in black with MC. In dashed red the particle position computed with MoD and in blue with MC. Dark colors indicate dIC whereas light ones sIC.

As opposed to the uniform flow case the carrier flow's velocity fluctuation, $u'$, for the stagnation flow is non-zero which affects several terms in the moment equations. Even with these extra terms, just like for the uniform flow, the mean stagnation flow solution described by (2.8) and (2.9) can also be approximated by the solution of the deterministic equation for $a = \overline{a}$. The latter position and velocity solution have a root mean square deviation of 0.0073 for $\overline{x}_p$ and 0.0053 for $\overline{u}_p$ as compared to the former. Both the terms $\overline{\phi' u'}$ and $\overline{\phi' u'_p}$ turn out to be negligible in (2.9).

The evolution of the velocity variance as governed by its moment equation (2.11) is affected by the second term on the right hand side, i.e.,$\overline{\phi' u'_p}(\overline{u} - \overline{u}_p)$. At $t \sim 1.6$ the relative velocity $(\overline{u} - \overline{u}_p)$ in this term changes sign when the particle phase begins to decelerate after its initial acceleration. The sign of $\overline{\phi' u'_p}$ in this term changes at $t \sim 1.6$ also as follows: in the first stage $u_p$ is monotonically increasing for all the forcing values of $\phi = a$ according to the analytical velocity solution (2.32); in stage two, some particles are accelerating and others are decelerating which yields different signs for $du_p/d\phi$ depending on $\phi$. Upon ensemble averaging it turns out that the mean of $du_p/d\phi$ is positive prior to $t \sim 1.6$ and negative after. In the third stage $u_p$ is monotonically decreasing with respect to $\phi$. So, the

correlation term $\overline{\phi' u'_p}$ changes sign at $t \sim 1.6$ and thus the term $\overline{\phi' u'_p}(\overline{u} - \overline{u}_p) > 0$.

In addition to the damping term that was discussed for the uniform flow case, the first term on the right hand side in the velocity variance equations (2.11) also involves the term $\overline{\phi} \overline{u' u'_p}$ for the stagnation flow case. Similar to the sign change of $\overline{\phi' u'_p}$ at $t \sim 1.6$, the sign of $\overline{\phi} \overline{u' u'_p}$ is the same as $\overline{u} - \overline{u_p}$ because of a comparable behavior of $du_p/du$ and $du_p/d\phi$. As a result $\overline{\phi} \overline{u' u'_p}$ is negative before $t \sim 1.6$ and positive thereafter. The values of the term $\overline{u' u'_p}$ are between $-0.002$ and $0.002$ and are thus of the the same order as the velocity variance $\sigma^2_{u_p}$ (See Fig. 2.15a). The term $\overline{\phi} \overline{u' u'_p}$ therefor has a significant effect on the variance dynamics. At early times it reduces the growth of the variance and at later times it enhances growth as compared to the uniform flow, where the term is zero.

The third order correlation terms (the third and fourth term in (2.11)) are observed to have a negligible contribution to the particle variance evolution. In comparing the maximum magnitude of each of the terms in the right hand side of (2.11) with respect to the left hand side over the time interval, we find that the terms $\overline{\phi' u' u'_p}$ and $\overline{u' u'^2_p}$ have at most a 3.0% and 1.0% contribution whereas the first and second terms have a significant 120% and 152% contribution to the "variance acceleration".

Figures 2.15a and 2.15b include the variance evolution for several distribution functions of the forcing $f_a$. As in the uniform flow case, the effect of the shape of $f_a$ is small on the order of 5% in the velocity variance and slightly more (order of 10%) in the position variance. The general trends are not affected by the shape of the forcing PDF.

The third position moment is negative throughout the time interval considered (Fig. 2.15b) indicating a non-symmetric position distribution that is skewed towards larger values of the particle coordinate. To understand the evolution of the particle velocity's third moment, we differentiate between two stages; firstly, when the mean interphase velocity $\overline{u} - \overline{u}_p$ is positive and the skewness shows a bias towards higher velocity values similar to the uniform flow case and as also illustrated in Fig. 2.1. Secondly, when $\overline{u} - \overline{u}_p \sim 0$ at first after which it becomes negative, i.e., $\overline{u} - \overline{u}_p < 0$ with a near zero skewness first

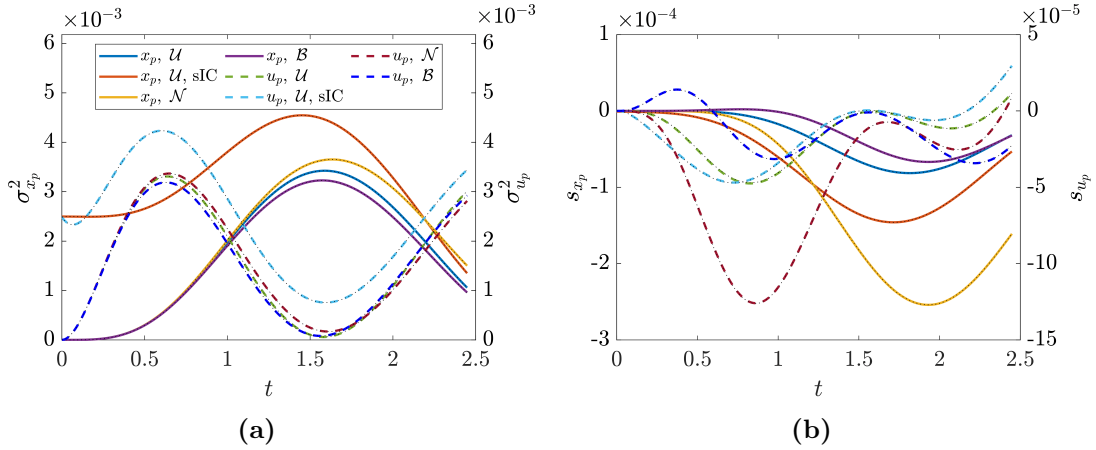


**Figure 2.15.** Computations for the SFR case with MC in color lines and with the MoM in black dots of the (a) second and (b) third central moments for the particle position and velocity and the three distributions considered for $a$ (see figure 2.6) and dIC. It is included the case of sIC for the uniform distribution. The legend in (a) is valid for (b) as well.

and decreasing after showing a bias towards small values of the particle coordinate when $\overline{u} - \overline{u}_p < 0$ right before the particles hit the wall. This second stage can be also understood through the evolution of the PDF that consists of the formation of the singular Dirac delta distribution for which the skewness is zero and its consequent behavior as illustrated in Fig. 2.1b with a change of the bias in the PDF.

Like in the uniform flow case, the evolution of the third central moment is affected by many different terms in the velocity skewness equation (2.13) as shown in Fig. 2.16. The fourth order correlation terms are important in the stagnation flow also, but because the velocity fluctuation is non-zero, $u' \neq 0$, the evolution of terms that involve $u'$ are non-trivial and require a separate and more in-depth analysis. We feel this is outside the scope of the current paper and we plan to report on the skewness behavior in more detail in future work.

Stochastic initial conditions do not only alter the evolution of the mean of the stagnation flow solution with dIC by a constant offset as was the case for the uniform flow (see Fig. 2.14), but the difference between the solutions with dIC and sIC changes

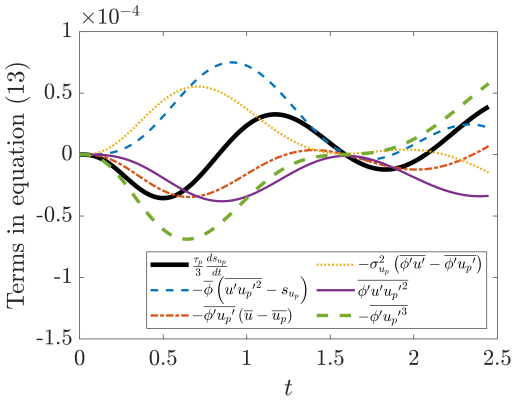


**Figure 2.16.** Terms in equation (2.13) versus time $t$ for the SFR case with dIC and a uniform forcing distribution.

considerably over the time interval and specifically at early times. The variance of the particle position and velocity is initially offset according to its initial values as shown in Fig. 2.15a, but then the difference with respect to the dIC case decreases as time evolves. This reduction can be understood by considering the stagnation flow solution where particles can non-physically cross the wall (i.e.,an opposed jet flow). For this flow all particles move towards the same final state with $x_p = 0$ and $u_p = 0$ in the asymptotic time limit, $t \to \infty$ and thus the position and velocity variance tend to zero.

Between the initial time and the infinite time, the terms $\overline{x_p' u_p'}$ and $\overline{u' u_p'}$ are responsible for the reduced variances. The contribution of $\overline{u' u_p'}$ which is negative for $t < 1.6$, particularly, causes a greater increase in the damping term for sIC as compared to dIC at early times. When the interphase velocity changes sign at $t \sim 1.6$ this term becomes positive and it will have the opposite effect. A physical interpretation is as follows: a more energetic initial state with higher velocity variance is more resistant to changes induced by stochastic forcing resulting in greater damping at early times. The term $\overline{x_p' u_p'}$ is positive in the acceleration stage and negative in the deceleration stage and its magnitude is greater for dIC as compared to sIC consistent with greater values of $u_p'$ for sIC.

Another considerable difference between the dIC and sIC is that the minimum in the velocity variance at $t \sim 1.6$ is non-zero for the stochastic case, while it is nearly zero

for the deterministic case. As a consequence, the singularity in the distribution function when the relative velocity changes sign can be expected to be less significant and the PDF can be expected to have a broader support.

**SFR case: Method of Distributions**

Using the same grid as was used for the uniform flow case, the PDF solution for the SFR case with a uniform forcing distribution, $f_a$, and dIC are computed and plotted for three instances in Fig. 2.17 at $t = 1.22$, $t = 1.60$ and $t = 2.15$. At time $t = 0$ the initial condition is identical to the uniform flow case plotted in Fig. 2.11a and it is therefor not repeated in Fig. 2.17. The MC results are also plotted in Fig. 2.17 and they are in excellent agreement with the MoD results.

During the first stage ($t < 0.6$) the joint PDF $f_{x_p u_p}$ deforms along the mean of the particle trajectory (depicted by the black solid line) showing a non-linear clustering of the particles in the $X_p - U_p$ plane towards high values. During the second stage ($0.6 < t < 1.6$) some particles accelerate and others decelerate leading to the near singular Dirac delta distribution at $t \sim 1.6$ (Fig. 2.17b). At later times ($t > 1.6$) the PDF of the particle velocity increases on the left front (Fig. 2.17c), confirming a bias toward lower velocities in a deceleration field as discussed in the MC results.

The position PDF solution has an increasing bias towards the large value of $X_p$ which is consistent with the asymptotic infinite time behavior of the non-physical solution where particles are permitted to cross the wall and where both the particle velocity and position distribution evolve to a Dirac delta centered at $X_p = 0$ and $U_p = 0$.

**SFF case: Monte Carlo results**

In a final test, the particle velocity is initialized with the carrier phase velocity at the particle position. The MC results for the mean with a two standard deviation bandwidth are plotted versus time in Fig. 2.18. In the SFF case, the particle phase only

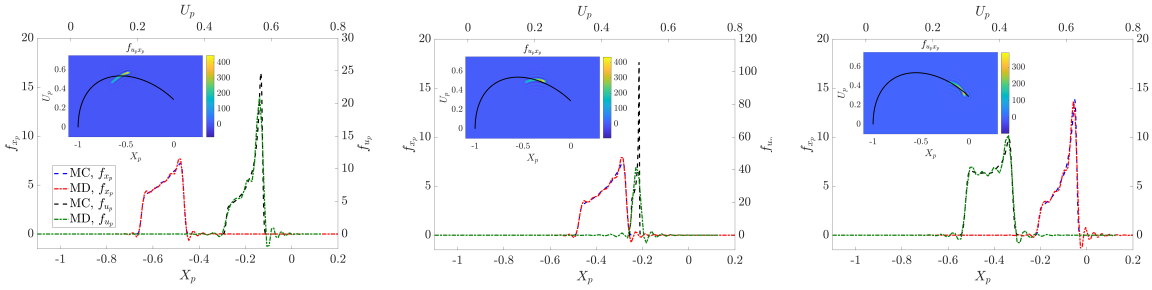


**Figure 2.17.** Marginals $f_{x_p}$ and $f_{u_p}$ at $t = [1.22, 1.60, 2.15]$ in $(a)$, $(b)$ and $(c)$, respectively, for the SFR test case with dIC and the uniform distribution for $f_a$. Contour plots are of the joint PDF $f_{x_p u_p}$ superposed with the mean of the particle phase solution.

decelerates which yields an evolution that is opposite to the uniform flow evolution as plotted in Fig. 2.1a, or an evolution that is very similar to the third "deceleration" stage of the SFR case for $t > 1.6$. The mean velocity decreases monotonically when the mean particle position increases towards the wall. This evolution is accompanied by an increase in the variances of both $x_p$ and $u_p$.

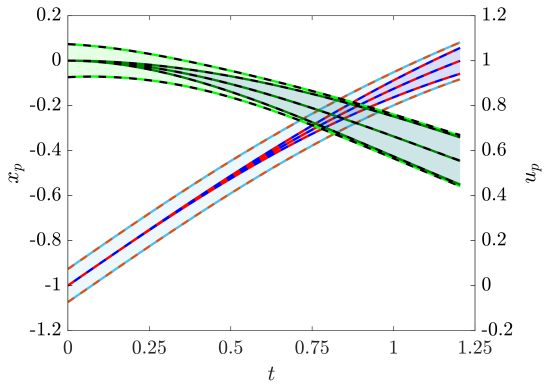


**Figure 2.18.** Two standard deviation interval along the mean for the test case SFF with a uniform forcing distribution. In dashed green the particle velocity computed with the MoD and in black with MC. In dashed red the particle position computed with MoD and in blue with MC. Dark colors indicate dIC whereas light ones sIC.

Because the SFF case is similar to the other two cases, the moment evolution results do not shed any additional light on the evolution of the stochastically forced particle phase. It is therefor omitted here.

**SFF case: Method of Distributions**

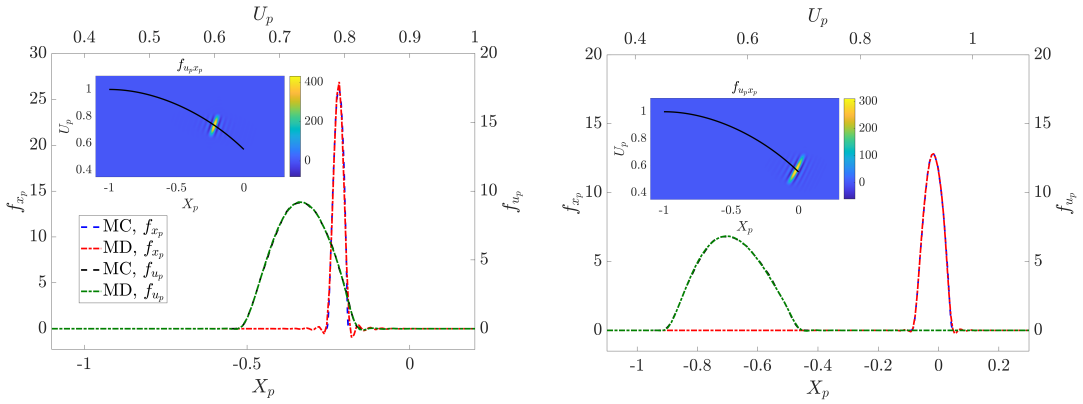


**(a)** **(b)**

**Figure 2.19.** Marginals $f_{x_p}$ and $f_{u_p}$ at $t = [0.87, 1.17]$ in $(a)$ and $(b)$ respectively,for the SFR test case with dIC and a uniform forcing distribution. Contours of the joint PDF $f_{x_p u_p}$ superposed with the mean of the particle phase solution.

The results for the uniform distribution forcing, $f_a$, for the SFF case are also very similar to the deceleration stage of the SFR case. Rather than reiterating that discussion, we choose a different stochastic forcing according to a beta distribution for $f_a$ in Fig. 2.6 which does not have steep gradients in $f_a$ like the uniform distribution. For a grid with the same size as described before, the distribution results for two different times are shown in Figs. 2.19a and 2.19b with a deterministic initial condition. Clearly, the solution does not show Gibbs oscillations and the MC results and the MoD are in excellent agreement.

As time evolves, the PDF of the particle position is advected with a positive characteristic velocity (2.14) and the particle velocity with a negative velocity according to (2.15). The PDFs widen in time as the response times of random particles is different for different stochastic forcing leading to variations in the particles velocities and positions. Both the position and velocity PDF display a non-Gaussian (non-symmetric) trend that is more subtle than for the uniform forcing.

### 2.6.4 Deterministic initial condition with regularized Dirac delta functions

One of the most important findings of this work relies on the use of regularized Dirac delta functions to compute deterministic initial conditions. Originally developed for singular source terms that account for the coupling of the Eulerian and Lagrangian phases in Ref. [73], this technique and its condition of vanishing moments is particularly convenient to account for dIC described by the Dirac delta function. To numerically compute equation (2.3), the initial conditions have to be accordingly discretized. As it is evident, is not possible to prescribe a real Dirac delta function numerically meaning to include the singularity of an infinite value in a single point and zero in the rest. Alternatively, the use of a regularization of the initial condition according to Ref. [73] is computationally doable. A Dirac delta $\delta(x)$ function is characterized by a first moment $x$ and zero for any of the next moments. The vanishing moment condition for its regularization allows to provide a number $m$ of moments that can be accurately represented by this regularization. This meas that we can define a regularized Dirac delta $\delta_\epsilon^{m,k}$ that has the first moment $x$ and up to $m$ zero moments (ideally indefinite zero moments as $\delta(x)$). Where $k$ is related to the curvature of the polynomial approximation and $\epsilon$ is the optimal support interval in which is defined. It is worth to mention that the parameter $m$ is the number of vanished moments if $m$ is an even number. On the contrary the number of vanished moments is $m-1$.

To illustrate the power of this technique, we show in Fig. 2.20a and 2.20b the evolution in time of the second and third moment of the SFR case with dIC and $a$ following the uniform distribution for different approximations of the Dirac delta function. It is compared the MC results with the MoD using a Gaussian, and two regularized Dirac delta functions with $m = 2$ and $m = 3$ respectively. For the MoD we use the Chebyshev collocation method as well and the same grid than in Section (2.6.3).

For the mean, all the approximations match the MC results (not showing here), as the Gaussian or the numeric Deltas can accurately be set up to have a certain mean. On the contrary, the Gaussian can not be defined such that the variance is zero. Consequently, the results with dIC are not properly represented in this way. The same happens for a numerical Delta with $m = 2$, since is an even number and then the vanishing moment conditions is $m - 1 = 1$ (only the mean is accurately represented). Note that the initial variance of the Gaussian and the $\epsilon$ for the numeric Deltas are different. To account for the dIC properly, we use a numeric Delta with $m = 3$. As opposed to the previous approximations, the first three moments would match the real Dirac delta function. In other words, the regularization allows the solution to account up to the moment three properly. The MoD results for this case match the MC results for the mean, deviation and third central moment (see Figs. 2.20a and 2.20b). This confirm the regularization of the Dirac delta function developed in [73] as a suitable tool for stochastic studies in general when deterministic initial conditions are applied in a numerical context.

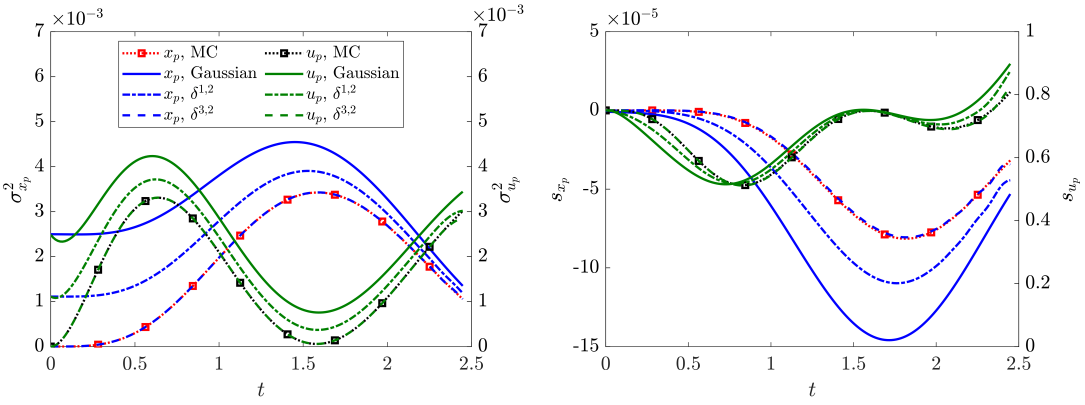


**Figure 2.20.** Comparison of different numeric approximations of the Dirac delta function for deterministic initial conditions for the SFR test case when $a$ follows the uniform distribution for (a) the second central moments and (b) the third central moments.

## 2.7 Summary of results

Several techniques and models including a Monte Carlo approach, a method of moments and a method of distributions are developed and compared for analysis of particle dynamics with stochastic forcing in one-way coupled Eulerian-Lagrangian formulations. Random solutions of two canonical flow problems are discussed including a particle phase accelerated in a uniform carrier flow and a particle phase released in a stagnation carrier flow with two initial conditions, one at rest and one initialized at the carrier flow velocity.

Starting from the Lagrangian particle equations for position and velocity with stochastic forcing, a closed PDF formulation is derived. A single hyperbolic partial differential equation, whose characteristic advection velocities are non-constant, governs the evolution of the PDF solution. In a single spatial dimension, the PDF depends on three variables at a given time, including the position, the velocity and a forcing coefficient.

A high-order spectral method with discontinuity regularization is necessary for the accurate solution of the hyperbolic partial differential equation that admits discontinuities. A polynomial regularization of a Dirac delta function with $m$ vanishing moments is shown to accurately capture the first $m$ moments of the PDF solution in time.

Moment equations are derived for the first three moments of the particle position and velocity, representing the mean, variance and skewness of the PDF. Monte Carlo results are used to determine correlations terms and to close the system of moment equations.

Analytical solutions are derived for the system of two linear ODEs that govern the dynamics of particles with a deterministic forcing in a one-dimensional uniform flow and stagnation flow. The particle solution in the stagnation flow has its final state with a zero velocity at the wall. Depending on the relative forcing the particle manifolds in the phase space (position/velocity space) tends to either a node or spiral.

The mean solution with random forcing can be approximated within 1% using a mere single deterministic solution at the mean forcing for all flow cases considered.

In flows where all randomly forced particles accelerate or decelerate, the velocity variance increases driven by a single correlation source term. A damping terms counters this source term. When the particle velocity settles, the velocity variance reduces to zero because of this damping. Higher-order correlation terms are generally negligible in the velocity variance equation. The position variance increases in accelerating flows and decreases in decelerating flows, i.e.,the random cloud expands and compresses, respectively. When the relative velocity changes sign, the particle variance approaches zero and the PDF has a very narrow support.

The skewness of the distribution function has a bias towards the carrier velocity to which the particle accelerates or decelerates. The bias of the distribution function is non-linear and more significant towards to the tail ends of the distribution function. The skewness equation is driven by a sourcing and a damping similar to the variance equation, but with different response time. High-order correlation terms are significant suggesting a complicated tail behavior of the PDF.

## 2.8 Acknowledgments

Sections 2.1 through 2.6.3 and Section 2.7, are a reprint of the material as it appears in Ref. [2], "Lagrangian models of particle-laden flows with stochastic forcing: Monte Carlo, moment equations, and method of distributions analyses", D. Domínguez-Vázquez, G. B. Jacobs and D. M. Tartakovsky, *Physics of Fluids* 33, 033326, 2021. D. Domínguez-Vázquez: conceptualization, investigation, original draft preparation, visualization. G. B. Jacobs: conceptualization, supervision, review & editing. D. M. Tartakovsky: conceptualization, supervision, review & editing.

# Chapter 3

# Point-cloud models for particle-laden flows in closed-form

## 3.1 Introduction

The reduced point-particle method permits the simulation of millions of particles [36] that are commonly encountered in large scale problems. The model reduction comes with limitations both in terms of numerical approximation and physics omissions, that are well documented in literature [178, 179, 180, 63, 104, 59, 181, 182, 76, 95], including convergence issues and approximation of the singular point distribution over a grid, considerable empiricism in particle forcing, omission of physics such as the finite size particle effects and wake effects, subgrid turbulence-particle interactions and particle-particle interactions, etc.

Another method for reducing computational degrees of freedom is to use high-order approximation in the form of smooth macro-particles that distribute the particle influence over a mesh using a Gaussian distribution or a polynomial distribution function. This approach was first introduced for discontinuous Galerkin based particle-mesh methods in Ref. [183] and later for finite difference based methods in Ref. [170]. Much effort has gone into the development of high-order distribution functions (also referred to as projection kernels) in the context of EL methods to approximate either a Dirac delta distribution of a point-particle [73, 184] or to numerically model the flow around a finite sized particle in

a consistent and convergent manner [185, 75]. However, less efforts have been put towards ensuring high-order corrections to the point tracer method in physical and phase space that should naturally accompany a high-order Euler-Lagrange discretization method and a distribution function that is mathematically smooth up to a certain order. We refer to a "tracer", to the Lagrangian algorithm that computes trajectories along the inertial point particles' paths or point clouds in time.

To address the shortcomings of CIC and high-order PSIC methods, we coined the Subgrid Particle-Averaged Reynolds Stress-Equivalent (SPARSE) formulation in Ref. [57]. SPARSE is based on a method of moments to capture the effect of sub-cloud scales in one-way coupled simulations. The method of moments derives governing equations for the moments of the variables of interest by using a Reynolds decomposition of the variables in average plus fluctuations as $\eta = \overline{\eta} + \eta'$ where $\overline{\eta'} = 0$. The method of moments reduces the computational cost in comparison to sampling methods but requires closure. We refer to the literature for a review of the method of moments in the context of particle-laden flows (see for example Refs. [186, 187, 171, 2, 98] and references therein). By combining a Reynolds averaging with a truncated Taylor expansion of the forcing correction within a cloud, SPARSE augments the CIC method in two ways. Firstly, it provides a second order correction to the forcing. Secondly, it accounts for interphase, drift, kinetic energy and stresses. In Ref. [58], SPARSE was extended for the simulation of two-way coupled and non-isothermal particle-laden flows by modeling the cloud deformation with a bivariate Gaussian function whose principle strains depend on the subgrid scale strain tensor. In tests of a shock interaction with a particle cloud it was shown that SPARSE captures the same physics as the point-particle model, but requires two orders of magnitude fewer degrees of freedom [58]. This is because SPARSE allows to compute clouds of point-particles as a single points, reducing the amount of equations to solve. So far, the SPARSE tracer has been closed *a priori* with data from PSIC simulations.

Here, we propose a closed SPARSE algorithm [3] that makes the tracer predictive.

Following the SPARSE approach [57, 58], covariance terms are closed using a combination of averaging and Taylor expansion of the carrier phase variables around the mean cloud location. To enable the closure, the SPARSE tracer presented in Ref. [57] is first extended to account for position, velocity and temperature covariances, i.e., to account for second moments of the particle phase. The resulting particle cloud tracer has a second order correction to the motion and deformation caused by the carrier phase velocity field along its mean trajectory. We perform a variety of one-way coupling computations, suitable for dilute flows, to verify accuracy and convergence including one-dimensional tests with prescribed velocity fields, the two dimensional stagnation flow, and the three dimensional ABC flow. We also validate SPARSE with a simulation of an isotropic turbulence flow, where the gas is simulated with a Direct Numerical Simulation (DNS) solver and the SPARSE particles are traced in the DNS flow field.

## 3.2 Closed SPARSE: Governing Equations

### 3.2.1 Point-Particle Method

For completeness, we start the derivation of SPARSE from the dimensional point-particle equations that describe the kinematics, dynamics and heat transfer of a small spherical particle immersed in a carrier flow as follows [38, 188, 170]

$$\frac{d\tilde{\boldsymbol{x}}_p}{d\tilde{t}} = \tilde{\boldsymbol{u}}_p, \tag{3.1a}$$

$$\tilde{m}_p \frac{d\tilde{\boldsymbol{u}}_p}{d\tilde{t}} = \frac{1}{2} C_D \frac{\pi \tilde{d}_p^2}{4} \tilde{\rho} \left|\tilde{\boldsymbol{u}} - \tilde{\boldsymbol{u}}_p\right| \left(\tilde{\boldsymbol{u}} - \tilde{\boldsymbol{u}}_p\right), \tag{3.1b}$$

$$\tilde{m}_p \tilde{c}_p \frac{d\tilde{T}_p}{d\tilde{t}} = Nu \tilde{k} \pi \tilde{d}_p \left(\tilde{T} - \tilde{T}_p\right), \tag{3.1c}$$

where $\tilde{\boldsymbol{x}}_p$, $\tilde{\boldsymbol{u}}_p$, $\tilde{T}_p$, $\tilde{m}_p$ and $\tilde{c}_p$ are the particle's position vector, velocity vector, temperature, mass and specific heat (at constant pressure), respectively. The carrier flow at the particle position is described by the velocity vector $\tilde{\boldsymbol{u}}$, density $\tilde{\rho}$, temperature $\tilde{T}$, conductivity $\tilde{k}$

and dynamic viscosity $\tilde{\mu}$. The mass of a spherical particle is related to its diameter $\tilde{d}_p$, and density $\tilde{\rho}_p$, as $\tilde{m}_p = \tilde{\rho}_p \pi \tilde{d}_p^3/6$. The $C_D$ is the drag coefficient and $Nu$ the Nusselt number that describes the ratio of convective to conductive heat transfer at the particle's boundary $Nu = h\tilde{d}_p/\tilde{k}$ where $h$ is the convective heat transfer coefficient. For a small particle Reynolds number, $Re_p = \tilde{\rho}\,|\tilde{\boldsymbol{u}} - \tilde{\boldsymbol{u}}_p|\,\tilde{d}_p/\tilde{\mu}$ and incompressible flow, the drag coefficient and Nusselt number are described analytically as $C_D = 24/Re_p$ and $Nu = 2$. For higher particle Reynolds numbers and/or other flow parameters, these can be empirically corrected [48, 49, 50, 52, 53] with the functions $f_1$ and $f_2$ as

$$C_D = \frac{24}{Re_p} f_1, \tag{3.2a}$$

$$Nu = 2 f_2. \tag{3.2b}$$

Using the non-dimensional variables $t = \tilde{t}/\tau_f$, $\boldsymbol{u} = \tilde{\boldsymbol{u}}/U_\infty$, $\rho = \tilde{\rho}/\rho_\infty$, $T = \tilde{T}/T_\infty$, $\mu = \tilde{\mu}/\mu_\infty$, $k = \tilde{k}/k_\infty$, $c = \tilde{c}/c_\infty$, $\boldsymbol{x}_p = \tilde{\boldsymbol{x}}_p/L_\infty$, $\boldsymbol{u}_p = \tilde{\boldsymbol{u}}_p/U_\infty$, $T_p = \tilde{T}_p/T_\infty$, $\rho_p = \tilde{\rho}_p/\rho_\infty$, $c_p = \tilde{c}_p/c_\infty$, $d_p = \tilde{d}_p/L_\infty$, where the $\infty$ subscript identifies reference scales, we arrive at the non-dimensional formulation

$$\frac{d\boldsymbol{x}_p}{dt} = \boldsymbol{u}_p, \tag{3.3a}$$

$$\frac{d\boldsymbol{u}_p}{dt} = \frac{f_1}{St}\left(\boldsymbol{u} - \boldsymbol{u}_p\right), \tag{3.3b}$$

$$\frac{dT_p}{dt} = \frac{2c_r}{3Pr}\frac{f_2}{St}\left(T - T_p\right), \tag{3.3c}$$

where $St = \tau_p/\tau_f$ is the Stokes number, i.e. the ratio of the characteristic particle time scale, $\tau_p = \tilde{\rho}_p \tilde{d}_p^2/\left(18\tilde{\mu}\right)$ to the convective carrier phase time scale, $\tau_f = L_\infty/U_\infty$. The Prandtl number is denoted by $Pr = \tilde{\mu}\tilde{c}/\tilde{k}$, and the specific heat ratio of the particle to the carrier phase with $c_r = c_p/c$. Defining a carrier phase, reference Prandtl number $Pr_\infty = \mu_\infty c_\infty/k_\infty$ and Reynolds number $Re_\infty = \rho_\infty U_\infty L_\infty/\mu_\infty$, we express the particle Reynolds number,

Stokes number and Prandtl number in terms of non-dimensional variables as follows

$$Re_p = Re_\infty \frac{\rho}{\mu} \left| \boldsymbol{u} - \boldsymbol{u}_p \right| d_p, \qquad St = Re_\infty \frac{\rho_p d_p^2}{18\mu}, \qquad Pr = Pr_\infty \frac{\mu c}{k}. \tag{3.4}$$

Without loss of generality, we take the dynamic viscosity, conductivity and specific heat ratio of the carrier phase to be constant so that $\mu = k = c = 1$.

### 3.2.2 SPARSE Particle Cloud Tracer

SPARSE was derived in Refs. [57, 58] for one- and two-coupled formulations in non-closed form, respectively. Here, we review the derivation for reference and to introduce notation. For a detailed description of the model derivation, we refer to the interested reader to Refs. [57, 58].

SPARSE models a cloud of particles using a method of averaging starting with the Reynolds decomposition of any instantaneous particle variable $\eta$ into its average and fluctuating component according to $\eta = \overline{\eta} + \eta'$, where the average is defined by its ensemble average

$$\overline{\eta} = \frac{1}{N_p} \sum_{i=1}^{N_p} \eta_i, \tag{3.5}$$

for $N_p$ particles within a cloud. We define the relative velocity $\boldsymbol{a}$ and the relative temperature $b$ as

$$\boldsymbol{a} = \boldsymbol{u} - \boldsymbol{u}_p, \tag{3.6a}$$

$$b = T - T_p, \tag{3.6b}$$

In SPARSE, we extend the functionality of the correction functions in (3.2a) and (3.2a) beyond the forcing correction for flow conditions outside the Stokes regime, to account for the variation of the forcing within the cloud region and associated velocity (phase) space

on the governing equations of the statistical moments. To do so, we start by assuming that the correction functions of the forcing depend on the relative velocity so that $f_1 = f_1(\boldsymbol{a})$ and $f_2 = f_2(\boldsymbol{a})$, which can be interpreted as a particle-phase in which the particle's inertial effects are dominant and Boussinesq number is small following our previous work on the interaction of a curtain of particles with a moving shock [170, 189, 171, 58]. Consequently, we Taylor expand this function around the mean velocity of the cloud to account for fluctuations in the cloud region, e.g. for $f_1$ this leads to

$$f_1\left(\overline{\boldsymbol{a}} + \boldsymbol{a}'\right) = f_1\left(\overline{\boldsymbol{a}}\right) + a_i' \left.\frac{\partial f_1}{\partial a_i}\right|_{\overline{\boldsymbol{a}}} + \frac{1}{2} a_i' a_j' \left.\frac{\partial^2 f_1}{\partial a_i \partial a_j}\right|_{\overline{\boldsymbol{a}}} + \mathcal{O}\left(\boldsymbol{a}'^3\right). \tag{3.7}$$

Here, we use index notation for brevity with indexes $i = 1, 2, 3$ and $j = 1, 2, 3$. Substituting this into (3.3) and Reynolds decomposing one finds

$$\frac{d\overline{x}_{p_i}}{dt} + \frac{dx'_{p_i}}{dt} = \overline{u}_{p_i} + u'_{p_i}, \tag{3.8a}$$

$$\frac{d\overline{u}_{p_i}}{dt} + \frac{du'_{p_i}}{dt} = \frac{1}{St}\left(f_1\left(\overline{\boldsymbol{a}}\right) + a_j' \left.\frac{\partial f_1}{\partial a_j}\right|_{\overline{\boldsymbol{a}}} + \frac{1}{2} a_j' a_k' \left.\frac{\partial^2 f_1}{\partial a_j \partial a_k}\right|_{\overline{\boldsymbol{a}}}\right)\left(\overline{a}_i + a_i'\right), \tag{3.8b}$$

$$\frac{d\overline{T}_p}{dt} + \frac{dT'_p}{dt} = \frac{2c_r}{3PrSt}\left(f_2\left(\overline{\boldsymbol{a}}\right) + a_i' \left.\frac{\partial f_2}{\partial a_i}\right|_{\overline{\boldsymbol{a}}} + \frac{1}{2} a_i' a_j' \left.\frac{\partial^2 f_2}{\partial a_i \partial a_j}\right|_{\overline{\boldsymbol{a}}}\right)\left(\overline{b} + b'\right). \tag{3.8c}$$

Averaging of this system leads to the non-dimensional SPARSE equations for the mean particle position, velocity and temperature [57]

$$\frac{d\overline{x}_{p_i}}{dt} = \overline{u}_{p_i}, \tag{3.9a}$$

$$St\frac{d\overline{u}_{p_i}}{dt} = \overline{a}_i f_1\left(\overline{\boldsymbol{a}}\right) + \overline{a_i' a_j'} \left.\frac{\partial f_1}{\partial a_j}\right|_{\overline{\boldsymbol{a}}} + \frac{\overline{a}_i}{2}\overline{a_j' a_k'} \left.\frac{\partial^2 f_1}{\partial a_j \partial a_k}\right|_{\overline{\boldsymbol{a}}} + \frac{1}{2}\overline{a_i' a_j' a_k'} \left.\frac{\partial^2 f_1}{\partial a_j \partial a_k}\right|_{\overline{\boldsymbol{a}}}, \tag{3.9b}$$

$$\frac{3PrSt}{2c_r}\frac{d\overline{T}_p}{dt} = \overline{b} f_2\left(\overline{\boldsymbol{a}}\right) + \overline{b' a_i'} \left.\frac{\partial f_2}{\partial a_i}\right|_{\overline{\boldsymbol{a}}} + \frac{\overline{b}}{2}\overline{a_i' a_j'} \left.\frac{\partial^2 f_2}{\partial a_i \partial a_j}\right|_{\overline{\boldsymbol{a}}} + \frac{1}{2}\overline{b' a_i' a_j'} \left.\frac{\partial^2 f_2}{\partial a_i a_j}\right|_{\overline{\boldsymbol{a}}}. \tag{3.9c}$$

Through the combination of Taylor expansion of the forcing and averaging, these governing model equations accounts for moments of velocity distribution in the cloud region on the

mean cloud dynamics. In previous work, we closed this system a priori with Monte-Carlo sample.

Note that we previously omitted the third term on the right hand sides of (3.9b) and (3.9c) as they pertain to derivatives of order higher than one of the forcing function which generally turns out to be smaller than the gradient. However, because this term after averaging is $\mathcal{O}\left(\overline{a'^2}\right)$ and thus potential similar in order of terms, we retain it here for completeness.

### 3.2.3 SPARSE with Second-Order Moments

In order to close the SPARSE equations, we must first extend the model (3.9) to include equations that govern the second order moments. These can be obtained following a standard method of moments procedure [57, 58, 98, 2], i.e., first obtain equations for the fluctuating variables by subtracting the averaged equations from the instantaneous equations; then multiplying or taking the inner product of the resulting system with the fluctuating variables and vectors, respectively; finally, averaging and neglecting terms on

the order of fluctuations to the third power or higher, we arrive at the following

$$\frac{d\overline{x}_{p_i}}{dt} = \overline{u}_{p_i}, \tag{3.10a}$$

$$St\frac{d\overline{u}_{p_i}}{dt} = \overline{a}_i\left(f_1\left(\overline{\boldsymbol{a}}\right) + \frac{1}{2}\overline{a'_j a'_k}\left.\frac{\partial^2 f_1}{\partial a_j \partial a_k}\right|_{\overline{\boldsymbol{a}}}\right) + \overline{a'_i a'_j}\left.\frac{\partial f_1}{\partial a_j}\right|_{\overline{\boldsymbol{a}}}, \tag{3.10b}$$

$$\frac{3PrSt}{2c_r}\frac{d\overline{T}_p}{dt} = \overline{b}\left(f_2\left(\overline{\boldsymbol{a}}\right) + \frac{1}{2}\overline{a'_i a'_j}\left.\frac{\partial^2 f_2}{\partial a_i \partial a_j}\right|_{\overline{\boldsymbol{a}}}\right) + \overline{b' a'_i}\left.\frac{\partial f_2}{\partial a_i}\right|_{\overline{\boldsymbol{a}}}, \tag{3.10c}$$

$$\frac{d}{dt}\left(\overline{x'_{p_i} x'_{p_j}}\right) = \overline{x'_{p_i} u'_{p_j}} + \overline{x'_{p_j} u'_{p_i}}, \tag{3.10d}$$

$$St\frac{d}{dt}\left(\overline{u'_{p_i} u'_{p_j}}\right) = \left(\overline{a'_i u'_{p_j}} + \overline{a'_j u'_{p_i}}\right) f_1\left(\overline{\boldsymbol{a}}\right) + \overline{a_i}\,\overline{u'_{p_j} a'_k}\left.\frac{\partial f_1}{\partial a_k}\right|_{\overline{\boldsymbol{a}}} + \overline{a_j}\,\overline{u'_{p_i} a'_k}\left.\frac{\partial f_1}{\partial a_k}\right|_{\overline{\boldsymbol{a}}}, \tag{3.10e}$$

$$\frac{3PrSt}{4c_r}\frac{d\overline{T'^2_p}}{dt} = \overline{T'_p b'} f_2\left(\overline{\boldsymbol{a}}\right) + \overline{b}\,\overline{T'_p a'_i}\left.\frac{\partial f_2}{\partial a_i}\right|_{\overline{\boldsymbol{a}}}, \tag{3.10f}$$

$$\frac{d}{dt}\left(\overline{x'_{p_i} u'_{p_j}}\right) = \overline{u'_{p_i} u'_{p_j}} + \frac{1}{St}\left(\overline{x'_{p_i} a'_j} f_1\left(\overline{\boldsymbol{a}}\right) + \overline{a_j}\,\overline{x'_{p_i} a'_k}\left.\frac{\partial f_1}{\partial a_k}\right|_{\overline{\boldsymbol{a}}}\right), \tag{3.10g}$$

$$\frac{d}{dt}\left(\overline{x'_{p_i} T'_p}\right) = \overline{u'_{p_i} T'_p} + \frac{2c_r}{3Pr}\frac{1}{St}\left(\overline{x'_{p_i} b'} f_2\left(\overline{\boldsymbol{a}}\right) + \overline{b}\,\overline{x'_{p_i} a'_j}\left.\frac{\partial f_2}{\partial a_j}\right|_{\overline{\boldsymbol{a}}}\right), \tag{3.10h}$$

$$St\frac{d}{dt}\left(\overline{u'_{p_i} T'_p}\right) = \overline{a'_i T'_p} f_1\left(\overline{\boldsymbol{a}}\right) + \overline{a}_i\,\overline{T'_p a'_j}\left.\frac{\partial f_1}{\partial a_j}\right|_{\overline{\boldsymbol{a}}} + \frac{2c_r}{3Pr}\left(\overline{b' u'_{p_i}} f_2\left(\overline{\boldsymbol{a}}\right) + \overline{b}\,\overline{u'_{p_i} a'_j}\left.\frac{\partial f_2}{\partial a_j}\right|_{\overline{\boldsymbol{a}}}\right). \tag{3.10i}$$

Because we have retained only terms on the order of fluctuations squared, this SPARSE formulation is a second order CIC model.

### 3.2.4 Closed SPARSE

The second-order SPARSE formulation in (3.10) is not yet closed as many of the terms have the form of a covariance of particle variables with carrier phase variables or a covariance between two carrier phase variables, and the carrier phase has an unknown distribution within the cloud region. To highlight those terms more explicitly, we make use of (3.6a) and (3.6b) to unroll terms related to the relative velocity and temperature

as follows

$$\overline{a}_i = \boxed{\overline{u_i}} - \overline{u}_{p_i}, \tag{3.11a}$$

$$\overline{b} = \boxed{\overline{T}} - \overline{T}_p, \tag{3.11b}$$

$$\overline{a'_i a'_j} = \boxed{\overline{u'_i u'_j}} + \overline{u'_{p_i} u'_{p_j}} - \boxed{\overline{u'_i u'_{p_j}}} - \boxed{\overline{u'_j u'_{p_i}}}, \tag{3.11c}$$

$$\overline{b' a'_i} = \boxed{\overline{T' u'_i}} + \overline{T'_p u'_{p_i}} - \boxed{\overline{T' u'_{p_i}}} - \boxed{\overline{T'_p u'_i}}, \tag{3.11d}$$

$$\overline{x'_{p_i} a'_j} = \boxed{\overline{x'_{p_i} u'_j}} - \overline{x'_{p_i} u'_{p_j}}, \tag{3.11e}$$

$$\overline{u'_{p_i} a'_j} = \boxed{\overline{u'_{p_i} u'_j}} - \overline{u'_{p_i} u'_{p_j}}, \tag{3.11f}$$

$$\overline{T'_p a'_i} = \boxed{\overline{T'_p u'_i}} - \overline{T'_p u'_{p_i}}, \tag{3.11g}$$

$$\overline{b' x'_{p_i}} = \boxed{\overline{T' x'_{p_i}}} - \overline{T'_p x'_{p_i}}, \tag{3.11h}$$

$$\overline{b' u'_{p_i}} = \boxed{\overline{T' u'_{p_i}}} - \overline{T'_p u'_{p_i}}, \tag{3.11i}$$

$$\overline{b' T'_{p_i}} = \boxed{\overline{T' T'_{p_i}}} - \overline{T'^2_p}, \tag{3.11j}$$

where the boxed terms need closing. To be consistent with the SPARSE framework, we need to account for the influence of the carrier phase at the mean location. We will rely on averaging and Taylor series expansions once more by expanding the carrier velocity and temperature in (3.11a) and (3.11b) around the mean cloud location, $\overline{\boldsymbol{x}}_p$, as follows

$$\overline{u}_i \approx \overline{u_i\left(\overline{\boldsymbol{x}}_p\right) + x'_{p_j} \left.\frac{\partial u_i}{\partial x_j}\right|_{\overline{\boldsymbol{x}}_p} + \frac{1}{2} x'_{p_j} x'_{p_k} \left.\frac{\partial^2 u_i}{\partial x_j \partial x_k}\right|_{\overline{\boldsymbol{x}}_p}} = u_i\left(\overline{\boldsymbol{x}}_p\right) + \frac{1}{2}\overline{x'_{p_j} x'_{p_k}} \left.\frac{\partial^2 u_i}{\partial x_j \partial x_k}\right|_{\overline{\boldsymbol{x}}_p}, \tag{3.12a}$$

$$\overline{T} \approx \overline{T\left(\overline{\boldsymbol{x}}_p\right) + x'_{p_i} \left.\frac{\partial T}{\partial x_i}\right|_{\overline{\boldsymbol{x}}_p} + \frac{1}{2} x'_{p_i} x'_{p_j} \left.\frac{\partial^2 T}{\partial x_i \partial x_j}\right|_{\overline{\boldsymbol{x}}_p}} = T\left(\overline{\boldsymbol{x}}_p\right) + \frac{1}{2}\overline{x'_{p_i} x'_{p_j}} \left.\frac{\partial^2 T}{\partial x_i \partial x_j}\right|_{\overline{\boldsymbol{x}}_p}. \tag{3.12b}$$

Note that the second term on the right hand side are zero after averaging.

We close the second moments in a similar way. For example,

$$\overline{u_i' u_j'} = \overline{u_i' \left(u_j - \overline{u}_j\right)} \approx \overline{u_i' \left( u_j\left(\overline{\boldsymbol{x}}_p\right) + x_{p_k}' \left.\frac{\partial u_j}{\partial x_k}\right|_{\overline{\boldsymbol{x}}_p} - \overline{u}_j \right)} = \overline{u_i' x_{p_k}'} \left.\frac{\partial u_j}{\partial x_k}\right|_{\overline{\boldsymbol{x}}_p}, \tag{3.13a}$$

$$\overline{T' u_i'} = \overline{T' \left(u_i - \overline{u}_i\right)} \approx \overline{T' \left( u_i\left(\overline{\boldsymbol{x}}_p\right) + x_{p_j}' \left.\frac{\partial u_i}{\partial x_j}\right|_{\overline{\boldsymbol{x}}_p} - \overline{u}_i \right)} = \overline{T' x_{p_j}'} \left.\frac{\partial u_i}{\partial x_j}\right|_{\overline{\boldsymbol{x}}_p}, \tag{3.13b}$$

$$\overline{T'^2} = \overline{T' \left(T - \overline{T}\right)} \approx \overline{T' \left( T\left(\overline{\boldsymbol{x}}_p\right) + x_{p_i}' \left.\frac{\partial T}{\partial x_i}\right|_{\overline{\boldsymbol{x}}_p} - \overline{T} \right)} = \overline{T' x_{p_i}'} \left.\frac{\partial T}{\partial x_i}\right|_{\overline{\boldsymbol{x}}_p}, \tag{3.13c}$$

close the Reynolds stress and the heat flux on the sub-cloud scale. Further closures of covariances are as follows

$$\overline{x_{p_i}' u_j'} \approx \overline{x_{p_i}' x_{p_k}'} \left.\frac{\partial u_j}{\partial x_k}\right|_{\overline{\boldsymbol{x}}_p}, \qquad \overline{u_{p_i}' u_j'} \approx \overline{u_{p_i}' x_{p_k}'} \left.\frac{\partial u_j}{\partial x_k}\right|_{\overline{\boldsymbol{x}}_p}, \tag{3.14a}$$

$$\overline{T_p' u_i'} \approx \overline{T_p' x_{p_j}'} \left.\frac{\partial u_i}{\partial x_j}\right|_{\overline{\boldsymbol{x}}_p}, \qquad \overline{x_{p_i}' T'} \approx \overline{x_{p_i}' x_{p_j}'} \left.\frac{\partial T}{\partial x_j}\right|_{\overline{\boldsymbol{x}}_p}, \tag{3.14b}$$

$$\overline{u_{p_i}' T'} \approx \overline{u_{p_i}' x_{p_j}'} \left.\frac{\partial T}{\partial x_j}\right|_{\overline{\boldsymbol{x}}_p}, \qquad \overline{T_p' T'} \approx \overline{T_p' x_{p_i}'} \left.\frac{\partial T}{\partial x_i}\right|_{\overline{\boldsymbol{x}}_p}. \tag{3.14c}$$

Substituting (3.11)–(3.14) into (3.10) closes the model. The resulting system of model equations is shown in Ref. [3].

**Error Estimates**

Because SPARSE uses a combination of a Taylor series and higher-moment truncation, naturally the model accuracy depends on these truncation errors. These errors intuitively depend on the spatial cloud size over which the Taylor series is expanded and over which the moments are determined.

To formalize through basic analysis, we consider the Taylor expansion of the carrier flow velocity around the average location of the particle cloud for the one-dimensional

model, as follows

$$\begin{aligned}\overline{u(x)} &= \overline{C_0 + C_1\left(x-\overline{x}_p\right) + C_2\left(x-\overline{x}_p\right)^2 + C_3\left(x-\overline{x}_p\right)^3 + \mathcal{O}\left(\left(x-\overline{x}_p\right)^4\right)} \\ &= C_0 + C_2\overline{x_p'^{\,2}} + C_3\overline{x_p'^{\,3}} + \mathcal{O}\left(\overline{x_p'^{\,4}}\right),\end{aligned} \tag{3.15}$$

where the constants are given by

$$C_0 = u(\overline{x}_p), \quad C_1 = \left.\frac{\partial u}{\partial x}\right|_{\overline{x}_p}, \quad C_2 = \frac{1}{2}\left.\frac{\partial^2 u}{\partial x^2}\right|_{\overline{x}_p}, \quad C_3 = \frac{1}{6}\left.\frac{\partial^3 u}{\partial x^3}\right|_{\overline{x}_p}. \tag{3.16}$$

Using the standard deviation $\sigma_{x_p}$ to express the two central moments we have $\overline{x_p'^{\,2}} = \sigma_{x_p}^2$ and $\overline{x_p'^{\,3}} = \gamma_{x_p}\sigma_{x_p}^3$, where $\gamma_{x_p}$ is the Pearson's coefficient of the third moment (or coefficient of skewness). Finally, the average of the carrier flow velocity is

$$\overline{u(x)} = C_0 + C_2\sigma_{x_p}^2 + C_3\gamma_{x_p}\sigma_{x_p}^3 + \mathcal{O}\left(\overline{x_p'^{\,4}}\right), \tag{3.17}$$

which indicates that the leading order term not included in the SPARSE formulation is proportional to the standard deviation of the macro-particle's location to the third power. This procedure can be applied similarly to the rest of the truncated terms. For example, for the term $\overline{u'^2}$ that is closed using expressions (3.13a) and (3.14a) we have

$$\begin{aligned}\overline{u'^2} &= C_1\overline{u'x_p'} + C_2\overline{u'x_p'^{\,2}} + \mathcal{O}\left(\overline{u'x_p'^{\,3}}\right) = C_1^2\overline{x_p'^{\,2}} + C_1C_2\overline{x_p'^{\,3}} + \mathcal{O}\left(\overline{x_p'^{\,4}}\right) \\ &= C_1^2\sigma_{x_p}^2 + C_1C_2\gamma_{x_p}\sigma_{x_p}^3 + \mathcal{O}\left(\overline{x_p'^{\,4}}\right),\end{aligned} \tag{3.18}$$

and for the term $\overline{u_p'u'}$ that is closed with (3.14a) one has

$$\overline{u_p'u'} = C_1\overline{u_p'x_p'} + C_2\overline{u_p'x_p'^{\,2}} + \mathcal{O}\left(\overline{u_p'x_p'^{\,3}}\right) = C_1\rho_{x_pu_p}\sigma_{x_p}\sigma_{u_p} + C_2\gamma_{x_pu_p}\sigma_{x_p}^2\sigma_{u_p} + \mathcal{O}\left(\overline{u_p'x_p'^{\,3}}\right), \tag{3.19}$$

where $\rho_{x_pu_p}$ is the Pearson's correlation coefficient of $x_p$ and $u_p$ and $\gamma_{x_pu_p}$ the Pearson's

coefficient of the third moment $\overline{u'_p x'^2_p}$.

To summarize, each term in SPARSE and therefor the SPARSE model is expected to be on the order of the third moment of the cloud location variance in the asymptotic range. Effectively, for this third-order model we thus have assumed a symmetric probability density distribution of the particle statistics in the cloud. The Pearson's coefficients is the proportionality constant on this error. It depends on the probability density function in space and velocity phase space.

**Adaptivity and Splitting**

The third-order error estimates indicates that the error reduces if the clouds size is reduced. This can be accomplished by adapting the cloud size through splitting of large clouds into smaller clouds. Associated with this splitting we expect a convergence of the SPARSE method with respect to subdivisions of the particle cloud along the variables $x_p$ and $u_p$ of the third order.

To illustrate the splitting of a particle cloud, here, we uniformly divide the particle phase's computational domain at initial conditions as defined by the limits of the physical and phase space of the particle variables according to $M_p = M_p^{x_p} M_p^{u_p}$, where $M_p$ is the total number of macro-particles and $M_p^{x_p}$ and $M_p^{u_p}$ are the number of divisions in physical and phase space along $x_p$ and $u_p$, respectively, that here we have considered to be equal $M_p^{x_p} = M_p^{u_p}$. The weight of each macro-particle is computed as the ratio of the point-particles contained in the macro-particle to the total number of particles $N_p$. The first two moments of the macro-particles are computed initially for each macro-particle. The splitting of the initial cloud is schematically illustrated in Figure 3.1. The Figure represents the initial time (left) and a later time (right) of a particle cloud represented by PSIC particles (points) and SPARSE macro-particles (ellipses).

Considering uniform splitting, the reduction in the standard deviation implies that each macro-particle has a fraction of the one of the initial cloud. This is $\sigma_{x_p k} \sim \sigma_{x_p} / M_p^{x_p}$

for the $k$-th macro-particle. Then, the constants $C_{0k}$, $C_{2k}$ and $C_{3k}$ for each macro-particle differ by the ones of the original cloud $C_0$, $C_2$ and $C_3$ for being evaluated at a small distance of the center. Each macro-particle is located at $\overline{x}_{p_k}$ where the distance to the center of the total cloud is the small quantity $|\overline{x}_p - \overline{x}_{p_k}|$ with $k = 1, \ldots, M_p$. According to this $C_0 \sim C_{0k}$, $C_2 \sim C_{2k}$ and $C_3 \sim C_{3k}$.

Additionally, the averaged coefficient of skewness $\gamma_{x_p}$ and $\gamma_{x_p u_p}$ and the Pearson's coefficient $\rho_{x_p u_p}$ can be assumed to be on the same order than the one of the initial cloud, provided that the gradients within the cloud are small which is needed for the Taylor series to be in the asymptotic range. Therefore, The leading order terms in (3.17)–(3.19) when splitting the initial cloud are

$$\sum_{k=1}^{M_p} w_k C_{3k} \gamma_{x_p k} \sigma_{x_p k}^3 \sim C_3 \gamma_{x_p} \left( \frac{\sigma_{x_p}}{M_p^{x_p}} \right)^3, \tag{3.20a}$$

$$\sum_{k=1}^{M_p} w_k C_{1k} C_{2k} \rho_{x_p u_p k} \gamma_{x_p k} \sim C_1 C_2 \gamma_{x_p} \left( \frac{\sigma_{x_p}}{M_p^{x_p}} \right)^3, \tag{3.20b}$$

$$\sum_{k=1}^{M_p} w_k C_{2k} \gamma_{x_p u_p k} \sigma_{x_p}^2 \sigma_{u_p k} \sim C_2 \gamma_{x_p} \left( \frac{\sigma_{x_p}}{M_p^{x_p}} \right)^2 \frac{\sigma_{u_p}}{M_p^{u_p}}. \tag{3.20c}$$

The reader is referred to Ref. [3] for additional insights on the derivation SPARSE model.

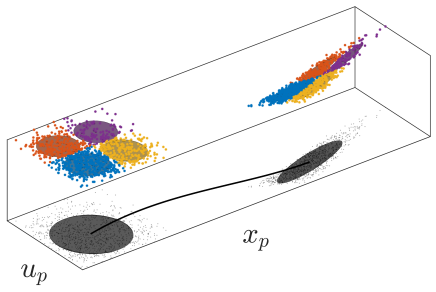


**Figure 3.1.** Splitting of the initial cloud of point-particles at $t = 0$ and a later time into $M_p = 4$ macro-particles for a one-dimensional case. Each of the four macro-particles are described with SPARSE and later joined using the relations (3.21).

## 3.3 Verification Tests

For verification purposes, we repeat the one-dimensional numerical tests with constant and linear forcings as described in Ref. [57]. We consider an additional one-dimensional test with a known empirical forcing that includes a more realistic dependence of the forcing correction with respect to the relative velocity. We note that these tests are intended to be numerical exercises to test consistency. They are not necessarily intended to have physical meaning. The analytical flow velocities $u$ and forcing functions $f_1$ are selected arbitrarily to evaluate the accuracy of the SPARSE formulation with different levels of complexity. The parameters of the resulting four test cases, including the carrier phase velocity fields, Stokes numbers and correction factor functions are summarized in Table 3.1.

All test cases are computed with a total number of particles of $N_p = 10,000$ and with initial conditions for position and velocity given according to the uniform density distributions $x_p(0) \sim \mathcal{U}(-1,1)$ and $u_p(0) \sim \mathcal{U}(-5,15)$. Here, $\mathcal{U}$ denotes a uniform distribution function and the arguments give the minimum and maximum value of the distribution. PSIC simulations are conducted to obtain the reference solution. For each test case, we compare the closed SPARSE method with the SPARSE method from [57] which was closed *a priori* and only traces the averages of the particle cloud. We refer to this model as "SPARSE *a priori*". We did not use subdivisions of a global group of particles into sub-clouds for this *a priori* closed model. For predictions with the closed SPARSE formulation, however, we have subdivided into $M_p$ number of sub-clouds to ensure accuracy and convergence. The global averages and variances of the combined set

of sub-clouds are given by

$$\overline{\phi} = \sum_{k=1}^{M_p} w_k \overline{\phi}_k, \tag{3.21a}$$

$$\overline{\eta'\theta'} = \sum_{k=1}^{M_p} w_k \overline{\eta'\theta'}_k + \sum_{k=1}^{M_p} w_k (\overline{\eta}_k - \overline{\eta})(\overline{\theta}_k - \overline{\theta}), \tag{3.21b}$$

for arbitrary solution variables $\phi$, $\eta$ and $\theta$. The weight $w_k$, of the $k$-th cloud represents the number of particles per cloud. Here, we take it as the ratio between the number of point-particles in the cloud $k$ denoted by $N_{p_k}$ and the total number of particles so that $w_k = N_{p_k}/N_p$.

SPARSE reduces the computational expense as compared to PSIC simulations when tracing a cloud of point-particles as a point. The PSIC description in three-dimensions of a non-isothermal cloud with $N_p$ particles requires the solution of $7N_p$ equations according to the system (3.3). For the same case, the closed SPARSE method with $M_p$ macro-particles solves $35M_p$ equations as described by the system (3.10). Generally, $M_p \ll N_p$ to reproduce accurate mean and variances of the cloud and the computational savings is on the order of $35M_p/(7N_p)$. In general, a measure of the reduction of degrees of freedom when using SPARSE as compared to PSIC can be defined making use of the variables $d$, that takes the values 1, 2 or 3 depending of the dimensions of the problem and $e$, that takes the value 0 for an isothermal simulation or 1 for a non-isothermal one. The ratio of the computational cost of SPARSE as compared to a PSIC method is

$$r = \left( \frac{3d + 2d^2 + 2e + 2de}{2d + e} \right) \frac{M_p}{N_p}. \tag{3.22}$$

To determine the difference between PSIC and SPARSE methods, we normalize

the $L_2$ norm of the moment difference with the $L_\infty$ norm of the PSIC result as follows

$$\varepsilon(\cdot) = \frac{\|(\cdot)^{\text{SPARSE}} - (\cdot)^{\text{PSIC}}\|_2}{\|(\cdot)^{\text{PSIC}}\|_\infty}. \tag{3.23}$$

The convergence rate of SPARSE is affected by the moment accuracy, and thus the inverse square root of the sub-cloud sample size, as well as the second order Taylor truncation of the forcing and the carrier phase field.

**Table 3.1.** Summary of the one-dimensional carrier flow velocity fields, $u(x)$, Stokes number, $St$, and forcing correction factor function, $f_1(u - u_p)$ for four one-dimensional test cases.

| Case Number | $u(x)$ | $St$ | $f_1(u - u_p)$ |
|---|---|---|---|
| 1 | 10 | 10 | $u - u_p$ |
| 2 | 10 | 10 | $\lvert u - u_p \rvert$ |
| 3 | $x + 5 + \cos(\pi(x + 5))$ | 1/24 | 1 |
| 4 | $9 + \cos(\pi x/10)$ | 1/2 | $1 + 0.15\,(0.9487(\lvert u - u_p \rvert))^{0.687}$ |

### 3.3.1 Linear Forcing in Constant Carrier Velocity Field, Case 1

In Case 1 the carrier phase velocity is taken constant $u(x) = 10$. The Stokes number is set to $St = 10$, and the correction factor of the forcing is linearly dependent on the relative velocity. In the constant carrier phase velocity field, the fluctuations of the velocity field are zero. Thus the sub-cloud carrier phase fluctuations are zero, $u' = 0$, and the covariance terms involving the carrier phase variables in the SPARSE formulation are zero also and cannot affect the (SPARSE) solution. The first derivative of the linear correction factor function, $f_1(u - u_p)$, with respect to the relative particle velocity is unity and the second derivative is zero. Therefore, terms with a second derivative of the forcing in (3.10b) and thus the the Taylor series expansion has no effect on the model accuracy for this case. In the constant carrier flow velocity, the cloud accelerates towards this velocity (Fig. 3.2a) and translates and widens correspondingly in the positive $x$-coordinate

(Figs. 3.2a and 3.2b, respectively). The averages and variances of the particle position and velocity determined with $N_p = 10^4$ PSIC particles are in excellent comparison with a SPARSE results that uses only $M_p = 16$ clouds. Moreover, a comparison of the moment differences (Fig. 3.2c) between the PSIC and SPARSE show a monotonic error reduction with an increasing number of clouds, providing evidence of a consistent convergence.

### 3.3.2 Positive Linear Forcing in Constant Carrier Velocity Field, Case 2

Case 2 differs from Case 1 only in the forcing function, which is is selected to be proportional to the *absolute* value of the relative velocity. This results in a more realistic positive (drag-like) forcing for negative relative velocities. The first and second moment trends for Case 2 are generally similar to Case 1 as shown in Figures 3.2d and 3.2e. Differences, such as the smaller position variance, $\overline{x_p'^2}$, for Case 2 as compared to Case 1, can be easily attributed to the changes in the positive forcing function, which moves all particles in the positive $x$-coordinate. The "SPARSE *a priori*" method is showing visible inaccuracies in the mean trace (Fig. 3.2d), whereas the SPARSE result compares well with PSIC. This is related to the subdivisions into sub-clouds for the closed SPARSE method. The "SPARSE *a priori*" method results are generated for a single global cloud without subdivisions. The closed SPARSE method's subdivision reduces the magnitude of the truncated third order correlation terms per sub-cloud in (3.10) and thus improves the accuracy of the global mean. Without the subdivision the third-order correlation leads to the difference observed in the "SPARSE *a priori*" model.

### 3.3.3 Constant Forcing in a Harmonically Varying Carrier Velocity Field, Case 3

In a third one-dimensional test, Case 3, we take the correction factor constant ($f_1 = 1$) and specify the carrier phase velocity field according to a growing, oscillating function, which lets us investigate the effect of the velocity variance in the carrier phase velocity

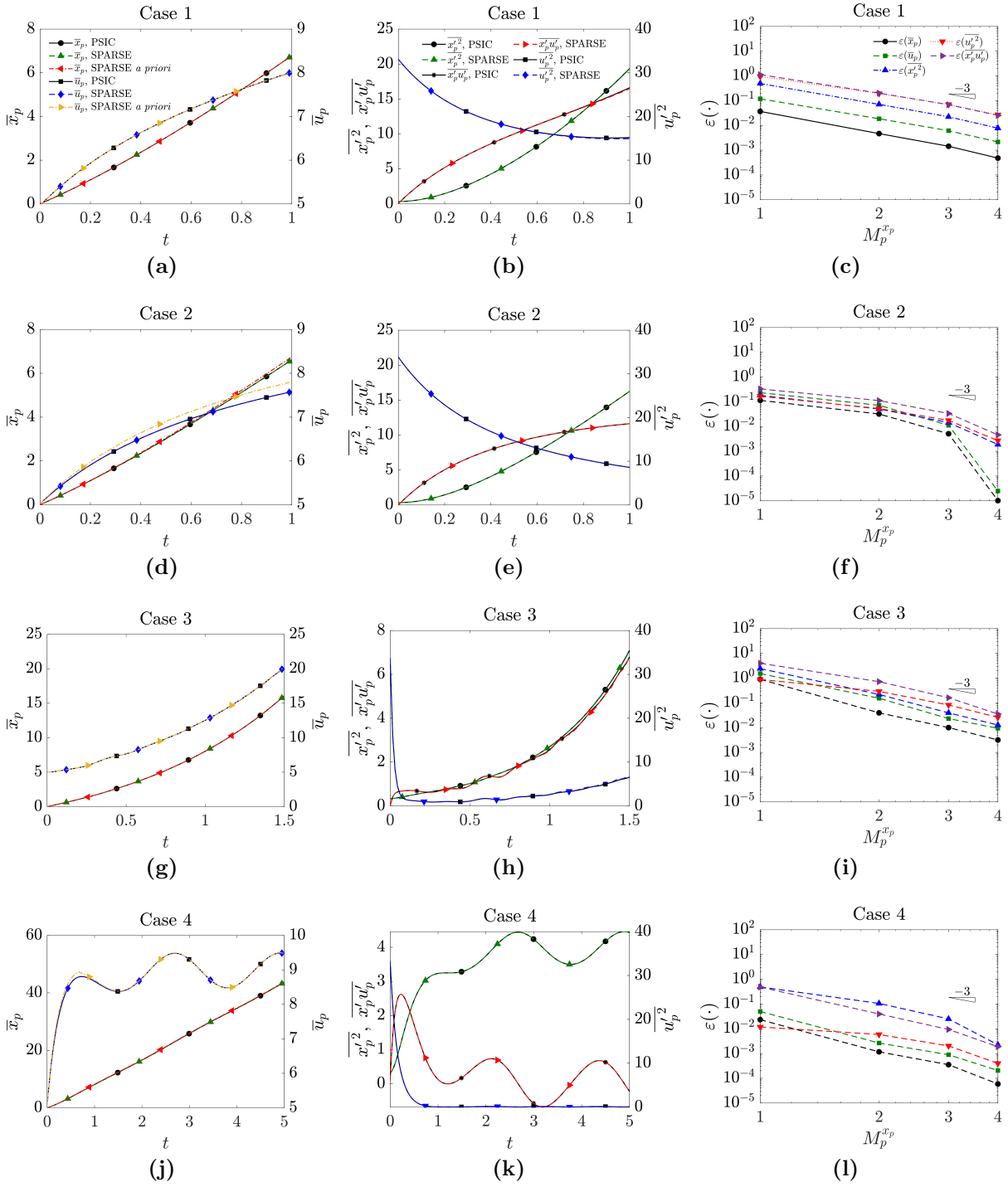


**Figure 3.2.** Comparison of the first (first column) and second (second column) moment results versus time between the closed SPARSE method with $M_p$=16, SPARSE *a priori*, and PSIC for the four, one-dimensional test cases, Case 1 (a,b), Case 2 (d,e), Case 3 (g,h) and Case 4 (j, k) as summarized in Table 3.1. The third column of figures show the error, $\epsilon$, as defined in (3.23) versus the number of sub-divisions, $M_p^{x_p}$, for SPARSE.

field. Specifically, in zeroth order models, the average flow field is poorly approximated at the average particle location such that $\overline{u(x_p)} \simeq u(\overline{x}_p)$, as discussed in Ref. [190]. In the closed SPARSE formulation, these fields are determined according to the closure model (3.11)–(3.14).

The particle velocity variance trend in Figure 3.2h shows a sharp initial drop in a time interval that is on the order of the Stokes number, after which it gradually grows while the particle phase is accelerated in the increasing carrier phase velocity field. At later times ($t > St$), the variance trends also show a dominant harmonic mode of similar frequency as the the oscillating carrier flow velocity. This oscillatory effect can also be observed in the particle location variance. The average particle velocity trend in Figure 3.2g closely follows the carrier flow velocity field at the average particle location because of the small Stokes number and the inherent particles' fast response to the carrier flow.

The results are in excellent agreement with the PSIC and the SPARSE *a priori* results. The error trends in Figure 3.2i show a monotonic convergence, an indication that the truncated terms in the Taylor expansion in (3.12)–(3.14) are smaller with an increased number of sub-clouds (per expectation).

### 3.3.4 Empirically Forced Particle Tracers in a Harmonically Varying Carrier Velocity Field, Case 4

In a final, most demanding, one-dimensional test, Case 4, we assume both the forcing function and the velocity field to have non-trivial, non-linear dependencies (see Table 3.1). The forcing is set by the well-known function of Schiller and Naumann ([191])

$$f_1 = 1 + 0.15 Re_p^{0.687}, \tag{3.24}$$

which is accurate for particle Reynolds numbers of $Re_p = Re_\infty |u - u_p| d_p < 10^3$. The reference Reynolds number is set to $Re_\infty = 10^2$, the Stokes number to $St = 1/2$, the relative

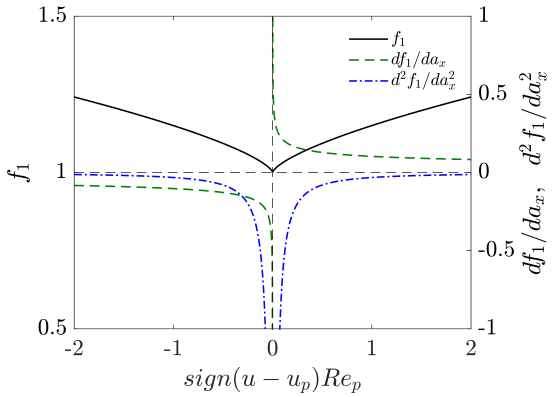


**Figure 3.3.** Drag coefficient correction factor $f_1$ in terms of the particle Reynolds number $Re_p$ with the sign of the relative velocity.

particle density to $\rho_p = 10^3$ and the non-dimensional particle diameter as $d_p = 9.478 \times 10^{-3}$ (according to (3.4)). For this case both the forcing and statistical truncation affect the accuracy of the SPARSE solution.

Before we discuss the SPARSE results, we make a few remarks on the Schiller and Naumann correction factor which is plotted versus the particle Reynolds number multiplied by the sign of the relative velocity in Figure 3.3. Also plotted are its first two derivatives with respect to the relative velocity $a_x = u - u_p$. The second derivative shows a singularity in the zero limit of the particle Reynolds number. This singularity can negatively affect accuracy through the terms that involves a second derivative in (3.10). This can occur if a SPARSE cloud experiences a change from acceleration to deceleration along its trajectory. To avoid the singularity we neglect the drag force correction effect and its derivatives by setting $f_1$ to unity for $Re_p < 0.1$ leading to the Stokes drag.

The particle phase's mean and variance trends are plotted in Figures 3.2j and 3.2k, respectively, and show that the particle cloud accelerates initially over a time proportional to the particle response time, until it reaches an oscillating plateau. Coinciding with this acceleration, the particle velocity variance reduces from its initial value to an oscillating trend with minima of approximately zero. The cloud size, proportional to the particle location variances, changes with the changes in the average relative velocity $\overline{u} - \overline{u}_p$: the

cloud grows when $\overline{u} - \overline{u}_p > 0$ and shrinks when $\overline{u} - \overline{u}_p < 0$. In transitioning from acceleration to deceleration, the front of the cloud decelerates faster than the tail, causing a switch in the relative velocity of the particles in the front with respect to the ones in the tail. Eventually, the cloud reaches a state in which the average relative velocity of the cloud is zero and the deviation of the particle velocity experiences a minimum, associated with a zero rate of change of the cloud size for that instant of time.

The SPARSE results are in excellent agreement with PSIC and SPARSE *a priori*, verifying the closed SPARSE method. The error reduces once again monotonically with an increase number of subdivisions of the cloud as shown in Figure 3.2l. The convergence rate is slightly smaller as compared to previous cases, as the Case 4 requires convergence of *both* the truncated Taylor series terms and the truncated, higher-order moment terms, where the accuracy for Case 1-3 is impacted by only one of the two truncations.

## 3.4 Two- and Three-Dimensional, One-Way Coupled, Particle-Laden Flow Tests

### 3.4.1 Stagnation Flow

To test the two-dimensional closed SPARSE formulation, we first consider a cloud traced in a carrier phase velocity field according to the analytical stagnation flow solution of [176] for an inviscid irrotational flow, in the domain $x \in [-\infty, 0]$ as follows

$$u = -kx, \tag{3.25a}$$

$$v = ky, \tag{3.25b}$$

where $y$ is the coordinate perpendicular to the flow direction, and $k$ is constant set to unity $k = 1$. To initialize a cloud of particles at rest, we sample from a uniform probability density distribution function with average location $\overline{x}_p = -1$ and $\overline{y}_p = 0$ and with deviations in space given by $\sigma_{x_p} = \sigma_{y_p} = 0.05$. Because the particles are initialized at rest, the average

and variance of the vertical and horizontal velocity components are zero, as well as any other moment involving a velocity component. Particles in the cloud are forced according to the Stokes drag corrected with the Schiller and Naumann correlation in (3.24). The reference Reynolds number in (3.4) is set to $Re_\infty = 10^4$. The Stokes number is selected to be unity $St = 1$ and the particle to fluid density ratio is set to $\rho_p = 10^3$.

A PSIC computation is performed for reference to determine the error of the closed SPARSE formulation. Because of the sampling error, well known to be proportional to $1/\sqrt{N_p}$, the moments of the sampled cloud differ from the uniform distribution used for the seeding. The average location of the sampled initial condition is $\overline{x}_p = -0.998$, $\overline{y}_p = 1.23 \times 10^{-3}$ and the deviations $\sigma_{x_p} = 4.98 \times 10^{-2}$ and $\sigma_{y_p} = 4.95 \times 10^{-2}$. The correlation is $\overline{x'_p y'_p} = 2.927 \times 10^{-5}$ at time zero. The remainder of the moments are zero because the cloud is at rest initially. To initialize a single SPARSE cloud ($M_p = 1$) we specify the initial condition according and consistently with the PSIC moments. With this initial condition, inaccuracies in the evolution of the third moment mostly affect the comparison between PSIC and closed SPARSE (see third bullet point in the Remarks on pp. 7), not in the least because the Taylor expansion of the linear velocity field in the stagnation flow case is exact and errors in the truncation of the Schiller and Naumann function are relatively small.

The traces of PSIC particles (red dots) and SPARSE clouds (green ellipses) are compared in Figure 3.4 for several instances of time. The radii of the ellipse and its orientation are set according to the eigenvalues and eigenvectors of the covariance matrix of the cloud's location in $x$- and $y$-direction computed from the SPARSE variables. The cloud compresses and expands in $x$- and $y$-direction, respectively, as it traverses the stagnating velocity field. The evolution of the first two moments computed with both approaches are depicted in Figure 3.5.

The trends of the $x$-location of the cloud can be divided into three stages (see [2] for a detailed discussion). In a first stage, all the point-particles in the cloud accelerate

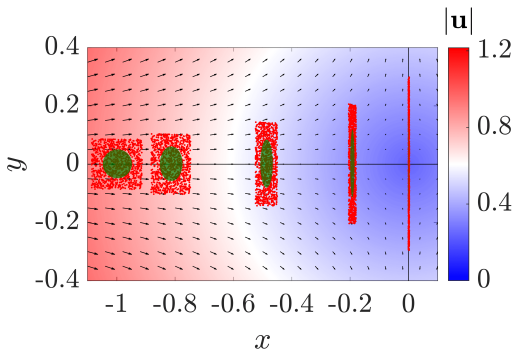


**Figure 3.4.** Evolution of the particle cloud immersed in the stagnation flow for different instants of time $t = [0,\ 0.5,\ 1.65,\ 2.2]$. The red dots represent the point-particles inside the cloud traced by a PSIC simulation and the green macro-particle is given by the SPARSE method. The background is colored according to the modulus of the stagnation flow field $\boldsymbol{u} = (u, v)^\top$.

with a positive relative velocity $u_i - u_{p_i} > 0$ for $1 \leq i \leq N_p$ towards a linearly decreasing carrier flow velocity. At some point the carrier flow velocity becomes less as compared to the velocity of some of the particles in the cloud. In this second stage, the cloud changes from having all the particles accelerating to all decelerating, producing a maximum in the average particle velocity $\overline{u}_p$ at approximately $t = 1$ (see Figure 3.5a). Correspondingly, the average horizontal particle location trend changes from a parabolic increase to a linear increase. After all the particles have crossed the zero relative velocity, all particles in the cloud decelerate towards the stagnation point, defining the third stage where $\overline{x}_p$ describes a parabolic downward trend. The variances of the particle phase velocity in the $x$-direction follow a similar trend of increase and decrease as shown in Figure 3.5c as its average counterpart. The range of horizontal velocities grows as the cloud accelerates and decreases in the third stage when decelerating, showing a maximum in the second stage. The horizontal size of the particle $\sigma_{x_p}$ decreases from its initial value as the cloud reaches the stagnation point. Second order correlations are depicted in Figures 3.5d–3.5f. The three stages are once again observed.

Figures 3.4 and 3.5 show that closed SPARSE is accurate within 1.5% compared

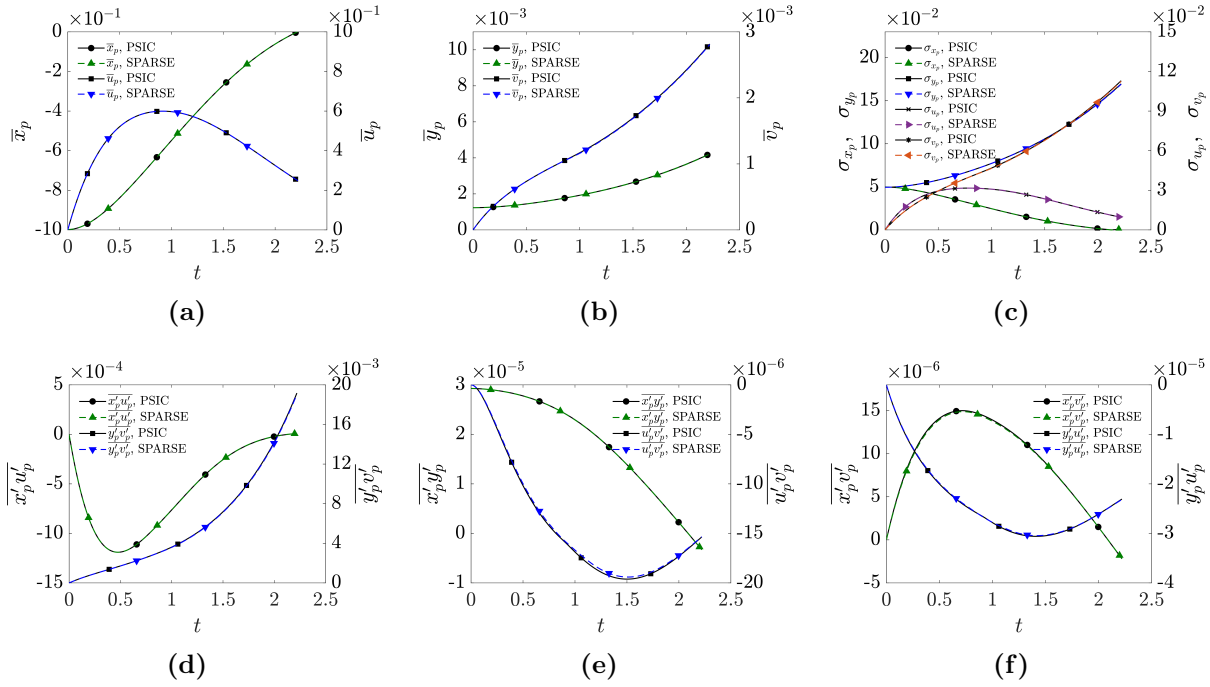


**Figure 3.5.** Averages (a) and deviations (b) of the particle phase for the closed SPARSE method and the PSIC method.

to the PSIC results for a time period on the order of at least three characteristic time scales. The relative error between the PSIC and SPARSE computations is related to the truncation of the third moments in the SPARSE equations and the Taylor expansion of the correction factor of the drag force $f_1$ given by (3.24). The matching between both approaches leads to a relative error less than 1% for all moments except for the maximum relative error of $\overline{u_p' v_p'}$ which is 1.5%, which indicates that the most sensitive variable to third order moments in the cloud is the correlation between the velocity components. The maximum relative error of the averages is 0.3% for $\overline{v}_p$ and the one of the deviations is 0.8% for $\sigma_{v_p}$. Because of the very good match for a single SPARSE cloud with a small number of PSIC particles, we do not investigate the effect of splitting clouds for this case.

### 3.4.2 ABC flow

Closed SPARSE is tested in three-dimensions by tracing clouds in the three-dimensional analytical velocity field of the so-called ABC flow. The ABC flow was introduced by [192] as part of the family of Beltrami flows satisfying that $\nabla \wedge \boldsymbol{u} = \boldsymbol{u}$. Any ABC flow is an exact steady solution of the Navier-Stokes equations

$$\frac{\partial \boldsymbol{u}}{\partial t} + \boldsymbol{u} \cdot \nabla \boldsymbol{u} = -\nabla p + \nu \nabla^2 \boldsymbol{u} + \boldsymbol{f}, \tag{3.26a}$$

$$\nabla \cdot \boldsymbol{u} = 0, \tag{3.26b}$$

where without loss of generality the density is assumed to be the unity, $p$ is the pressure, $\nu$ the dynamic viscosity and the forcing $\boldsymbol{f}$ is giving by

$$\boldsymbol{f} = \nu \left( A \sin z + C \cos y,\ B \sin x + A \cos z,\ C \sin y + B \cos x \right), \tag{3.27}$$

where for small Reynolds number, i.e., $\nu \gg 1$, the only stable solution is given by the ABC flow field $\boldsymbol{u} = (u, v, w)^\top$ with

$$u = A \sin z + C \cos y, \tag{3.28a}$$

$$v = B \sin x + A \cos z, \tag{3.28b}$$

$$w = C \sin y + B \cos x. \tag{3.28c}$$

The ABC flow has been extensively used to study chaotic effects in turbulence ([193, 194]) and non-linear dynamics ([195, 196, 197]). Here, we use it to test SPARSE clouds immersed in the ABC carrier phase flow. The carrier phase flow is independent of time, i.e., steady, and is specified according to (27). In other words, this field is not used as an initial condition to a time-dependent numerical prediction of the carrier-flow field.

We set the constants of the carrier flow field to $A = \sqrt{3}$, $B = \sqrt{2}$ and $C = 1$. Ten

thousand particles ($N_p = 10^4$) are released at rest with initial location $\overline{x}_p = \overline{y}_p = \overline{z}_p = \pi$ and standard deviations $\sigma_{x_p} = \sigma_{y_p} = \sigma_{z_p} = 0.08$ according to a uniform distribution where all variables are statistically independent at the initial time. The initial velocity averages and variances are zero since all point-particles are at rest initially. The correction factor $f_1$ used is taken according to (3.24) and the SPARSE simulation is computed with different levels of splitting, i.e., the single cloud is uniformly divided into $M_p = [1,\ 2,\ 3,\ 4,\ 5,\ 6]^3$ number of smaller clouds along $x_p$, $y_p$ and $z_p$ such that $M_p = M_p^{x_p} M_p^{y_p} M_p^{z_p}$ with $M_p^{x_p} = M_p^{y_p} = M_p^{u_p}$. Similar to the stagnation flow test case, the sampled initial condition for PSIC is used as initial condition for the closed SPARSE simulation. The reference Reynolds number is set to $Re_\infty = 250$ and the density ratio is $\rho_p = 10^4$. Four clouds with different Stokes numbers $St = [1,\ 2,\ 5,\ 10]$ are traced for 8 time units, during which the carrier flow was verified with Navier-Stokes simulations (not shown here) to not have a significant time-dependent change as compared to the initial velocity field. The non-dimensional particle diameters according to (3.4) for the four different clouds simulated are $d_p = [2.68,\ 3.8,\ 6,\ 8.49] \times 10^{-3}$. This leads to volume fractions of $[0.91,\ 2.57,\ 10.15,\ 28.70](\%)$ at the initial time. The larger volume fractions are nonphysical because collisions can be expected to affect the dynamics, but despite this the tests can still be used for purpose of assessing the formal, numerical accuracy and correct implementation of the 3D SPARSE model against PSIC as they both assume a non-collisional particle phase.

The average trajectories (solid black lines) of the four clouds are visualized in Figures 3.6a–3.6d. Three-dimensional prolates, whose axes are scaled with the principle strains, depict the cloud size. Single point-particles traced with the PSIC method are depicted as points for different instances of time. The cloud trajectories are in large determined by the the coherent structures of the ABC flow as visualized by the vorticity contours in each plane of the boundaries of Figures 3.6a–3.6d. The $x$ component of the particle velocity initially increases as the particle cloud is accelerated by one of these large flow structures. After the initial acceleration, the clouds are transported primarily

in $x$-direction and its lateral motion is affected only in a secondary manner by smaller vortices in the $x-y$ and $x-z$ planes. Therefore, the velocity and locations along $x$ are greater (see Figures 3.7a and 3.7b), whereas the average particle phase solutions in the perpendicular directions remain on the same order of magnitude. As evidence of the excellent match between PSIC and the closed SPARSE method we select the case for $St = 2$ to show the results of all moments of the cloud in Figure 3.7. The averages of the cloud location and velocity in Figures 3.7a and 3.7b show no visible difference between both approaches. The particle phase variances are captured with the SPARSE method as shown in Figures 3.7c and 3.7d. We note that at later time $t > 7$, the variances show visible errors that are on the order of percentages, an indication that at that instance the truncation errors are no longer negligible. The terms that correlate sub-cloud scale position and velocity fluctuations in multiple directions can be either positive or negative, indicating the combined grow of the cloud in the mixed direction. These correlated second moments combining position and velocity are shown in Figures 3.7e–3.7i and show also relative error on the order of percentages for later times.

To evaluate the convergence of the SPARSE solution with an increase number of clouds, we perform computations for each case and subdivide (or split) in each spatial dimension up to six subdivisions, meaning a total of $M_p = 6^3$ macro-particles for the maximum level of splitting. The results in Figures 3.7a–3.7i correspond to the maximum level of splitting. To obtain a measurement of the particle averages we use the modulus of the average particle location and velocity and for a measure of the cloud's deviation in locations and velocities we use a geometrical average as follows

$$|\overline{\mathbf{x}}_p| = \sqrt{\overline{x}_p^2 + \overline{y}_p^2 + \overline{z}_p^2}, \qquad |\overline{\mathbf{u}}_p| = \sqrt{\overline{u}_p^2 + \overline{v}_p^2 + \overline{w}_p^2}, \tag{3.29a}$$

$$\delta_{x_p} = \left(\sigma_{x_p}\sigma_{y_p}\sigma_{z_p}\right)^{1/3}, \qquad \delta_{u_p} = \left(\sigma_{u_p}\sigma_{v_p}\sigma_{w_p}\right)^{1/3}. \tag{3.29b}$$

The convergence of those measurements is shown in Figure 3.8 according to the error

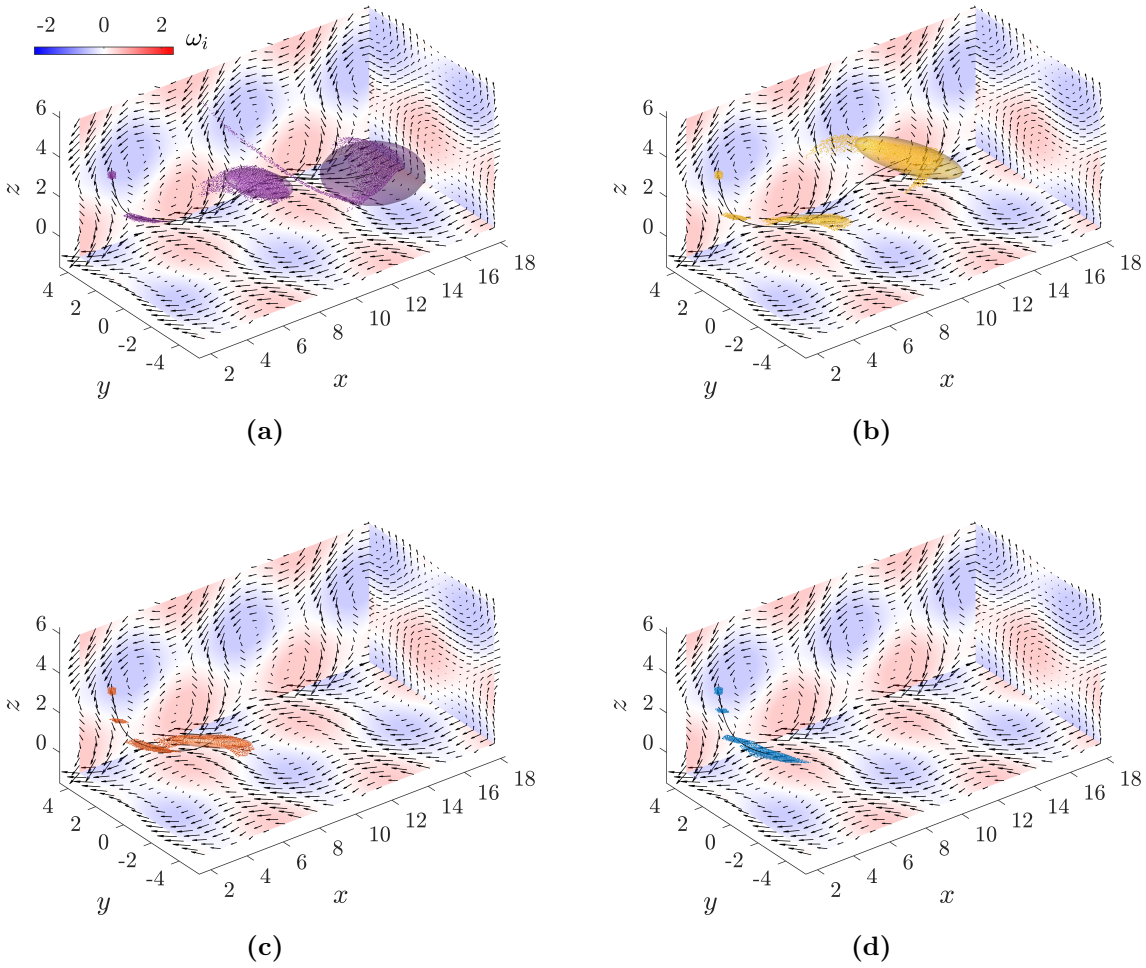


**Figure 3.6.** Results of the ABC flow test case. Four SPARSE cloud trajectories carried by an ABC flow for Stokes numbers $St = [1,\ 2,\ 5,\ 10]$ are depicted in Figures (a), (b) , (c) and (d) respectively. Along the trajectory, the the SPARSE macro-particles are depicted with prolates scaled by the principle strains given by the second moments and the point-particles traced with PSIC are depicted as points for different instants of times $t = [0,\ 2.67,\ 5.33,\ 8]$. The carrier flow is visualized with the vorticity component corresponding to each plane superposed with velocity vector fields.

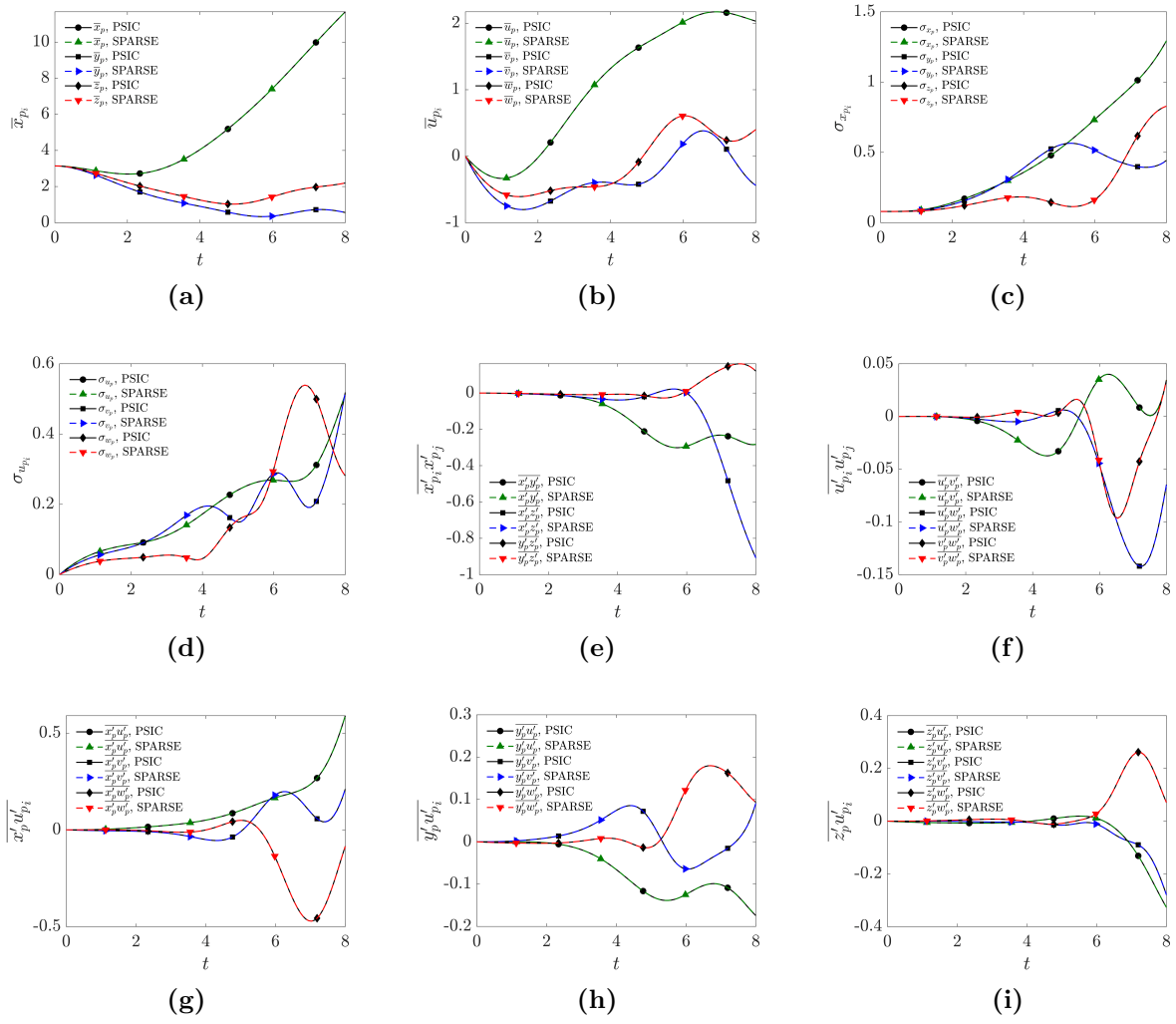


**Figure 3.7.** Results of the SPARSE method compared with PSIC computations of the ABC flow for the average particle location (a), particle velocity (b), deviations in particle position (c) and particle velocity (d) as well as cross-terms in particle location (e) and in particle velocity (f) for $St = 2$.

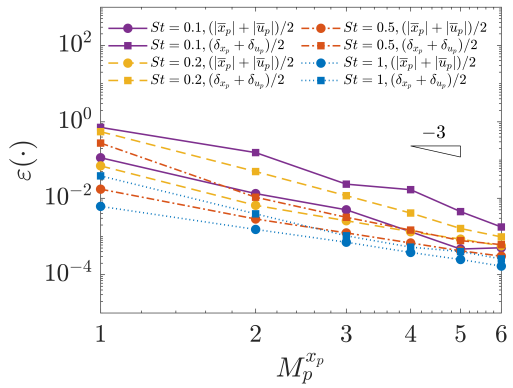


**Figure 3.8.** Convergence of the SPARSE method as compared with the PSIC approach for the average modulus of the particle location and velocity and representative particle deviation in position and velocity computed as the averages of the magnitudes in (3.29) when splitting into $M_p = M_p^{x_p} M_p^{y_p} M_p^{z_p}$ macro-particles where $M_p^{x_p} = M_p^{y_p} = M_p^{z_p}$. The error $\varepsilon(\cdot)$ of the magnitudes shown in the legend (defined in (3.23)) shows a third order convergence rate. The Figure includes the results for the four clouds represented in Figure 3.6 with $St = [1,\ 2,\ 5,\ 10]$.

defined in (3.23) where the colors of the plots match with the clouds as depicted in Figure 3.6. These trends show the expected convergence of the SPARSE method when the initial condition is subdivided in macro-particles as derived in Section 3.2.4. The errors are generally smaller for clouds with a greater Stokes number. This is consistent with the proportionality of the right hand side of the system of closed SPARSE equations (3.10) with $1/St$. The truncated terms are also proportional to $1/St$ and thus reduced with an increase in $St$. A physics analogy that intuitively explains this error behavior, is that clouds with more inertia are more reticent to deformation according to the fluid flow and the eventual grow of high order moments (or errors) within the cloud.

### 3.4.3 Isotropic turbulence

To test the three-dimensional SPARSE formulation in a non-analytical, computed and complex velocity field, we revisit the simulation of a decaying isotropic turbulence ([198, 199]) performed in Ref. [57]. The isotropic turbulence simulation is performed in a cube with periodic boundary conditions on all sides with the validated discontinuous

Galerkin code as described in Ref. [200] and references therein, where the initial condition is adopted from Ref. [201].

Computations are performed on a domain $\Omega$ spanned by coordinates $(x, y, z)$, defining a cube of size $2\pi$ so that $\Omega = [0, 2\pi] \times [0, 2\pi] \times [0, 2\pi]$. The reference Reynolds number is $Re_\infty = 2357$ and the initial turbulent Mach number $Ma_0 = 0.05$ [201]. The physical particles are initialized over a cubic domain of size $l_0 = 0.1$ stretching approximately 3 grid cells in each direction with $N_p = 27,000$ total point-particles uniformly distributed in each direction. The particles are released at rest and according to a one-way coupling, assuming that the flow is dilute, the particles have small but not negligible inertia with a Stokes number $St = 0.5$ but the flow is not perturbed by them. The temperature of all point-particles is unity at $t$=0. The non-dimensional particle diameter is $d_p = 2 \times 10^{-3}$ and the ratio of densities $\rho_p = 10^3$. The drag and heat transfer correction factors for this case are adopted from Refs. [48, 188] and read as

$$f_1 = \left(1 + 0.38\frac{Re_p}{24} + \frac{Re_p^{0.5}}{6}\right)\left[1 + \exp\left(\frac{-0.43}{M_p^{4.67}}\right)\right], \tag{3.30a}$$

$$f_2 = 1 + 0.3Re_p^{0.5}Pr^{0.33}. \tag{3.30b}$$

The computed carrier phase velocities are used to determine the particle Reynolds as defined in (3.4) and the particle Mach number $M_p = |\boldsymbol{u} - \boldsymbol{u}_p|/\sqrt{T_f}$, in the forcing correction factors (3.30). The Prandtl number is $Pr = 0.7$ and the relative heat capacity is set to unity $c_r = 1$.

The result of the computations for a thousand macro-particles $M_p = 10^3$, uniformly distributed in space is shown in Figure 3.9 for several instants of time where the $27,000$ point-particles computed with the PSIC method are shown as points and the SPARSE clouds as ellipsoids using the covariance matrix of the cloud location in three dimensions. Contours of the turbulent kinetic energy $k$ visualize the carrier phase's turbulent structures

on the boundaries of the cube. The particles initially at rest react to the carrier flow. As compared to the fluid tracers (not shown), the inertial tracers have a smoother response. After some time, the initial cube of particles is dispersed and the macro-particles are advected and deformed according to the carrier flow.

The average particle location and velocity defined in (3.29a) computed with the PSIC and SPARSE methods are compared in Figure 3.10a. The plots show that the mean location and velocity initially change according to the dynamics of the eddies at the cloud location. As the cloud spreads and the fluid velocity is sampled over a larger area, the fluid velocity through the cloud approaches zero after an initial acceleration because the turbulence is isotropic, making the average velocity in the box to evolve towards zero. The deviations of the cloud's location is plotted versus time in Figure 3.10b and show a general increase in all three dimensions consistent with turbulent diffusion mechanisms [202]. The particle standard deviations of the sub-cloud scale velocity increase from an initial rest state in which the standard deviations are zero towards a trend that correlates with the decaying carrier phase turbulence as seen in Figure 3.10d. The temperature average is almost constant and the standard deviation of the temperature small as shown in Figure 3.10c because the turbulence Mach number is low and the flow is near isothermal. The standard deviation of the particle temperature of the cloud behaves similar to the one of the particle velocity, starting from an initial value zero according to a uniform temperature in the cloud to increase with an oscillating trend governed by the changes in the carrier phase flow temperature. The results by PSIC and SPARSE methods are in an excellent agreement for the average magnitudes of the particle cloud as well as for its deviations. The rest of the second moments not shown in Figure 3.10 are also well captured by the SPARSE method. The maximum discrepancy in the first two moments when comparing SPARSE with PSIC show a relative error of 3% or smaller validating the closed SPARSE tracer.

The computational efficiency of the SPARSE tracer versus the point particle tracer

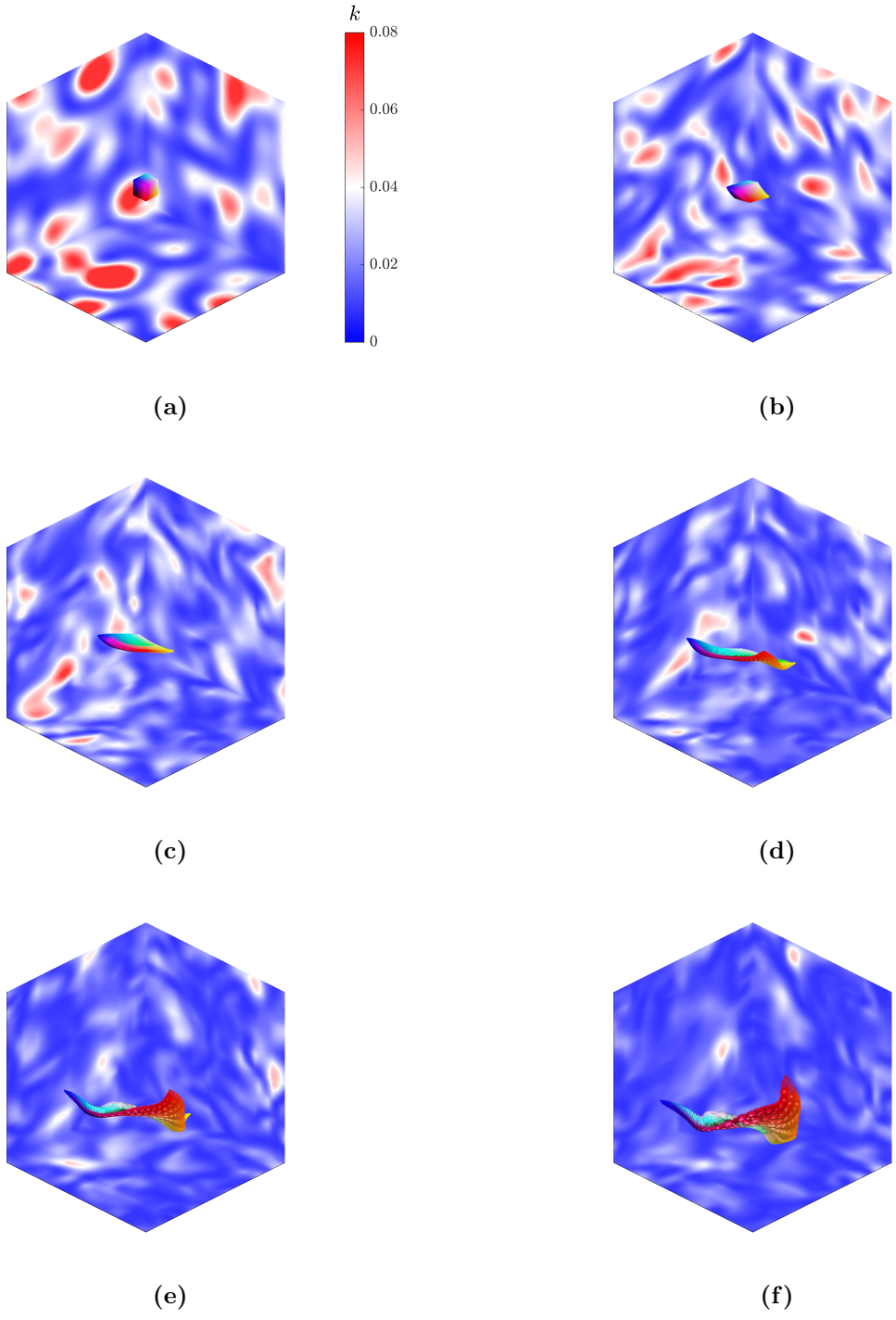


**Figure 3.9.** Locations of the particles and macro-particles tracked with PSIC and SPARSE methods for the isotropic decaying turbulence case at times (a) $t = 0$, (b) $t = 0.8$, (c) $t = 1.6$, (d) $t = 2.4$, (e) $t = 3.2$ and (f) $t = 4$. The contours show the turbulent kinetic energy in the boundaries of the domain. The point-particles are represented with points and the macro-particles with ellipsoids.

depends on a number of factors for this three-dimensional isotropic turbulence simulation. Firstly, the number of ODEs of the SPARSE model as compared to PSIC is 1/0.1852 larger. Despite this near factor five increased number of equations, SPARSE is computational far more efficient, because secondly each macro-particle models hundreds of point particles which leads to saving according to (3.22) and thirdly because SPARSE has a third order convergence rate (Figure 3.11) of the statistics whereas PSIC converges according the inverse of the square root of the number of samples, i.e., number of particles. To obtain accurate estimates of the increased computational efficiency, a combination of these factors determine the computational efficiency. For an accurate estimate of code, the algorithms have to be optimized with various computer languages, which is beyond the scope of the current paper.

## 3.5 Summary of results

A closed SPARSE tracer is developed that predicts the dynamics of the first two statistical moments of groups of particles and traces them as a single point. This cloud or macro-particle approach accounts for the effects of carrier phase velocity distribution and the sub-cloud's second moments of the particle phase and carrier phase. The tracer combines a truncated Taylor expansion of the forcing correction factors around the cloud's mean relative velocity and a Reynolds decomposition of the ensemble averages of the particle variables within the cloud. Using a Taylor expansion, averaging and truncation, the extended SPARSE formulation provides a closed set of equations for the first two moments of the particle cloud. The closure expresses unknown combined moments of both phases in terms of those known moments of the disperse phase that are traced with the SPARSE method. This closes the SPARSE tracer method that so far has been used with an *a priori* closure.

The SPARSE method reduces the computational expense for the tracing of the first

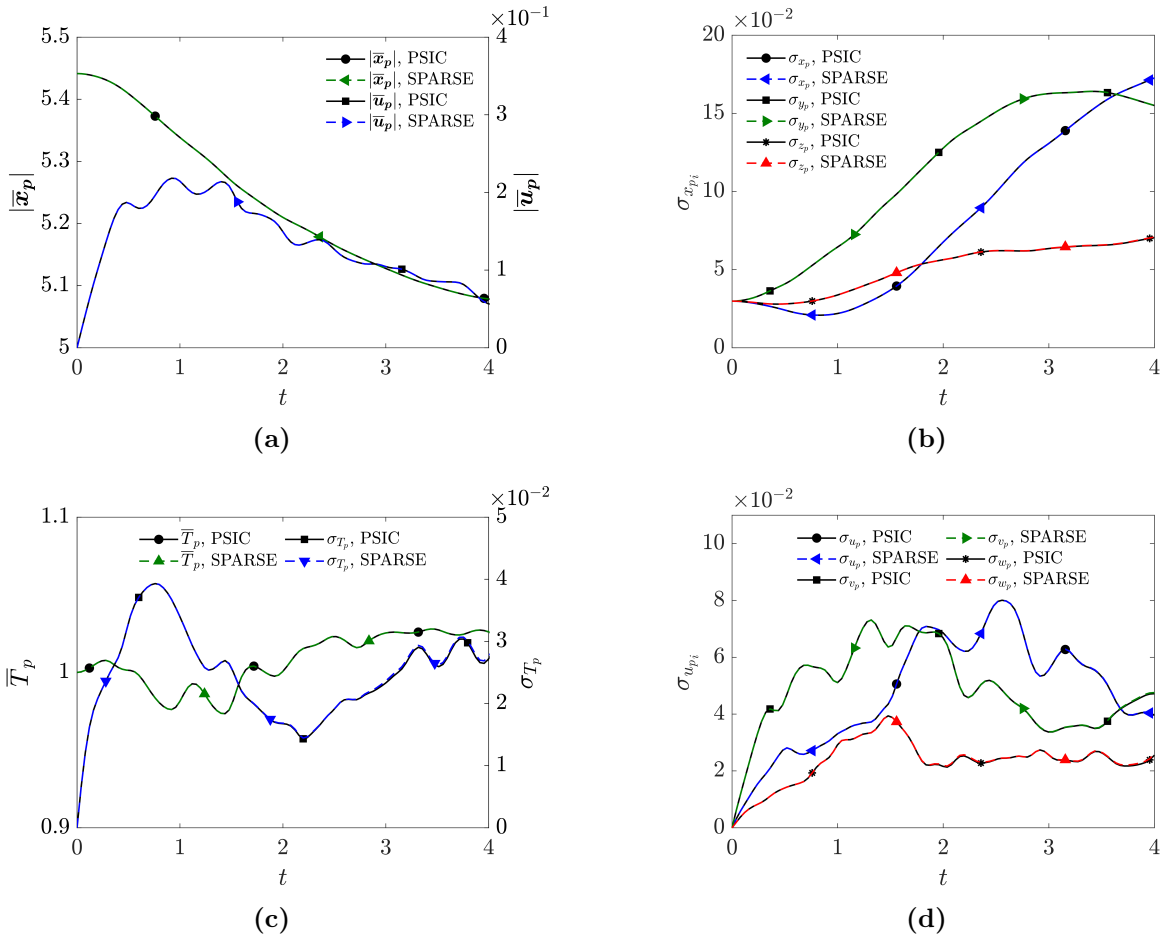


**Figure 3.10.** Statistics of the inertial particle cloud in the three-dimensional decaying isotropic turbulence case computed with PSIC and SPARSE methods; (a) average module of the particle cloud location and velocity, (b) spatial deviations of the particle cloud, (c) temperature mean and deviation and (c) deviations of the particle cloud velocity.

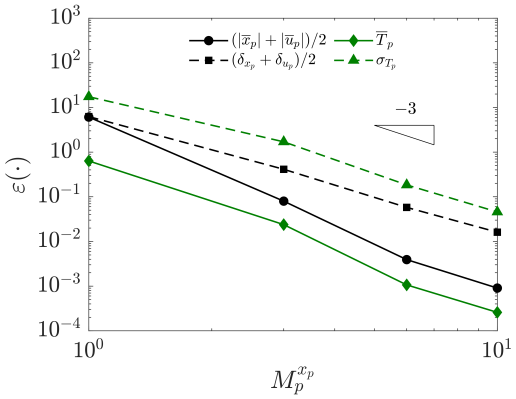


**Figure 3.11.** Convergence of the SPARSE method as compared with the PSIC approach for the average modulus of the particle location and velocity and representative particle deviation in position and velocity computed as the averages of the magnitudes in (3.29) and average and standard deviation of the particle temperature.

two statistical moments of a cloud as compared to a simulation with the PSIC method by reducing the required degrees of freedom. It improves upon the accuracy of commonly used zeroth order Cloud-in-Cell models through a second order moment correction by expanding the forcing function in the surroundings of the cloud. The error of the SPARSE tracer is a function of the truncated terms of the Taylor expansions and the truncation of higher-order statistical moments that are shown in test cases to converge with the size of the macro-particle to the third power.

The closed SPARSE method is verified and validated against PSIC results for analytical one-, two- and three-dimensional flows where the relative errors are either negligible or small percentages in all the test cases.

The SPARSE tracer is accurate for finite time and will require merging and join of macro-particles to adapt the number of macro-particles needed depending on the error of the model as the simulation evolves.

## 3.6 Acknowledgments

Sections 3.1 through 3.5, are a reprint of the material as it appears in Ref. [3], "Closed SPARSE—A predictive particle cloud tracer", D. Domínguez-Vázquez, B. F. Klose and G. B. Jacobs, *International Journal of Multiphase Flow*, 161, 104375, 2023. D. Domínguez-Vázquez: conceptualization, investigation, original draft preparation, visualization. B.F. Klose: data generation, supervision. G. B. Jacobs: conceptualization, supervision, review & editing.

# Chapter 4

# SPARSE-R: A point-cloud tracer with random forcing

## 4.1 Introduction

Here, the SPARSE–R method [4] is introduced, that accounts for both randomness of the empirical or data–driven forcing functions and/or stochasticity of the subcloud dynamics, extending the SPARSE model described in Chapter 3. We define the random forcing function via series expansions involving proper sets of random as proposed in Ref. [99] to trace randomly forced (rF) particle clouds. The SPARSE–R method is designed to capture the first two moments of the particle phase by computing a closed set of equations in Lagrangian form combining Taylor expansions around the average magnitudes of the cloud with Reynolds averaging. The SPARSE–R method exhibits a third order convergence rate with respect to the standard deviations of the particle phase variables. By subdividing or splitting the particle cloud into subclouds (see Fig. 1.1 right) the accuracy of the method is ensured. Using a mixture distribution (MD) of Gaussians, SPARSE–R approximates higher order moments and enables the reconstruction of the PDF of the of the underlying point–particle population. The computational savings as compared with Monte Carlo (MC) simulations using the PSIC description (MC–PSIC), is proportional to the number of point–clouds or subclouds divided by the total number of point–particles. Because of the slow convergence of MC, the number of samples (point–

particles) is several order of magnitudes larger than the number of subclouds needed for an accurate SPARSE–R simulation, ensuring computational savings. The SPARSE–R method computes the moments and the PDF of the particle phase in a closed and computationally efficient manner that makes it scalable to complex flows. It combines the advantages of the MoM in a closed form, reduction of the computational cost as compared to sampling methods, with the advantages of PDF methods, full statistical description able to capture rare events linked to fat-tailed PDFs in the solution. Considering the MC–PSIC simulations the ground truth, we compare the SPARSE–R method with the MC–PSIC method in a variety of verification tests on dilute, one–way coupled particle–laden flow problems with prescribed velocity fields, and a numerical simulation of an isotropic turbulence flow, where the gas is simulated with a compressible discontinuous Galerkin (DG) DNS solver.

## 4.2 SPARSE–R: point–cloud model with random forcing

### 4.2.1 Point–particle model

The non–dimensional governing point–particle equations for a small spherical particle immersed in a carrier flow where the inertial effects are dominant is given by

$$\frac{\mathrm{d}\boldsymbol{x}_p}{\mathrm{d}t} = \boldsymbol{u}_p, \tag{4.1a}$$

$$\frac{\mathrm{d}\boldsymbol{u}_p}{\mathrm{d}t} = \frac{f_1}{St}\left(\boldsymbol{u} - \boldsymbol{u}_p\right), \tag{4.1b}$$

$$\frac{\mathrm{d}T_p}{\mathrm{d}t} = \frac{2c_r}{3Pr}\frac{f_2}{St}\left(T - T_p\right), \tag{4.1c}$$

where $\boldsymbol{x}_p$, $\boldsymbol{u}_p$ and $T_p$ are the non–dimensional particle location, velocity and temperature and $\boldsymbol{u}$ and $T$ are the non–dimensional velocity and temperature of the carrier flow evaluated at the particle location. The Prandtl number $Pr = \tilde{\mu}\tilde{c}/\tilde{k}$ is defined with the dimensional dynamic viscosity $\tilde{\mu}$, specific heat capacity $\tilde{c}$ and conductivity $\tilde{k}$ of the flow. The Stokes

number $St = \tau_p/\tau_f$ is defined with the characteristic time of the particles $\tau_p = \tilde{\rho}_p \tilde{d}_p^2/\left(18\tilde{\mu}\right)$ where $\tilde{\rho}_p$ and $\tilde{d}_p$ are the dimensional density and diameter of the particles and $\tau_f = L_\infty/U_\infty$ is the characteristic time of the flow defined with a reference length and velocity. Making use of reference values denoted with subscript infinite, we define the reference Prandtl number $Pr_\infty = \mu_\infty c_\infty/k_\infty$ and Reynolds number $Re_\infty = \rho_\infty U_\infty L_\infty/\mu_\infty$, one can rewrite the non–dimensional numbers in terms of the reference values

$$Re_p = Re_\infty \frac{\rho}{\mu}|\boldsymbol{u} - \boldsymbol{u}_p| d_p, \qquad St = Re_\infty \frac{\rho_p d_p^2}{18\mu}, \qquad Pr = Pr_\infty \frac{\mu c}{k} \tag{4.2}$$

using the non–dimensional variables $\rho = \tilde{\rho}/\rho_\infty$, $\mu = \tilde{\mu}/\mu_\infty$, $k = \tilde{k}/k_\infty$, $c = \tilde{c}/c_\infty$, $\rho_p = \tilde{\rho}_p/\rho_\infty$, $c_p = \tilde{c}_p/c_\infty$ and, $d_p = \tilde{d}_p/L_\infty$. The specific heat ratio of the two phases is defined as $c_r = c_p/c$.

The correction factors of exchanged momentum and energy are given by the functions $f_1$ and $f_2$ which correct the analytical laminar solution for the drag coefficient $C_D$ and Nusselt number $Nu$ (based on the particle diameter) as

$$C_D = \frac{24}{Re_p} f_1, \tag{4.3a}$$

$$Nu = 2 f_2. \tag{4.3b}$$

These functions, are also denoted the *forcing functions*, typically correct for higher particle Reynolds and Mach numbers and/or other flow parameters [48, 49, 50, 51, 52, 53, 54].

### 4.2.2 Point–cloud SPARSE model

Following the SPARSE approach as described in Refs. [57, 58, 3], we model a cloud of particles with the MoM using a Reynolds decomposition of any instantaneous scalar particle variable $\phi$ into its average and fluctuating component according to $\phi = \overline{\phi} + \phi'$,

where the average is defined by its ensemble average

$$\overline{\phi} = \frac{1}{N_p} \sum_{i=1}^{N_p} \phi_i, \tag{4.4}$$

for $N_p$ point–particles within a cloud. Using the Reynolds decomposition for the variables of the two phases including the forcing functions $f_1$ and $f_2$, the system of equations for the kinematics, dynamics and thermodynamics of a stochastic cloud of point–particles can be written as

$$\frac{\mathrm{d}\overline{\boldsymbol{x}}_p}{\mathrm{d}t} + \frac{\mathrm{d}\boldsymbol{x}'_p}{\mathrm{d}t} = \overline{\boldsymbol{u}}_p + \boldsymbol{u}'_p, \tag{4.5a}$$

$$\frac{\mathrm{d}\overline{\boldsymbol{u}}_p}{\mathrm{d}t} + \frac{\mathrm{d}\boldsymbol{u}'_p}{\mathrm{d}t} = \frac{1}{St}\left(\overline{f}_1 + f'_1\right)\left(\overline{\boldsymbol{u}} + \boldsymbol{u}' - \overline{\boldsymbol{u}}_p - \boldsymbol{u}'_p\right), \tag{4.5b}$$

$$\frac{\mathrm{d}\overline{T}_p}{\mathrm{d}t} + \frac{\mathrm{d}T'_p}{\mathrm{d}t} = \frac{2c_r}{3PrSt}\left(\overline{f}_2 + f'_2\right)\left(\overline{T} + T' - \overline{T}_p - T'_p\right), \tag{4.5c}$$

that after manipulation and averaging leads to the equations for the first two moments of the particle phase

$$\frac{\mathrm{d}\overline{x}_{p_i}}{\mathrm{d}t} = \overline{u}_{p_i}, \tag{4.6a}$$

$$St\frac{\mathrm{d}\overline{u}_{p_i}}{\mathrm{d}t} = \overline{f}_1\left(\overline{u}_i - \overline{u}_{p_i}\right) + \overline{f'_1 u'_i} - \overline{f'_1 u'_{p_i}}, \tag{4.6b}$$

$$\frac{3PrSt}{2c_r}\frac{\mathrm{d}\overline{T}_p}{\mathrm{d}t} = \overline{f}_2\left(\overline{T} - \overline{T}_p\right) + \overline{f'_2 T'} - \overline{f'_2 T'_p}, \tag{4.6c}$$

$$\frac{\mathrm{d}}{\mathrm{d}t}\left(\overline{x'_{p_i} x'_{p_j}}\right) = \overline{x'_{p_i} u'_{p_j}} + \overline{x'_{p_j} u'_{p_i}}, \tag{4.6d}$$

$$St\frac{\mathrm{d}}{\mathrm{d}t}\left(\overline{u'_{p_i} u'_{p_j}}\right) = \overline{f}_1\left(\overline{u'_i u'_{p_j}} + \overline{u'_j u'_{p_i}} - 2\overline{u'_{p_i} u'_{p_j}}\right) + \overline{f'_1 u'_{p_i}}\left(\overline{u}_j - \overline{u}_{p_j}\right) + \overline{f'_1 u'_{p_j}}\left(\overline{u}_i - \overline{u}_{p_i}\right), \tag{4.6e}$$

$$\frac{3PrSt}{4c_r}\frac{\mathrm{d}\overline{T'^2_p}}{\mathrm{d}t} = \overline{f}_2\left(\overline{T'T'_p} - \overline{T'_p}\right) + \overline{f'_2 T'_p}\left(\overline{T} - \overline{T}_p\right), \tag{4.6f}$$

$$\frac{\mathrm{d}}{\mathrm{d}t}\left(\overline{x'_{p_i} u'_{p_j}}\right) = \overline{u'_{p_i} u'_{p_j}} + \frac{1}{St}\left[\overline{f}_1\left(\overline{x'_{p_i} u'_j} - \overline{x'_{p_i} u'_{p_j}}\right) + \overline{f'_1 x'_{p_i}}\left(\overline{u}_j - \overline{u}_{p_j}\right)\right], \tag{4.6g}$$

$$\frac{\mathrm{d}}{\mathrm{d}t}\left(\overline{x'_{p_i} T'_p}\right) = \overline{u'_{p_i} T'_p} + \frac{2c_r}{3PrSt}\left[\overline{f}_2\left(\overline{x'_{p_i} T'} - \overline{x'_{p_i} T'_p}\right) + \overline{f'_2 x'_{p_i}}\left(\overline{T} - \overline{T}_p\right)\right], \tag{4.6h}$$

$$\begin{aligned}\frac{\mathrm{d}}{\mathrm{d}t}\left(\overline{u'_{p_i} T'_p}\right) = {} & \frac{1}{St}\left[\overline{f}_1\left(\overline{u'_i T'_p} - \overline{u'_{p_i} T'_p}\right) + \overline{f'_1 T'_p}\left(\overline{u}_i - \overline{u}_{p_i}\right)\right] \\ & + \frac{2c_r}{3PrSt}\left[\overline{f}_2\left(\overline{u'_{p_i} T'} - \overline{x'_{p_i} T'_p}\right) + \overline{f'_2 u'_{p_i}}\left(\overline{T} - \overline{T}_p\right)\right],\end{aligned} \tag{4.6i}$$

where index notation with $i = 1, 2, 3$ and $j = 1, 2, 3$ is used to present a compact version of the equations. Note that for any two vectorial variables $\boldsymbol{\eta}$ and $\boldsymbol{\xi}$, the term $\overline{\eta_i' \xi_j'}$ is a component of a three by three tensor, whereas $\overline{\eta}_i$ is a the component of a three–dimensional vector. For the general three–dimensional case we have $\boldsymbol{x}_p = (x_p \; y_p \; z_p)^\top$ and $\boldsymbol{u}_p = (u_p \; v_p \; w_p)^\top$. For a combined moment of a scalar $\phi$ and a vectorial magnitude $\boldsymbol{\eta}$, the term $\overline{\phi' \eta_i'}$ represent the $i-$th component of a vector. Note that the system of equations (4.6) truncates moments that are greater than third order while the equations for the first moments (4.6a)–(4.6c) are not truncated. In the second moment equations (4.6d)–(4.6i) high–order terms are neglected.

### 4.2.3 Random forcing SPARSE–R model

The dependencies of both correction functions $f_1$ and $f_2$ correct for physics that deviate from the case of creeping flow over a spherical particle. In the PSIC model, those functions have generally been used as exact force models that depend only on the particle phase and the carrier phase. In practice, however, they can be known only within confidence intervals as they are approximate curve fits to experimental and computational data that have sources of systematic uncertainty or epistemic uncertainty. Alternatively, the forcing function can be interpreted in the context of stochastic models to account for stochasticity of subgrid scales. In other words, the function may be used to account for aleatoricism in the particle forcing.

To model confidence intervals, we follow Refs. [57, 58, 3], and consider the functions $f_1$ and $f_2$ to be dependent on the relative velocity $\boldsymbol{a} = \boldsymbol{u} - \boldsymbol{u}_p$ and the random coefficients $\alpha_i$ and $\beta_i$ with $i = 1, \ldots, N$ where $N$ is the number of modes considered. First proposed in Ref. [99] and then later also used in Ref. [6], the correction functions with quantified

uncertainty can be described with a series expansion as

$$f_1(\boldsymbol{a}) = \sum_{i=1}^{\infty} \alpha_i \psi_i(\boldsymbol{a}) \approx \sum_{i=1}^{N} \alpha_i \psi_i(\boldsymbol{a}), \qquad f_2(\boldsymbol{a}) = \sum_{i=1}^{\infty} \beta_i \zeta_i(\boldsymbol{a}) \approx \sum_{i=1}^{N} \beta_i \zeta_i(\boldsymbol{a}), \tag{4.7}$$

where the variables $\alpha_i$ and $\beta_i$ are correlated or uncorrelated random coefficients that quantify the uncertainty in the forcing defined by the joint PDF $f_{\boldsymbol{\alpha\beta}}(\alpha_1, \ldots, \alpha_N, \beta_1, \ldots, \beta_N)$ and the orthogonal basis functions $\psi_i$ and $\zeta_i$. We assume $f_1$ and $f_2$ to have compact support on $\boldsymbol{a} \in [\boldsymbol{a}_{min},\ \boldsymbol{a}_{max}]$. We take both $\psi_i$ and $\zeta_i$ as a Chebyshev polynomial of the first kind. Because the forcing function is approximated by a polynomial, it can only be accurate within the interval of the independent variable that the polynomial depends on, i.e., $\boldsymbol{a}$. In SPARSE the forcing function and its derivative are evaluated only at the mean relative velocity $\overline{\boldsymbol{a}}$. So, if the SPARSE solution predicts a mean relative velocity outside of the accurate polynomial range, then the forcing function will need to be approximated within a new interval.

Using (4.7) and decomposing the stochastic variables in average plus fluctuation, the mean and variance of the forcing functions are given by

$$\overline{f}_1 = \sum_{i=1}^{N} \overline{\alpha}_i \psi_i(\boldsymbol{a}), \tag{4.8a}$$

$$\sigma_{f_1}^2 = \overline{\left( \sum_{i=1}^{N} \alpha_i' \psi_i(\boldsymbol{a}) \right)^2} = \sum_{i=1}^{N} \overline{\alpha_i'^2} \psi_i^2(\boldsymbol{a}) + \sum_{i \neq j}^{N(N-1)/2} 2\overline{\alpha_i' \alpha_j'} \psi_i(\boldsymbol{a}) \psi_j(\boldsymbol{a}), \tag{4.8b}$$

and equivalently for $f_2$. The variance of the forcing function is then described by the second moments of the coefficients and captures the uncertainty in the forcing functions by combining $N$ modes. As an example consider an empirical forcing that is based on the Schiller and Naumann (SN) correlation [203] given by

$$g_1 = 1 + 0.15 Re_p^{0.687}. \tag{4.9}$$

In Figure 4.1a, this forcing is plotted with an unknown confidence interval modeled by the first five Chebyshev modes $\psi_1, \ldots, \psi_5$ where the random coefficients $\alpha_1, \ldots, \alpha_5$ are considered uncorrelated. Two standard deviation bounds are depicted when considering the standard deviation of all modes zero except for the modes one $\sigma_{i\neq 0} = 0$, third $\sigma_{i\neq 3} = 0$ and fifth $\sigma_{i\neq 5} = 0$ in dashed, dash–dotted and dotted lines respectively. The number of random modes is chosen such that the series expansion can accurately approximate complex dependencies of the confident interval with the relative velocity. Considering only the first mode to be random (i.e., only $\alpha_1$ is given by a PDF and the rest $\alpha_2, \ldots, \alpha_N$ are deterministic) the standard deviation $\sigma_{f_1}$ does not change with respect to the relative velocity (Fig. 4.1a dashed line). By combining modes, more complex functions and confidence interval can be approximated by (4.8b). In Figure 4.1b (dashed line), we show a combination of only two modes that localizes a particle Reynolds number where the forcing is defined with a smaller confidence interval.

We consider a representation of the random function by a single mode as

$$f_1(\boldsymbol{a}) = \alpha g_1(\boldsymbol{a}), \qquad f_2(\boldsymbol{a}) = \beta g_2(\boldsymbol{a}), \tag{4.10}$$

where $g_1$ and $g_2$ carry the dependencies with the relative velocity and the random coefficients are reduced to $\alpha$ and $\beta$ with given PDFs $f_\alpha(\alpha)$ and $f_\beta(\beta)$. For the Schiller and Naumann correlation this yields $f_1 = \alpha(1 + 0.15Re_p^{0.687})$ which corresponds to the dash–dotted line in Figure 4.1b. This confidence interval for a single mode representation with the Reynolds number is consistent with trends reported in literature (see for example [204]).

The average of the random coefficients, $\alpha$ and $\beta$, in (4.10) is unity, $\overline{\alpha} = \overline{\beta} = 1$. The second moments of the coefficients $\overline{\alpha'^2}$, $\overline{\beta'^2}$ and $\overline{\alpha'\beta'}$ are the measures that quantify the uncertainty in this forcing function. The second moments propagate non–linearly into the solution of the SPARSE–R cloud. For a deterministic forcing the moments are zero.

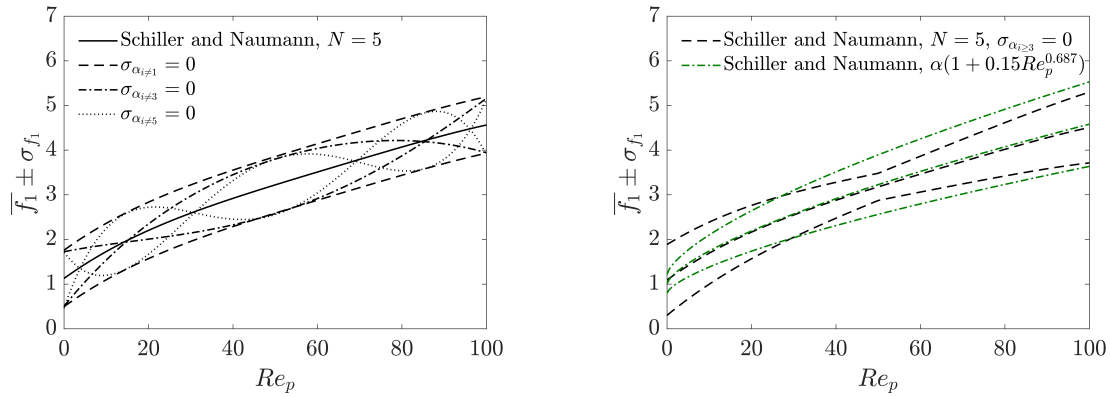


**Figure 4.1.** Two bandwidth representation of the random forcing function $f_1$ when the SN correlation is fitted with the first five modes; (a) considering random only in the first (dashed line), third (dash–dotted line) and fifth (dotted line) modes; (b) combining the random modes first and second (dashed line) and taking $f_1 = \alpha(1 + 0.15Re_p^{0.687})$ (dash–dotted line). The particle Reynolds number is $Re_p = Re_\infty|\boldsymbol{a}|d_p$ according to (4.2) where constant density and viscosity are considered.

### 4.2.4 Closure model

The SPARSE–R equations in (4.6) are not yet closed for terms that are on the order of fluctuations squared and that are function of a combination of particle phase and flow variables, and correction functions. To close (4.6), we follow the procedure in Ref. [3]. The carrier flow velocity $\boldsymbol{u}$ and temperature $T$ fields are Taylor expanded around the average particle location truncating terms of order greater than two. By using a Taylor expansion, we obtain an estimate of the carrier flow field at the particle locations within the cloud region and can be interpreted as interpolation within the cloud region. The forcing functions $f_1$ and $f_2$ are also expanded around the average values of the relative velocity and random coefficients of the particle cloud. For completeness, we review the closure approach and discuss it for random forcing.

Starting with the interpolation of the mean carrier flow velocity and temperature, we Taylor expand at the average particle location of the cloud. Let $\phi$ be a flow variable

(for example, a velocity component $u_i$ or the temperature $T$), then

$$\overline{\phi} \approx \overline{\phi\left(\overline{\boldsymbol{x}}_p\right) + x'_{p_i} \left.\frac{\partial \phi}{\partial x_i}\right|_{\overline{\boldsymbol{x}}_p} + \frac{1}{2} x'_{p_i} x'_{p_j} \left.\frac{\partial^2 \phi}{\partial x_i \partial x_j}\right|_{\overline{\boldsymbol{x}}_p}} = \phi\left(\overline{\boldsymbol{x}}_p\right) + \frac{1}{2}\overline{x'_{p_i} x'_{p_j}} \left.\frac{\partial^2 \phi}{\partial x_i \partial x_j}\right|_{\overline{\boldsymbol{x}}_p}, \tag{4.11}$$

which relates the solution evaluated at the averaged cloud's location, the second derivative of the carrier phase at the averaged cloud's location and the covariances of the locations of the particle cloud $\overline{x'_{p_i} x'_{p_j}}$ which are governed by equation (4.6d).

To close second moments, we proceed similarly by Taylor expanding the flow variables. Depending on the type of term to close, the Taylor expansion has to be applied once or twice to find a closure. If the term involves two variables different from the particle phase variables (particle position, velocity or temperature), it has to be applied twice whereas if it contains a combination of a flow variable or forcing function with a particle variable, it has to be applied only once. For example, for a term involving a generic particle variable $\xi_p$ and carrier phase variable $\eta$, it follows that

$$\overline{\xi'_p \eta'} = \overline{\xi'_p \left(\eta - \overline{\eta}\right)} \approx \overline{\xi'_p \left(\eta\left(\overline{\boldsymbol{x}}_p\right) + x'_{p_i} \left.\frac{\partial \eta}{\partial x_i}\right|_{\overline{\boldsymbol{x}}_p} - \overline{\eta}\right)} = \overline{\xi'_p x'_{p_i}} \left.\frac{\partial \eta}{\partial x_i}\right|_{\overline{\boldsymbol{x}}_p}, \tag{4.12}$$

where $\xi_p$ can be any of the components of the particle location $\boldsymbol{x}_p$, velocity $\boldsymbol{u}_p$ or temperature $T_p$ and $\eta$ can be any component of the flow field $\boldsymbol{u}$ or temperature $T$. A second moment, however, that combines two flow variables $\xi$ and $\eta$ (components of the flow field or temperature), has to be Taylor expand twice to close it as follows

$$\overline{\xi' \eta'} \approx \overline{\xi' x'_{p_i}} \left.\frac{\partial \eta}{\partial x_i}\right|_{\overline{\boldsymbol{x}}_p} \approx \overline{x'_{p_i} \left(\xi(\overline{\boldsymbol{x}}_p) + x'_{p_j} \left.\frac{\partial \xi}{\partial x_j}\right|_{\overline{\boldsymbol{x}}_p} - \overline{\xi}\right)} \left.\frac{\partial \eta}{\partial x_i}\right|_{\overline{\boldsymbol{x}}_p} = \overline{x'_{p_i} x'_{p_j}} \left.\frac{\partial \xi}{\partial x_j}\right|_{\overline{\boldsymbol{x}}_p} \left.\frac{\partial \eta}{\partial x_i}\right|_{\overline{\boldsymbol{x}}_p}, \tag{4.13}$$

where the approximation in (4.12) has been applied first to expand $\eta$ and then to $\xi$.

To account for uncertainties in the forcing functions $f_1$ and $f_2$ we expand as follows

$$\begin{aligned}\overline{f}_1 &\approx \overline{f_1|_{\overline{\alpha},\overline{\boldsymbol{a}}} + \alpha' \left.\frac{\partial f_1}{\partial \alpha}\right|_{\overline{\alpha},\overline{\boldsymbol{a}}} + a_i' \left.\frac{\partial f_1}{\partial a_i}\right|_{\overline{\alpha},\overline{\boldsymbol{a}}} + \frac{\alpha'^2}{2} \left.\frac{\partial^2 f_1}{\partial \alpha^2}\right|_{\overline{\alpha},\overline{\boldsymbol{a}}} + \frac{\alpha' a_i'}{2} \left.\frac{\partial^2 f_1}{\partial \alpha \partial a_i}\right|_{\overline{\alpha},\overline{\boldsymbol{a}}} + \frac{a_i' a_j'}{2} \left.\frac{\partial^2 f_1}{\partial a_i \partial a_j}\right|_{\overline{\alpha},\overline{\boldsymbol{a}}}} \\ &= f_1\left(\overline{\alpha},\overline{\boldsymbol{a}}\right) + \frac{1}{2}\overline{\alpha' a_i'} \left.\frac{\partial g_1}{\partial a_i}\right|_{\overline{\alpha},\overline{\boldsymbol{a}}} + \frac{1}{2}\left(\overline{u_i' u_j'} - \overline{u_i' u_{p_j}'} - \overline{u_j' u_{p_i}'} + \overline{u_{p_i}' u_{p_j}'}\right) \left.\frac{\partial^2 f_1}{\partial a_i \partial a_j}\right|_{\overline{\alpha},\overline{\boldsymbol{a}}},\end{aligned} \tag{4.14}$$

where $f_1$ depends linearly on the random coefficient $\alpha$ according to (4.10) and the identity $\overline{a_i' a_i'} = \overline{u_i' u_j'} - \overline{u_i' u_{p_j}'} - \overline{u_j' u_{p_i}'} + \overline{u_{p_i}' u_{p_j}'}$ has been used. Note that, the procedure is easily extendable to $N$ randomly weighted modes according to (4.7) by adding the partials of the functions $\psi_i$ and $\zeta_i$. It can also applied to determine the correction function $f_2$. The resulting expression in (4.14) contains the terms $\overline{u_i' u_{p_j}'}$ and $\overline{u_i' u_j'}$ that need to be closed using the relations (4.12) and (4.13), respectively. The terms that correlate random coefficients and particle variables quantify epistemic uncertainty. In the limit that the standard deviations of the PDFs of the random coefficients go to zero, the random and deterministic forcing functions coincide and SPARSE–R model simplifies to SPARSE.

For the second moments involving the forcing functions with any particle variable $\xi_p$, the closure is applied as follows

$$\begin{aligned}\overline{\xi_p' f_1'} = \overline{\xi_p'\left(f_1 - \overline{f}_1\right)} &\approx \overline{\xi_p'\left(f_1\left(\overline{\alpha},\overline{\boldsymbol{a}}\right) + \alpha' \left.\frac{\partial f_1}{\partial \alpha}\right|_{\overline{\alpha},\overline{\boldsymbol{a}}} + a_i' \left.\frac{\partial f_1}{\partial a_i}\right|_{\overline{\alpha},\overline{\boldsymbol{a}}} - \overline{f}_1\right)} \\ &= \overline{\alpha' \xi_p'} g_1\left(\overline{\alpha},\overline{\boldsymbol{a}}\right) + \left(\overline{\xi_p' u_i'} - \overline{\xi_p' u_{p_i}'}\right) \left.\frac{\partial f_1}{\partial a_i}\right|_{\overline{\alpha},\overline{\boldsymbol{a}}},\end{aligned} \tag{4.15}$$

where the identities $\partial f_1/\partial \alpha = g_1$, according to (4.10), and $a_i = u_i - u_{p_i}$ have been used. The resulting expression in (4.15) contains the unclosed term $\overline{\xi_p' u_i'}$ that can be closed using the relation (4.12). For the term $\overline{\alpha' \xi_p'}$ however (combinations of particle variables with random coefficients), we can not apply the closure procedure because the gradients of the random coefficients within the cloud are unknown, preventing its Taylor expansion.

Rather, we use the MoM to derive moment equations that govern these terms

$$\frac{\mathrm{d}}{\mathrm{d}t}\left(\overline{\alpha' x'_{p_i}}\right) = \overline{\alpha' u'_{p_i}}, \tag{4.16a}$$

$$St\frac{\mathrm{d}}{\mathrm{d}t}\left(\overline{\alpha' u'_{p_i}}\right) = \overline{f}_1\left(\overline{\alpha' u'_i} - \overline{\alpha' u'_{p_i}}\right) + \overline{\alpha' f'_1}\left(\overline{u}_i - \overline{u}_{p_i}\right), \tag{4.16b}$$

$$\frac{3PrSt}{2c_r}\frac{\mathrm{d}}{\mathrm{d}t}\left(\overline{\alpha' T'_p}\right) = \overline{f}_2\left(\overline{\alpha' T'} - \overline{\alpha' T'_p}\right) + \overline{\alpha' f'_2}\left(\overline{T} - \overline{T}_p\right), \tag{4.16c}$$

where $\alpha$ can also be substituted by $\beta$. If we considered an expansion with $N$ modes, relations (4.16) have to be solved for each of the $N$ random coefficients for $\overline{\alpha_i x'_{p_j}}$, $\overline{\alpha_i u'_{p_j}}$ and $\overline{\alpha_i T'_p}$ with $i = 1, \ldots, N$.

In equations (4.16), terms combining the random coefficients and the forcing functions are expressed as

$$\overline{\alpha' f'_1} \approx \overline{\alpha'^2} g_1\left(\overline{\alpha}, \overline{\boldsymbol{a}}\right) + \left(\overline{\alpha' u'_i} - \overline{\alpha' u'_{p_i}}\right)\left.\frac{\partial f_1}{\partial a_i}\right|_{\overline{\alpha},\overline{\boldsymbol{a}}}, \tag{4.17a}$$

$$\overline{\alpha' f'_2} \approx \overline{\alpha'\beta'} g_2\left(\overline{\beta}, \overline{\boldsymbol{a}}\right) + \left(\overline{\alpha' u'_i} - \overline{\alpha' u'_{p_i}}\right)\left.\frac{\partial f_2}{\partial a_i}\right|_{\overline{\beta},\overline{\boldsymbol{a}}}, \tag{4.17b}$$

following a similar Taylor expansion. Finally, the only remaining terms that require closure in (4.17) combine the random coefficients with the fluid phase (as for example $\overline{\alpha' u'_i}$). Those terms, generally expressed as $\overline{\alpha'\eta'}$ where $\alpha$ is exchangeable with $\beta$ and $\eta$ is any scalar flow variable, close as follows

$$\overline{\alpha'\eta'} \approx \overline{\alpha' x'_{p_i}}\left.\frac{\partial \eta}{\partial x_i}\right|_{\overline{\boldsymbol{x}}_p}, \tag{4.18}$$

that relates again to the system of equations (4.16).

For closure of correlations of the forcing functions and a flow variable, the procedure has to be applied twice. Generalizing, $\eta$ for any flow variable (velocity components or

temperature), it follows that

$$\overline{\eta' f_1'} \approx \overline{x_{p_i}' f_1'} \left.\frac{\partial \eta}{\partial x_i}\right|_{\overline{\alpha},\overline{\boldsymbol{a}}} \approx \left[\overline{\alpha' x_{p_i}'} g_1\left(\overline{\alpha},\overline{\boldsymbol{a}}\right) + \left(\overline{x_{p_i}' u_j'} - \overline{x_{p_i}' u_{p_j}'}\right) \left.\frac{\partial f_1}{\partial a_j}\right|_{\overline{\alpha},\overline{\boldsymbol{a}}}\right] \left.\frac{\partial \eta}{\partial x_i}\right|_{\overline{\alpha},\overline{\boldsymbol{a}}}, \tag{4.19}$$

where the term $\overline{x_{p_i}' u_j'}$ is closed using the relation (4.12) and $\overline{\alpha' x_{p_i}'}$ is closed with (4.16a).

Equations (4.11)–(4.19) represent the closed form of the randomly forced SPARSE–R model. Its solution depends on inputs of the averages of the carrier flow fields and forcing functions. The accuracy of the SPARSE was shown to be of third order for the deterministic model consistent with the order of the truncations of the Taylor series and moment equations. Similarly here, the accuracy of the randomly forced model depends on: (a) the truncation of terms on the order of statistical correlations of order greater than two and (b) the truncation of the Taylor series terms greater than second order. The SPARSE–R method is closed and thus *predictive*. It converges with a third order expected rate with the size of the initial particle cloud given by the standard deviations in phase space consequently with the retained terms in the SPARSE–R formulation. The analysis of the leading order truncated terms in SPARSE–R is added in the Appendix C for completeness.

### 4.2.5 Numerical implementation

#### Tracing

The numerical solution of the governing system of equations (4.6) and (4.11)–(4.19) requires four stages including (1) locating the host grid or carrier flow domain of the point–cloud, (2) interpolating the flow variable and gradients at the point–cloud's location (because this is a point–cloud, there is only one location, that happens to be the mean location), (3) determining the forcing gradients at the cloud's mean location and (4) integrating in time. The first stage requires algorithms that are similar to the PSIC method. We locate host cell as described in Ref. [71] if needed. For the second stage, we

either use analytical solutions or interpolations [71, 183] that are consistent with the carrier phase solver. A third order total variation diminishing (TVD) Runge–Kutta scheme [175] is used for time integration.

For the third (interpolation) stage we need to compute the first and second derivatives of the forcing functions $f_1$ and $f_2$ with respect to the relative velocity components and similarly the first and second derivatives of the carrier flow velocity and temperature with respect to space. The derivatives of an analytical forcing function can be precomputed and evaluated at the average values during the time integration in the fourth stage. A polynomial approximation of the forcing function requires the numerical evaluation of the derivative. At each location, this derivative is interpolated at the required average values during the time integration. In a similar fashion, for analytically prescribed carrier phase flows, the derivatives are precomputed analytically and evaluated at the average cloud's location during the time integration. If the carrier phase is computed numerically, the derivatives of velocity and temperature field with respect to space are numerically determined and interpolated at the average cloud's location during the fourth (time integration) stage.

**Splitting and convergence**

To compare point–cloud tracer results with MC–PSIC results in the tests below, we define the initial state of a point–particle cloud by its first two moments computed from the point–particles contained in the cloud. As an example, for any two particle variables $\xi_p$ and $\eta_p$, a first moment $\overline{\eta}_p$ and second moment $\overline{\xi'_p \eta'_p}$ are computed as

$$\overline{\eta}_p = \frac{1}{N_p} \sum_{i=1}^{N_p} \eta_{p_i}, \tag{4.20a}$$

$$\overline{\xi'_p \eta'_p} = \frac{1}{N_p} \sum_{i=1}^{N_p} \left(\xi_{p_i} - \overline{\xi}_p\right) \left(\eta_{p_i} - \overline{\eta}_p\right), \tag{4.20b}$$

for a cloud containing $N_p$ point–particles.

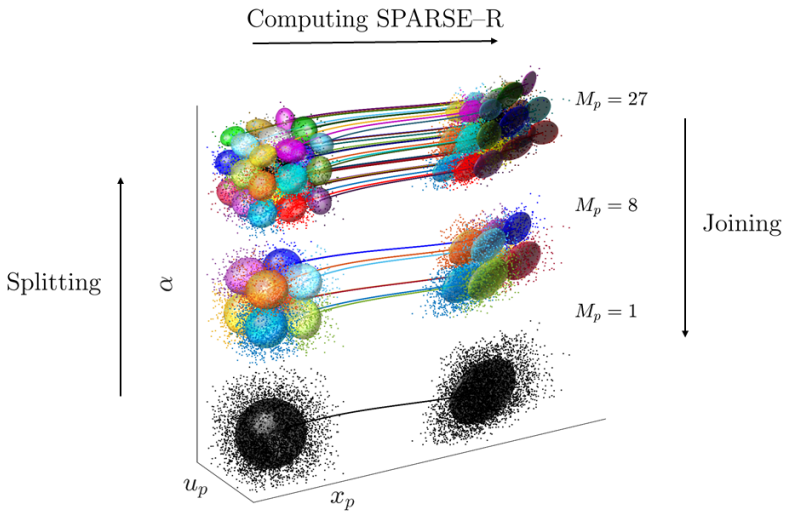


**Figure 4.2.** Illustration of a cloud of $N_p = 10^3$ point–particles represented by its point–particles depicted as points and subclouds (point–clouds) as ellipses at the initial time $t = 0$ and a later time $t > 0$. The initial cloud is split into $M_p$ subclouds whose moments are computed from the PSIC particles according to the splitting algorithm [4].

SPARSE was shown to be third–order accurate for a union of computational clouds with respect to the standard deviations in each independent (physical and phase space) dimension in Ref. [3]. To improve accuracy, a splitting algorithm was proposed that converges the solution according to this rate by reducing the cloud's sizing and increasing the number of clouds along each independent dimension. To split, we divide the cloud of point–particles at the initial time into a union of uniform sets. For example for a one–dimensional case we divide the cloud in $\alpha - x_p - u_p$, which leads to $M_p = M_p^{\alpha} M_p^{x_p} M_p^{u_p}$ subclouds with $M_p^{\alpha}$, $M_p^{x_p}$ and $M_p^{u_p}$ the number of divisions along $\alpha$, $x_p$ and $u_p$ respectively. Considering uniform splitting along all dimensions, in the general three–dimensional non–isothermal case one has $M_p = M^{N+d+e}$ where $N$ is the number of modes considered in the random forcing, $d = 1, 2, 3$ is the dimension of the problem and $e = 1$ for non–isothermal and $e = 0$ for isothermal flow. We identify $M$ as the level of splitting of the cloud. The

splitting algorithm is schematically illustrated in Figure 4.2, which visualizes the sampling of a group of point particles and its division into $M_p = 1$, $M_p = 2^3$ and $M_p = 3^3$ subclouds, corresponding to the levels of splitting $M = [1,\ 2,\ 3]$, in the three dimensional space spanned by the particle's coordinate $x_p$, its velocity $u_p$ and the random forcing coefficient $\alpha$. Once the cloud is split, the moments of each subcloud are computed using the relations in (4.20). For further details of the algorithm, we refer to [3, 4].

The moments of the cloud composed by the total number of point–particles, i.e., without splitting, are post–processed by joining each subcloud $k$, with $k = 1, \ldots, M_p$ as follows

$$\overline{\phi} = \sum_{k=1}^{M_p} w_k \overline{\phi}_k, \tag{4.21a}$$

$$\overline{\xi'\eta'} = \sum_{k=1}^{M_p} w_k \overline{\xi'\eta'}_k + \sum_{k=1}^{M_p} w_k (\overline{\xi}_k - \overline{\xi})(\overline{\eta}_k - \overline{\eta}), \tag{4.21b}$$

for any three solution variables $\phi$, $\eta$ and $\xi$. We will refer to this as the *Cumulative Cloud* throughout the paper, i.e., a multivariate Gaussian description of the accumulation of the subclouds where the moments of each of them have been computed with SPARSE–R and then joined with (4.21). The moments of the Cumulative Cloud converge to the Monte Carlo results using (4.20) with the level of splitting. The relations (4.21) are exact and do not add any approximation error to the computation.

The Cumulative Cloud can be visualized as an ellipsoid or a prolate spheroid for any three variables of the particle phase and ellipse for any two variables by scaling the principle axis, in the directions of the eigenvectors of the covariance matrix, with the eigenvalues of the covariance matrix in the $N + d + e$ dimensional space. For example, for

three particle variables $\phi$, $\xi$ and $\eta$, one has the following covariance matrices

$$K_{\phi\xi\eta} = \begin{bmatrix} \overline{\phi'^2} & \overline{\phi'\xi'} & \overline{\phi'\eta'} \\ \overline{\phi'\xi'} & \overline{\xi'^2} & \overline{\xi'\eta'} \\ \overline{\phi'\eta'} & \overline{\xi'\eta'} & \overline{\eta'^2} \end{bmatrix}, \quad K_{\phi\xi} = \begin{bmatrix} \overline{\phi'^2} & \overline{\phi'\xi'} \\ \overline{\phi'\xi'} & \overline{\xi'^2} \end{bmatrix}, \quad K_{\phi\eta} = \begin{bmatrix} \overline{\phi'^2} & \overline{\phi'\eta'} \\ \overline{\phi'\eta'} & \overline{\eta'^2} \end{bmatrix}, \quad K_{\xi\eta} = \begin{bmatrix} \overline{\xi'^2} & \overline{\xi'\eta'} \\ \overline{\xi'\eta'} & \overline{\eta'^2} \end{bmatrix}. \tag{4.22}$$

Note that this representation may be also performed for a set of samples of the variables $\phi$, $\xi$ and $\eta$ in a discrete manner from MC–PSIC results.

In approximation, moments greater than second of the Cumulative Cloud can also be computed as follows

$$\overline{\phi'\xi'\eta'} = \sum_{k=1}^{M_p} w_k \left(\overline{\phi}_k - \overline{\phi}\right)\left(\overline{\xi}_k - \overline{\xi}\right)\left(\overline{\eta}_k - \overline{\eta}\right), \tag{4.23}$$

which is the equivalent of a Monte Carlo sampling of point–particles, but for the SPARSE–R subclouds. In (4.23) $\overline{\phi}$, $\overline{\xi}$ and $\overline{\eta}$ are the average values of the Cumulative Cloud and $k$ is an index that loops over all subclouds. The PDF of the Cumulative Cloud is non–Gaussian and can be reconstructed using a mixture distribution by adding weighted Gaussians that are defined with the two moments of each subcloud for a given level of splitting. The PDF of any particle variable $\phi$ of a cloud split into $M_p$ subclouds can be computed as

$$f_\phi(\phi) = \sum_{k=1}^{M_p} \frac{w_k}{\sqrt{2\pi\overline{\phi'^2_k}}} \exp\left(-\frac{\left(\phi - \overline{\phi}_k\right)^2}{2\overline{\phi'^2_k}}\right). \tag{4.24}$$

**Error measurement**

The computational savings of using SPARSE–R can be estimated by determining the reduction of degrees of freedom as compared with MC–PSIC, i.e., the number of variables to solve along time. The ratio of computational cost of SPARSE–R as compared

to a MC–PSIC when considering $N$ modes to define the forcing functions is

$$r = \frac{2N\left(d + e\left(d+1\right)\right) + 2d^2 + 3d + 2e\left(d+1\right)}{2d+e}\left(\frac{M_p}{N_p}\right). \tag{4.25}$$

The factor multiplying $M_p/N_p$ in the above expression is equal to 7 for a three–dimensional $d = 3$ non–isothermal $e = 1$ simulation or smaller if simplified to less dimensions or isothermal when considering a single mode $N = 1$. Generally, we find that $N_p \gg M_p$ to reproduce accurate results by the SPARSE–R method, ensuring computational savings.

To measure the errors of the SPARSE–R method, we normalize the $L_2$ norm of the difference between the MC–PSIC and SPARSE–R results of a given variable with the $L_\infty$ norm of the MC–PSIC result as follows

$$\varepsilon(\cdot) = \frac{\|(\cdot)^{\text{SPARSE–R}} - (\cdot)^{\text{MC–PSIC}}\|_2}{\|(\cdot)^{\text{MC–PSIC}}\|_\infty}. \tag{4.26}$$

We also define averaged magnitudes of the first and second moments $\mu_1$ and $\mu_2$ respectively that for a SPARSE–R computation with $N_{var}$ number of variables $\phi_j$ with $j = 1, \ldots, N_{var}$, are given by

$$\mu_1 = \left(\sum_{j=1}^{N_{var}} \overline{\phi}_j^2\right)^{1/2}, \qquad \mu_2 = \begin{vmatrix} \overline{{\phi'_1}^2} & \cdots & \overline{\phi'_{N_{var}}\phi'_1} \\ \vdots & \ddots & \vdots \\ \overline{\phi'_1\phi'_{N_{var}}} & \cdots & \overline{{\phi'_{N_{var}}}^2} \end{vmatrix}, \tag{4.27}$$

that combined with (4.26) provides an error measure for all $N_{var}$ dependent solution variables in (4.6).

## 4.3 Numerical experiments

### 4.3.1 One–dimensional sinusoidal velocity field

To test the accuracy of SPARSE–R as compared to MC–PSIC, we consider a cloud of point–particles carried by an isothermal one–dimensional sinusoidal flow velocity field given by

$$u(x) = 1 + \frac{1}{2}\sin(2x), \tag{4.28}$$

where the forcing $f_1$ is defined according to (4.10) and $g_1$ according to the the Schiller and Naumann correlation such that

$$f_1 = \alpha\left(1 + 0.15Re_p^{0.687}\right). \tag{4.29}$$

This test is not necessarily physical, but the sinusoidal velocity field is typical and representative of a modal (Fourier) analysis in chaotic flows. The simple one–dimensional flow enables testing and verification of accuracy. Moreover, it provides fundamental insights into the behavior of cloud dynamics that can serve as a reference for physically relevant simulations.

The initial condition is set according to a uniform distribution $\mathcal{U}$ to sample the initial locations $x_{p_0}$ and velocities $u_{p_0}$ such that

$$x_{p_0} \sim \mathcal{U}\left[x_{p_0 min},\ x_{p_0 max}\right], \quad u_{p_0} \sim \mathcal{U}\left[u_{p_0 min},\ u_{p_0 max}\right]. \tag{4.30}$$

We test the formulation for both, dF and rF particles with $\alpha = 1$ and

$$\alpha \sim \mathcal{U}\left[\alpha_{min},\ \alpha_{max}\right], \tag{4.31}$$

respectively. The uniform distributions $\mathcal{U}$ are defined by the limit values $\alpha_{min}$ and $\alpha_{max}$, which are directly related to its average and standard deviation as $\alpha_{min} = \overline{\alpha} - \sqrt{3}\sigma_\alpha$ and $\alpha_{max} = \overline{\alpha} + \sqrt{3}\sigma_\alpha$ with $\overline{\alpha} = 1$ and $\sigma_\alpha = 0.3$. We also initialize the particle locations and velocities, according to the uniform distributions (4.30), with $\overline{x}_{p_0} = \overline{u}_{p_0} = 0$, $\sigma_{x_{p_0}} = 0.2$ and $\sigma_{u_{p_0}} = 0.1$. Initially, the variables $\alpha$, $x_{p_0}$ and $u_{p_0}$ are statistically independent and uncorrelated and therefore, the following moments are zero

$$\overline{\alpha' x'_{p_0}} = \overline{\alpha' u'_{p_0}} = \overline{x'_{p_0} u'_{p_0}} = 0. \tag{4.32}$$

The particle response time is set to $St = 0.5$, i.e., the particle time scale is similar to the carrier flow convective time scale, such that the inertial effects are significant and of influence to test. We also set the reference Reynolds number to $Re_\infty = 10^4$ so that the relative particle Reynolds number is greater than unity and the forcing of the particles lies in a regime beyond the Stokes drag. The non–dimensional particle density is $\rho_p = 250$ and the non–dimensional particle diameter $d_p = 2 \times 10^{-3}$.

To develop a general understanding of the effect of the deterministic and random forcing functions on the solution behavior of clouds of particles in a sinusoidal carrier field, we first discuss the traces of three groups of PSIC point–particles that are computed with a deterministic forcing function according to three values of $\alpha$, including $\alpha_{min}$, $\alpha_{max}$, and $\overline{\alpha} = (\alpha_{min} + \alpha_{max})/2 = 1$. We will refer to these deterministic forced cloud traces as dF clouds throughout the rest of the paper. The groups for each $\alpha$ contain $N_p = 10^5$ particles to ensure a converged MC moment error that scales according to $1/\sqrt{N_p}$.

The locations of the point–particles so computed are visualized in Fig. 4.3a for different instants of time in the phase space $x_p - u_p$. Initially, all clouds coincide. As time progresses, each group accelerates in positive direction because the carrier velocity (black line) is positive, which combined with negligible particle velocities at early times yields a positive relative particle velocity. The relative velocity has the same sign as the

acceleration, and thus is positive at each particle location also. Each point–particle cloud accelerates proportionally to the magnitude of its forcing coefficient, $\alpha$. For $\alpha \to \infty$ the particle time response $St/\alpha \to 0$ and the trajectory tends to that of a particle without inertia (a tracer). For small $\alpha$, the time response increases. In the limit $\alpha \to 0$, the time response tends to infinity $St/\alpha \to \infty$ and its movement is asymptotically zero. At later times, the clouds accelerate and decelerate successively around the average unity value of the carrier phase velocity. Because of its inertia, each particle's trajectory has a phase delay and decrease of amplitude as compared to those of the carrier flow velocity field (4.28). Initially uniformly distributed around the average location $(x_{p_0}, u_{p_0}) = (0, 0)$, the particle clouds stretch and rotate in phase space while they are simultaneously advected by the flow.

A more detailed understanding of the groups' rotation and deformation characteristics can be obtained by the four quadrant depiction of the three tracers (first three rows) in time (four columns) in Fig. 4.3b. In each quadrant the particles are colored according to a shade of a color scheme. Moreover, the mean location, the principle stretching and rotation of the clouds in each quadrant and of a Cumulative Cloud can be represented by the mean location, the principle axes and the rotation of an ellipse, based on the average $(\overline{x}_p, \overline{u}_p)$ and the eigenvalues and eigenvectors of the covariance matrix $K_{x_p u_p}$. These moments are of course precisely the moments that are modeled by SPARSE and the MC–PSIC moment results can thus be used for comparison and assessment of the predictive accuracy of SPARSE. The ellipses and groups of point–particles show that particles in different quadrants align naturally in phase space over a time interval that is on the order of $St/\alpha$ as the velocities of all particles are damped towards the carrier velocity. The particle clouds are straining in the $x_p - u_p$ plane consistently with the velocity gradient of the carrier phase and the particles' inertia. At the initial time this velocity gradient is positive and thus the particle cloud widens in the physical space. A particle group with a smaller response time, $St/\alpha$ stretches more along the velocity gradient. In phase space the cloud

compresses as it settles to the carrier velocity.

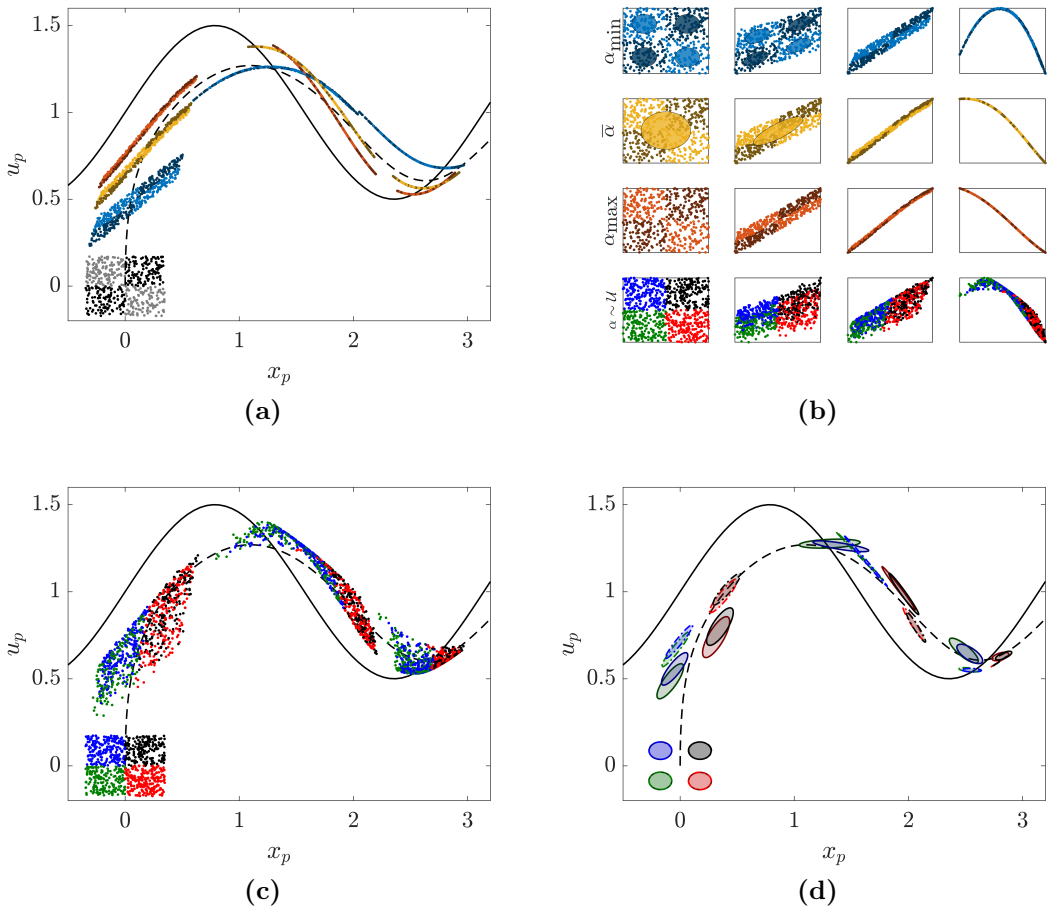


**Figure 4.3.** Particle phase solution of the sinusoidal one–dimensional test case for: (a) dF particle clouds for three deterministic values of the random coefficient $\alpha_{min}$, $\overline{\alpha}$ and $\alpha_{max}$ for four instants of time computed with MC–PSIC divided in quadrants by colors; (b) point–particle clouds at four instants of time for the cases in (a) and (c) in zoomed $x_p - u_p$ axis divided in quadrants by colors and with ellipses representing the total set of particles (second row) or subsets (first row); (c) rF cloud considering $\alpha \sim \mathcal{U}$ for four instants of time with coloring according to quadrants in $x_p - u_p$, i.e., each quadrant has a distribution of values of $\alpha$; and (d) SPARSE–R solution with $M = 2$ of the same case than in (c) with ellipses with continuous border line for the lower range of $\alpha$ and dot-dashed border line for the larger range of $\alpha$. The times in (a), (c) and (d) are $t = [0,\ 0.35,\ 1.75,\ 2.98]$ and for (b) $t = [0,\ 0.1,\ 0.35,\ 1.75]$. The flow is depicted with a black continuous line in (a), (c) and (d). For a better visualization, 500 point–particles are depicted from the $N_p = 10^5$ used for the computations.

A randomly forced cloud tracer with $\alpha \sim \mathcal{U}$ does not concentrate along a line like

the dF cloud, but distributes over a region according to the probability of the forcing coefficient and of the associated deterministic tracers (Fig. 4.3c). This distribution is a measure of the uncertainty in the solution. The footprint of the distributed particles in phase space for an rF cloud is the confidence interval that concisely visualizes this uncertainty. The rF cloud's dispersion can be understood qualitatively as a summation of the dF tracers that are determined with forcing coefficients that randomly span the range of the PDF forcing coefficient. Roughly this can be seen as a summation of the locations of the dF clouds in rows 1 to 3 in Fig. 4.3b. In addition to this increased dispersion, the distributions of rF clouds in each quadrant overlap and can thus be said to be more mixed at later times. The driving mechanisms for this enhanced mixing and increase in the associated confidence intervals is the virtual stress correlation between the random forcing and the flow field fluctuations that appears in the SPARSE–R formulation and that drives the uncertainty in the rF cloud's solution. The dF cloud that is forced according to the average value of $\bar{\alpha}$ compares closely with the mean solution of a rF cloud (compare second and fourth row in Fig. 4.3b). A comparison of the second moments between the rF cases and dF cases shows that with an increased randomness interval $[\alpha_{min},\ \alpha_{max}]$ in the forcing function, the confidence interval as measured by second moments in the particle solution increases. The randomness is directly proportional to the range of particle response times (or inertia) as defined by $St/\alpha$. A larger response time range naturally yields an increased dispersion as measured by the second moments.

Using the SPARSE–R point–cloud tracer we can compute the dispersion of the clouds of point–particles depicted in Figs. 4.3a– 4.3c at a reduced computational cost. Splitting the cloud in quadrants so that $M = 2$, i.e., two divisions along $\alpha$, $x_p$ and $u_p$, we specify the first two moments of each subdivision (subset of point–particles) as initial conditions for the point–cloud simulation (see Fig. 4.2). The resulting phase space depicted with an ellipse for each subcloud is represented in Fig 4.3d for different instants of time. The solution in each quadrant is now represented by two ellipses along the $\alpha$ dimension

that coincide initially in phase space. At later times the two ellipses are located at different positions and are deformed differently because they are forced differently. The point clouds show the same trends in terms of advection, straining and rotation as compared to the groups of MC–PSIC particles.

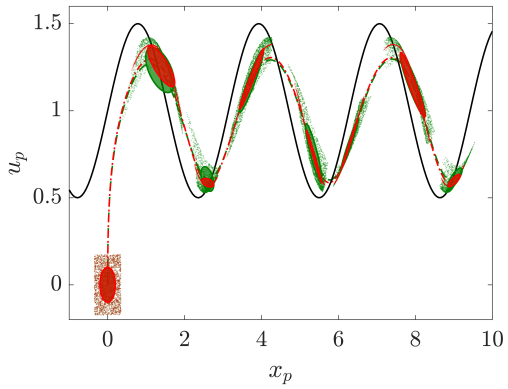


**Figure 4.4.** Particle phase solution of the sinusoidal one–dimensional test case for the rF (green) and dF (red) computed with SPARSE–R with $M = 7$ as ellipses for the Cumulative Cloud at different instants of time along the average particle phase (green dashed line for rF and red dot-dashed line for dF). The point–particles are depicted as points with the corresponding coloring. The flow is depicted with a black continuous line. The time instants are $t = [0,\ 1.43,\ 2.85,\ 4.28,\ 5.73,\ 7.15,\ 8.5,\ 10]$. For a better visualization, 500 point–particles are depicted from the $N_p = 10^5$ used for the computations.

We assess the accuracy of the point–cloud tracer by comparing computational results for different levels of splitting $M = 1, \ldots, 7$, such that the total number of subclouds is $M_p = M^2$ for the dF case (along $x_p$ and $u_p$) and $M_p = M^3$ for the rF case (along $\alpha$, $x_p$ and $u_p$) respectively. Figure 4.4 compares the Cumulative Cloud solution for the rF and dF case with $M = 7$ and shows that the deterministic and random solutions while different are strongly correlated. In fact, a comparison of their average trajectories in Fig. 4.6a in phase space shows that they are within 3% of each other. They match so surprisingly well, because the second moments on the right hand side of the first moment equations are negligible as compared to the dominant acceleration term $\overline{f}_1(\overline{u} - \overline{u}_p)$. This is however not the case for the second moment equations and their solution that depend on the second and third moments [2] as plotted in Figures 4.6a– 4.7f. The maximum difference between

the rF and dF solution for the second moments is 20% in $\sigma_{u_p}$ (see Fig. 4.6c) in the initial acceleration stages. The standard deviations and correlations show an oscillatory trend. The solutions for the rF cloud are mostly different from the dF cloud near its maxima.

The second moments $\overline{\alpha' x'_p}$ and $\overline{\alpha' u'_p}$ can be interpreted as "virtual" stresses that cause the mixing of the random cloud. We dub these stresses virtual, because they are not physical and only affect the random sample space. The two correlations of the force coefficients with location and velocity are oscillatory and in phase with their respective position and velocity standard deviation trends. This phase-locked behavior indicates that the virtual stress cross-correlations are greater if the principle strain of the random cloud is greater in the related physical or phase space dimension (in general physics, the stress-strain relation is well-known [202]). Note that these terms have a zero value for the dF case because $\alpha' = 0$ and they are thus not included the figure.

Figure 4.5 shows the MC–PSIC and Cumulative Cloud solution from a different perspective in the $f_1 - Re_p$ plane. The dF cloud follows the line described by the deterministic forcing function. The rF cloud is distributed in the space spanned by the forcing and the relative velocity and can be visualized and computed with SPARSE–R using the ellipsoidal approximation. The results show that the particle's relative Reynolds number is initially high (on the order of 20) when the clouds accelerate. Later, the particle cloud oscillates around moderate values of $Re_p$ associated with a lower correction of the Stokes drag and a forcing function closer to unity despite the randomness in $\alpha$.

Figure 4.6f confirms the theoretical third–order convergence rate of SPARSE–R with respect to the level of splitting $M$. We find that for $M = 7$ the maximum relative error of all first and second moments of the rF particle cloud computed with SPARSE–R as compared to MC–PSIC is 1% for the variable $\sigma^2_{u_p}$. For the rest of variables of the particle phase the error is lower than that, which denotes good agreement between the SPARSE–R and MC–PSIC results. The relative error for the other second moments involving $\alpha$ is at most 1.5% (for $\overline{\alpha' x'_p}$). For the dF case, the maximum relative error occurs also in the

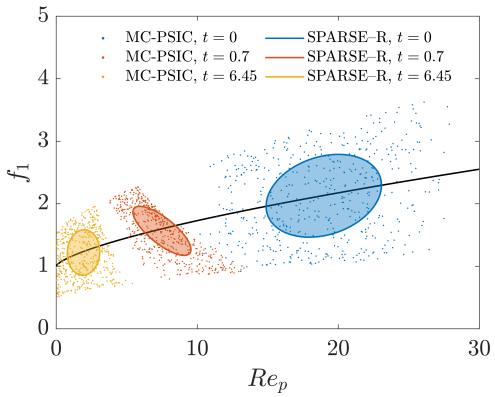


**Figure 4.5.** Forcing of the Cumulative Cloud of the sinusoidal one–dimensional test case for three instants of times computed with SPARSE–R ($M = 7$) depicted as ellipses in $f_1 - Re_p$ space and point–particles computed with MC–PSIC depicted as points. For a better visualization, 500 point–particles are depicted from the $N_p = 10^5$ used for the computations.

variance of the particle velocity with a value of 0.1%. The computational savings are significant even for $M = 7$. The ratio of computational cost of SPARSE–R as compared to MC–PSIC defined as in (4.25) that takes into account the reduction of degrees of freedom is $r = 1.7 \cdot 10^{-3}$ for the dF case and $r = 1.2 \cdot 10^{-2}$ for the rF case, that translates to a 0.17% and a 1.2% of the computational cost respectively as compared to MC–PSIC. We conduct tests at three different wavenumbers (not shown here). We expect that with an increasing wave number, it is necessary to increase the number of clouds while reducing the compact support of each cloud. This so–called splitting as described in Ref. [3] ensures that the solution is in the asymptotic convergence range of the model. For example, for a case with a wavenumber of 4, we confirm that the theoretical convergence rate is observed if we split the domain into $M > 5$ number of clouds per dimension.

Using multiple clouds, we can compose the PDF of the Cumulative Cloud with the sum of weighted Gaussians as defined in (4.24). In Figure 4.8 we show these PDFs and compare them to the MC–PSIC method for the rF case. Clearly, the PDF is not trivial, i.e. not symmetric or Gaussian and SPARSE–R accurately predicts it. The evolution of PDF of the particle location in time computed with MC–PSIC (Fig. 4.8a) compares well

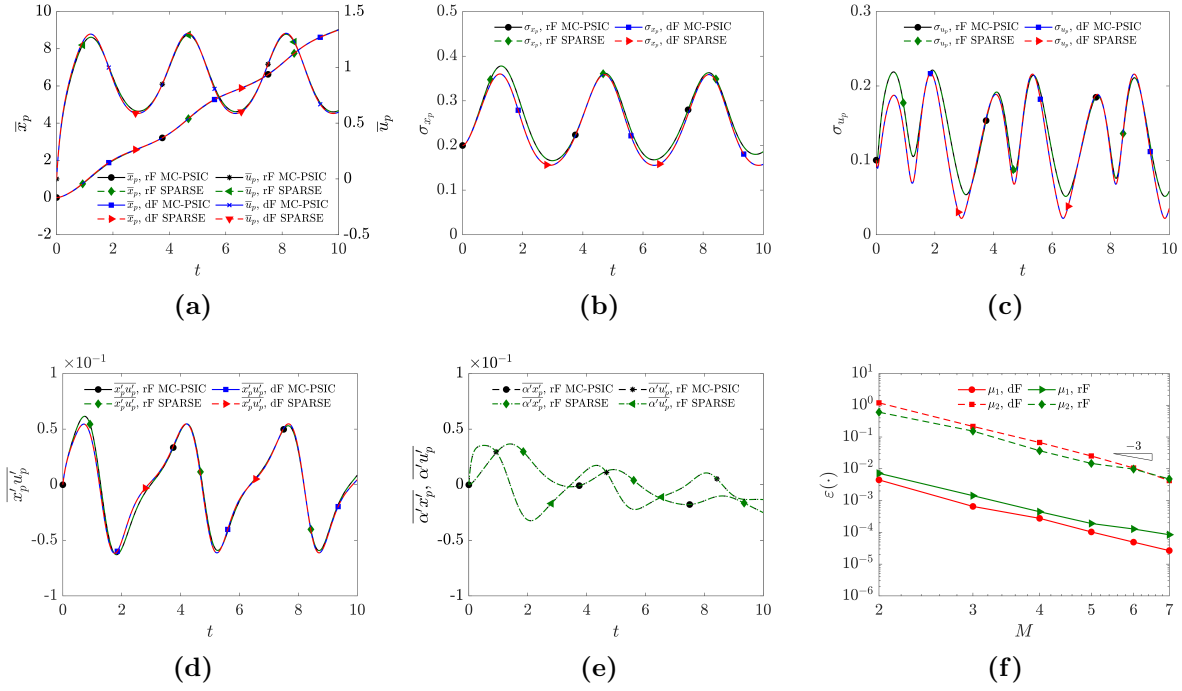


**Figure 4.6.** First and second moments of the one–dimensional sinusoidal velocity field test case for stochastic and deterministic forcing computed with SPARSE–R and MC–PSIC. Figure (a) shows the average particle location and velocity, (b) standard deviation of the particle location, (c) standard deviation of the particle velocity, (d) combined second moment of the particle phase, (e) combined second moments of the random coefficient and particle phase variables and (f) expected convergence of SPARSE.

with SPARSE–R (Fig. 4.8b). In a similar manner, for the PDF of the particle velocity, we show in Figures 4.8d–4.8f contour maps of the PDF along time computed with MC–PSIC (Fig. 4.8d) and SPARSE–R (Fig. 4.8e) and compare both at the same time instant in Figure 4.8f. The mixture distribution composed by Gaussians shows oscillations related to the underlying Gaussian representation of each subcloud. The results are within a 5% agreement and SPARSE–R uses two order of magnitudes fewer degrees of freedom than the MC–PSIC approach. Additionally, third order moments computed according to (4.23) are depicted in Fig. 4.7 for the dF and rF cases computed with SPARSE–R and MC–PSIC showing also agreement.

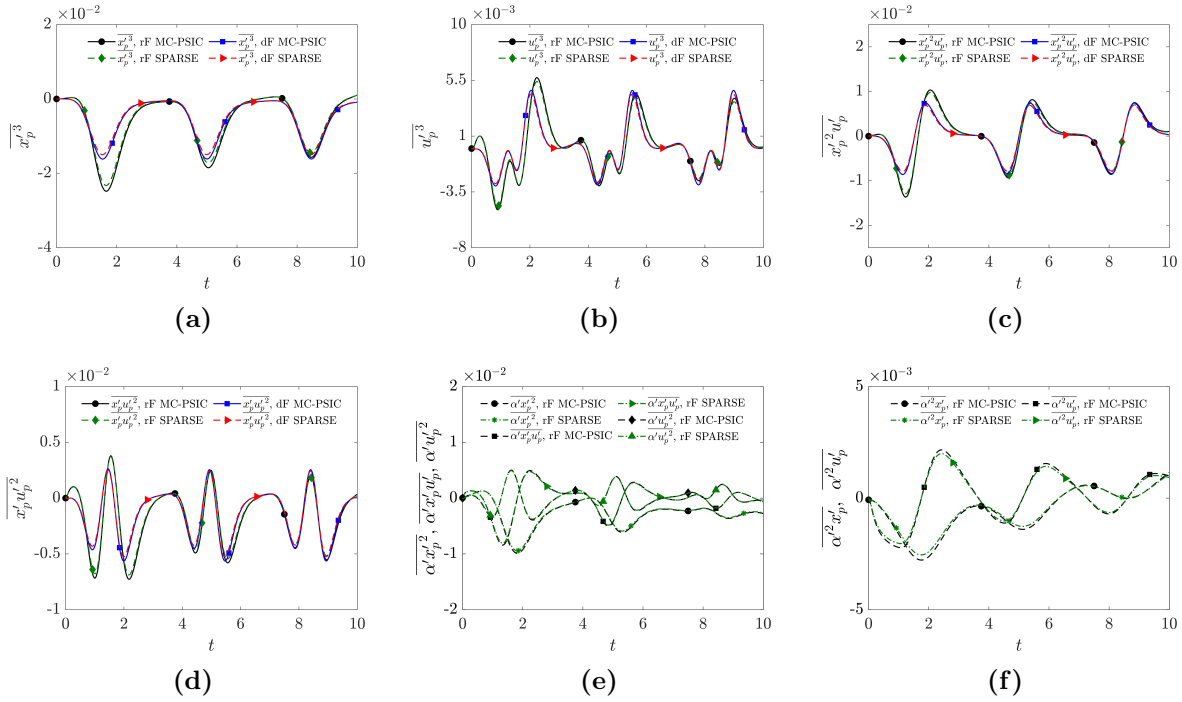


**Figure 4.7.** Third moments of the one–dimensional sinusoidal velocity field test case for rF and dF cases computed with SPARSE–R and MC–PSIC using the relation (4.23); (a) shows the skewness of the particle position; (b) the particle velocity; (c) and (d) combined third moments of the particle phase; and (e) and (f) combined third moments of the random coefficient and particle phase variables.

### 4.3.2 Stagnation flow

The two–dimensional stagnation flow is analytically described according to [176] for an inviscid irrotational fluid, in the domain $(x, y) \in [-\infty, 0] \times [-\infty, \infty]$ by

$$u = -kx, \tag{4.33a}$$

$$v = ky, \tag{4.33b}$$

where $y$ is the coordinate perpendicular to the flow direction, and $k$ is a constant. Point–particles carried by this flow admit an analytical solution for their trajectories as well [2]. These analytical descriptions are helpful for testing and understanding of the basic characteristics and canonical behaviour of the solutions of dF and rF clouds of particles.

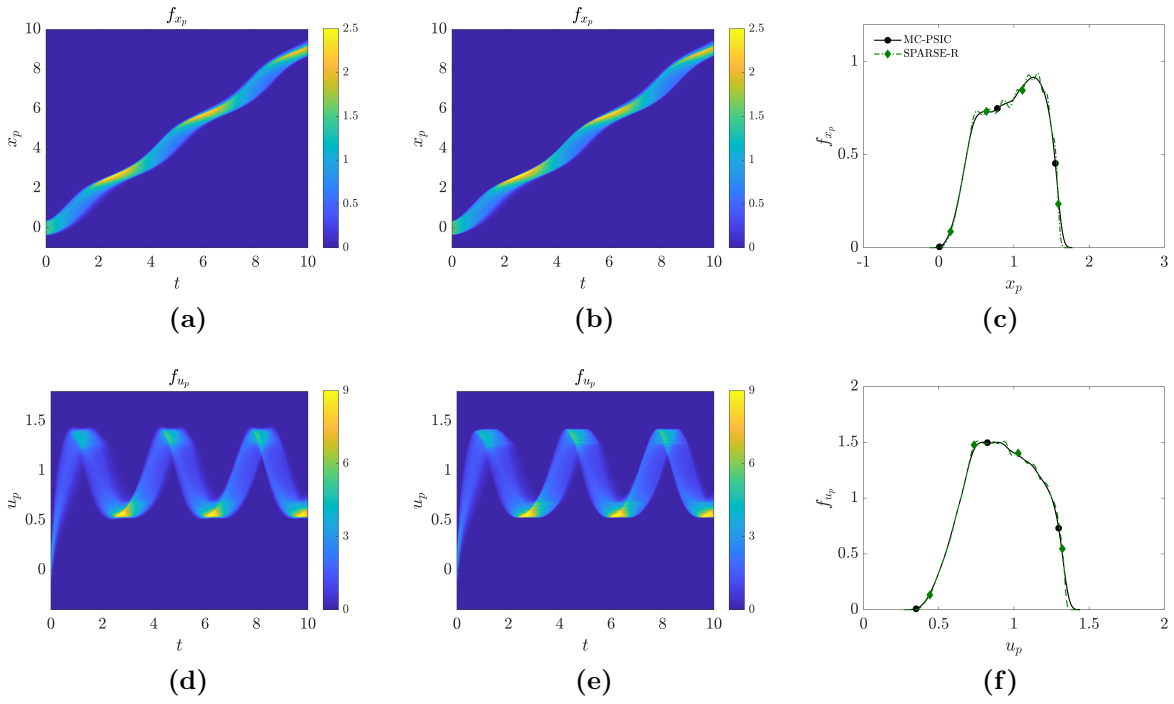


**Figure 4.8.** PDFs of the components of the particle location $f_{x_p}$ and velocity $f_{u_p}$ for the rF case computed with MC–PSIC and SPARSE–R methods for the one–dimensional sinusoidal velocity field test case. The Figure shows: PDF of $x_p$ computed with (a) MC–PSIC and (b) SPARSE–R and (c) comparison of both methods at time $t = 0.3$ and the corresponding results for $u_p$ in (d)–(f). The legend in (c) also corresponds to (f).

Moreover, because there is symmetry with respect to the horizontal axes, the equations decouple by coordinates and similarities between rF and dF clouds under symmetry conditions can be analyzed. Closure terms that depend on the linear flow velocity field are exact because the Taylor expansion of the linear field is exact.

Following [2], we reduce the complexity of the test further by assuming a forcing function that sets $f_1 = \alpha$ with $g_1 = 1$ in (4.10), i.e. the forcing function is random but not dependent on the relative velocity, so that the only the truncation of non–zero terms is that of the third moments in the second moment equations (4.6e), (4.6g) and (4.16). For reference, we present the complete closed system of equations for this form of the forcing function in Appendix D.

We specify initial conditions for the cloud's location and velocity by sampling from

uniform distributions according to

$$x_{p_0} \sim \mathcal{U}\left[x_{p_{0min}},\ x_{p_{0max}}\right], \quad y_{p_0} \sim \mathcal{U}\left[y_{p_{0min}},\ y_{p_{0max}}\right], \tag{4.34a}$$

$$u_{p_0} \sim \mathcal{U}\left[u_{p_{0min}},\ u_{p_{0max}}\right], \quad v_{p_0} \sim \mathcal{U}\left[v_{p_{0min}},\ v_{p_{0max}}\right]. \tag{4.34b}$$

With the particle cloud initially at rest, both components of the velocity $u_p$ and $v_p$ are zero for all point–particles contained in the cloud. For the rF case the random coefficient $\alpha$ is also sampled from an uniform distribution

$$\alpha \sim \mathcal{U}\left[\alpha_{min},\ \alpha_{max}\right], \tag{4.35}$$

whereas for the dF case the coefficient $\alpha$ is deterministic with $\alpha' = 0$. The averages of the distribution functions are $\overline{x}_p = -1$, $\overline{y}_{p_0} = \overline{u}_{p_0} = \overline{v}_{p_0} = 0$, and the standard deviations $\sigma_{x_{p_0}} = \sigma_{y_{p_0}} = \sigma_{u_{p_0}} = \sigma_{v_{p_0}} = 0.08$. For the rF case, we also define $\overline{\alpha} = 1$ and $\sigma_\alpha = 0.3$ whereas for the dF all point–particles have the same value of $\alpha$ with zero fluctuations so that $\alpha = \overline{\alpha} = 1$, $\sigma_\alpha = 0$. Second moments combining any of the variables $\alpha$, $x_{p_0}$, $y_{p_0}$, $u_{p_0}$ and $v_{p_0}$ are zero initially because the variables are considered uncorrelated at $t = 0$. However, because in computational practice we can only use the limited number of samples, $N_p = 10^5$, these moments include sampling errors that converge at the rate $1/\sqrt{N_p}$ with respect to the averages and second moments described above. The initial condition for the SPARSE–R method is determined by sampling the point–particles as described in Section 4.2.5. We set the Stokes number and the constant $k$ in (4.33) to unity so that $St = k = 1$.

Figure 4.9 shows the solutions of the rF and dF cases identified with green and red colors, respectively. The particle cloud is advected by the flow field in the time interval $t \in [0,\ 2.52]$ in which the average location of the dF cloud reaches the wall located at $x = 0$. The solution is presented in the three–dimensional space $\alpha - x_p - y_p$ in Figure 4.9a for

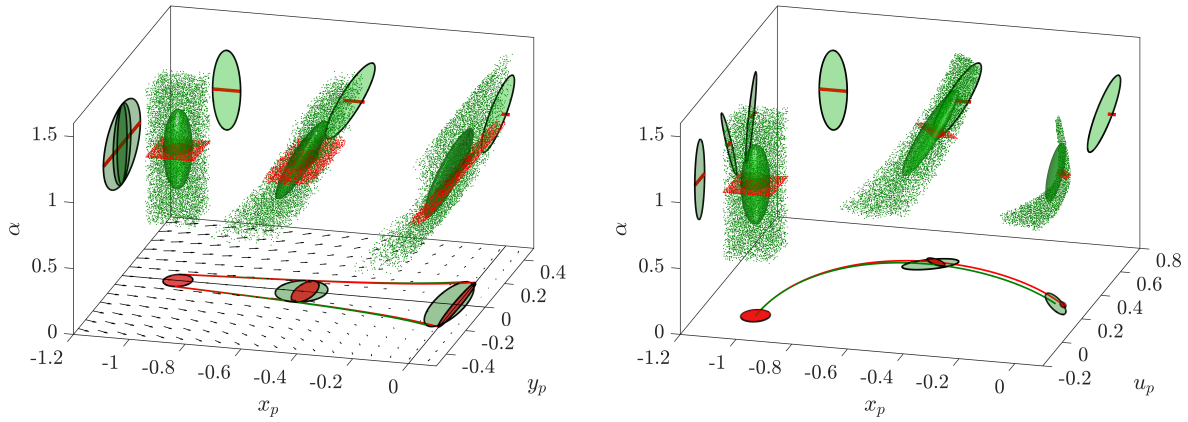


**Figure 4.9.** Evolution of the particle cloud immersed in the stagnation flow for different instants of time $t = [0,\ 0.5,\ 1.65,\ 2.2]$. The dots represent the point–particles traced by the MC–PSIC method and the Cumulative Cloud traced with the SPARSE–R method is represented by an ellipsoid for the rF case (red) and dF case (green). The projections of the SPARSE–R solution are represented in the background planes.

three instants of time $t = [0,\ 1.26,\ 2.52]$. The point–particles (computed with MC–PSIC) are depicted as points and the point–cloud (computed with SPARSE–R) is represented by either a ellipse in the dF case (because $\alpha = 1$ for all particles then the $\alpha$ collapses in a single point) or a prolate spheroid for the rF case with a magnitude and direction of the principle axes that are equal to eigenvalues and direction of the eigenvectors of the covariance matrices. The two covariance matrices used to represent the SPARSE–R solution for the rF case in Figure 4.9 are $K_{\alpha x_p y_p}$ and $K_{\alpha x_p u_p}$ whose eigenvalues are given by the following Characteristic polynomials

$$\lambda^3 - \left(\overline{x_p'^2} + \overline{y_p'^2} + \overline{\alpha'^2}\right)\lambda^2 + \left(\overline{\alpha'^2}\left(\overline{x_p'^2} + \overline{y_p'^2}\right) + \overline{x_p'^2}\ \overline{y_p'^2} - \overline{x_p' y_p'}^2 - \overline{\alpha' x_p'}^2 - \overline{\alpha' y_p'}^2\right)\lambda$$
$$+ \overline{x_p'^2}\overline{\alpha' y_p'}^2 + \overline{y_p'^2}\overline{\alpha' x_p'}^2 + \overline{\alpha'^2}\overline{x_p' y_p'}^2 - \overline{x_p'^2}\ \overline{y_p'^2}\ \overline{\alpha'^2} - 2\overline{x_p' y_p'}\ \overline{\alpha' x_p'}\ \overline{\alpha' y_p'} = 0, \tag{4.36}$$

and

$$\lambda^3 - \left(\overline{x_p'^2} + \overline{u_p'^2} + \overline{\alpha'^2}\right)\lambda^2 + \left(\overline{\alpha'^2}\left(\overline{x_p'^2} + \overline{u_p'^2}\right) + \overline{x_p'^2}\ \overline{u_p'^2} - \overline{x_p' u_p'}^2 - \overline{\alpha' x_p'}^2 - \overline{\alpha' u_p'}^2\right)\lambda$$
$$+ \overline{x_p'^2}\overline{\alpha' u_p'}^2 + \overline{u_p'^2}\overline{\alpha' x_p'}^2 + \overline{\alpha'^2}\overline{x_p' u_p'}^2 - \overline{x_p'^2}\ \overline{u_p'^2}\ \overline{\alpha'^2} - 2\overline{x_p' u_p'}\ \overline{\alpha' x_p'}\ \overline{\alpha' u_p'} = 0, \tag{4.37}$$

respectively. The projections of the solution onto the planes $x_p - y_p$, $\alpha - x_p$ and $\alpha - y_p$ are also plotted in Figure 4.9a. Accordingly, in Figure 4.9b the projections in planes $x_p - u_p$, $\alpha - x_p$ and $\alpha - u_p$ are also plotted. For the rF case, the projections are represented by ellipses in all those planes. For the dF case the projections simply lead to lines. We also show the first two moments of both dF and rF clouds computed with the MC–PSIC and SPARSE–R methods in Figure 4.10 for comparison. The solution shown in Figures 4.9 and 4.10 corresponds to a level of splitting $M = 5$. Note that the initial condition is split along the random parameters $\alpha$ and the two components of the particle velocity and location. According to this, for the dF case the total number of subclouds is related to the level of splitting $M_p = M^4$ and for rF $M_p = M^5$.

The clouds approach the stagnation point along the $x-$axis as depicted in Figure 4.9a in the $x_p - u_p$ plane. The average horizontal location and velocity trends show three different stages in time, including a first stage of acceleration, a second transitional stage and a third deceleration stage. These stages are observed for both the rF and dF clouds. Because the front of the cloud decelerates while the tail is still increasing its velocity, the standard deviations of the horizontal velocity $\sigma_{u_p}$ in the second stage show a minimum at $t \approx 1.6$ (see Figure 4.10d) for the rF case. The dF case does not exhibit this minimum in $\sigma_{u_p}$, but decreases monotonically over the entire time interval and plateaus only at that time instant. In the third stage all point–particles in the cloud region decelerate towards the stagnation point. Because of the symmetry of the problem, the mean vertical location and velocity should be zero. The results, however, show a slight initial motion in the

negative $y$ direction as a result of the Monte Carlo sampling error that is on the order of $10^{-4}$ for $N_p = 10^5$ (see Figure 4.10b). Over time this non–zero initial condition leads to vertical motion that is consistent with the three stages.

To assess the uncertainty in the rF point–cloud tracer, we compare the dF and the rF SPARSE cloud prediction in the phase space $x_p - u_p$ in Figure 4.9b. The three stages can once again be observed in the evolution of $\sigma_{x_p}$, but are notably different for dF and rF as follows: in the first stage $\sigma_{x_p}$ decreases for the dF cloud (see also Fig. 4.10c) whereas for the rF cloud it increases. The latter increase is a result of the mix of fast and slow responses to the fluid velocity of the point–particles in the rF cloud. This mix is consistent with the range of the random force coefficients, $\alpha$, and the resulting range in the time responses of the point–particles as given by $St/\alpha$. In fact, the enhanced mixing of the rF cloud in space is a result of the virtual stress per the correlation of the coefficient $\alpha$ and the particle phase variables $x_p$ and $u_p$ (as was also the case for the sine field test discussed above) as it appears in the equations (D.1e) that govern $\overline{x'_p u'_p}$. This term in turn is the only driving source term in the dynamics of $\sigma_{x_p}$ in (D.1c). The magnitude of the term $\overline{\alpha}\left(k\overline{x'^2_p} + \overline{x'_p u'_p}\right)$ in equation (D.1e) is approximately the same for rF and dF with $\overline{\alpha} = 1$, whereas the second term on the right hand side, $\overline{\alpha' x'_p}\,(k\overline{x}_p + \overline{u}_p)$, is initially on the order of $\overline{\alpha' x'_p}$, which in turn is governed by equations (D.1f)–(D.1g). In (D.1f)–(D.1g) the only term that is initially different from zero is $\overline{\alpha'^2}\,(k\overline{x}_p + \overline{u}_p)$ and it is therefor the root cause for the increase of $\sigma_{x_p}$ in the rF cloud.

In vertical direction the solution is symmetric and it turns out that because of this symmetry that $\sigma_{y_p}$ evolves identically for rF and dF. This can be understood using the simplification of the point–cloud equations in the $y$–direction for the $y$–symmetric Hiemenz flow (Appendix D), which shows that the term $-\overline{\alpha' y'_p}$ in equation (D.2e) is multiplied by the average vertical relative velocity which is zero over the simulated time interval (assuming no sampling errors). Ergo, the random forcing does not change the vertical stress or strain (Figure 4.9a), which suggests that the uncertainty in solution is zero in

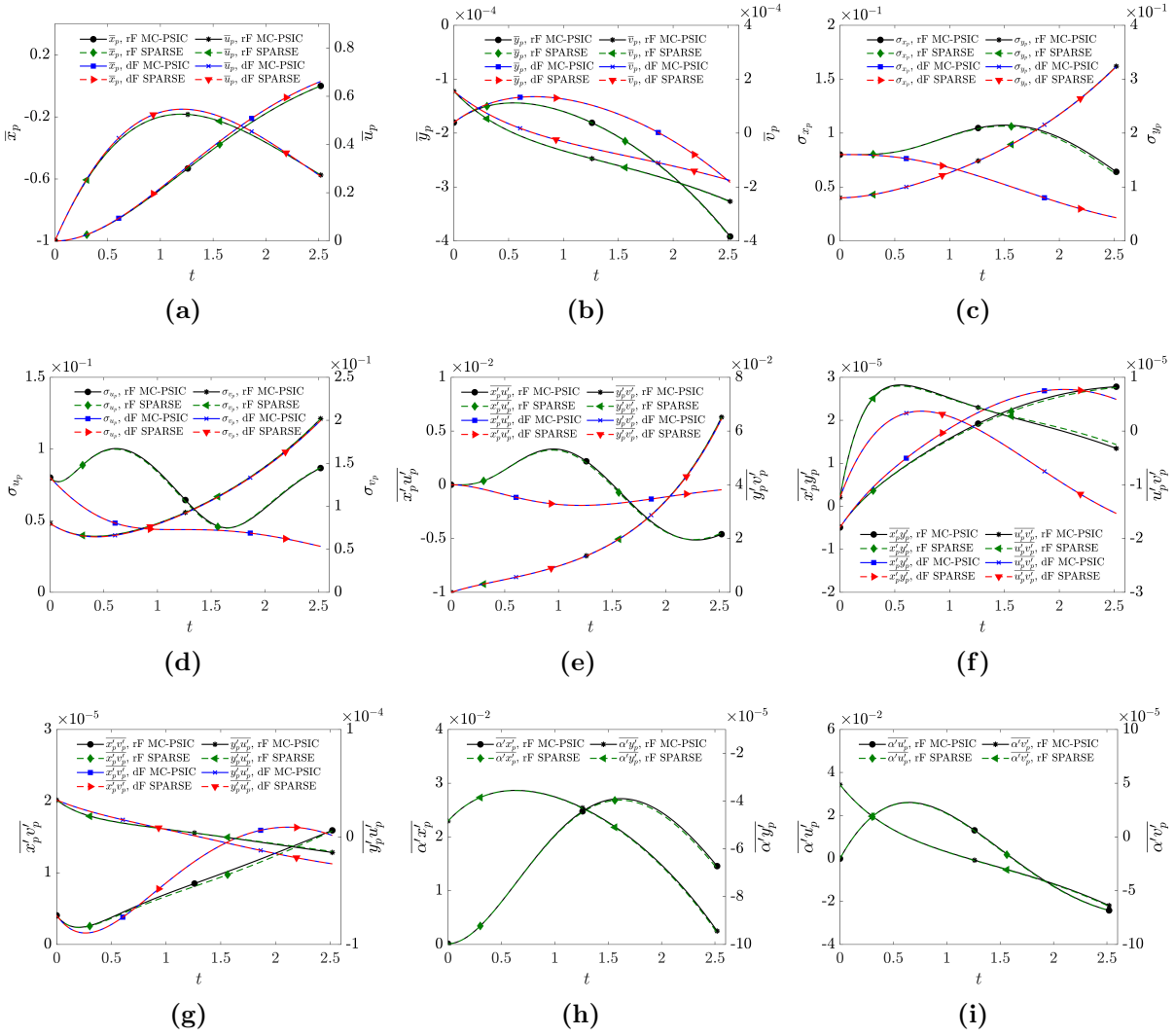


**Figure 4.10.** First two moments for of the stagnation flow test case for the rF and dF particles computed with the SPARSE–R and MC–PSIC methods. Including (a) horizontal and (b) vertical averages of the phase, (c) and (d) deviations of the particle phase, (e)–(g)combined moments of the particle variables and (h)–(i) combined moments of the particle variables and the random coefficient $\alpha$. The superscript 'S' indicates rF and 'D' dF.

vertical direction. This results generalizes to any particle–laden that is symmetric and is randomly forced according to a symmetric PDF. We conclude that in these case the uncertainty in the forcing does not propagate into the solution. A closer inspection of $\sigma_{y_p}$in Figure 4.10c shows trends on the order of the sampling errors. These trends as in $x$–direction are governed by the intrinsic interaction of correlation terms in the governing

system in $y$–direction.

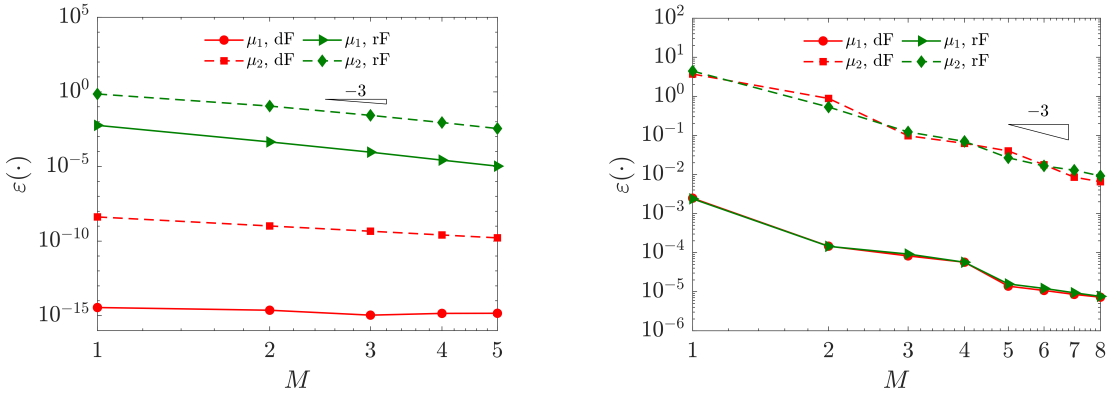


**Figure 4.11.** Errors, $\varepsilon(\cdot)$, plotted versus number of clouds per dimension, $M$, show a third convergence rate of the moment of the SPARSE (dF) and SPARSE–R (rF) method for the (a) stagnation flow case and (b) isotropic turbulence test case.

In Figure 4.11a we plot the relative error versus splitting levels in the range $M = 1, \ldots, 5$. The third order convergence rate is once more validated. The dF test cases reaches machine precision and does not require splitting to reduce the errors. We find that for the maximum level of splitting ($M = 5$) considered which leads to $M_p = 3,125$ and $M_p = 625$ for the rF and dF cases respectively, the greatest relative error of all first and second moments of the particle phase computed with SPARSE–R as compared to MC–PSIC is 3% and it occurs $\sigma^2_{u_p}$. The remaining variables of the cloud show smaller relative errors as compared to MC–PSIC, validating the SPARSE–R method. The ratio of computational cost of SPARSE–R as compared to MC–PSIC defined as in (4.25) is $r = 0.022$ for the dF case and $r = 0.141$ for the rF case. This shows that using SPARSE–R implies only a 14.1% of the computational effort that takes to solve the problem with the MC–PSIC method for the rF case and a 2.2% for the dF case.

Consistent with the observations made for the sine test case, we confirm that the solution converges with third order accuracy for all three Stokes numbers (not shown) and that the difference in confidence interval between rF and dF increases with a larger range

of randomness, and thus particle response times as proportional to $St/\alpha$.

### 4.3.3 Isotropic turbulence

Following the validation of the dF clouds as presented in Ref. [3], we test the randomly forced SPARSE–R formulation in a decaying isotropic turbulence velocity field. For a detailed description of the test setup we refer to that article. Summarizing for completeness, the isotropic turbulence simulation is performed in a cube with periodic boundary conditions with the validated discontinuous Galerkin code as described in Ref. [200] and references therein. Initial conditions are adopted from Ref. [201]. The simulation is performed on a domain $\Omega$ spanned by coordinates $(x, y, z)$, defining a cube of size $2\pi$ so that $\Omega = [0, 2\pi] \times [0, 2\pi] \times [0, 2\pi]$.

As in the previous test cases, we seed a cloud of $N_p = 10^5$ Monte Carlo point–particles in the flow. The particles in the cloud are initially at rest and therefore the cloud's average velocity is $\overline{u}_p = \overline{v}_p = \overline{w}_p = 0$. The cloud's temperature is set constant such that $T_p' = 0$ for the cloud with $\overline{T}_p = 1$. The locations of point–particles are sampled from the uniform distribution functions

$$x_{p_0} \sim \mathcal{U}\left[x_{p_{0min}}, x_{p_{0max}}\right], \quad y_{p_0} \sim \mathcal{U}\left[y_{p_{0min}}, y_{p_{0max}}\right], \quad z_{p_0} \sim \mathcal{U}\left[z_{p_{0min}}, z_{p_{0max}}\right]. \tag{4.38}$$

The random momentum and energy coefficients, $\alpha$ and $\beta$ are also sampled from an uniform distribution

$$\alpha = \beta \sim \mathcal{U}\left[\alpha_{min}, \alpha_{max}\right]. \tag{4.39}$$

The average and standard deviation values are $\overline{x}_p = \overline{y}_p = \overline{z}_p = \pi$, $\overline{\alpha} = 1$, $\sigma_{x_{p_0}} = \sigma_{y_{p_0}} = \sigma_{z_{p_0}} = 0.05$ and $\sigma_\alpha = 0.3$. For the dF case $\sigma_\alpha = 0$.

The drag and heat transfer correction factors for this case are adopted from [48]

and [188] respectively and read as

$$f_1 = \alpha \left(1 + 0.38\frac{Re_p}{24} + \frac{Re_p^{0.5}}{6}\right)\left[1 + \exp\left(\frac{-0.43}{M_p^{4.67}}\right)\right], \tag{4.40a}$$

$$f_2 = \alpha \left(1 + 0.3 Re_p^{0.5} Pr^{0.33}\right). \tag{4.40b}$$

The computed carrier phase velocities are used to determine the particle Reynolds as defined in (4.2) and the particle Mach number $M_p = |\boldsymbol{u} - \boldsymbol{u}_p|/\sqrt{T_f}$, in the forcing correction factors (4.40). The Prandtl number is $Pr = 0.7$, the relative heat capacity is set to unity $c_r = 1$ and the density ratio of the two phases is $\rho_p = 250$. We also set the Stokes number to be $St = 0.5$ such that the inertia is dominant in the dynamics of the point–particles. The non–dimensional particle diameter is $d_p = 4 \cdot 10^{-3}$ according to (4.2). The isotropic turbulence case is set up with a reference Reynolds $Re_\infty = 2,357$ and Mach number $M_\infty = 0.05$ [201].

Using splitting along the particle locations and the random parameter $\alpha$ for the point–cloud simulation, it follows that for the rF case the total number of subclouds is $M_p = M_p^{x_p} M_p^{y_p} M_p^{z_p} M_p^{\alpha} = M^4$ with superscripts indicating the dimension where the divisions are performed. For the dF case then we have $M_p = M^3$. We consider several levels of splitting $M = 1, \ldots, 8$ that correspond to a maximum number of subclouds of $M_p = 4,096$ and $M_p = 512$ for rF and dF cases respectively. Note that in this test case, all relative errors should be expected to be non–zero because the flow is non–linear and the correction functions of the forcing depend on the relative velocity of the particles through the particle Reynolds and Mach numbers and so all Taylor and moment truncation affect the accuracy of SPARSE–R.

In Figure 4.12 we show the rF test case results for three equispaced instants of times in the interval $t \in [0,\ 4]$. The MC–PSIC particles are depicted as points and the SPARSE–R clouds as prolate spheroids for a level of splitting with $M = 4$ which defines

four subclouds along the variables $x_p$, $y_p$, $z_p$ and $\alpha$. We select this somewhat coarser level of splitting for the clarity of the visualization in Figures 4.12a–4.12c. The SPARSE–R subclouds are colored according to the spatial four divisions along each coordinate to identify the point–particles that correspond to each point–cloud. The same color has been used for a given subcloud and its corresponding point–particles in the Figures 4.12a–4.12c. The background planes represents contours of the turbulent kinetic energy of the carrier phase's turbulent structures for each instant of time. The ellipsoids for each subcloud computed with SPARSE–R are represented using the eigenvalues and eigenvectors of the covariance matrix of the locations $x_p$, $y_p$ and $z_p$. To enhance clarity of the visualization, in Figures 4.12d–4.12f we show the evolution in time of the point–particles and point–clouds that intersect a plane passing through the center of the domain where only one slice of $4 \times 4$ clouds is represented. The particles initially at rest respond to the carrier flow producing a deformation of the initial cube where the cloud of point–particles is defined. Governed by the inertial effects, the response is smoother as compared with the changes in the carrier flow. As time evolves, the particle cloud is dispersed occupying an increasingly larger domain.

In Figure 4.13, we show the results of first and second moments for the rF and dF where the level of splitting corresponds to the maximum division in the convergence study $M = 8$ (see Figure 4.11b). In particular, to concisely show the agreement between the MC–PSIC and the SPARSE–R results we group moments into vectors and matrices and compute their modulus and determinant, respectively. The first moments of the average location and velocity are entries in the vectors with the following moduli

$$|\overline{\boldsymbol{x}}_p| = \left(\overline{x}_p^2 + \overline{y}_p^2 + \overline{z}_p^2\right)^{1/2}, \qquad |\overline{\boldsymbol{u}}_p| = \left(\overline{u}_p^2 + \overline{v}_p^2 + \overline{w}_p^2\right)^{1/2}, \tag{4.41}$$

which are plotted in Figures 4.13a and 4.13b. The average temperature $\overline{T}_p$ is depicted in Figure 4.13c. For the second moments of the particle phase, we define the following

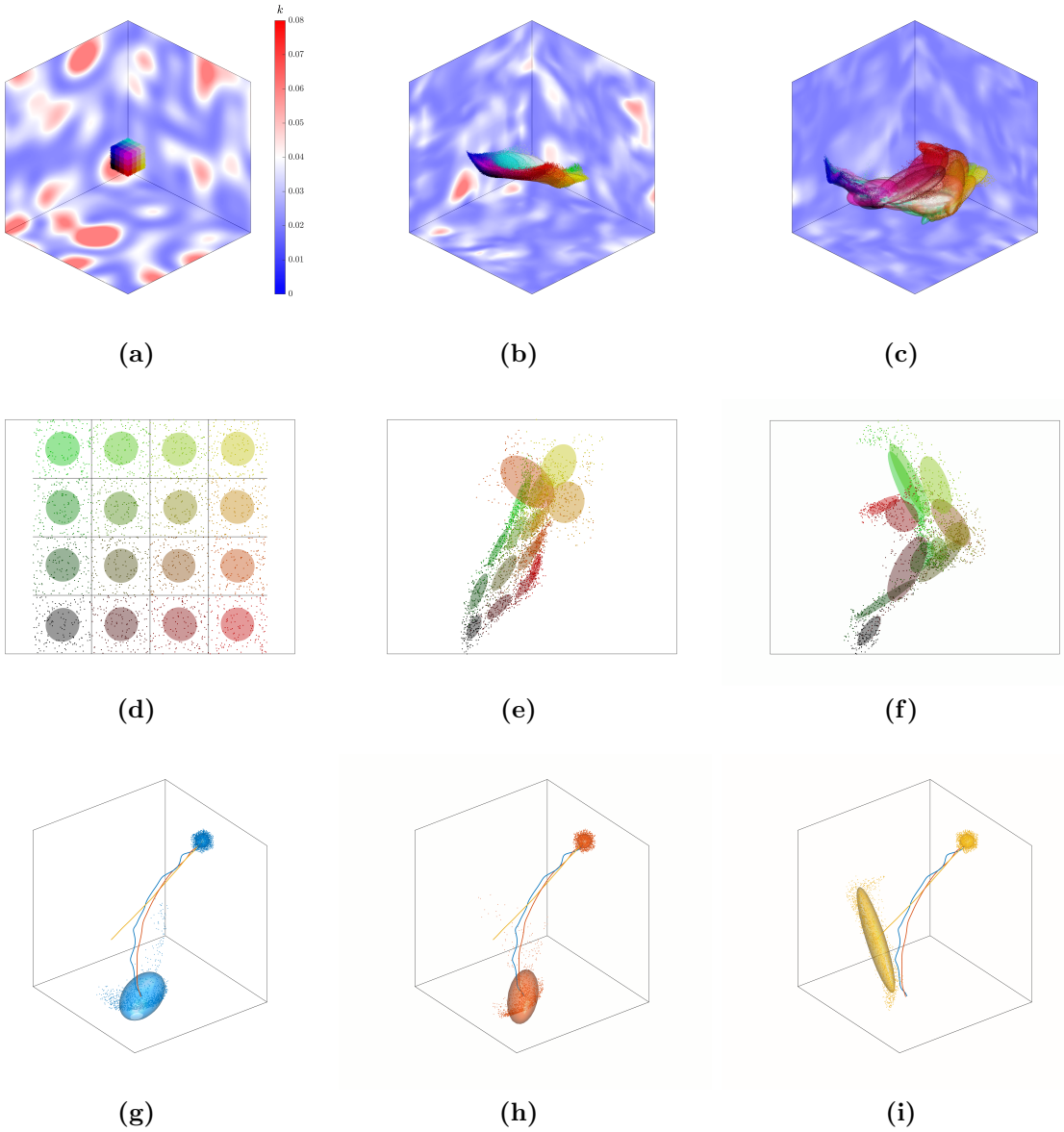


**Figure 4.12.** Locations of the point–particles and point–clouds computed with MC–PSIC and SPARSE–R methods respectively for the isotropic turbulence case with $St = 0.5$ for a level of splitting of $M = 4$ at times (a) $t = 0$, (b) $t = 2$, (c) $t = 4$. The contours show the turbulent kinetic energy of the flow in the boundaries of the domain. The PSIC particles are represented with dots and the SPARSE–R clouds with ellipsoids. In (d)–(f) the projection of the clouds to a $x - y$ plane passing through the center of the cloud for $St = 0.5$. In (g)–(i) the evolution of a point–cloud (and the corresponding point–particles) used to split for (g) $St = 0.1$ (h) $St = 0.5$ and (i) $St = 2$.

matrices

$$K_{x_p} = \begin{bmatrix} \overline{x_p'^2} & \overline{x_p'y_p'} & \overline{x_p'z_p'} \\ \overline{x_p'y_p'} & \overline{y_p'^2} & \overline{y_p'z_p'} \\ \overline{x_p'z_p'} & \overline{y_p'z_p'} & \overline{z_p'^2} \end{bmatrix}, \quad K_{x_pu_p} = \begin{bmatrix} \overline{x_p'u_p'} & \overline{x_p'v_p'} & \overline{x_p'w_p'} \\ \overline{y_p'u_p'} & \overline{y_p'v_p'} & \overline{y_p'w_p'} \\ \overline{z_p'u_p'} & \overline{z_p'v_p'} & \overline{z_p'w_p'} \end{bmatrix}, \quad K_{u_p} = \begin{bmatrix} \overline{u_p'^2} & \overline{u_p'v_p'} & \overline{u_p'z_p'} \\ \overline{u_p'v_p'} & \overline{v_p'^2} & \overline{v_p'w_p'} \\ \overline{u_p'w_p'} & \overline{v_p'w_p'} & \overline{w_p'^2} \end{bmatrix}, \tag{4.42}$$

whose determinants are depicted in Figures 4.13d, 4.13e and 4.13g. The following vectors are defined based on correlations between particle locations, velocities, temperatures and the random coefficient $\alpha$

$$k_{x_pT_p} = \begin{bmatrix} \overline{x_p'T_p'} \\ \overline{y_p'T_p'} \\ \overline{z_p'T_p'} \end{bmatrix}, \quad k_{u_pT_p} = \begin{bmatrix} \overline{u_p'T_p'} \\ \overline{v_p'T_p'} \\ \overline{w_p'T_p'} \end{bmatrix}, \quad k_{\alpha x_p} = \begin{bmatrix} \overline{\alpha' x_p'} \\ \overline{\alpha' y_p'} \\ \overline{\alpha' z_p'} \end{bmatrix}, \quad k_{\alpha u_p} = \begin{bmatrix} \overline{\alpha' u_p'} \\ \overline{\alpha' v_p'} \\ \overline{\alpha' w_p'} \end{bmatrix}. \tag{4.43}$$

The moduli are shown in Figures 4.13f, 4.13h, 4.13j, and 4.13k. Finally, the standard deviation of the particle temperature $\sigma_{T_p}$ and second moment of the random coefficient and temperature $\overline{\alpha' T_p'}$ are presented in Figures 4.13i and 4.13l. In this manner, the twelve scalars plotted in Figure 4.13 combine all 42 moments of the particle phase (including the moments that relate to the random coefficient $\alpha$) and it so admits a comparison of MC–PSIC and SPARSE–R results for the complete statistical description of the particle clouds. Note that for the dF case $k_{\alpha x_p}$, $k_{\alpha u_p}$ and $\overline{\alpha' T_p'}$ are not shown because $\alpha' = 0$.

The first moments of the particle cloud (Figures 4.13a–4.13c) show that the the mean cloud motion for the rF and dF case are in close agreement within 3%. For an analogous reason that was used to explain that stagnation flow solutions are identical for the dF and the rF test case in the symmetrical vertical direction, the first moments solutions for dF and rF are similar because of the near–isotropy in this turbulent flow also. Note while the carrier flow is isotropic in the periodic box, the cloud is initialized in only a portion of it, and the carrier phase in this portion is not precisely isotropic. This

means that the uncertainty in the forcing can and does propagate in the dispersed solution, as witnessed by the small deference in dF and rF. Specifically, fast and slow responding, randomly forced particle trajectories average such that the resulting two moments match those of the dF solution with the average time response of the rF case. The velocity average (Figure 4.13b) reaches a maximum in an initial acceleration of the cloud to reach the decreasing carrier phase velocity field. After that, a decrease in velocity of the particle cloud follows the decay of turbulence in the flow and the inertia in the particle phase somewhat smoothens the response as compared with fluid tracers (that move at the flow velocity). This effect is related to the Stokes number as seen in Figures 4.12g–4.12i. For large values of $St$, the response of the cloud to the carrier flow fluctuations, is slow. In that sense, the cloud's average trajectory dissipates the fluctuations along the path. For small values of $St$, the opposite is true and carrier flow variations results in changes of the average trajectory of the cloud. The average temperature of the cloud oscillates around the initial and average value during the entire simulation (unity). The maximum relative error in the first moments of the particle phase is 0.9% and 0.7% for the average modulus of the particle velocity $|\overline{\boldsymbol{u}}_p|$ for the rF and dF cases respectively.

The second moment trends are shown in Figures 4.13d–4.13i. Figure 4.13d plots the determinant, $|K_{x_p}|$, which is equal to product of the eigenvalues of $K_{x_p}$. This metric can thus be interpreted a measure of the spatial spread of the particle cloud because it is equal to the product of principle strains (eigenvalues) of the cloud. It shows that the turbulent field mixes (or diffuses) the dispersed phase which leads to a increase in the cloud's footprint in space. This spatial growth is similar for the dF and rF case because of the near isotropic flow conditions. At later times the cloud occupies a larger portion of the computational domain and thus the conditions are more isotropic then, and the dF and rF moments are mostly in closer agreement. The trends of the determinants in Figures 4.13g–4.13i for the remaining second moments exhibit a rather complex behavior. Its discussion is beyond the scope of the current article that aims to present and validate

the rF point–cloud model. It can be concluded, however, that all moments show a very good comparison between rF SPARSE–R and MC–PSIC. The maximum relative error in $|K_{x_p u_p}|$ for the rF and dF case are 4.5% and 8% respectively. Note that the accuracy for the governing equations of the moments of the point–cloud tracer in $K_{x_p u_p}$ are directly dependent on truncated statistical moments of order greater than two. In Figure 4.11b we plot the convergence of the SPARSE errors with respect to the level of splitting $M$, confirming once again the theoretical third order convergence rate.

One might expect that the particle response to the fluid changes is slower and thus particles disperse less for larger Stokes numbers. However, comparing the cloud size at the final time $t = 4$ for a Stokes number of $St = 2$, (Figure 4.12i) with the smaller Stokes numbers, $St = 0.5$ (Figure 4.12g) and $St = 0.1$ (Figure 4.12h) shows that the magnitude of second moments (and thus the dispersion) in one of the principle directions is increased for the largest Stokes number. As we already discussed for the sine and the stagnation test cases, this can be explained to some extent by the larger randomness and associated larger range in response times. More research is needed to understand why the dispersion is larger in one direction only in this homogeneous turbulent flow. We plan to report on that in future work.

As a final validation and illustration of the capability of SPARSE–R, we present PDFs of the Cumulative Cloud in Figures 4.14 and 4.15. We compare the evolution of the PDF contours computed with MC–PSIC with the SPARSE–R method. For three specific instants of time $t = [0.75,\ 2,\ 4]$, the PDFs are computed using (4.24) and plotted versus the random variable only. These figures illustrate that SPARSE–R predicts the PDF with same level of detail as MC–PSIC. For example, the shift of the PDF from a single peak to a double peak in $f_{x_p}$ is captured at time $t = 4$.

## 4.4 Summary of results

A closed-form Lagrangian point–cloud model is coined that determines the first and second statistical moments of groups of randomly forced particles within a cloud region at a single (singular) point in a computationally efficient manner. The union of several point–clouds can determine the PDF and higher order statistical moments of the union, which we dub a Cumulative Cloud. The model propagates the uncertainty in the forcing function, as described by series expansion, that can be either the confidence interval in data–driven and/or empirical forcing models or the stochastic force variance on the sub–cloud scales, into its solution.

Like its deterministically forced sibling, the model is derived using the SPARSE approach, which combines a truncated method of moments and a truncated Taylor series expansion of the forcing function and the carrier flow variable at the points–cloud's mean location and relative velocity. The randomly forced SPARSE–R method is also closed, i.e., the formulation is self-contained, independent of Monte Carlo results to close higher order correlations of variables in principle unknown. The convergence of these truncated terms is proportional to the standard deviation of the particle variables to the third power. This third–order convergence rate is verified in numerical tests.

The second moments of the variables in the Taylor expanded cloud and its influence on the acceleration of the cloud are relatively small as compared to the first moments. As a result a point–cloud that is deterministically forced with the mean of the random forcing function provides a reasonable estimate of the mean of the randomly forced point–cloud for the three test cases considered.

The difference of the second moments determined with SPARSE–R approach and the deterministic SPARSE solution provides an accurate estimate of propagation of the uncertainty of the forcing function into confidence intervals of the solution. It is observed that the propagation of randomness in the forcing into the confidence interval of the

particle solution grows with the Stokes number.

A virtual stress that correlates the random coefficients of the series expansion, with the dispersed phase fluctuations mixes the samples of the randomly forced particle solution in phase space. These stresses are correctly and accurately modeled by SPARSE–R and thus SPARSE–R gives direct insight in the fundamental driving mechanics of uncertainty propagation in a solution by inspection and comparison of the magnitudes of the moments on the rights hand side of the closed systems of dynamic, SPARSE–R ordinary differential equations.

The virtual stress is negligible in directions of symmetry or in isotropic flows, because correlations with respect to the fluctuations forcing coefficients multiply with zero mean field solutions. Then randomness does not affect the footprint of the clouds because fast and slow responding particles cancel each other's motions. This was illustrated in stagnation flow and an isotropic turbulence.

## 4.5 Acknowledgments

Sections 4.1 through 4.4, are a reprint of the material as it appears in Ref. [4], "SPARSE-R: A point-cloud tracer with random forcing", D. Domínguez-Vázquez and G. B. Jacobs, *International Journal of Multiphase Flow*, 170, 104653, 2024. D. Domínguez-Vázquez: conceptualization, investigation, original draft preparation, visualization. G. B. Jacobs: conceptualization, supervision, review & editing.

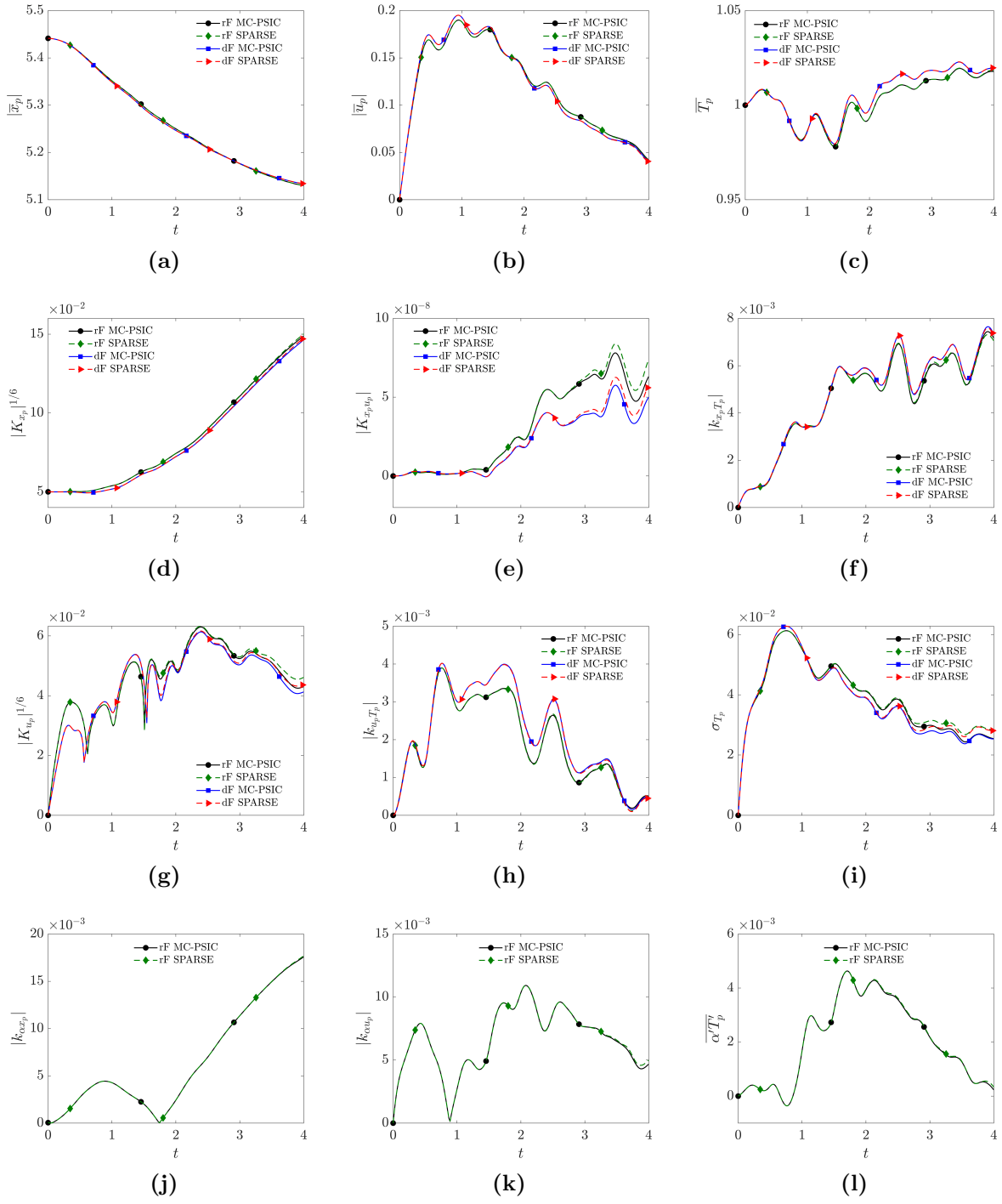


**Figure 4.13.** Statistics of the rF and dF inertial particle clouds in the three–dimensional decaying isotropic turbulence case with $St = 0.5$ computed with MC–PSIC and SPARSE–R model; (a)–(c) average values of the first moments of the particle phase, (d)–(i) average values of second moments of the particle phase and (j)–(l) average values of second moments combining the particle phase and random coefficient $\alpha$.

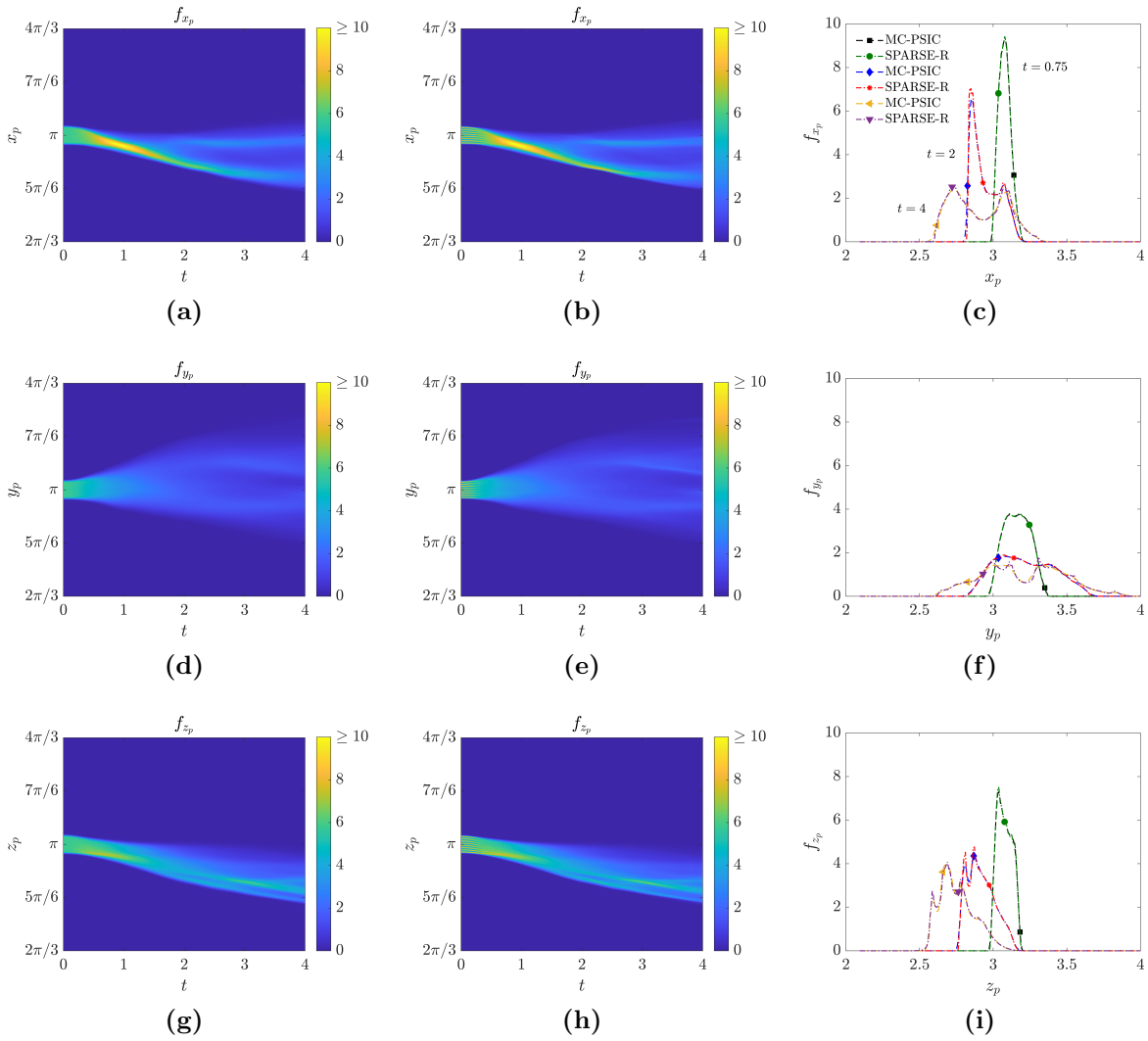


**Figure 4.14.** PDFs of the components of the particle locations $f_{x_p}$, $f_{y_p}$ and $f_{z_p}$ for the rF case computed with MC–PSIC and SPARSE–R methods for the isotropic turbulence test case with $St = 0.5$. The Figure shows: PDF of $x_p$ computed with (a) MC–PSIC and (b) SPARSE–R and (c) comparison for different times and the corresponding result for $y_p$ in (d)–(f) and for $z_p$ in (g)–(i). The legend in (c) also corresponds to (f) and (i) where the solution is plotted at times $t = [0.75,\ 2,\ 4]$ for both methods.

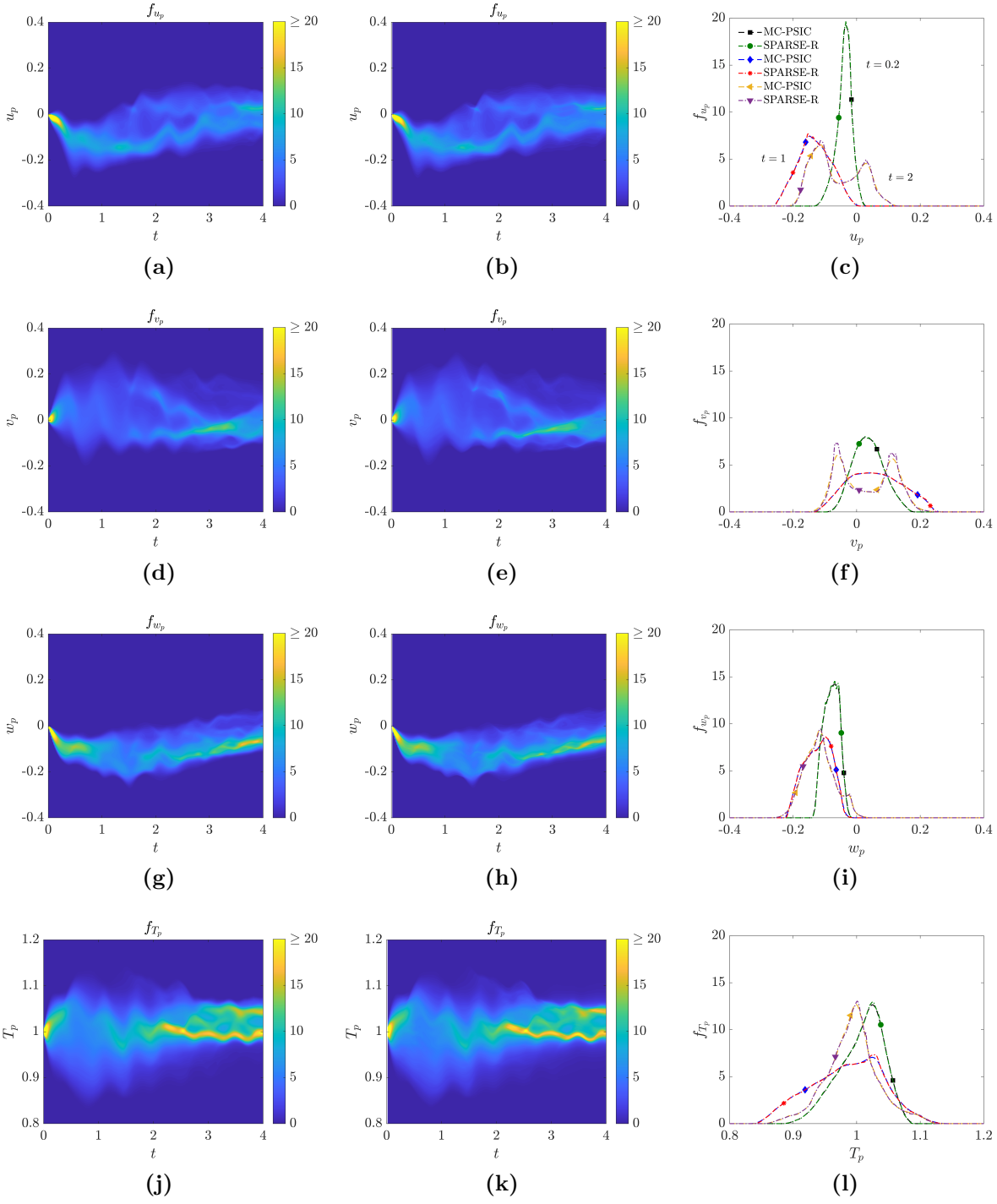


**Figure 4.15.** PDFs of the particle velocity components and temperature for the rF case computed with MC–PSIC and SPARSE–R methods for the isotropic turbulence test case with $St = 0.5$. The Figure shows: PDF of $u_p$ computed with (a) MC–PSIC and (b) SPARSE–R and (c) comparison for different times, and the equivalent for $v_p$ in (d)–(f), for $w_p$ in (g)–(i) and for $T_p$ in (j)–(l).

# Chapter 5

# Lagrangian PDF models of multi-phase flows with randomly forced inertial particles

## 5.1 Introduction

Within the EL framework, the scale of interest determines the selection of a particular model. Large-scale problems typically rely on the point-particle assumption [37, 38] and trace *deterministic* Lagrangian paths of individual volumeless particles according to an analytical or empirical forcing law [205, 66]. Thus, at any time $t$, a particle's location, $\boldsymbol{x}_{\mathrm{p}}(t)$, and velocity, $\boldsymbol{u}_{\mathrm{p}}(t)$, satisfy deterministic equations of motion,

$$\frac{\mathrm{d}\boldsymbol{x}_{\mathrm{p}}}{\mathrm{d}t} = \boldsymbol{u}_{\mathrm{p}}, \tag{5.1a}$$

$$\frac{\mathrm{d}\boldsymbol{u}_{\mathrm{p}}}{\mathrm{d}t} = \boldsymbol{f}(\boldsymbol{u}, \boldsymbol{u}_{\mathrm{p}}; \boldsymbol{\xi}). \tag{5.1b}$$

The sum of the forces acting on the particle, $\boldsymbol{f}$, includes the undisturbed flow force, the added mass force, the quasi-steady drag force, the viscous history force and the gravitational force. These forces might depend on the carrier flow field $\boldsymbol{u}(\boldsymbol{x}, t)$ and its derivatives, and involve a set of $N_\xi$ parameters, $\boldsymbol{\xi} = \{\xi_n : \ n = 1, \ldots, N_\xi\}$, such as the Stokes number, the fluid to particle density ratio, particle diameter, particle shape and

flow viscosity among others [104].

The Maxey-Riley-Gatignol (MRG) equation for $\boldsymbol{f}$ [44, 43] is an example of the analytical forcing laws for a spherical particle; it is the default approach for most deterministic point-particle methods [66, 67], even though its applicability range is limited. Its derivation assumes a single particle in the limit of zero particle Reynolds number. The failure to account for the influence of neighboring particles results in a mismatch between predictions of the point-particle model and PR–DNS, especially for moderate-to-high particle mass loads [1, 206, 207].[1] And the low Reynolds number limit condition is not met in compressible particle-laden flows at high speeds and for large particle diameter [58]. These shortcomings of the MRG relation are ameliorated by using empirical factors to fit either experimental data or PR-DNS results. Examples of such factors are the [48] correction for high Reynolds and Mach numbers, the particle-agglomerate correction [209, 210, 211] and correction factors non-spherical shapes [204, 212, 213].

These and other curve-fitted empirical correctors are subject to uncertainty, especially when "discovered" via machine-learning techniques [6, 214]. Quantifying this uncertainty in a probabilistic manner improves the validity range of the resulting stochastic point-particle methods [98, 2]. Another motivation for the adoption of a probabilistic framework is that the deterministic Lagrangian paths described by Eq. (5.1) ignore apparent randomness in particle dynamics. This randomness stems from unresolved forces in, e.g., a deterministic drag relation assigned to a point-particle; *stochastic* Lagrangian approaches account for this phenomena by treating some of the forces in $\boldsymbol{f}$ as random [215, 216]. Finally, deterministic treatment of Eq. (5.1) assumes carrier flow velocity $\boldsymbol{u}(\boldsymbol{x}, t)$ to be deterministic. For turbulent flows, the carrier flow field is routinely computed via large-eddy simulations (LES) or the Reynolds-averaged Navier-Stokes (RANS) equations. The unresolved, subgrid fluctuations in such computations can be included in the particle description stochastically

[1] Models that do consider inter-particle forces include the pairwise interaction extended point-particle (PIEP) model [90, 91, 92, 93] and the microstructure-informed probability-driven point-particle (MPP) model [94, 97, 208].

in either Eulerian [87, 217, 171] or Lagrangian [132, 133, 134, 135, 136, 137, 36] models.

While stochastic carrier-velocity fluctuations influence a particle's motion, the particle's kinetics at the subgrid level induces carrier-velocity fluctuations. This phenomenon is variously referred to as pseudo-turbulence kinetic energy (PTKE) fluctuations [60] or subgrid particle-averaged Reynolds-stress equivalent [57]. The SPARSE method and its subsequent enhancements [58, 3, 4] provide a closed point-cloud approach to describe particle ensembles by a set of statistical moments. The SPARSE method can also accommodate randomness in the forcing $\boldsymbol{f}$ due to uncertainty in its empirical description [4]. These and other stochastic descriptions of the particle path [131, 138, 139, 1, 141, 143, 144] replace the deterministic Eq. (5.1) with its stochastic (Langevin-type) counterpart [119],

$$\mathrm{d}\boldsymbol{X}_\mathrm{p} = \boldsymbol{U}_\mathrm{p}\mathrm{d}t + \boldsymbol{b}_x\mathrm{d}\boldsymbol{W}_x, \tag{5.2a}$$

$$\mathrm{d}\boldsymbol{U}_\mathrm{p} = \boldsymbol{\mathcal{F}}(\boldsymbol{U}, \boldsymbol{U}_\mathrm{p}; \boldsymbol{\Xi})\,\mathrm{d}t + \boldsymbol{b}_u\mathrm{d}\boldsymbol{W}_u. \tag{5.2b}$$

Here, the uppercase quantities denote random counterparts of the corresponding deterministic (lowercase) quantities in Eq. (5.1); $\boldsymbol{b}_x$ and $\boldsymbol{b}_u$ are (generally unknown) diffusion tensors; and $\mathrm{d}\boldsymbol{W}_x$ and $\mathrm{d}\boldsymbol{W}_u$ are Wiener increments of, respectively, the particle's position $\boldsymbol{X}_\mathrm{p}(t)$ and velocity $\boldsymbol{U}_\mathrm{p}(t)$ for the time interval $\mathrm{d}t$. This general formulation of stochastic particle dynamics encompasses multiple models. The position-Langevin (PL) approach [141], originally developed for fluid tracers, includes $\mathrm{d}\boldsymbol{W}_x$, while setting $\mathrm{d}\boldsymbol{W}_u \equiv \boldsymbol{0}$ and using the deterministic $\boldsymbol{f}$ and $\boldsymbol{\xi}$ from Eq. (5.1) in place of their random counterparts $\mathbf{F}$ and $\boldsymbol{\Xi}$. The velocity Langevin (VL) approach [141] uses $\mathrm{d}\boldsymbol{W}_u$ to account for unknown/undescribed forces by the deterministic point-particle method, related to particle collisions and influence of neighboring particles, in addition to the deterministic part of the forcing given by $\boldsymbol{f}$ in lieu of the random counterpart $\boldsymbol{\mathcal{F}}$, and sets $\mathrm{d}\boldsymbol{W}_x \equiv 0$. The force-Langevin (FL) model [141, 143] adds Wiener increments to the hydrodynamical force, described by an additional Langevin equation, not included in (5.2), and added to the deterministic part

$\boldsymbol{f}$ while setting $\mathrm{d}\boldsymbol{W}_x = \mathrm{d}\boldsymbol{W}_u \equiv 0$.

A solution to the Langevin Eqs. (5.2) is the joint probability density function (PDF) $f_{\boldsymbol{XU}}(\boldsymbol{x}_\mathrm{p}, \boldsymbol{u}_\mathrm{p}, t)$, whose temporal evolution in the phase-space $(\boldsymbol{x}_\mathrm{p}, \boldsymbol{u}_\mathrm{p})$ is described by a Fokker-Planck equation [e.g., 218]. In general, the derivation of such equations requires closure approximations, which can be empirically obtained by, e.g., analyzing PR-DNS results [143]. This procedure is computationally expensive, because of the slow convergence of sampling techniques used to solve the Langevin equations and the high dimensionality of the Fokker-Plank equation. (If the particle-laden flow takes place in $d$ spatial dimensions, then the Fokker-Plank equation for $f_{\boldsymbol{XU}}$ is solved in $2d$ phase-space dimensions, plus time.) This high cost is a reason why most studies in this framework are limited to the second moments of $f_{\boldsymbol{XU}}(\boldsymbol{x}_\mathrm{p}, \boldsymbol{u}_\mathrm{p}, t)$, rather than the full PDF [1, 141, 143, 144].

A way to obviate the need for closure construction is to derive an exact $(2d + N_\xi)$-dimensional deterministic (Liouville-type) equation for the joint PDF $f_{\boldsymbol{XU\Xi}}(\boldsymbol{x}_\mathrm{p}, \boldsymbol{u}_\mathrm{p}, \boldsymbol{\xi}, t)$ for the particle's position and velocity, $\boldsymbol{X}_\mathrm{p}(t)$ and $\boldsymbol{U}_\mathrm{p}(t)$, and random model parameters $\boldsymbol{\Xi}$ [2]. While a high-order spectral method can be deployed to solve this high-dimensional parabolic partial-differential equation (PDE) [2], this solution covers the entire $(2d + N_\xi)$-dimensional augmented phase-space over the entire time horizon of interest, i.e., spans the Eulerian domain with near-zero solution values in sub-domains far away from the regions with high concentrations of particles. That renders this Eulerian solution strategy computationally intensive.

To take advantage of the localized nature of PDF solutions, we propose to deploy the Lagrangian-Charpit method [219, 220, 221, 222, 223, 224, 225, 226]. It is developed for nonlinear hyperbolic PDEs and reduces to the method of characteristics (MoC) for linear equations, such as the Liouville equation. In addition to localization, this Lagrangian approach offers several other advantages over classical high-order PDE solvers. First, the use of high-order methods and filtering techniques to solve a high-dimensional hyperbolic PDE would compromise the solution's non-negativity to maintain stability. Second, many

numerical methods for hyperbolic PDEs suffer from Gibbs oscillations and singularities, which are absent in the MoC. Third, the MoC provides a deterministic flow map to track individual points in the high-dimensional phase space, i.e., each solution of the particle phase associated to a probability for it to occur, may be computed independently; this allows rare events to be traced independently.

We present a novel Eulerian-Lagrangian methodology to model particle-laden flows with randomly forced point-particles. To accommodate data-driven (equation-free) forcing functions, the methodology deploys a polynomial chaos expansion (PCE) to represent stochastic forcings $\boldsymbol{F}$ [99, 2, 6, 4]; the random constants in these expansions form a set of random coefficients $\boldsymbol{\Xi}$. Then, the method of distributions [227] is used to derive a Liouville equation for the joint PDF $f_{\boldsymbol{XU\Xi}}(\boldsymbol{x}_\mathrm{p}, \boldsymbol{u}_\mathrm{p}, \boldsymbol{\xi}, t)$. Next, this high-dimensional PDE is solved via the MoC, resulting in a set of ordinary differential equations that comprise a flow map for the joint PDF and its support. Finally, we modify the quadrature technique [228, 229], which is compatible with discontinuous-Galerkin discretization of DNS solvers, to compute the marginals $f_{\boldsymbol{X}}(\boldsymbol{x}_\mathrm{p}, t)$ and $f_{\boldsymbol{U}}(\boldsymbol{u}_\mathrm{p}, t)$ and their moments via marginalization of the joint PDF $f_{\boldsymbol{XU\Xi}}(\boldsymbol{x}_\mathrm{p}, \boldsymbol{u}_\mathrm{p}, \boldsymbol{\xi}, t)$.

## 5.2 Liouville equation for particle-laden flows

To simplify the method's exposition, we consider $d$-dimensional particle-laden flows with one-way coupling between the carrier fluid and particle dynamics, i.e., flows in a dilute regime wherein the inertia is dominant. The incompressible carrier fluid has density $\rho$ and dynamic viscosity $\mu$; its flow velocity, $\boldsymbol{u}(\boldsymbol{x}, t) : \mathbb{R}^d \times [0, \infty) \to \mathbb{R}^d$, is known with certainty, i.e., deterministic. The random forces acting on a small particle of diameter $D$, $\boldsymbol{\mathcal{F}}(\cdot)$ in Eq. (5.2), reduce to the inertial (drag) force, which depends on the difference between the (random) particle velocity $\boldsymbol{U}_\mathrm{p}(t)$ and the carrier velocity at the (random) particle location, $\boldsymbol{X}_\mathrm{p}(t)$, i.e., $\boldsymbol{\mathcal{F}} = \boldsymbol{\mathcal{F}}(\boldsymbol{u}(\boldsymbol{X}_\mathrm{p}(t), t) - \boldsymbol{U}_\mathrm{p}(t))$. For carrier flow with characteristic length $L$ and

non-zero velocity component $u_\infty$ aligned with the $x_1$ direction, and for particle density $\rho_\mathrm{p}$, the characteristic times for carrier flow and particle dynamics are

$$\tau_\mathrm{f} = L_\infty/u_\infty \qquad \text{and} \qquad \tau_\mathrm{p} = \rho_\mathrm{p} D^2/(18\mu),$$

respectively. The average flow dynamics is characterized by the Reynolds numbers for carrier flow and particle dynamics, $\mathrm{Re}_\infty$ and $\mathrm{Re}_\mathrm{p}$, and by the Stokes number St, defined as

$$\mathrm{Re}_\infty = \frac{\rho u_\infty L}{\mu}, \qquad \mathrm{Re}_\mathrm{p} = \frac{\rho \|\boldsymbol{u} - \boldsymbol{U}_\mathrm{p}\|_2 D}{\mu} = \mathrm{Re}_\infty \|\tilde{\boldsymbol{u}} - \tilde{\boldsymbol{U}}_\mathrm{p}\|_2 \tilde{D}, \qquad \mathrm{St} = \frac{\tau_\mathrm{p}}{\tau_\mathrm{f}} = \mathrm{Re}_\infty \frac{\tilde{\rho}_\mathrm{p} \tilde{D}^2}{18}, \tag{5.3}$$

where $\tilde{\boldsymbol{u}}(\tilde{\boldsymbol{X}}_\mathrm{p}(\tilde{t}), \tilde{t}) = \boldsymbol{u}(\boldsymbol{X}_\mathrm{p}(t), t)/u_\infty$, $\tilde{\boldsymbol{X}}_\mathrm{p} = \boldsymbol{X}_\mathrm{p}/L$, $\tilde{t} = t u_\infty/L$, $\tilde{\boldsymbol{U}}_\mathrm{p} = \boldsymbol{U}_\mathrm{p}/u_\infty$, and $\tilde{D} = D/L$. In terms of these dimensionless numbers, the dimensionless drag force is written as

$$\tilde{\mathcal{F}} = \frac{\tilde{\boldsymbol{u}} - \tilde{\boldsymbol{U}}_\mathrm{p}}{\mathrm{St}} \phi(\mathrm{Re}_\mathrm{p}).$$

The function $\phi(\mathrm{Re}_\mathrm{p}) : \mathbb{R}^+ \to \mathbb{R}^+$ represents a random correction to the classical Stokes drag force, such that $\phi(\mathrm{Re}_\mathrm{p}) \equiv 1$ for small spherical particles in incompressible laminar flow. Rather than relying on an uncertain empirical functional form of $\phi(\cdot)$, we represent it via orthogonal polynomials $\psi_i(\cdot)$ [99, 4, 6],

$$\phi(\mathrm{Re}_\mathrm{p}; \boldsymbol{\Xi}) = \sum_{i=1}^{N_\xi} \Xi_i \psi_i(\mathrm{Re}_\mathrm{p}), \tag{5.4}$$

where the random coefficients $\Xi_i$ $(i = 1, \ldots, N_\xi)$ form a vector $\boldsymbol{\Xi} \in \mathbb{R}^{N_\xi}$ of length $N_\xi$. These coefficients have the domain of definition $\Omega_{\boldsymbol{\Xi}} \in \mathbb{R}^{N_\xi}$ are characterized by a joint PDF $f_{\boldsymbol{\Xi}}(\boldsymbol{\xi}) : \Omega_{\boldsymbol{\Xi}} \to \mathbb{R}^+$.

In addition to the possible uncertainty in the particle's initial state, the uncertainty in the correction factor $\phi$ is the sole source of randomness affecting the particle dynamics

in the dilute regime. Hence, Langevin Eqs. (5.2) reduce to

$$\frac{\mathrm{d}\boldsymbol{X}_\mathrm{p}}{\mathrm{d}t} = \boldsymbol{U}_\mathrm{p}, \tag{5.5a}$$

$$\frac{\mathrm{d}\boldsymbol{U}_\mathrm{p}}{\mathrm{d}t} = \frac{\boldsymbol{u} - \boldsymbol{U}_\mathrm{p}}{\mathrm{St}}\phi(\mathrm{Re}_\mathrm{p}; \boldsymbol{\Xi}). \tag{5.5b}$$

Note that, here and below, all the physical quantities are dimensionless, even though we drop the tildes $\tilde{\cdot}$ to simplify the notation. While the general formulation of particle dynamics is given by stochastic ODEs (5.2), the model in Eqs. (5.5) is an example of ODEs with random coefficients. Regardless of this distinction, its solution are random processes $\boldsymbol{X}_\mathrm{p}(t)$ and $\boldsymbol{U}_\mathrm{p}(t)$, which are described by either their joint PDF $f_{\boldsymbol{XU}}(\boldsymbol{x}_\mathrm{p}, \boldsymbol{u}_\mathrm{p}; t)$ or, equivalently, by the joint cumulative distribution function $F_{\boldsymbol{XU}}(\boldsymbol{x}_\mathrm{p}, \boldsymbol{u}_\mathrm{p}; t) \equiv \mathbb{P}[\boldsymbol{X}_\mathrm{p}(t) \leq \boldsymbol{x}_\mathrm{p}, \boldsymbol{U}_\mathrm{p}(t) \leq \boldsymbol{u}_\mathrm{p}]$, where $\boldsymbol{x}_\mathrm{p}$ and $\boldsymbol{u}_\mathrm{p}$ are coordinates in the domain of definition of $\boldsymbol{X}_\mathrm{p}(t)$ and $\boldsymbol{U}_\mathrm{p}(t)$, $(\boldsymbol{x}_\mathrm{p}, \boldsymbol{u}_\mathrm{p}) \in \Omega_{\boldsymbol{XU}} \subset \mathbb{R}^d \times \mathbb{R}^d$. The derivation of a deterministic PDE for $F_{\boldsymbol{XU}}(\boldsymbol{x}_\mathrm{p}, \boldsymbol{u}_\mathrm{p}; t)$ or $f_{\boldsymbol{XU}}(\boldsymbol{x}_\mathrm{p}, \boldsymbol{u}_\mathrm{p}; t)$ would require a closure approximation [e.g., 218, 230]. Instead, we use the method of distributions to derive an exact deterministic (Liouville-type) PDE for the joint PDF, $f_{\boldsymbol{XU\Xi}}(\boldsymbol{x}_\mathrm{p}, \boldsymbol{u}_\mathrm{p}, \boldsymbol{\xi}; t) : \Omega_{\boldsymbol{XU}} \times \Omega_{\boldsymbol{\Xi}} \times \mathbb{R}^+ \to \mathbb{R}^+$, between the model's random inputs $\boldsymbol{\Xi}$ and outputs $\boldsymbol{X}_\mathrm{p}(t)$ and $\boldsymbol{U}_\mathrm{p}(t)$:

$$\frac{\partial f_{\boldsymbol{XU\Xi}}}{\partial t} + \boldsymbol{u}_\mathrm{p} \cdot \nabla_{\boldsymbol{x}_\mathrm{p}} f_{\boldsymbol{XU\Xi}} + \frac{1}{\mathrm{St}} \nabla_{\boldsymbol{u}_\mathrm{p}} \cdot \left[ (\boldsymbol{u} - \boldsymbol{u}_\mathrm{p}) f_{\boldsymbol{XU\Xi}} \sum_{i=1}^{N_\xi} \xi_i \psi_i(\|\boldsymbol{u} - \boldsymbol{u}_\mathrm{p}\|_2) \right] = 0. \tag{5.6}$$

We refer the reader to [2] for a complete derivation. It is worthwhile emphasizing that $\boldsymbol{x}_\mathrm{p}$, $\boldsymbol{u}_\mathrm{p}$, and $\boldsymbol{\xi}$ are deterministic coordinates spanning the domain $\Omega_{\boldsymbol{XU}} \times \Omega_{\boldsymbol{\Xi}}$. Thus, Eq. (5.6) is a deterministic linear PDE with variable coefficients, in which the derivatives are taken with respect to $\boldsymbol{x}_\mathrm{p}$ and $\boldsymbol{u}_\mathrm{p}$, and $\boldsymbol{\xi}$ plays the role of a parameter.

Equation (5.6) is subject to the initial condition

$$f_{\boldsymbol{XU\Xi}}(\boldsymbol{x}_\mathrm{p}, \boldsymbol{u}_\mathrm{p}, \boldsymbol{\xi}; 0) = f^{\mathrm{in}}_{\boldsymbol{XU\Xi}}(\boldsymbol{x}_\mathrm{p}, \boldsymbol{u}_\mathrm{p}, \boldsymbol{\xi}) = f^{\mathrm{in}}_{\boldsymbol{XU}}(\boldsymbol{x}_\mathrm{p}, \boldsymbol{u}_\mathrm{p}) f_{\boldsymbol{\Xi}}(\boldsymbol{\xi}), \tag{5.7}$$

with the latter equality reflecting the statistical independence between the initial state of the particle, $\boldsymbol{X}_{\rm p}(0)$ and $\boldsymbol{U}_{\rm p}(0)$, and the model parameters $\boldsymbol{\Xi}$. A functional form of $f^{\rm in}_{\boldsymbol{XU}}(\cdot)$ reflects the degree of uncertainty in the initial state. If the latter is known with certainty, $\boldsymbol{X}_{\rm p}(0) = \boldsymbol{x}^{\rm in}_{\rm p}$ and $\boldsymbol{U}_{\rm p}(0) = \boldsymbol{u}^{\rm in}_{\rm p}$, then $f^{\rm in}_{\boldsymbol{XU}}(\boldsymbol{x}_{\rm p}, \boldsymbol{u}_{\rm p}) = \delta(\boldsymbol{x}_{\rm p} - \boldsymbol{x}^{\rm in}_{\rm p})\delta(\boldsymbol{u}_{\rm p} - \boldsymbol{u}^{\rm in}_{\rm p})$, where $\delta(\cdot)$ is the $d$-dimensional Dirac delta function.

Let $\boldsymbol{y} = (\boldsymbol{x}_{\rm p}, \boldsymbol{u}_{\rm p}, \boldsymbol{\xi}) \in \Omega \equiv \Omega_{\boldsymbol{XU}} \times \Omega_{\boldsymbol{\Xi}}$ denote a point in the augmented phase space $\Omega \in \mathbb{R}^N$, which has dimension $N = 2d + N_\xi$. At any time $t$, the joint PDF $f_{\boldsymbol{XU\Xi}}(\boldsymbol{y}; t)$ in (5.11) and (5.12) has the following properties:

$$f_{\boldsymbol{XU\Xi}}(\boldsymbol{y}; t) \geq 0, \quad \forall\ \boldsymbol{y} \in \Omega; \qquad \int_\Omega f_{\boldsymbol{XU\Xi}}(\boldsymbol{y}; t) \mathrm{d}\boldsymbol{y} = 1. \tag{5.8}$$

The joint PDF $f_{\boldsymbol{XU\Xi}}(\boldsymbol{y}, t)$ typically has a compact support $\Omega_\epsilon \subset \Omega$,

$$\Omega_\epsilon(t) = \{\boldsymbol{y} : f_{\boldsymbol{XU\Xi}}(\boldsymbol{y}, t) \leq \epsilon\}, \tag{5.9a}$$

where the small positive constant $\epsilon$ is selected such that

$$\int_{\Omega_\epsilon} f_{\boldsymbol{XU\Xi}}(\boldsymbol{y}; t) \mathrm{d}\boldsymbol{y} \approx 1, \tag{5.9b}$$

with a prescribed accuracy.

## 5.3 Lagrangian solution of Liouville equation

We introduce a deterministic Lagrangian PDF formulation that traces the joint PDF and its support along characteristic lines of the Liouville equation. The MoC solution of Eq. (5.5) starts by treating the independent coordinates $\boldsymbol{x}_{\rm p}$ and $\boldsymbol{u}_{\rm p}$ as functions of time,

$\boldsymbol{x}_{\mathrm{p}}(t)$ and $\boldsymbol{u}_{\mathrm{p}}(t)$, so that the full time-derivative of $f_{\boldsymbol{XU\Xi}}(\boldsymbol{x}_{\mathrm{p}}(t), \boldsymbol{u}_{\mathrm{p}}(t), \boldsymbol{\xi}; t)$ is

$$\frac{\mathrm{d}f_{\boldsymbol{XU\Xi}}}{\mathrm{d}t} = \frac{\partial f_{\boldsymbol{XU\Xi}}}{\partial t} + \frac{\mathrm{d}\boldsymbol{x}_{\mathrm{p}}}{\mathrm{d}t} \cdot \nabla_{\boldsymbol{x}_{\mathrm{p}}} f_{\boldsymbol{XU\Xi}} + \frac{\mathrm{d}\boldsymbol{u}_{\mathrm{p}}}{\mathrm{d}t} \cdot \nabla_{\boldsymbol{u}_{\mathrm{p}}} f_{\boldsymbol{XU\Xi}}. \tag{5.10}$$

Comparing (5.10) with (5.6), we obtain equations for characteristics,

$$\frac{\mathrm{d}\boldsymbol{x}_{\mathrm{p}}}{\mathrm{d}t} = \boldsymbol{u}_{\mathrm{p}}, \tag{5.11a}$$

$$\frac{\mathrm{d}\boldsymbol{u}_{\mathrm{p}}}{\mathrm{d}t} = \boldsymbol{h}(\boldsymbol{x}_{\mathrm{p}}, \boldsymbol{u}_{\mathrm{p}}), \qquad \boldsymbol{h}(\boldsymbol{x}_{\mathrm{p}}, \boldsymbol{u}_{\mathrm{p}}) \equiv \frac{1}{\mathrm{St}}(\boldsymbol{u}(\boldsymbol{x}_{\mathrm{p}}, t) - \boldsymbol{u}_{\mathrm{p}}) \sum_{i=1}^{N_\xi} \xi_i \psi_i \left( \|\boldsymbol{u}(\boldsymbol{x}_{\mathrm{p}}, t) - \boldsymbol{u}_{\mathrm{p}}\|_2 \right), \tag{5.11b}$$

along with

$$\frac{\mathrm{d}f_{\boldsymbol{XU\Xi}}}{\mathrm{d}t} = -[\nabla_{\boldsymbol{u}_{\mathrm{p}}} \cdot \boldsymbol{h}(\boldsymbol{x}_{\mathrm{p}}, \boldsymbol{u}_{\mathrm{p}})] f_{\boldsymbol{XU\Xi}}. \tag{5.11c}$$

The system of ODEs (5.11) is subject to the initial conditions

$$\boldsymbol{x}_{\mathrm{p}}(0) = \boldsymbol{\eta}_x, \qquad \boldsymbol{u}_{\mathrm{p}}(0) = \boldsymbol{\eta}_u, \qquad f_{\boldsymbol{XU\Xi}}(\boldsymbol{x}_{\mathrm{p}}(0), \boldsymbol{u}_{\mathrm{p}}(0), \boldsymbol{\xi}, 0) = f^{\mathrm{in}}_{\boldsymbol{XU}}(\boldsymbol{\eta}_x, \boldsymbol{\eta}_u) f_{\boldsymbol{\Xi}}(\boldsymbol{\xi}), \tag{5.12}$$

where values of $(\boldsymbol{\eta}_x, \boldsymbol{\eta}_u) \in \mathbb{R}^{2d}$ label individual characteristics, with $\boldsymbol{\xi} \in \mathbb{R}^{N_\xi}$ acting as a parameter.

A flow-map representation of Eqs. (5.11) is presented in Appendix E. Numerical procedures used to solve these ODEs and to compute the marginals and moments of the joint PDF $f_{\boldsymbol{XU\Xi}}$ are outlined below.

## 5.4 Numerical implementation

Let $\mathcal{Y} = \{\boldsymbol{y}_1, \ldots, \boldsymbol{y}_{M_{\mathrm{tot}}}\}$ denote a collection of $M_{\mathrm{tot}}$ grid points used to discretize the hypercube $\Omega$. To simplify the presentation, we use the same number of points in each

dimension, $M$, so that

$$M_{\text{tot}} = M^N.$$

In Cartesian coordinates, for the $i$th component of vector $\boldsymbol{y}$ defined on the interval $y_i^{\min} \leq y_i \leq y_i^{\max}$, this tensorial grid is defined using, e.g., equispaced nodes

$$y_{ij_i} = y_i^{\min} + (y_i^{\max} - y_i^{\min})\frac{j_i - 1}{M - 1}, \tag{5.13a}$$

or the scaled Chebyshev-Gauss-Lobato (CGL) nodes

$$y_{ij_i} = y_i^{\min} + (y_i^{\max} - y_i^{\min})\frac{1}{2}\left[1 - \cos\left(\frac{j_i - 1}{M - 1}\pi\right)\right], \tag{5.13b}$$

with $i = 1, \ldots, N$ and $j_i = 1, \ldots, M$ for any $i$. The $(N+1)$-th tensor $y_{ij_i}$ has $NM^N$ entries and its rank is $(N + 1)$.

In this notation, the initial condition in Eq. (5.12) is discretized as

$$y_{ij_k} \equiv \begin{cases} \eta_{x_{j_k}} & \text{for} \quad i = 1, \ldots, d \\ \eta_{u_{j_k}} & \text{for} \quad i = d + 1, \ldots, 2d \\ \xi_{j_k} & \text{for} \quad i = 2d + 1, \ldots, N \end{cases} \tag{5.14a}$$

and

$$f_{\boldsymbol{XU\Xi}_{j_k}} = f^{\text{in}}_{\boldsymbol{XU}}(y_{ij_k}; i = 1, \ldots, 2d) f_{\boldsymbol{\Xi}}(y_{ij_k}; i = 2d + 1, \ldots, N), \tag{5.14b}$$

with $i, k = 1, \ldots, N$ and $j_k = 1, \ldots, M$ for any $k$.

In the Eulerian framework, the size of the hypercube $\Omega$, i.e., the values of $y_i^{\min}$ and $y_i^{\max}$ for $i = 1, \ldots, N$, are determined by the (truncated) domain of definition of the random variables $\boldsymbol{X}_{\text{p}}(t)$, $\boldsymbol{U}_{\text{p}}(t)$, and $\boldsymbol{\Xi}$. The size of $\Omega$ is sufficiently large to accommodate

the compact support of $f_{\boldsymbol{XU\Xi}}(\boldsymbol{y};t)$, $\Omega_\epsilon(t) \in \Omega$ in (5.9). At any time $t$, $\Omega$ includes regions of zero or negligibly small values of $f_{\boldsymbol{XU\Xi}}(\boldsymbol{y};t)$, e.g., along the $\boldsymbol{u}_\mathrm{p}$ [2] and $\boldsymbol{x}_\mathrm{p}$ coordinates as particles in turbulent environments exhibit preferential concentration [231] that are linked to attractors [232]. In the Lagrangian framework, we track the spatial evolution of $\Omega_\epsilon(t)$ by updating the support of the joint PDF given by the discrete locations stored in the tensor $y_{ij_i}$ and evolved in time with (5.11a)–(5.11b), and use $\Omega_\epsilon(t)$ as the computational domain. With the flow map notation introduced in the Appendix E, the time evolution of $\Omega_\epsilon(t)$ is given by the flow map $\mathcal{F}_{t_0}^t$. This localization reduces the simulation cost since the size of $\Omega_\epsilon(t)$ is significantly smaller than the size of $\Omega$. This saving alleviates the curse of dimensionality, which plagues numerical solutions of high-dimensional Eulerian PDEs like Eq. (5.6).

On the discretized domain $\Omega_\epsilon$, we use the third-order total variation diminishing (TVD) Runge-Kutta method [175] to solve ODEs (5.11) with the initial condition (5.14). Post-processing of the resulting solution $f_{\boldsymbol{XU\Xi}}(\boldsymbol{y};t)$ yields statistical moments of $\boldsymbol{X}_\mathrm{p}(t)$ and $\boldsymbol{U}_\mathrm{p}(t)$ and marginal PDFs, e.g., $f_{\boldsymbol{X}}(\boldsymbol{x}_\mathrm{p};t)$ and $f_{\boldsymbol{U}}(\boldsymbol{u}_\mathrm{p};t)$.

### 5.4.1 Computation of moments

A numerical solution to Eqs. (5.11a) and (5.11b) yields the flow map $\boldsymbol{y}(t) = \mathcal{F}_0^t(\boldsymbol{\eta}_x, \boldsymbol{\eta}_u, \boldsymbol{\xi})$, while a numerical solution to Eq. (5.11c) yields the flow map $f_{\boldsymbol{XU\Xi}}(\boldsymbol{y};t) = \mathcal{Z}_0^t(\boldsymbol{y}(t), f_{\boldsymbol{XU}}^\mathrm{in}, f_{\boldsymbol{\Xi}})$ (see Appendix E). Given these maps, the ensemble averages of the

particle position and velocity, $\bar{\boldsymbol{X}}_{\mathrm{p}}(t)$ and $\bar{\boldsymbol{U}}_{\mathrm{p}}(t)$, are evaluated as

$$\begin{aligned}\bar{X}_{\mathrm{p}i} &= \int_{\Omega_\epsilon} x_{\mathrm{p}i} f_{\boldsymbol{XU\Xi}}(\boldsymbol{y};t) J \mathrm{d}\boldsymbol{\eta}_x \mathrm{d}\boldsymbol{\eta}_u \mathrm{d}\boldsymbol{\xi} \\ &\approx \sum_{j_1=1}^{M} \cdots \sum_{j_N=1}^{M} w_{j_1} \cdots w_{j_N} y^n_{i,j_1,\ldots,j_N} J^n_{j_1,\ldots,j_N} f^n_{\boldsymbol{XU\Xi} j_1,\ldots,j_N},\end{aligned} \tag{5.15a}$$

$$\begin{aligned}\bar{U}_{\mathrm{p}i} &= \int_{\Omega_\epsilon} u_{\mathrm{p}i} f_{\boldsymbol{XU\Xi}}(\boldsymbol{y};t) J \mathrm{d}\boldsymbol{\eta}_x \mathrm{d}\boldsymbol{\eta}_u \mathrm{d}\boldsymbol{\xi} \\ &\approx \sum_{j_1=1}^{M} \cdots \sum_{j_N=1}^{M} w_{j_1} \cdots w_{j_N} y^n_{i+d,j_2,\ldots,j_N} J^n_{j_1,\ldots,j_N} f^n_{\boldsymbol{XU\Xi} j_1,\ldots,j_N},\end{aligned} \tag{5.15b}$$

for $i = 1, \ldots, d$, and $j_k = 1, \ldots, M$ for any $k = 1, \ldots, N$. Time has been discretized by $t_n = n\Delta t$, with $n = 0, \ldots, N_t$ and $\Delta t = t/(N_t - 1)$. The weights $w_{j_k}$ correspond to the trapezoidal rule. Here, $J$ is the determinant of the Jacobian of the mapping of the initial grid, $\boldsymbol{y}(0) = (\boldsymbol{\eta}_x, \boldsymbol{\eta}_u, \boldsymbol{\xi})$, onto its counterpart at time $t$, $\boldsymbol{y}(t) = (\boldsymbol{x}_{\mathrm{p}}(t), \boldsymbol{u}_{\mathrm{p}}(t), \boldsymbol{\xi})$:

$$J = |\boldsymbol{J}| = \left| \frac{\partial \boldsymbol{y}(t)}{\partial \boldsymbol{y}(0)} \right|, \tag{5.16}$$

Its finite-differences approximation for interior points is

$$J^n_{j_k} = \begin{vmatrix} \frac{y^n_{1,j_1+1,j_2,\ldots} - y^n_{1,j_1-1,j_2,\ldots}}{y^0_{1,j_1+1,j_2,\ldots} - y^0_{1,j_1-1,j_2,\ldots}} & \cdots & \frac{y^n_{k,j_1+1,j_2,\ldots} - y^n_{k,j_1-1,j_2,\ldots}}{y^0_{1,j_1+1,j_2,\ldots} - y^0_{1,j_1-1,j_2,\ldots}} & \cdots & \frac{y^n_{N,j_1+1,j_2,\ldots} - y^n_{N,j_1-1,j_2,\ldots}}{y^0_{1,j_1+1,j_2,\ldots} - y^0_{1,j_1-1,j_2,\ldots}} \\ \vdots & \ddots & & & \vdots \\ \frac{y^n_{1,\ldots,j_k+1,\ldots} - y^n_{1,\ldots,j_k-1,\ldots}}{y^0_{k,\ldots,j_k+1,\ldots} - y^0_{k,\ldots,j_k-1,\ldots}} & & \frac{y^n_{k,\ldots,j_k+1,\ldots} - y^n_{k,\ldots,j_k-1,\ldots}}{y^0_{k,\ldots,j_k+1,\ldots} - y^0_{k,\ldots,j_k-1,\ldots}} & & \\ \vdots & & & \ddots & \\ \frac{y^n_{1,\ldots,j_N+1,\ldots} - y^n_{1,\ldots,j_N-1}}{y^0_{N,\ldots,j_N+1} - y^0_{N,\ldots,j_N-1}} & \cdots & & & \frac{y^n_{N,\ldots,j_N+1,\ldots} - y^n_{N,\ldots,j_N-1}}{y^0_{N,\ldots,j_N+1} - y^0_{N,\ldots,j_N-1}} \end{vmatrix}, \tag{5.17}$$

with a proper modification for points on the boundaries of $\Omega_\epsilon(t)$. The discrete values of the support and joint PDF in (5.15) are advected with the flow maps $\mathcal{F}_0^{t_n}$ and $\mathcal{Z}_0^{t_n}$ in tonsorial form from the initial time to the posterior time $t_n$.

### 5.4.2 Computation of marginals

The computation of marginals consist in reducing the dimensionality of the joint PDF along the marginalized dimensions. We particularly describe here the marginalization along the $k$-th dimension of the joint PDF. Then, the resulting marginal PDF depends on the reduced phase space vector, defined by $\hat{\boldsymbol{y}} = (y_1, \ldots, y_{k-1}, y_{k+1}, y_N) \in \Omega_\epsilon^k$, with $\Omega_\epsilon^k \in \mathbb{R}^{N-1}$. The marginal along the $k$-th dimension can be defined as $f_{\hat{\boldsymbol{y}}}(\hat{\boldsymbol{y}}; t) : \Omega_\epsilon^k \times \mathbb{R}^+ \to \mathbb{R}^+$. The integration to marginalize the joint PDF is performed by defining first an interpolator operator $\mathcal{I}(\boldsymbol{y}, f_{\boldsymbol{XU\Xi}}, \mathbf{y}) : \Omega_\epsilon \times \mathbb{R}^+ \times \Omega_\epsilon \to \mathbb{R}^+$ that takes a Lagrangian solution given by $\boldsymbol{y}$ and $f_{\boldsymbol{XU\Xi}}$, evolved in time with the corresponding flow maps (see Appendix E), and interpolates it to a new tensorial grid that is aligned with the coordinate system. This new tensorial grid is defined by

$$y^n_{Cij_i} = \min(y^n_{ij_i}) + \left[\max(y^n_{ij_i}) - \min(y^n_{ij_i})\right] \frac{j_i - 1}{M - 1}, \tag{5.18}$$

which is equispaced, and contains the support of the joint PDF given in the scattered discrete grid $y^n_{ij_i}$ and also has $M$ points along each dimension. Then, the joint PDF is interpolated to the new tensorial grid by

$$\mathrm{f}^n_{\boldsymbol{XU\xi}_{j_i}} = \mathcal{I}(y^n_{ij_i}, f^n_{\boldsymbol{XU\xi}_{j_i}}, y^n_{Cij_i}), \tag{5.19}$$

and the marginal along the $k$-th dimension is computed as

$$f^n_{\hat{\boldsymbol{y}}_{j_m}}(y^n_{Cij_m}; t_n) \approx \int_{\min(y^n_{kj_i})}^{\max(y^n_{kj_i})} \mathrm{f}_{\boldsymbol{XU\Xi}}(\boldsymbol{y}; t) dy_k \approx \sum_{j_k=1}^{M} w_{j_k} \mathrm{f}^n_{\boldsymbol{XU\Xi}_{j_1,\ldots,j_k,\ldots,j_N}}, \tag{5.20}$$

where $m = 1, \ldots, N-1$ and $j_i = 1, \ldots, M$, for any $i = 1, \ldots, N$; with the trapezoidal rule applied in the grid aligned with the coordinates along the $k$-th dimension. We note that the interpolator $\mathcal{I}$ can be for example the linear staggered interpolant defined in `griddata`

or `scatteredInterpolant` in MATLAB or `griddata` in the SciPy Python library. The interpolated values of the joint PDF in the new grid that lie outside of the hypercube defined by the grid $y^n_{ij_i}$ are assigned to zero because they are outside of the compact support of the joint PDF (5.9). By successively integrating along the remaining dimensions, other marginals can be computed.

### 5.4.3 Spectral methods to compute moments and marginals

To compute the moments and marginals with high-order schemes we use the method described in [229, 233] where high-order computations of FTLE were presented. We start by defining tensorial Lagrange interpolant of order, $Q = M - 1$, in $N$ dimensions on an orthogonal unit hypercube as follows

$$P^Q(\boldsymbol{\zeta}) = \sum_{j_1=1}^{M} \cdots \sum_{j_N=1}^{M} l_{j_1}(\zeta_1) \cdots l_{j_N}(\zeta_N) = 1, \tag{5.21}$$

with $\zeta_k \in [0, 1]$ with $k = 1, \ldots, N$ and $j_k = 1, \ldots, M$ for any $k$. In (5.21), each $l_j$ is the one-dimensional Lagrange polynomial defined by

$$l_j(\zeta) = \prod_{i=1,\ i\neq j}^{M} \frac{\zeta - \zeta_i}{\zeta_j - \zeta_i}. \tag{5.22}$$

Notice that by construction $\sum_{j_k=1}^{M} l_{j_k}(\zeta_k) \equiv 1$ for any $k$. As before, we have used the same number of points $M$ along each dimension.

For a two- and three-dimensional augmented phase space, i.e., for $N = 2$ with $\boldsymbol{y} = (y_1, y_2) = (x_\mathrm{p}, u_\mathrm{p})$ or $N = 3$ with $\boldsymbol{y} = (y_1, y_2, y_3) = (x_\mathrm{p}, u_\mathrm{p}, \xi)$ respectively, a single element $\mathcal{D} \subset \Omega_\epsilon(t)$ is mapped into the unit square or cube respectively by the mapping

$$\boldsymbol{y} = \boldsymbol{\Theta}(\boldsymbol{\zeta}) : \mathbb{R}^N \to \mathbb{R}^N,$$

which are given in the Appendix F for both cases. At the initial time, the element is initialized with the tensorial grid (5.13b) which map to the quadrature points in computational space by $y_{ij_i} = \boldsymbol{\Theta}(\zeta_{ij_i})$. See Appendix F for $N = 2$ and $N = 3$. For readability and clearness, we remove the first index in the notation by expressing the symbol in bold and consider hereafter $N = 3$ such that the mapping of the grid points can be expressed as $\boldsymbol{y}_{ijk} = \boldsymbol{\Theta}(\boldsymbol{\zeta}_{ijk})$, with $i, j, k = 1, \ldots, M$. Then, we define $Q$-th polynomial approximation of $\boldsymbol{y}$ in the element $\mathcal{D}$ at the time $t$ by

$$\boldsymbol{y} \approx \boldsymbol{y}^Q(\boldsymbol{\zeta}; t) = \sum_{i=1}^{M}\sum_{j=1}^{M}\sum_{k=1}^{M} \boldsymbol{y}_{ijk} l_i(\zeta_1) l_j(\zeta_2) l_k(\zeta_3), \tag{5.23}$$

where the explicit notation of time has been dropped but the nodal values $\boldsymbol{y}_{ijk}$ are the corresponding quadrature nodes in physical space at the current time $t$, computed with the flow map $\mathcal{F}_0^t$. Similarly, the joint PDF mapped with the flow map $\mathcal{Z}_0^t$ is approximated by

$$f_{XU\Xi} \approx f^Q_{XU\Xi}(\boldsymbol{\zeta}; t) = \sum_{i=1}^{M}\sum_{j=1}^{M}\sum_{k=1}^{M} f_{XU\Xi ijk} l_i(\zeta_1) l_j(\zeta_2) l_k(\zeta_3). \tag{5.24}$$

At the initial time, points in the phase space are initialized at the quadrature nodes, $\boldsymbol{y}_{0ijk}$, corresponding to $\boldsymbol{\zeta}_{ijk}$ in computational domain with the mapping $\boldsymbol{y}_{0ijk} = \boldsymbol{\Theta}(\boldsymbol{\zeta}_{ijk})$ (see Figs. 5.1a and 5.1c for the case $N = 2$). For a later time $t$, the points in physical domain are mapped with $\boldsymbol{y}_{ijk} = \mathcal{F}_0^t(\boldsymbol{y}_{0ijk})$ (see Fig. 5.1b). To find the corresponding points in computational space to $\boldsymbol{y}_{ijk}$, we apply the inverse of the transfinite mapping function $\boldsymbol{\Theta}$ with the Newton-Raphson method using the quadrature nodes as initial guess because the map $\boldsymbol{\Theta}$ does not have analytical explicit inverse. The result may be expressed formally as $\boldsymbol{\zeta}'_{ijk} = \boldsymbol{\Theta}^{-1}(\boldsymbol{y}_{ijk})$, where the locations in computational space do not coincide with the quadrature nodes such that $\boldsymbol{\zeta}'_{ijk} \neq \boldsymbol{\zeta}_{ijk}$ except along the boundaries. The quadrature points in physical space at time $t$ denoted by $\boldsymbol{y}'_{ijk}$ have to be found via iteration using

the interpolant defined with the unknown quadrature nodes $\boldsymbol{y}'_{ijk}$ evaluated at the known locations $\boldsymbol{y}_{ijk}$ which map to $\boldsymbol{\zeta}'_{ijk}$ such that one has

$$\boldsymbol{y}_{lnm} = \sum_{i=1}^{M}\sum_{j=1}^{M}\sum_{k=3}^{M} \boldsymbol{y}'_{ijk} l_i(\zeta'_{1lmn}) l_j(\zeta'_{2lmn}) l_k(\zeta'_{3lmn}), \tag{5.25}$$

with $l, m, n = 1, \ldots, M$ indices along the evaluation and $i, j, k = 1, \ldots, M$ to construct the interpolant. In matrix-vector form this can be expressed as

$$\hat{y}_q = \hat{y}'_p I_{pq}, \tag{5.26}$$

where $I_{pq}$ is the interpolation matrix

$$I_{pq} = l_i(\zeta_{1lmn}) l_j(\zeta_{2lmn}) l_k(\zeta_{3lmn}), \tag{5.27}$$

and $\hat{y}_p$ and $\hat{y}'_p$ are contiguously aligned so that $p = iM^2 + jM + k$ and $q = lM^2 + mM + n$. By inverting (5.26) we have

$$\hat{y}'_p = I^{-1}_{pq} \hat{y}'_q. \tag{5.28}$$

The locations $\hat{y}'_p$ are based on an orthogonal, tensorial, quadrature grid and forms the basis at time $t$. Similarly, we interpolate the map of the joiont PDF by applying the same interpolation matrix

$$\hat{f}'_{XU\Xi p} = I^{-1}_{pq} \hat{f}_{XU\Xi q}, \tag{5.29}$$

where both $\hat{y}'_p$ and $\hat{f}'_{XU\Xi q}$ are defined at the quadrature nodes and thus suited for the computation of the Jacobian $\mathcal{J} = |\partial \boldsymbol{y} / \partial \boldsymbol{\zeta}|$ with the use of the mapping function $\boldsymbol{\Theta}$. The moments and marginals for $N = 3$ are computed in Appendix G, following the

same procedure from Sections 5.4.1 and 5.4.2 adapted for our high-order technique. The latter's use to compute the Jacobian for $N = 2$ and $N = 3$ is described in [229, 233]; the quadratures using the single-element high-order descriptors are our innovation.

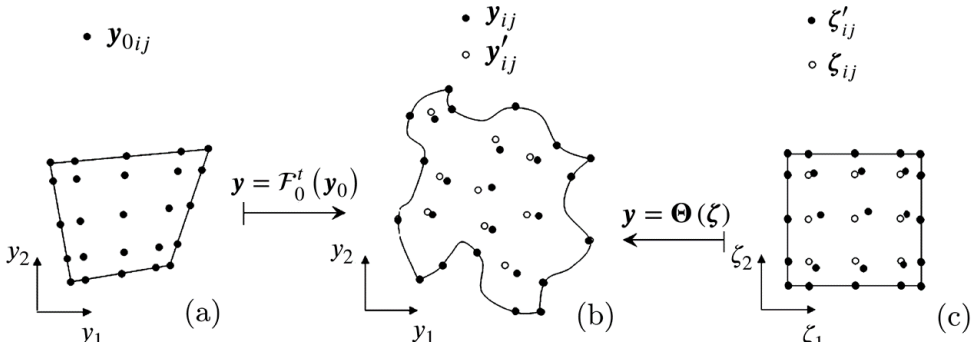


**Figure 5.1.** Computation of flow maps in (a) an element at initial time $t = 0$, (b) the element at a later time $t > 0$, and (c) the mapped element to computational space for $N = 2$. The mapped points in computational space for time $t = 0$, $\boldsymbol{\zeta}_{ij}$, are the quadrature nodes. At $t > 0$, the element in physical space is mapped by $\boldsymbol{y}_{ij} = \mathcal{F}_0^t(\boldsymbol{y}_{0ij})$; except for the boundary points, the mapped points in the computational space are not the quadrature points. They are found using the Newton-Raphson method to invert the mapping function $\boldsymbol{\Theta}$, such that $\boldsymbol{\zeta}'_{ij} = \boldsymbol{\Theta}^{-1}(\boldsymbol{y}_{ij})$, with $\boldsymbol{\zeta}'_{ij} \neq \boldsymbol{\zeta}_{ij}$. The quadrature nodes at the later time in physical space $\boldsymbol{y}'_{ij}$ are found via the interpolation scheme from [229, 233].

The number of degrees of freedom to march in time when using the MoC is $D_{\mathrm{L}} = (N + 1)M^N$. In the Eulerian formulation, the number of degrees of freedom is $D_{\mathrm{E}} = M^N$. However, the localized Lagrangian domain $\Omega_\epsilon(t)$ is much smaller than the Eulerian domain $\Omega$. Hence, for similar accuracy, the number of points per dimension in the Lagrangian approach ($M_{\mathrm{L}}$) is smaller than that in the Eulerian approach ($M_{\mathrm{E}}$). If $M_{\mathrm{E}} = cM_{\mathrm{L}}$ with the constant $c > 1$, the number of degrees of freedom in both approaches is related by

$$D_{\mathrm{E}} = \frac{c^N}{N+1} D_{\mathrm{L}}.$$

The numerical experiments presented below and in in [2] show an order of magnitude difference between $M_{\mathrm{E}}$ and $M_{\mathrm{L}}$ i.e., $c \approx 10$. Additionally, our Lagrangian method requires a numerical solution to ODEs, whereas the corresponding Eulerian formulation solves a high-dimensional hyperbolic PDE; the latter needs filtering and regularization techniques,

which increase the computational effort.

## 5.5 Numerical experiments

We conduct a series of numerical experiments to demonstrate the salient features of our Lagrangian PDF method.

### 5.5.1 Deterministically forced particles

**Test 1: smooth functions.**

The first test case is dedicated to study the numerical properties of the Lagrangian approach for cases with periodic smooth functions. We define the initial condition with Gaussian distributions corresponding to a Maxwellian state of the particles in phase space $x_p - u_p$, in a one-dimensional problem $d = 1$ with deterministic forcing $\phi = 1$. This two-dimensional augmented phase space $N = 2$ suffices for this purpose, whose numerical characteristics are applicable for solutions described by smooth periodic functions in higher dimensions. The particle phase solution is then fully described by the joint PDF $f_{XU}$. Deterministic Stokes drag forcing is suitable for a particle phase with low particle Reynolds numbers. The chosen flow corresponds to the stagnation flow as defined by [176] for which the MoC admits analytical solution of the Lagrangian PDF model (see Appendix H). In the horizontal direction $x$, the stagnation flow is defined by $u = -\kappa x$, with $\kappa$ a constant taken to be unity here. We test the Lagrangian framework for low-order (linear for interpolation, second order for integration) and high-order (spectral for interpolation and integration) schemes. Additionally, for validation and comparison, we use the MC-PSIC method and the Eulerian solver developed in [2] based on Chebyshev spectral collocation method to solve the Eulerian PDF equation.

A particle particle cloud is initialized with a bivariate Normal distribution at the average particle location and velocity $(\bar{X}_{\mathrm{p}0},\ \bar{U}_{\mathrm{p}0}) = (-1, 1)$ with standard deviations $\sigma_{X_{\mathrm{p}0}} = \sigma_{U_{\mathrm{p}0}} = 0.05$. At the initial time, the particle position and velocity are statistically

independent such that $f_{XU}^{\text{in}}(x_{\text{p}}, u_{\text{p}}) = f_X^{\text{in}}(x_{\text{p}}) f_U^{\text{in}}(u_{\text{p}})$, with $X_{\text{p0}} \sim \mathcal{N}(\bar{X}_{\text{p0}}, \sigma^2_{X_{\text{p0}}})$ and similarly for $U_{\text{p0}}$. The Stokes number is $St = 1$ such that the inertial effects are dominant in the particle dynamics. In the Lagrangian approach, the definition of the compact support requires clipping of the initial condition to an interval defined by $[-5\sigma,\ 5\sigma]$ per dimension.

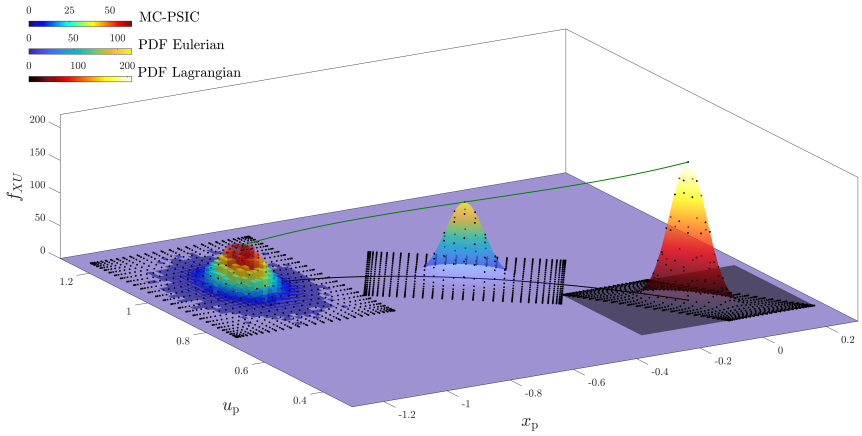


**Figure 5.2.** Joint PDF $f_{XU}$ for Test 1 computed with MC-PSIC, the Eulerian PDF approach and the Lagrangian PDF approach with high-order schemes for three different times $t = [0\ 0.6\ 1.2]$. At the initial time, the MC-PSIC solution is represented for a reconstructed solution with $30 \times 30$ bins. At the second time the Eulerian solver is used to plot the solution, defined in the domain $\Omega$ with a $401 \times 401$ Chebyshev grid (see [2]). At the final time, the Lagrangian PDF solution is depicted with a spectral interpolant based on a $31 \times 31$ grid (also depicted in the previous times). The time evolution of the maximum is analytically traced with the MoC (green continuous line).

In the MC-PSIC method, a sampled initial condition composed by $N_s = 10^6$ point-particles is evolved in time with (5.5). The convergence error is known to be proportional to $1/\sqrt{N_s}$, requiring a high number of samples to be reduced. At any given time, the joint PDF is reconstructed by dividing the domain in cells or bins and counting the particles per cell. However, the solution is conditioned to minimum amount of particles per cell required. We ensure that there are at least ten particles per cell. For a given sampled solution, this leads to solution dependency on the number of cells employed. Without the use of kernels to smooth the resulting PDF, which are dependent on an optimal bandwidth [234, 235], the solution is discontinuous (see Figure 5.2).

As an alternative to MC-PSIC that does not rely on sampling, we solve the Eulerian PDF equation (5.6). This particularly requires the use of high-order discretization techniques as discussed in [2]. The PDF equation admits discontinuous solutions for two distinct reasons. The initial condition may include discontinuities as for example if deterministic initial conditions or Uniform distributions are considered, or independently of the initial condition, the solution may evolve to situations in which particles concentrate in a small region in phase space and/or travel at a similar (or equal) speed, leading to high gradients in the PDFs. Because of these reasons, filtering and regularization techniques may be needed to solve the PDF equation in Eulerian form. In Figure 5.2, we show the Eulerian PDF solution at an intermediate time where the domain $\Omega$ is defined to cover all possible trajectories form initial to final time. Because the joint PDF is smooth enough, filtering and regularization are not needed in this particular test case to keep the solution stable. For the same reason, Gibbs oscillations do not condition the accuracy of the solution.

The Lagrangian framework offers additional advantages. In addition to the independence of sampling errors, it improves upon its Eulerian counterpart because of the simplification of the governing equations from PDEs to ODEs. As a result, it is unaffected by the CFL stability condition for time integration according to a given grid. The spatial accuracy however when evaluating the interpolant is subjected to interpolation errors despite the fact that for traced points the only error to consider is related to time integration. We show in Figure 5.2 at the final time, the interpolated solution in a refined grid and the nodes that compose the spectral interpolant. The solution in Lagrangian form follows the particle cloud with its movement, reducing the size of the domain $\Omega_\epsilon(t)$ needed to compute the solution at a given time, that only covers the region surrounding non–zero values of the joint PDF. Moreover, events of interest may be traced independently along time in the phase space. A comparison of the time evolution of the maximum and minimum of the joint PDF with the three approaches used is shown in Figure 5.3a. The MC-PSIC method

leads to noisy solutions and dependency on the number of cells used to reconstruct the joint PDF. The Eulerian approach, provides an accurate solution particularly when the solution is smooth. For comparison, we also show a filtered solution where overshoots and undershoots appear compromising the local accuracy of the solution and violating the non-negativity condition of PDFs. The Lagrangian approach however, may be used to track that single event instead, reducing the problem to the computation of a single ODE which gives the exact analytical solution. For example the point with maximum probability is $f_{XU}^{\max} = f_X^{\text{in}}(-1) f_U^{\text{in}}(1) e^{t/\text{St}}$ depicted also in Figure 5.2.

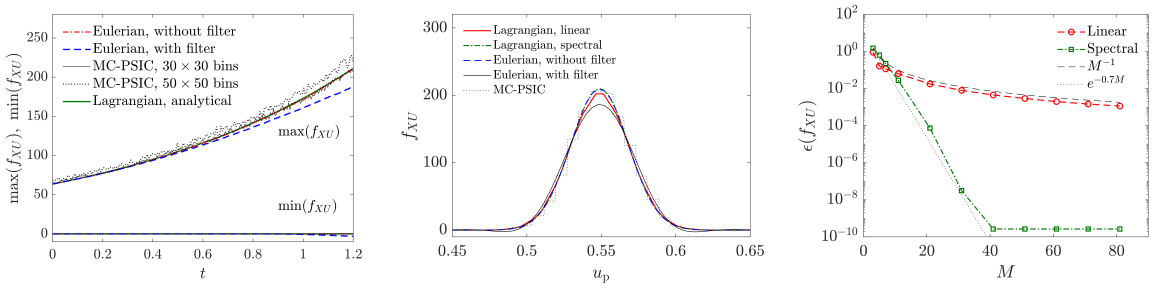


**Figure 5.3.** Numerical results for Test 1. In (a) the time evolution of the maxima and minima of the joint PDF $f_{x_p u_p}$ computed with MC-PSIC, the Eulerian solver with and without filtering and regularization, and the Lagrangian solver; in (b) the comparison of the joint PDF along the line $X_p = 0$ at the final time $t = 1.2$ for the different methods and in (c) the convergence of the interpolant of the joint PDF for the Lagrangian approach with a linear and spectral scheme.

The evaluation of the joint PDF along lines provides also additional insights. Figure 5.3b shows the solution at the final time along the line $x_\text{p} = 0$. The MC-PSIC solution is discontinuous with constant values of the joint PDF within each cell as opposed to the PDF approaches. The Eulerian solution is shown for both cases, with and without filtering where the effect of the filter is shown to smoothen the function, reducing its maximum and minimum (see also Figure 5.3a). The Lagrangian solution with a spectral scheme is shown to accurately reproduce the results of the Eulerian solver with a grid composed by only $21 \times 21$ points in the $x_\text{p} - u_\text{p}$ space. When using the linear interpolant

however, the matching is less accurate and straight lines near the maximum where the curvature of the solution is larger can be appreciated. However, considering the computational savings as compared with the Eulerian solver that employs a $401 \times 401$ grid, the Lagrangian approach is more convenient computationally. The convergence of the interpolated Lagrangian solution with the different numerical schemes is as expected, linear and spectral accordingly (Figure 5.3c). For very low number of nodes, $M < 7$, the linear interpolant exhibits less error than the spectral interpolant. The use of only a few nodes in the spectral interpolant causes the global representation the solution to be given by a polynomial of not enough order and oscillations between nodes are expected when evaluating the interpolant. However, for $M > 7$, the spectral interpolation is more accurate as a result of its rapid convergence. For only $M = 21$ nodes, the spectral interpolant is already several orders of magnitudes more accurate than the linear for the same amount of points. This global representation leads to an error distribution within the domain, as it can be seen in Figure 5.4, as opposed to linear case where the error is localized near areas of high curvature in the solution.

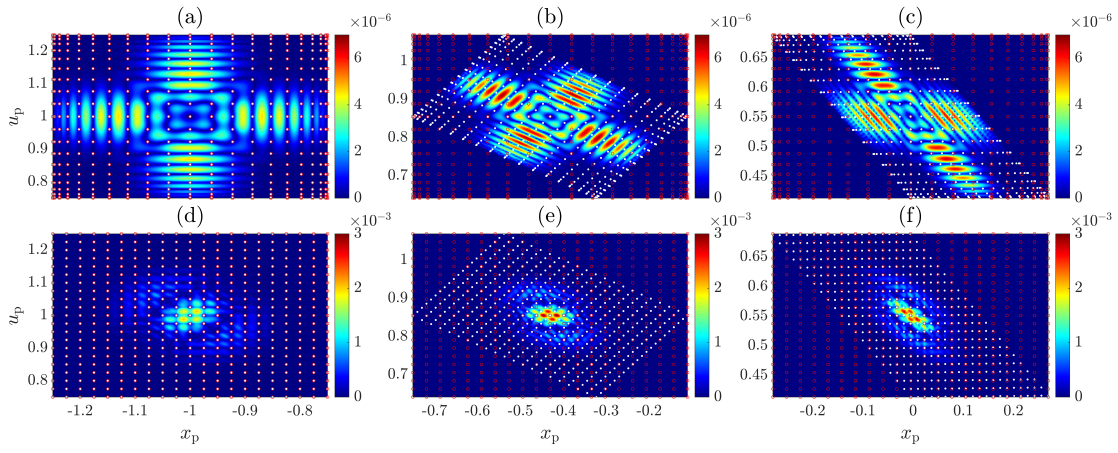


**Figure 5.4.** Errors for Test 1 for the Lagrangian approach using a spectral interpolant (a)–(c) and linear interpolant (d)–(f) for times $t = [0\ 0.6\ 1.2]$. The red dots represent the grid aligned with the axis used for the marginalization step where the solution is interpolated from the non-aligned grid (white dots).

Concerning the computation of marginals, we proceed by defining a container element aligned with the axis (Fig. 5.4) and interpolating the solution to it to later integrate. For a marginally resolved case, with only $M = 11$, we observe good agreement between MC-PSIC and the linear interpolant, whereas the spectral one shows discrepancies (see Figure 5.5a). This is also the case for the marginal $f_U$ (not shown). However, for a small increase of the number of nodes to $M = 21$ (Fig. 5.5b), the spectral interpolant is already much more accurate as a result of its exponential convergence, similar to the analysis to the two-dimensional interpolant of $f_{XU}$ (see Figures 5.3c and 5.4). It is worth mentioning that the trapezoidal rule also experiences exponential convergence at low number of points (Fig. 5.5c), related to the periodicity of the solution [236], for which its convergence is given by the convergence of the Fourier approximation of the function to integrate with the number of modes considered. This unusual situation enhances the general second order convergence of the trapezoidal rule which is shown after the number of nodes exceeds a threshold (about $M \approx 11$ in this case). The Clenshaw Curtis quadrature on the other hand, shows exponential convergence once the asymptotic regime is reached, leading to a better approximation than the trapezoidal rule for $M > 21$.

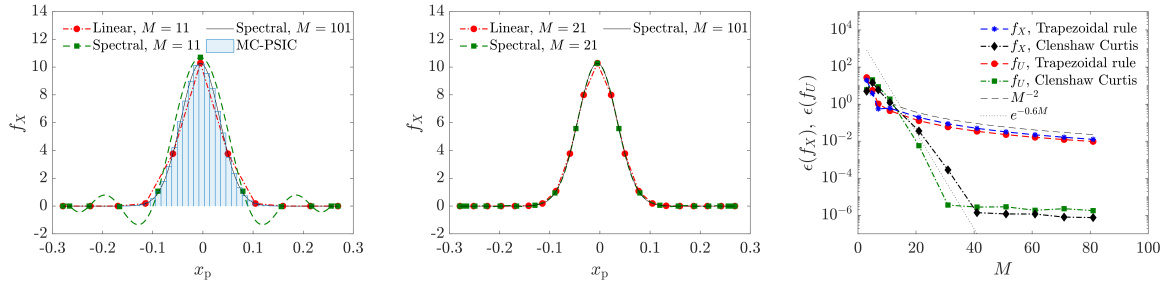


**Figure 5.5.** Results for deterministically forced test case with periodic functions. Marginals computed with (a) $M = 11$ nodes and (b) $M = 21$ nodes with the Lagrangian approach using the linear and spectral interpolants compared with MC-PSIC, and in (c) the convergence with the number of nodes of both interpolants. The linear interpolant is combined with the Trapezoidal rule and the spectral with Clenshaw Curtis to perform the integrals to marginalize.

The first and second moments of the joint PDF may also be computed with the different approaches presented. If they are computed with the MC-PSIC method, the convergence of the moments with the number of samples scales at the slow rate of $1/\sqrt{N_s}$. The Eulerian PDF approach may also be used to compute moments where if filtering is used, the vanishing moment condition of the regularized Dirac delta employed in the kernels of the filter [74], conditions the amount of moments that the solution accurately preserves along time [2]. In the Lagrangian framework, we compute the moments with both, a low and high-order scheme. In the Lagrangian approach, the computation of moments is performed by integrating along all dimensions using the corresponding Jacobian. We find that the trapezoidal rule also exhibits exponential convergence for low nuumber of points and second order convergence after a threshold. The Clenshaw Curtis quadrature maintains spectral convergence once the asymptotic regime is reached until machine precision error is found (Figure 5.6). The clipping of the initial condition prevents the periodicity of the solution because the derivatives on the extremes of the Gaussian functions are not exactly zero. According to that, if less clipping is applied to the initial condition, the trapezoidal rule is expected to be more accurate. Extending the interval in which we clip the initial condition to $[-7\sigma,\ 7\sigma]$, the exponential convergence of the trapezoidal rule is consistently extended and becomes more accurate for increasing number of nodes (Fig. 5.6, dark red curve). For low number of nodes however, the errors are higher as compared to the more clipped solution as a result of the extension of the interval to approximate the solution (for the same amount of points per direction).

**Test 2: non-smooth functions.**

The second test case is dedicated to solutions with high gradients or in general non-smooth functions. We select the same setup as for the previous case but the initial

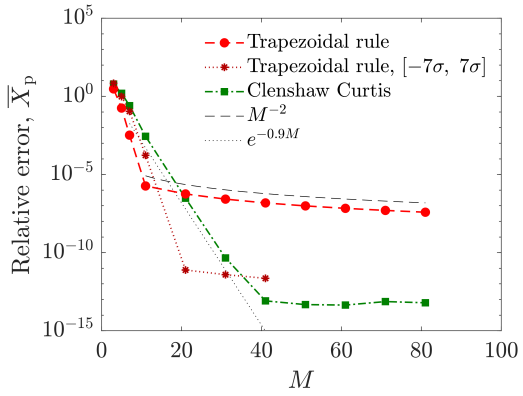


**Figure 5.6.** Convergence of the moments with the number of nodes for the deterministically forced case for periodic functions computed with the Lagrangian approach with linear and spectral schemes combined with the Trapezoidal Rule and Clenshaw Curtis respectively.

condition is defined with Uniform distribution functions such that

$$X_{\mathrm{p}0} \sim \mathcal{U}(\bar{X}_0 - \sqrt{3}\sigma_{X_{\mathrm{p}0}},\ \bar{X}_{\mathrm{p}0} + \sqrt{3}\sigma_{X_{\mathrm{p}0}}),$$

and similarly for the velocity, with the same average values and standard deviations $\sigma_{X_{\mathrm{p}0}} = \sigma_{U_0} = 0.1$. The initial condition then is defined with compact support in the interval where the Uniform distributions have a non-zero value. Therefore, the initial element is defined without clipping the joint PDF.

For the non-smooth initial condition that presents sharp gradients, the Eulerian PDF approach requires filtering and regularization to be stable. At any given time, the solution is smoothen by the filtering operation and as a result of the high gradients, Gibbs oscillations appear, where overshoots and undershoots compromise the local accuracy of the solution. A full review in detail of the Eulerian approach was carried out in [2]. The convergence of the filtered solution far from regions of sharp gradients, is defined by the vanishing moment conditions of the kernels used in the filtering [73, 74]. When using MC-PSIC, the solution can also be reconstructed similarly to the previous test case by dividing the domain in cells and reconstructing the PDF. The presence of gradients are

related to adjacent cells with a high disparity of samples. For the Lagrangian approach, the interpolants are affected by the smoothness of the solution when the solution is interpolated or integrated. However, the tracing of single events in the parameter space is not affected by the presence of high gradients, being possible to trace analytically the solution for this test case as for the previous one. In Figure 5.7a, the tracing of the maximum and minimum of the joint PDF is compared with MC-PSIC and the Eulerian solver. The MC-PSIC solution is dependent on the number of samples. The Eulerian filtered solution locally modifies the joint PDF, preventing the solution to preserve the non-negativity condition of PDFs. This leaves the Lagrangian approach as the only alternative to maintain local accuracy with independence of the presence of high gradients in the solution.

This also translates to the evaluation of the interpolants traced with the Lagrangian approach. The comparison along a line $x_{\mathrm{p}} = 0$ at the final time of the joint PDF is shown in Figure 5.7b. The Eulerian solution (with regularization and filtering) shows oscillations near the high gradients. The MC-PSIC solution is in qualitatively agreement with the other methods with no major complication than the fact that the solution is non-smooth within its support. The Lagrangian solution offers an exact description of the solution. In this particular case, as the joint PDF stays constant within its support at a given time, the linear interpolant is already exact. The interpolant is affected by the geometry of the support, that in this case is described by straight lines, and the smoothness of the function defined in the support (the joint PDF), constant in this case. For this reason, the linear and spectral interpolants are equally accurate.

The marginalization of non-smooth solutions is highly affected by presence of high gradients in the solution. In particular, we show in Figures 5.8a and 5.8b the marginal of the particle position for $M = 11$ and $M = 41$ nodes computed with the MoC with linear and spectral interpolants. For a marginally resolved case with low number of points, both solutions show oscillations as interpolation errors. These errors are minimized for an increase number of nodes but because of the presence of gradients, the convergence rate is

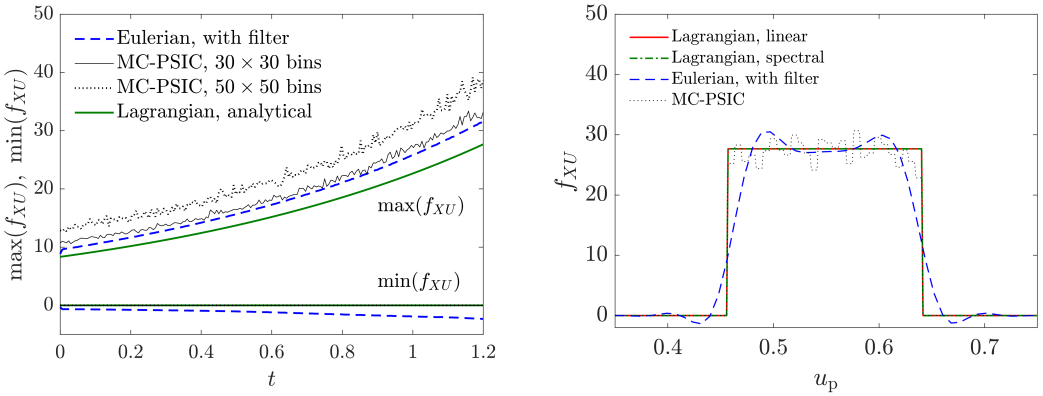


**Figure 5.7.** Numerical results for Test 2. In (a) the time evolution of the maxima and minima of the joint PDF $f_{XU}$ computed with MC-PSIC, the Eulerian approach with filtering and regularization and the Lagrangian approach; in (b) the comparison of the joint PDF along the line $x_\mathrm{p} = 0$ at the final time $t = 1.2$ for the different methods.

limited by a $M^{-1}$ rate (Figure 5.8c).

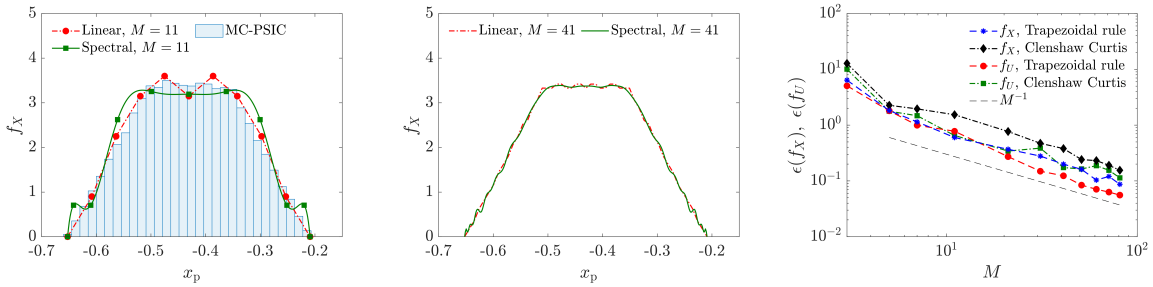


**Figure 5.8.** Numerical results for Test 2. Marginals computed with (a) $M = 11$ nodes and (b) $N = 21$ nodes with the Lagrangian approach using the linear and spectral interpolants compared with MC-PSIC, and in (c) the convergence with the number of nodes of both interpolants. The linear interpolant is combined with the Trapezoidal rule and the spectral with Clenshaw Curtis to perform the integrals to marginalize.

The computation of the moments when gradients are present in the solution is also affected by it as compared to the smooth case. In particular, we find that the computation of first moments with the linear interpolant with Trapezoidal rule and spectral interpolant with Clenshaw Curtis quadrature provide machine precision errors (see Fig. 5.9). This

occurs because the integrand is a constant as a result of a linear mapping with constant Jacobian and the fact that the joint PDF stays constant within its support. However, for the second moments, the integrand contains not only the joint PDF and the Jacobian but also the term $(x_\mathrm{p} - \bar{X}_\mathrm{p})^2$ which is second order in $x_\mathrm{p}$ (and similarly for other second moments) that makes the integrand non-linear. For this reason, the linear interpolant plus Trapezoidal rule exhibits second order convergence whereas the spectral plus Clenshaw Curtis is exact for $M > 3$. This behavior is observed also in the rest of the first and second moments not shown in Figure 5.9.

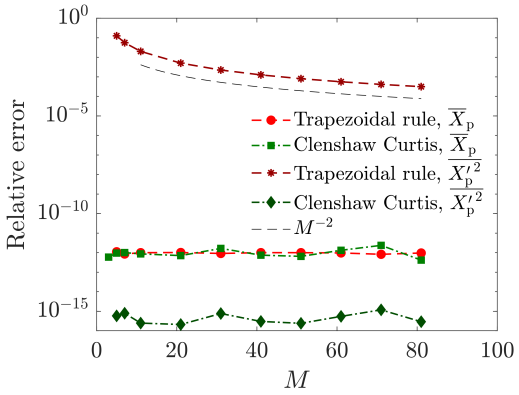


**Figure 5.9.** Convergence of the moments with the number of nodes for Test 2, computed with the Lagrangian approach with linear and spectral schemes combined with the Trapezoidal rule and Clenshaw Curtis quadrature, respectively.

### 5.5.2 Randomly forced particles

**Test 3: stagnation flow.**

The consideration randomness in the forcing function described by (5.4) implies that the random coefficients $\Xi_i$ with $i = 1, \ldots, N_\xi$ follow PDFs different from Dirac delta distribution, i.e., the variables $\Xi_i$ are not provided deterministically, and account for uncertainties in the forcing model. As an example, a combination of $N_\xi = 10$ Chebyshev modes $\psi_i(Re_p)$ suffices to accurately represent the Schiller and Naumann correlation $1 + 0.15 Re_p^{0.687}$ in the interval $Re_p \in [0,\ 50]$, where the joint PDF of the random coefficients $f_{\boldsymbol{\Xi}}(\boldsymbol{\xi})$ governs the stochasticity in the forcing. In Figure 5.10, we show such approximation

of the Schiller and Naumann where only the first coefficient is random and the rest deterministic according to (5.4), so that $\Xi_1 \sim f_{\Xi_1}(\xi_1)$ and $\Xi_i \sim \delta(\Xi_i - 1)$ for $i = 2, \ldots, 10$. We then rename the only random coefficient as $\Xi = \Xi_1$. The variance of such forcing is constant along the particle Reynolds number as the first Chebyshev mode $\psi_1(Re_p)$ is a constant. The general forcing model (5.4) may describe any general dependency of the forcing with the particle Reynolds number (see for example [6] and [4]). We also depicted the Stokes drag with constant standard deviation along $Re_p$ where simply $\phi = \Xi$.

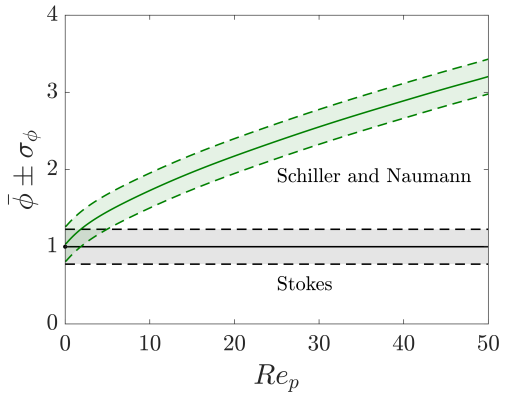


**Figure 5.10.** Two standard deviation bounds of random forcing models defined with (5.4). In black, the Stokes drag with a constant confidence interval defined by $\phi = \Xi$ with $\Xi \sim \mathcal{N}(1, 0.1^2)$. In green, the Schiller and Naumman correlation with a constant confidence interval defined with ten modes where $\sum_{i=1}^{10} \psi_i(Re_p) \simeq 1 + 0.15 Re_p^{0.687}$ and the first coefficient is $\Xi_1 \sim \mathcal{N}(1, 0.1^2)$ and the rest unity $\Xi_i = 1$, with $i = 2, \ldots, 10$.

In this test case, we analyze the evolution of the PDFs of the particle phase when groups of particles are released in the stagnation flow [176] as in the previous three test cases. Point-particles carried by this flow admit an analytical solution for their trajectories as well [2]. As in the previous cases, we choose $St = 1$. The particle parameters are $d_p = 2.7 \cdot 10^{-3}$ and $\rho_p = 250$ that when considering $Re_\infty = 10^4$ leads to particle Reynolds larger than unity such that a correction of the Stokes drag is suitable to be applied. We release a particle cloud defined by Gaussian distribution functions such that the average values of the particle position and velocity are $(\bar{X}_{\mathrm{p0}},\ \bar{U}_{\mathrm{p0}}) = (-1, 1)$ and the standard deviations $\sigma_{X_{\mathrm{p0}}} = \sigma_{U_{\mathrm{p0}}} = 0.05$. The initial location and velocity as

well as the random coefficient are statistically independent such that at the initial time one has $f_{XU\Xi}(x_\mathrm{p}, u_\mathrm{p}, \xi; 0) = f_X^\mathrm{in}(x_\mathrm{p}) f_U^\mathrm{in}(u_\mathrm{p}) f_\Xi(\xi)$. For the random coefficient we consider $\Xi \sim \mathcal{N}(1, 0.1^2)$ for both, the Stokes and the Schiller and Naumann correction represented in Figure 5.10.

In the MC-PSIC approach, each sampled particle exhibits a delayed and damped trajectory as compared to a fluid tracer (without inertia) which is governed by its sampled value of the random forcing. The evolution in time of a cloud of particles when the forcing is consider random is distinctly different than that of considering deterministic forcing, described by significantly different PDFs. In Figure 5.11a, samples for three different values of the random coefficient $\Xi$, namely $\bar{\Xi} - \sigma_\Xi$, $\bar{\Xi}$ and $\bar{\Xi} + \sigma_\Xi$ are shown. A sampled particle group or cloud with a deterministic value of the coefficient, $\Xi^*$, for all particles, corresponds to realizations with an effective inertia $St/\Xi^*$ for the whole particle cloud (see Fig. 5.11a left and Fig. 5.11c first three rows). In that case, with a single deterministic value of the random coefficient, the cloud behaves coherently. Notice that the divisions by quadrants in Figure 5.11c (first three rows) in phase space remain during the time evolution. After times larger than the Stokes number, changes in the flow may produce transport of particles from one quadrant into another as the cloud is advected and deformed and this distinction according to the initial quadrants may disappear over time. However, in the case of considering random forcing, this distinction disappears in a time frame smaller than the average Stokes number of the cloud $St/\bar{\Xi}$. Particles from different quadrants quickly mix with each other as the particle cloud is advected by the flow. Also, there is a change in the topology of the cloud in phase space as compared to the deterministically forced cases. For deterministically forced clouds, the phase space topology corresponds to a joint PDF that is approximately a multivariate Gaussian for most of the simulation (times on the order of the Stokes number) as opposed to the randomly forced cloud where non-Gaussianity appears quickly as a result of the randomness in the forcing. Both, variations of the flow within the cloud region and the consideration of random forcing

originate non-Gaussianty but the randomness in the forcing has an almost immediate effect in third and higher moments. This leads to non-Gaussian effects in the solution related to random forcing occurring in a much faster time scale as compared to considering deterministic forcing.

In Figure 5.11b we represent the samples of the randomly forced cloud in the augmented phase space. The parametric effect of the random coefficient shows that particles with high values of the random coefficient have low inertia whereas samples with low values of the random coefficient have high inertia. The the mixing between quadrants for the randomly forced case (Fig. 5.11c fourth row) is related to a cloud with a distribution of inertia governed by the PDF of the random coefficient and therefore, a mix in time responses of particles.

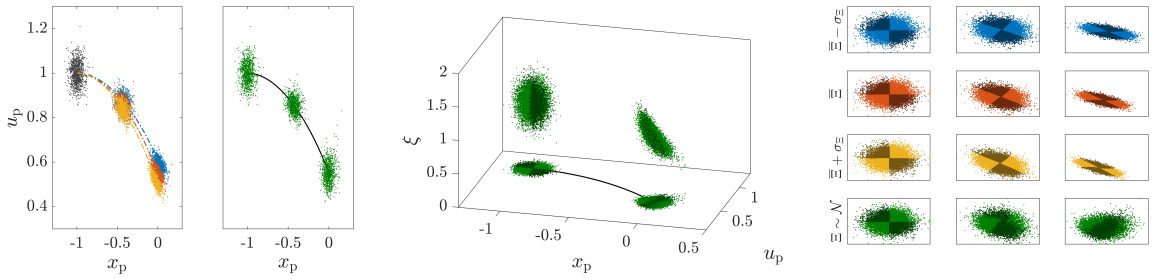


**(a)** **(b)** **(c)**

**Figure 5.11.** Solutions based on the MC-PSIC method for Test 3. In (a), three deterministically forced samples depicted at three different times in phase space (left) and the corresponding randomly forced solution (right). In (b), The randomly forced solution in the augmented phase space $x_p - u_p - \xi$ for the initial and final time. In (c), the four cases depicted in (a) by rows for three different times (columns) with a quadrant distinction according to the initial condition. The forcing model is based on the Stokes drag in 5.10.

In the Lagrangian approach, the deterministic characteristic lines link particles with their probability to occur, and each particle becomes a possible event with known probability traced along a deterministic characteristic line in phase space. As a difference with Langevin approaches, these samples are not fictitious particles [129] but *possible*

particles, as its equations and properties are deterministic. In fact, they do not need to be sampled but selected to specifically cover the region of phase space that defined the support of the joint PDF. In Figure 5.12, we show the mapping of the joint PDF from the initial to final time of the randomly forced particle cloud with a correspondence one-to-one of each point. The probability of each particle (event) is known in the initial condition and can be mapped to a later time in a deterministic manner as opposed to samples of the MC-PSIC approach (see Fig. 5.11b). This way, the full statistical description of the cloud is deterministically traced in the augmented phase space. The values of the joint PDF of each event is represented with a colormap in Fig. 5.12. The marginalization over the three different dimensions, leading to bidimensional marginals is shown projected in the corresponding planes after having interpolated to the container element and integrated numerically. This can be performed with the linear and/or spectral schemes analyzed previously, where the analysis of the numerical properties of both approaches for periodic functions holds for this particular case as well. The convergence analysis (not shown) for this case is qualitatively the same than the one described in Section 5.5.1 when evaluating the interpolants and the integrations to marginalize and compute moments.

The comparison of the joint PDF $f_{XU}$ for a deterministic and random forcing is shown in Figures 5.13a and 5.13b respectively, particularly for the consideration of the Stokes limit ($Re_p$ small). The trajectories of the particles conforming the mapping of the support of the joint PDF depend non-linearly on $\xi$ (see Appendix H). This causes tails (associated with non-zero high moments) to appear on the joint PDF when the vertical component in Fig. 5.12 is integrated, i.e., when marginalizing along $\xi$. This results on a significant difference of the marginal $f_{XU}$ when the forcing includes uncertainty as opposed to being described deterministically. The PDF equation gives the means to

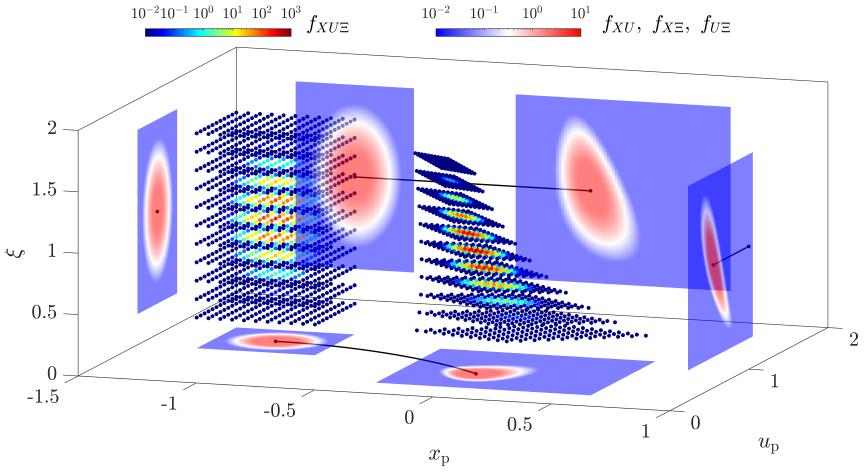


**Figure 5.12.** Joint PDF for Test 3, computed with the Lagrangian approach. The solution is depicted at the initial and final time where the joint PDF is represented in the augmented phase space $x_p - u_p - \xi$ and the two–dimensional marginals and projected in the corresponding planes. The marginal $f_{XU}$ is depicted in the plane $x_p - u_p$, $f_{X\Xi}$ in $x_p - \xi$ and $f_{U\Xi}$ in $u_p - \xi$. The random forcing used is the Stokes model in 5.10.

directly quantify this difference which resides formally in the term

$$\int_{-\infty}^{\infty} \xi f_{XU\Xi} d\xi, \tag{5.30}$$

that does not participate in the PDF equation for a deterministically forced cloud. In fact, such term is the only difference between the Liouville equation of a deterministically forced case with the randomly forced case after marginalizing along $\xi$. It is important to highlight here that despite the relatively simple choices of the test case, i.e., initial condition defined by Gaussian distributions and linear flow as well as Stokes forcing ($\phi = 1$ for deterministically forced and $\phi = \Xi$ for randomly forced, see Fig. 5.10), the output of the system in highly non-Gaussian at shorter times than the Stokes number, presenting a joint PDF with a convoluted shape in the $x_p - u_p$ phase space that would not be accurately

described by Gaussian models.

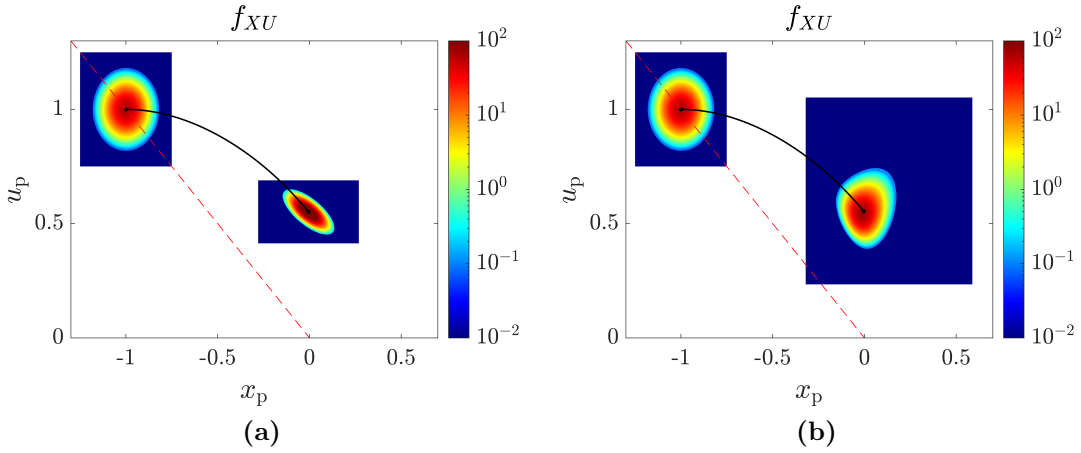


**Figure 5.13.** Solution of the PDF $f_{XU}$ for Test 3 with (a) deterministic and (b) random forcing computed with the Lagrangian approach. The random forcing used is the Stokes model in Fig. 5.10.

The general random forcing model as described in (5.4) allows to account for finite Reynolds number, correcting the Stokes drag (green curve in Fig. 5.10). We evaluate for this case the consideration of Stokes drag or the Schiller and Naumann (SN) correction for both, deterministic and randomly forced particle clouds. The SN forcing has a value of approximately two for a finite particle Reynolds number of order ten. With the current parameters of the test case, the particle cloud exhibits values of the particle Reynolds on the interval $Re_p \in [0\ 25]$. Therefore, we report a significant influence in the statistics by the consideration of finite particle Reynolds number in the forcing. Particles that deviate from the trajectory of tracers in the $x_\mathrm{p} - u_\mathrm{p}$ phase space and therefore have non-zero relative velocity (and $Re_p$), are forced at higher values that those at the speed that a tracer would have at that location. As a result, despite the flow is linear, the support of the joint PDF is non-linearly mapped and the evolution of the joint PDF is also affected by it (see equations (5.11c)).

With respect to the first moments (Fig. 5.14a), the consideration of randomness in the forcing as a result of empirical uncertainty does not change considerably the

solution. However, correction of the Stokes drag for finite particle Reynolds numbers has an appreciable impact in the averages of the particle solution. The second and third moments however (Figs. 5.14b and 5.14c), are affected by both, the consideration of uncertainty in the forcing as well as the particular forcing model used, Stokes or Schiller and Naumann. Only the consideration of deterministic Stokes drag leads to statistics that can be accurately described by a Gaussian model as the skewness remains zero along time (Fig. 5.14c). The importance of quantifying the uncertainty in the forcing function and introducing it in the model is crucial to accurately predict the evolution of particle statistics even for simple flows and Gaussian initial conditions. Non-linear effects of the uncertainty in the forcing and corrections for finite particle Reynolds of the forcing affect the evolution of the joint PDF in a non-trivial manner, here fully described by the PDF approach in Lagrangian form.

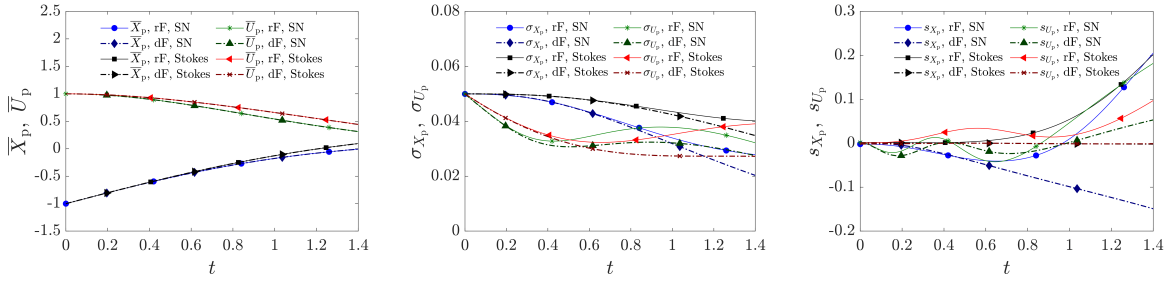


**(a)** **(b)** **(c)**

**Figure 5.14.** Time evolution of the (a) first (b) second and (c) third moments for Test 3. Deterministic forcing (dF) and random forcing (rF) are considered as well as Stokes and Schiller and Naumann (SN) forcing models as presented in Fig. 5.10. The skewness is normalized using the corresponding standard deviation such that $s_{X_\mathrm{p}} = \overline{X_\mathrm{p}'^3}/\sigma^3_{X_\mathrm{p}}$ equivalently for the particle velocity.

**Test 4: flow around a cylinder.**

The von Kármán vortex street [237] has been used in several studies of coherent Lagrangian structures and particle laden flows [238, 239, 240, 241]. We chose the same parameters that in the cited studies, that have been shown to approximate the solution

of the Navier-Stokes equations for this geometry for $Re_\infty \approx 250$. We release a quiescent particle deterministically located at $(x_\mathrm{p},\ y_\mathrm{p}) = (-2,\ 0.2)$ at $t = 0$, with Stokes number $St = 0.5$ and randomly forced. Because the Reynolds of the flow is relatively low, the particle Reynolds number is smaller than unity and the Stokes approximation holds, for particle parameters in concordance with the point-particle assumption. Because of that, we chose the Stokes drag with uncertainty presented in Fig. 5.10. We consider $\Xi$ given by a Normal distribution $\Xi \sim \mathcal{N}(1, 0.1^2)$ and Uniform distribution $\Xi \sim \mathcal{U}(0.8, 1.2)$.

A single particle randomly forced describes a curve in the augmented phase space parametrized with the random coefficient shown in Figure 5.15a for five equidistant instants of time in the interval $t = [0\ 1.5]$. For a given time, the solution describes possible particle positions for inertia $St/\xi$, such that high values of the random coefficient are associated with a fast response and low values of the random coefficient to a slow inertial response. Using the Lagrangian approach in this two-dimensional flow, the link of the probability of those events is traced in time and linked to particle movement as it is advected by the flow (Fig. 5.15b). High values of the random coefficient are also linked to rapid growth of the probability of such events, that can be traced independently. The method of characteristics can be used to trace the evolution of single particles with the use of flow maps without spatial numerical approximation, capturing accurately the discontinuities in the solution. The equivalent computation using an Eulerian approach is a hard task that requires convoluted numerical techniques. Equivalently for the MC-PSIC method, the reconstruction of PDFs defined along a parametrized curve may lead to under predictions related to the reconstruction process of the joint PDF by cell divisions.

## 5.6 Summary of results

A deterministic Lagrangian PDF framework to trace the evolution in time of the randomly forced particle phase is developed. The procedure is based on the method of

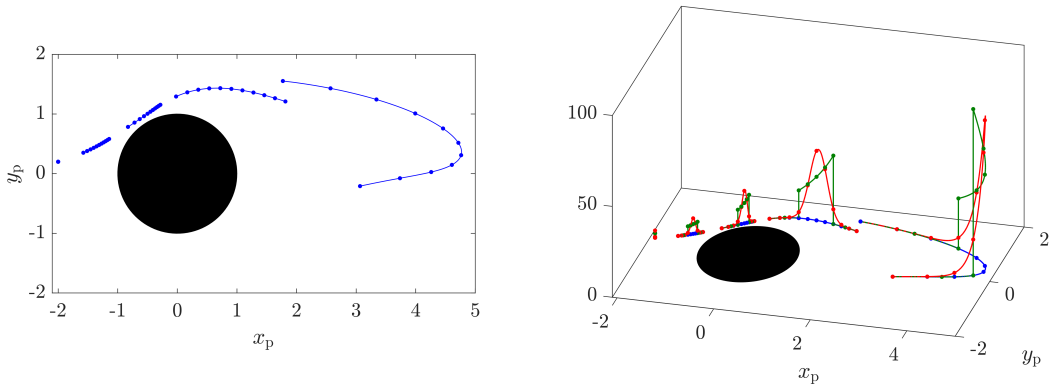


**(a)** **(b)**

**Figure 5.15.** Temporal evolution of a randomly forced particle in a cylinder flow given by the model in [237] with either Gaussian (red) or uniformly (greed) distributed $\alpha$, for five instants of time in the interval $t = [0\ 1.5]$. In (a), the mapping of the particle locations (blue) and in (b) the corresponding mapped probability.

characteristics to solve the Liouville governing PDF equation derived with the method of distributions, taking advantage of its hyperbolicity. The method considers randomness in the particle forcing as a result of empirical uncertainty in non-analytical forcing models. It is then suitable for scenarios in which forcing models are not available analytically and have been learned either by experiments or numerical computations in a data-driven manner.

This approach circumvents previous reported difficulties in solving the governing PDE equation in Eulerian form that requires the use of high-order numerical methods combined with filtering and regularization. In particular, the mapping of single events with the computation of ODEs can be performed with no spatial approximations in an inexpensive manner. Local computation of the solution is possible such that the domain of computation can be defined where the particles lie, saving computational effort as compared to Eulerian methods.

We presented both low- and high-order schemes to compute moments and marginals of the joint PDF with expected convergences and numerical properties. We particularly

find that in the case of smooth periodic solutions, a linear discretization scheme provides also spectral convergence as the Trapezoidal rule converges as fast as the Fourier coefficients for periodic functions.

The test cases verify the proposed framework comparing with previously developed grid-based methods and MC-PSIC computations. Considering random forcing as a result of the use of uncertain drag correlations introduces a distinctly different dynamical response of particle groups as opposed to considering analytical drag laws where the forcing is deterministic. The solution of the joint PDF becomes non-Gaussian even for relatively simple settings where initial conditions and random coefficients are considered Gaussian, i.e., the outputs of the system become non-Gaussian with independence of the inputs; in shorter times than the Stokes number. The evolution in time of the averages of the particle phase remain similar for small variations in the flow within the cloud region for a limited time, smaller than the characteristic time of the particles. Moments higher than the first differ significantly, resulting in an under predicted particle statistics when uncertainty in the drag model is not considered, i.e., when using deterministic drag models.

## 5.7 Acknowledgments

Sections 5.1 through 5.6, are a reprint of the material as it appears in Ref. [5], "Lagrangian Liouville models of multiphase flows with randomly forced inertial particles", D. Domínguez-Vázquez, S. A. Castiblanco-Ballesteros, G. B. Jacobs and D. M. Tartakovsky. D. Domínguez-Vázquez: conceptualization, investigation, methodology, original draft preparation, visualization. S.A. Castiblanco-Ballesteros: methodology. G. B. Jacobs: conceptualization, supervision, review & editing. D. M. Tartakovsky: conceptualization, supervision, review & editing.

# Chapter 6

# Particle forcing reconstruction from limited observation with quantified uncertainty

## 6.1 Introduction

The physics of dispersed particles in unsteady and turbulent flow fields is intricate. This has been and continues to be the inspiration for a significant amount of research on the modeling of particle-laden flow. While several textbooks [178, 242, 243] and review articles [67] have summarized a large number of approaches and an even larger number of models, a key issue in constructing robust and accurate computational models for the dynamic behavior of the dispersed particle fields remains the formulation of accurate particle forcing models. The primary objective of this work is to establish a methodological framework for physics-based inverse modeling of particle forcing dynamics, coupled with uncertainty quantification. This framework is designed to address scenarios where sparse and noisy measurement data along particle trajectories are available.

### 6.1.1 Particle Forcing Models

The forcing of a small single smooth spherical object in a flow is well-known and described analytically for low Reynolds and Mach numbers by the Maxey-Riley equation [44]. Resolution requirements and the complexity of the interactions between

wakes, boundary layers, turbulence, and shocks, however, limit the accurate measurement and prediction for flow conditions outside of that range. At higher Reynolds numbers, the flow separates and can become unstable and the forcing depends on subtle linear and non-linear instabilities that can be sensitive to small changes in the flow conditions. For scenarios with high-Reynolds number effects, for example, simulations of explosively dispersed particle fields originating from a high-speed moving source, basic empirical forcing models have been used [170, 189]. However, it is clear that the accuracy of such models is affected by unsteady forcing [59] and unsteady carrier-phase effects [244]. In fact, high-speed particle flow has spurred model development over the last decade [245, 189] and led to studies that determine either theoretically, experimentally, or through machine learning the particle forcing of single particles affected by moving shocks and arrays of particle affected by shock diffraction [246].

In addition to the impact of flow conditions, a range of geometric parameters can affect the particle forcing. For example, micro- and meso-scopic, but crucial geometric imperfections and deformation of (condensed) particles' surfaces impact momentum and energy exchange with a carrier flow. A harmonic perturbation of cylindrical shape for example can change the dominant vorticity generation by shear to a baroclinic mechanism [247] and yield different forcing. Just these few examples show how many parameters and flow conditions can affect forcing models, and it should not be surprising that an accurate and comprehensive forcing model has eluded the community and realistically is not feasible for all conditions.

As an alternative to understanding the effect of more flow conditions (free-stream turbulence, free-stream velocity profile, stratification, etc.) or particle geometry and the formulation of even more additional and new forcing corrections, we might consider the forcing problem from an inverse perspective and resolve the limitations of modeling and experiment through inference and optimization from observational and simulated data using analytical relations and inputs and outputs of simulation and experiment. Could we,

for example, infer the forcing from limited trajectory data? Or might it be possible to assume a random forcing model with a confidence interval and improve this forcing with a limited amount of high-resolution data? To this end, an intelligent framework is required that systematically and robustly improves forcing models and associated macro-response protocols with a robust uncertainty quantification using limited, experimental data.

### 6.1.2 Inverse methods

The inference of particle forcing from sparse measurements can be accomplished from an inverse-problem perspective. The dependence of particle trajectory data onto the forcing law is highly nonlinear, obtained from solving the physical governing equations. In general, for such nonlinear physics-constrained inverse problems, both data-based methods and physical model-based approaches can be considered. Data-based methods aim at learning a massive amount of data as a distribution, often in reduced-order latent space. Methods such as Generative adversarial networks (GANs), Auto-encoders, or Long-Short-Term Memory (LSTM) [248, 249] can successfully discover the intrinsic coordinates of the data and take into account the effect of observing by evaluating the probability distribution conditioned on those observations. However, given the efficiency and practicality of these methods, a thorough physical analysis of the results is often difficult because the foundation is not the governing equation. Model-based methods, on the other hand, initiate from the governing equation and often need to solve the adjoint equations to obtain the gradient of the cost function [250]. To maintain consistency with the forward solver and ensure numerical stability during optimization, the discrete adjoint operator is often derived and implemented [251]. Furthermore, the adjoint fields by solving the adjoint equations give a clear interpretation of the physical meaning [252] as the domain of dependence.

Although uncertainty quantification is straightforward under probabilistic frameworks for data-based methods, for model-based methods such as adjoint methods, it is generally more difficult. For nonlinear dynamics, the distribution of the control vector

deviates from Gaussian and samples of the probability distribution can be drawn from Hamiltonian Monte Carlo (HMC) using the gradient Langevin dynamics [253].

To account for parametric, empirical, and structural uncertainty fluctuations in forcing models, a probabilistic (stochastic), point-particle, and multi-scale perspective as was taken in Refs. [98, 2, 4]. Starting from known empirical models and/or surrogate forcing models from high-resolution simulations [102], that account for Reynolds, Mach number, and other parameters, we can describe the forcing and its dependencies within confidence intervals according to a probability density function. Stochastic dynamic models are formulated that propagate this distribution into the stochastic solutions of trajectories [2].

Here, we infer forcing models using a combination of governing dynamic equations that govern the location and velocity of a particle modeled as a singular point with an unknown forcing and adjoint formulations. We develop a theoretical framework that determines forcing for one-way coupled passive particles, under the assumption that the ambient velocity fields are known. The remainder of the paper is organized as follows: firstly we delve into point-particle and its forcing models, deriving the optimization framework by employing adjoint dynamics. Subsequently, we apply this framework to two distinct test cases: the Arnold–Beltrami–Childress (ABC) flow and a decaying isotropic turbulence flow.

## 6.2 Problem Formulation

Consider the motion of a single particle with trajectory $\boldsymbol{x}_p(t)$ and velocity $\boldsymbol{u}_p(t)$. The non-dimensional governing equations for the particle read

$$\frac{d\boldsymbol{x}_p}{dt} = \boldsymbol{u}_p, \quad \frac{d\boldsymbol{u}_p}{dt} = \frac{f}{St}\left(\boldsymbol{u} - \boldsymbol{u}_p\right), \tag{6.1}$$

where $\boldsymbol{u}$ is the ambient velocity at the particle location $\boldsymbol{x}_p$. The Stokes number $St$ is defined as the ratio between the characteristic time of the flow and the particle phase, expressed in terms of the reference Reynolds number as $St = Re_\infty \frac{\rho_p d_p^2}{18}$. Here $d_p$ is the non-dimensional particle diameter and $\rho_p$ is the density ratio of the two phases. The unknown forcing $f$ is assumed to be a function of the slip velocity, $a = |\boldsymbol{u} - \boldsymbol{u}_p|$.

Our objective is to infer the particle forcing from limited observations of particle location collected along the trajectory. The measurement is generated by employing the forcing model for Stokes flow, which incorporates a correction for high Reynolds numbers [189]. The model is described as follows:

$$f(a) = \left(1 + 0.38\frac{Re_p}{24} + \frac{1}{6}\sqrt{Re_p}\right), \tag{6.2}$$

where the particle Reynolds number is defined as $Re_p = Re_\infty a d_p$. This forcing is considered the unknown ground truth by the inverse model and is also utilized to validate the inferred forcing obtained through inverse modeling techniques.

To facilitate numerical optimization, the forcing function is projected onto a finite-dimensional space by discretizing it as a linear combination of basis functions, represented by the following decomposition:

$$f(a) = \sum_i \alpha_i \psi_i(a), \quad \psi_i(a) = \cos\left(i\frac{2\pi d_p Re_\infty}{2Re_{p,max}}a\right), \tag{6.3}$$

where $Re_{p,max}$ is set to be slightly more than the maximum particle Reynolds number encountered in the simulation. We denote the parameters $\boldsymbol{\alpha}$ as our control vector for dimension reduction of the forcing model. Inference of the forcing function $f$ is simplified to determining the values of $\boldsymbol{\alpha}$.

### 6.2.1 Adjoint optimization algorithm

We focus on a special case, where the measurement of the particle location is only available at a single measurement time $t_m$. In this case, information about the forcing function is related to the observation in an indirect and nonlinear manner. To address this, we formulate a minimization problem where the cost function is defined as the difference between the computed and observed particle locations, namely,

$$J = \frac{1}{2}||\boldsymbol{x}_m - \boldsymbol{x}_p(t_m)||^2. \tag{6.4}$$

For more general cases where measurements are available for several different $t_m$, a simple summation of the individual cost functions can be adopted the derivation is still valid.

To satisfy the governing equations 6.1 while minimizing the cost function 6.4, we augment the cost function with the Lagrange multiplier $\boldsymbol{x}_p^\dagger,\ \boldsymbol{u}_p^\dagger$, resulting in the Lagrangian $\mathcal{L}$,

$$\mathcal{L} = J + \int_t \left[ \boldsymbol{x}_p^\dagger \cdot \left( \frac{d\boldsymbol{x}_p}{dt} - \boldsymbol{u}_p \right) dt + \boldsymbol{u}_p^\dagger \cdot \left( \frac{d\boldsymbol{u}_p}{dt} - \frac{f}{St} \left( \boldsymbol{u} - \boldsymbol{u}_p \right) \right) \right] dt. \tag{6.5}$$

If the forcing parameters $\boldsymbol{\alpha}$ are perturbed by $\Delta\boldsymbol{\alpha}$, the change of forcing would result in a deviation of $\boldsymbol{x}_p$ and $\boldsymbol{u}_p$ from its original trajectory, perturbed by the amount $\Delta\boldsymbol{x}_p$ and $\Delta\boldsymbol{u}_p$, respectively. The perturbation of the ambient velocity $\boldsymbol{u}\big|_{\boldsymbol{x}_p}$ can be described as a function of $\Delta x$ using a Taylor expansion,

$$\Delta\boldsymbol{u}\big|_{\boldsymbol{x}_p} = \nabla\boldsymbol{u}\big|_{\boldsymbol{x}_p} \cdot \Delta\boldsymbol{x}_p. \tag{6.6}$$

The change of forcing $f(a)$ can be evaluated as,

$$\begin{aligned}\Delta[f(a)] &= \Delta\left[\sum_i \alpha_i \psi_i(|\boldsymbol{u}-\boldsymbol{u}_p|)\right] \\ &= \sum_i \Delta\alpha_i\psi_i(|\boldsymbol{u}-\boldsymbol{u}_p|) + \frac{f'(a)}{a}\left(\nabla\boldsymbol{u}\big|_{\boldsymbol{x}_p}\cdot\Delta\boldsymbol{x}_p - \Delta\boldsymbol{u}_p\right)\cdot(\boldsymbol{u}-\boldsymbol{u}_p)\,.\end{aligned} \tag{6.7}$$

The perturbation of the cost function can be evaluated as,

$$\begin{aligned}\Delta\mathcal{L} =& \frac{\partial J}{\partial \boldsymbol{x}_p}\Delta\boldsymbol{x}_p + \frac{\partial J}{\partial \boldsymbol{u}_p}\Delta\boldsymbol{u}_p + \int_t \boldsymbol{x}_p^\dagger\cdot\left(\frac{d\Delta\boldsymbol{x}_p}{dt} - \Delta\boldsymbol{u}_p\right)dt \\ &+ \int_t \boldsymbol{u}_p^\dagger\cdot\left\{\frac{d\Delta\boldsymbol{u}_p}{dt} - \frac{1}{St}f(a)\left(\nabla\boldsymbol{u}\cdot\Delta\boldsymbol{x}_p - \Delta\boldsymbol{u}_p\right) - \frac{1}{St}\Delta[f(a)]\left(\boldsymbol{u}-\boldsymbol{u}_p\right)\right\}dt.\end{aligned} \tag{6.8}$$

Through integration by parts, the adjoint equations are derived,

$$\begin{aligned}\Delta\mathcal{L} = &\int_t \Delta\boldsymbol{x}_p\cdot\underbrace{\left[-\frac{d\boldsymbol{x}_p^\dagger}{dt} - \frac{1}{St}\left(\nabla\boldsymbol{u}\right)^T\cdot\left[f(a)\boldsymbol{u}_p^\dagger + \frac{f'(a)}{a}\left[(\boldsymbol{u}-\boldsymbol{u}_p)\cdot\boldsymbol{u}_p^\dagger\right](\boldsymbol{u}-\boldsymbol{u}_p)\right] + \frac{\partial J}{\partial\boldsymbol{x}_p}\right]}_{=0,\ \text{adjoint equations}}dt \\ &+ \int_t \Delta\boldsymbol{u}_p\cdot\underbrace{\left[-\frac{d\boldsymbol{u}_p^\dagger}{dt} - \boldsymbol{x}_p^\dagger + \frac{1}{St}\left[f(a)\boldsymbol{u}_p^\dagger + \frac{f'(a)}{a}\left[(\boldsymbol{u}-\boldsymbol{u}_p)\cdot\boldsymbol{u}_p^\dagger\right](\boldsymbol{u}-\boldsymbol{u}_p)\right] + \frac{\partial J}{\partial\boldsymbol{u}_p}\right]}_{=0,\ \text{adjoint equations}}dt \\ &- \frac{1}{St}\int_t\sum_i \Delta\alpha_i\psi_i(|\boldsymbol{u}-\boldsymbol{u}_p|)\,\boldsymbol{u}_p^\dagger\cdot(\boldsymbol{u}-\boldsymbol{u}_p)\,dt.\end{aligned} \tag{6.9}$$

In the case of the single measurement at $t_m$, the derivatives of the cost function are,

$$\frac{\partial J}{\partial\boldsymbol{x}_p} = (\boldsymbol{x}_p(t_m)-\boldsymbol{x}_m)\,\delta(t-t_m), \quad \frac{\partial J}{\partial\boldsymbol{u}_p} = \boldsymbol{0}. \tag{6.10}$$

in backward time axis $\tau = t_m - t$. The initial conditions of the adjoint simulations are defined as,

$$\boldsymbol{x}_p^\dagger = \boldsymbol{u}_p^\dagger = \boldsymbol{0}, \quad \tau = 0. \tag{6.11}$$

Although the source term of the adjoint equation, $\partial J/\partial\boldsymbol{x}_p$ can be taken into account in

the initial condition instead, we here retain the most general form so that the adjoint equations apply to a general cost function. Also notice that the adjoint equation involves a singularity around $a = |\boldsymbol{u} - \boldsymbol{u}_p| = 0$, corresponding to the vanishing forcing when $\boldsymbol{u} - \boldsymbol{u}_p = \boldsymbol{0}$ in the forward equation.

By solving the adjoint equations backward in time, we obtain the final gradients as,

$$\frac{\partial \mathcal{L}}{\partial \alpha_i} = -\frac{1}{St} \int_t \psi_i(|\boldsymbol{u} - \boldsymbol{u}_p|) \boldsymbol{u}_p^\dagger \cdot (\boldsymbol{u} - \boldsymbol{u}_p)\, dt. \tag{6.12}$$

In the current study, the discretization of the adjoint equations is derived from summation by parts using the discretized forward equations. The discrete adjoint calculates the gradient directions $\partial H / \partial \boldsymbol{\alpha}$ accurately to machine zero and guarantees the convergence of the optimization algorithm.

### 6.2.2 Hamiltonian Monte Carlo

Hamilitonian Monte Carlo (HMC) is an efficient Markov Chain Monte Carlo (MCMC) method rooted in Hamiltonian dynamics. Suppose the posterior distribution of the unknown forcing parameters $\boldsymbol{\alpha}$ follows this distribution:

$$p(\boldsymbol{\alpha}) \sim \exp\left(-\frac{J(\boldsymbol{\alpha})}{\sigma^2}\right). \tag{6.13}$$

Given that the cost function $J$ is quadratic in the deviation of particle locations, the above expression allows for sampling from the posterior distribution of $\boldsymbol{\alpha}$ when measurements follow a Gaussian distribution. To sample from this posterior, HMC constructs a Hamiltonian system with a fictitious momentum variable $\boldsymbol{r}$:

$$H(\boldsymbol{\alpha}, \boldsymbol{r}) = \frac{J}{\sigma^2} + \frac{1}{2} \boldsymbol{r}^T \mathbf{M}^{-1} \boldsymbol{r}, \tag{6.14}$$

and we will sample from the joint distribution

$$\pi(\boldsymbol{\alpha}, \boldsymbol{r}) \sim \exp\left(-\frac{J(\boldsymbol{\alpha})}{\sigma^2} - \frac{1}{2}\boldsymbol{r}^T\mathbf{M}^{-1}\boldsymbol{r}\right), \tag{6.15}$$

for which we ignore the part for the momentum and obtain the marginal distribution for $\boldsymbol{\alpha}$. The sampling is done by selecting $\boldsymbol{r}$ from its Gaussian distribution and integrating equation (6.14) using symplectic algorithms such as leapfrog. Additionally, a Metropolis-Hastings step is incorporated to enhance the efficiency of the sampling [254]. Algorithmically, this approach extends the original adjoint-based gradient descent algorithm to a probabilistic framework by introducing randomness.

The pseudocode in algorithm 1 summarized the procedure of HMC. The gradient of the cost function, $\nabla_{\boldsymbol{\alpha}}$ is evaluated from adjoint simulations and using equation (6.12). Importantly, the computational cost for solving the adjoint equation is comparable to solving the forward problem and does not depend on the number of unknown parameters, such as the size of $\boldsymbol{\alpha}$. In this study, the parameters for HMC are selected to optimize both the efficiency of equation solving and the convergence behavior of the Monte Carlo sampling process.

## 6.3 Applications

### 6.3.1 Forcing inference in the ABC flow

We first consider the Arnold–Beltrami–Childress (ABC) flow, a three-dimensional steady analytical solution of the Euler equation, with the constants of the carrier flow field chosen as $A = \sqrt{3}$, $B = \sqrt{2}$ and $C = 1$. The forcing function is expanded using Fourier modes, as illustrated in equation (6.3). A total number of seven Fourier modes is enough to efficiently represent the forcing function in (6.2). The particle is initialized at location $x_p = y_p = z_p = 2\pi$ at rest. The reference Reynolds number and Stokes number are $Re_\infty = 250$ and $St = 1$, respectively. The particle density ratio is $\rho_p = 500$ and the

**Input:** A starting parameter $\alpha_0$ and step size $\delta t$
**Output:** Samples of the parameter $\alpha_i$ drawn from its posterior distribution.
**for** $i \leftarrow 1$ ***to*** $N$ **do**
  Draw $\boldsymbol{r}_{i-1}$ from $\mathcal{N}(0, \mathbf{M})$
  $(\tilde{\boldsymbol{\alpha}}_0, \tilde{\boldsymbol{r}}_0) \leftarrow (\boldsymbol{\alpha}_{i-1}, \boldsymbol{r}_{i-1})$
  **for** $j \leftarrow 0$ ***to*** $L-1$ **do**
    $\tilde{\boldsymbol{r}}_j \leftarrow \tilde{\boldsymbol{r}}_j - \frac{1}{2}\delta t \nabla_{\boldsymbol{\alpha}} \mathcal{J}(\tilde{\boldsymbol{\alpha}}_j)$
    $\tilde{\boldsymbol{\alpha}}_{j+1} \leftarrow \tilde{\boldsymbol{\alpha}}_j + \delta t \mathbf{M}^{-1} \tilde{\boldsymbol{r}}_j$
    $\tilde{\boldsymbol{r}}_j \leftarrow \tilde{\boldsymbol{r}}_{j+1} - \frac{1}{2}\delta t \nabla_{\boldsymbol{\alpha}} \mathcal{J}(\tilde{\boldsymbol{\alpha}}_{j+1})$
  **end**
  Metropolis-Hasting algorithm:
  $p \leftarrow \min\{1, \exp(-H(\tilde{\boldsymbol{\alpha}}_L, \tilde{\boldsymbol{r}}_L) + H(\boldsymbol{\alpha}_{i-1}, \boldsymbol{r}_{i-1}))\}$
  Draw $\beta$ from uniform distribution in $[0, 1]$
  **if** $\beta \leq p$ **then**
    $\boldsymbol{\alpha}_i \leftarrow \tilde{\boldsymbol{\alpha}}_L$
  **end**
  **else**
    $\boldsymbol{\alpha}_i \leftarrow \boldsymbol{\alpha}_{i-1}$
  **end**
**end**
Use $\boldsymbol{\alpha}_i$ as samples of $\boldsymbol{\alpha}$

**Algorithm 1:** Hamiltonian Monte Carlo.

non-dimensional particle diameter $d_p = 0.012$. The initial location of the particle at rest is known, and the observations of the three coordinates of the particle location are available at $t_m = 8$. These observations are made at a non-dimensional time of eight Stokes time units, ensuring that the particle trajectory is dominated by an inertial response to changes in the flow field.

Using the gradient of the cost function, following equation (6.12), we adopted the Quasi-Newton iterative algorithm to infer the forcing parameters. The initial guess is a constant forcing $f = \alpha_0$, i.e., $\alpha_1 = \alpha_2 = \ldots = \alpha_6 = 0$. We start from initial guesses with $\alpha_0$ ranging from 0 to 4 and arrive at different solutions of the forcing that drives the cost function sufficiently small, namely $J < 10^{-6}$. Results of various inferred forcing functions are plotted in figure 6.1($a$) in grey colors, darker color represents larger $\alpha_0$ in the initial guess and the red line marks the true forcing function. The collection of inferred forcing demonstrates the ill-posedness of the problem, where an infinite number of possible

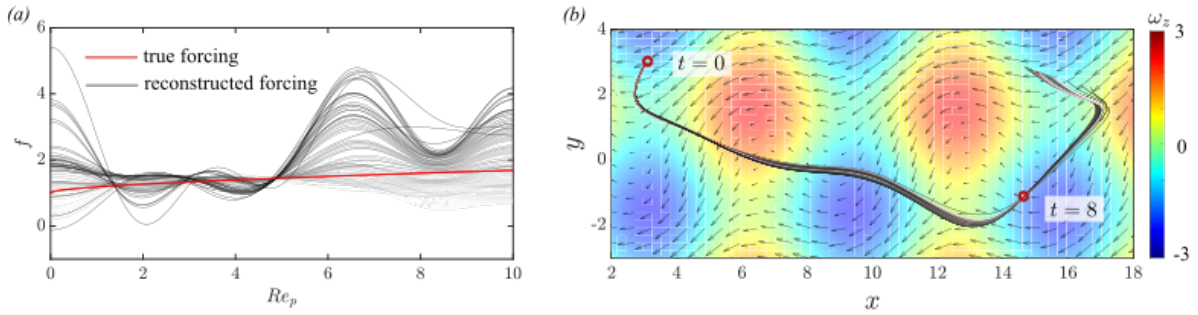


**Figure 6.1.** (a) Collection of inferred forcing starting from different initial guesses $f = \alpha_0 \in [0, 4]$, darker color marks higher values of $\alpha_0$ in the initial guess. The red line marks the true forcing. (b) Top view of the collection of inferred particle traces. The locations of the particle at the initial $t = 0$ and observation time $t = 8$ are known and marked by the red circle. The colors of the particle traces correspond to the ones in (a). Colored contours show the vorticity $\omega_z$ of the background flow field at $z = 0$.

solutions exist. However, the particle trajectories from the inferred forcing are plotted in figure 6.1($b$) follow only slightly different paths that coincide at $t = 8$ before they further deviate. This also implies that even with a large range of function $f$, the form of the forcing can only permit a limited reachable region for the particle.

To further quantify the uncertainty of the forcing function $f$, the HMC algorithm is adopted. The noise level $\sigma$ influences the efficiency of the algorithm: A noise level too large would result in an unconstrained forcing function with an unreasonable range. A noise level too small would cause large curvatures in the landscape of the cost function and invite extra difficulty for sampling. With the noise level $\sigma = 0.01$, the posterior distribution for the coefficients $\alpha_i$ of these modes is evaluated using HMC and shown in figure 6.2.

To estimate the forcing uncertainty, we start from the true forcing parameters and throw away the first hundred iterations of the HMC. This procedure is coined "burn-in" and allows HMC to explore the parameter space and reach the typical set before taking samples. The HMC-estimated posterior probability distribution of the forcing is plotted as colored contours in figure 6.2($a$). The mean and standard deviation of the inferred

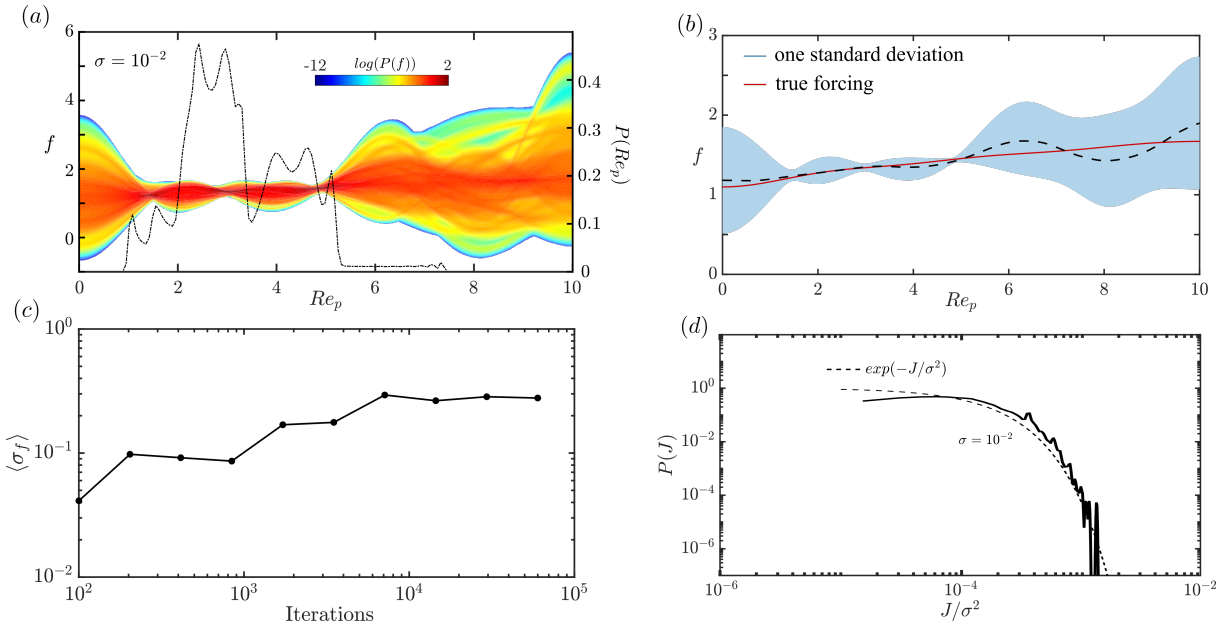


**Figure 6.2.** (a): Logarithm of the Probability Density Function (PDF) depicting the distribution of the forcing $f$ during the HMC process. The solid line represents the distribution of the particle Reynolds number $R_p$ along the particle trajectory. (b) The shaded region highlights the forcing function within one standard deviation. The red solid line represents the true forcing, while the black dashed line shows the mean of the inferred forcing. (c) Evolution of the averaged standard deviation of the forcing distribution as more iterations are performed during HMC. (d) Probability distribution of the cost function during HMC. Dashed lines mark the theoretical prediction of the PDF for the cost function.

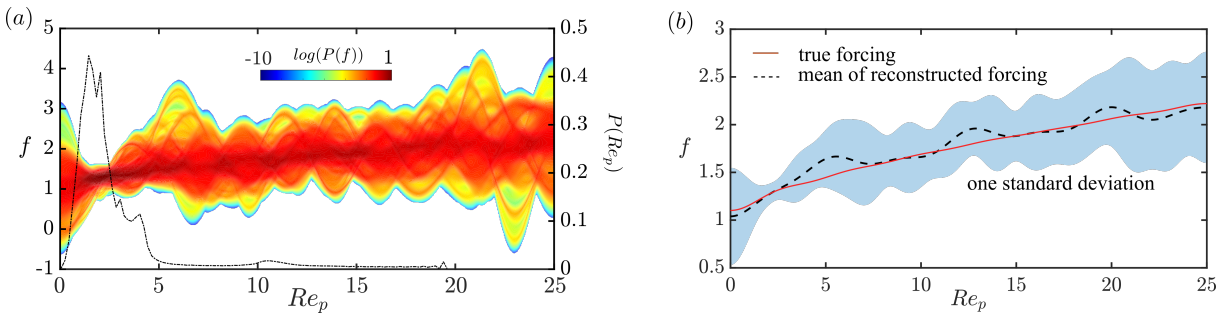


**Figure 6.3.** (a): Logarithmic of the Probability Density Function (PDF) of the forcing $f$ inferred using HMC. The solid line shows the distribution of the particle Reynolds number $Re_p$ along the particle trajectory. (b) Dashed lines represent the mean (expected values) of the forcing while the shaded region marks the forcing function within one standard deviation. The true forcing is shown by the red solid line.

forcing are plotted in figure 6.2($b$). Convergence is measured by the mean standard deviation $\langle\sigma\rangle$ shown in panel ($c$), and the distribution of the cost function during the HMC sampling shown in panel ($d$), where the dashed lines mark the theoretical results of $P(J) \sim \exp(-J/\sigma^2)$. The forcing inference is much more accurate in the range $1 < Re_p < 5$ than at other particle Reynolds numbers. This trend can be attributed to two underlying reasons. Firstly, the accuracy of the forcing inference is influenced by the frequency of $Re_p$ along the particle trajectory. The history of $Re_p$ shown in the background of figure 6.2($a$) is compared with the confidence interval of the inferred forcing, indicating that the forcing with lower uncertainty coincides with the high frequency of $Re_p$ along the particle trajectories. Secondly, as the particle's speed relative to the ambient fluid increases, the momentum effect becomes more significant. For larger $Re_p$, inertia plays a more dominant role, and the impact of the forcing becomes almost negligible, making the determination for large $Re_p$ significantly more challenging.

### 6.3.2 Homogeneous Isotropic Turbulence

The algorithm is also tested in three-dimensional homogeneous isotropic turbulence in a cubic domain $\Omega = [0, 2\pi] \times [0, 2\pi] \times [0, 2\pi]$. The flow fields are obtained with a discontinuous Galerkin compressible DNS solver ([200] and references therein). For the

definition of the initial condition of the flow field, we adopted the one used in [201, 3]. The particle is initialized at location $(x_p,\ y_p,\ z_p)^\top = (\pi,\ \pi,\ 2\pi/3)^\top$ with velocity $(u_p,\ v_p,\ w_p)^\top = (0,\ 0,\ 1.5)^\top$. The Reference Reynolds number is $Re_\infty = 2,357$, the Stokes number is unity $St = 1$, the particle density ratio is $\rho_p = 250$ and the non-dimensional particle diameter $d_p = 0.0055$. The observation is taken when the particle travel for six Stokes time units, i.e. $t_m = 6$.

The results of uncertainty quantification using 15 Fourier modes are shown in figure 6.3. The probability of occurrence for different Reynolds numbers, $P(Re_p)$ along the trajectories during the HMC sampling are also plotted in figure 6.3($a$). The uncertainty of the forcing function $f$ is the smallest for the $Re_p$ with the most occurrence along the particle trajectory. This result is very similar to that in the ABC flow. Once again large $Re_p$ yields a more important role of inertia, rendering the determination of forcing much more challenging.

## 6.4 Summary of results

A data assimilation framework is established, to estimate the forcing of particles as a function of the relative velocity $a = |\boldsymbol{u} - \boldsymbol{u}_p|$ based on sparse, noisy measurements of particle locations. This optimization framework relies on the adjoint dynamics of the particles, coupled with Hamiltonian Markov Chain (HMC) methods for uncertainty quantification when measurements are affected by Gaussian noise.

The efficacy of this algorithm is demonstrated in both the Arnold–Beltrami–Childress (ABC) flow and isotropic turbulence with a Stokes number of unity. The results show that the algorithm efficiently identifies forcing functions, enabling accurate guidance of particles to their observed locations. Importantly, the uncertainty quantification provided by HMC highlights the ill-posed nature of the problem when observations are noisy. The accuracy of the inferred forcing is found to depend on the history of the particle Reynolds

number along the trajectory, with the most accurate results observed for $1 < Re_p < 5$ in both flows.

The implications of the research extend beyond the confines of this study. This work represents a crucial initial step in the field of data assimilation for particle forcing determination, employing adjoint particle dynamics. It not only provides valuable insights into the kinematics of particle-laden flows using experimental data but also contributes significantly to the development of data-driven reduced-order models for particle-flow interactions.

## 6.5 Acknowledgments

Sections 6.1 through 6.4, are a reprint of the material as it appears in "Adjoint-based particle forcing reconstruction and uncertainty quantification", D. Domínnguez-Vázquez, Q. Wang and G. B. Jacobs, in Ref. [6]. D. Domínguez-Vázquez: conceptualization, investigation, methodology, visualization, review & editing. Q. Wang: conceptualization, investigation, methodology, visualization, original draft preparation. G. B. Jacobs: conceptualization, supervision, review & editing.

# Chapter 7

# Fokker-Planck, Langevin and Liouville models of particle statistics

## 7.1 Introduction

Typical models of turbulent particle-laden flows involve spatial scales ranging from tens of meters (the application scale) to microns (the smallest scales of turbulence and particulates). Consequently, a predictive simulation based on "first principles" is not practical and a portion of the smaller scales has to be treated empirically through stochastic "subgrid-scale" models, as it is done in, e.g., large-eddy simulations (LES) or Reynolds-averaged Navier-Stokes (RANS) models. In the context of particle-laden flows, this stochasticity stems from either turbulence of a carrier gas/liquid (subgrid velocity fluctuations) or from random particle kinetics.

Classical kinetic theory [105, 106, 107] deals with stochasticity on the particle phase through an equation for the joint probability density function (PDF) in the six–dimensional phase space composed by particle position and velocity. This equation requires a closure approximation, which can be derived either analytically or numerically [108, 109, 110, 111, 112, 255, 256, 113, 114, 115, 116, 117, 118, 103, 119]. The high–dimensionality of this formulation leads to the so–called curse of dimensionality, which has inspired reduced formulations based on a number of moments of the joint PDF [120, 121, 123, 124, 125, 126, 127, 128].

Equivalent stochastic differential equations (SDEs), which in this field are referred to as a generalized Langevin model [119], can be used to reduce the dimensionality of this PDF equation. The model relies on Wiener increments and random walks to account for stochasticity in particle trajectories [129, 130]; more recent versions of such stochastic models of the dispersed particle phase have been proposed in the literature [131, 132, 133, 134, 135, 136, 137, 36, 138, 139, 256, 1, 140, 141, 142, 143, 145, 146]. A representative formulation of this Langevin approach, in $d$ spatial dimensions, describes the temporal evolution of an inertial point particle's location, $\boldsymbol{X}_\mathrm{p}(t) \in \mathbb{R}^d$, and velocity, $\boldsymbol{U}_\mathrm{p}(t) \in \mathbb{R}^d$, by adding Wiener increments to the particle position and velocity to Newton's second law

$$\mathrm{d}\boldsymbol{X}_\mathrm{p} = \boldsymbol{U}_\mathrm{p}\mathrm{d}t + \boldsymbol{b}_x(\boldsymbol{X}_\mathrm{p}, \boldsymbol{U}_\mathrm{p}, t)\,\mathrm{d}\boldsymbol{W}_x, \tag{7.1a}$$

$$\mathrm{d}\boldsymbol{U}_\mathrm{p} = \boldsymbol{\mu}_a(\boldsymbol{X}_\mathrm{p}, \boldsymbol{U}_\mathrm{p}, t)\mathrm{d}t + \boldsymbol{b}_u(\boldsymbol{X}_\mathrm{p}, \boldsymbol{U}_\mathrm{p}, t)\,\mathrm{d}\boldsymbol{W}_u. \tag{7.1b}$$

The particle's slow-varying average acceleration, $\boldsymbol{\mu}_a \in \mathbb{R}^d$, might depend in general on $\boldsymbol{U}_\mathrm{p}$ and $\boldsymbol{X}_\mathrm{p}$ through the evaluation of the bulk-flow velocity at the particle position, $\boldsymbol{u}(\boldsymbol{X}_\mathrm{p}, t) \in \mathbb{R}^d$ and the relative velocity of the two phases, time, and other model parameters. The particle's fast-varying dynamics is represented by the (random) Wiener process $\boldsymbol{W}_u(t) \in \mathbb{R}^m$, whose strength is encapsulated in the (deterministic) diffusion tensor $\boldsymbol{b}_u \in \mathbb{R}^{d\times m}$ that, in general, varies with $\boldsymbol{X}_\mathrm{p}$, $\boldsymbol{U}_\mathrm{p}$, and time $t$. Similarly, Wiener increments $\boldsymbol{W}_x(t) \in \mathbb{R}^m$ are usually added to the particle position with diffusion tensor $\boldsymbol{b}_x \in \mathbb{R}^{d\times m}$ (see for example Refs. [141, 257]). The joint PDF of the particle position and velocity, $f_{\boldsymbol{XU}}(\boldsymbol{x}_\mathrm{p}, \boldsymbol{u}_\mathrm{p}; t)$, in the case of Gaussian white-noise in (7.1), satisfies the $(2d)$-dimensional Fokker-Planck equation

$$\frac{\partial f_{\boldsymbol{XU}}}{\partial t} + \nabla_{\boldsymbol{x}_\mathrm{p}} \cdot (\boldsymbol{u}_\mathrm{p} f_{\boldsymbol{XU}}) + \nabla_{\boldsymbol{u}_\mathrm{p}} \cdot (\boldsymbol{\mu}_a(\boldsymbol{x}_\mathrm{p}, \boldsymbol{u}_\mathrm{p}, t) f_{\boldsymbol{XU}}) = \nabla \cdot (\boldsymbol{\mathcal{D}} \nabla f_{\boldsymbol{XU}}), \tag{7.2}$$

with the diffusion tensor $\boldsymbol{\mathcal{D}} = \boldsymbol{b}\boldsymbol{b}^\top/2 \in \mathbb{R}^{2d\times 2d}$ and $\nabla = (\nabla_{\boldsymbol{x}_\mathrm{p}}, \nabla_{\boldsymbol{u}_\mathrm{p}})^\top \in \mathbb{R}^{2d}$.

At least two major challenges hinder the development of consistent Langevin models for particle-laden flows. First, since the Wiener process is Gaussian and white noise, it gives rise to the Gaussian PDF $f_{\boldsymbol{XU}}(\boldsymbol{x}_\mathrm{p}, \boldsymbol{u}_\mathrm{p}; t)$. Yet, empirically observed (and numerically simulated) single-point statistics of particles are rarely Gaussian [258, 259, 182, 260, 2], which suggests that models like (7.1) provide *ad hoc* (and possibly inaccurate) representations of subgrid particle dynamics. Second, closure models for diffusion coefficients in turbulent flows, let alone particle-laden turbulent flows, remain one of the open problems in fluid mechanics. In addition to having these foundational issues, the Langevin approach is also computationally expensive when Monte Carlo methods are used to estimate the tails of joint PDFs.

A way to overcome these limitations is to replace the Wiener increments in (7.1) with random forcings, which are represented via series expansions involving proper sets of random variables [149, 150, 2, 4, 5]. This approach replaces (stochastic) Langevin equations (7.1) with a coupled system of $2d$ ordinary differential equations with random coefficients,

$$\frac{\mathrm{d}\boldsymbol{X}_\mathrm{p}}{\mathrm{d}t} = \boldsymbol{U}_\mathrm{p} + \sum_{i=1}^{N} \boldsymbol{Z}_i \circ \boldsymbol{\varphi}_i(\boldsymbol{X}_\mathrm{p}, \boldsymbol{U}_\mathrm{p}, t), \tag{7.3a}$$

$$\frac{\mathrm{d}\boldsymbol{U}_\mathrm{p}}{\mathrm{d}t} = \boldsymbol{\mu}_a(\boldsymbol{X}_\mathrm{p}, \boldsymbol{U}_\mathrm{p}, t) + \sum_{i=1}^{N} \boldsymbol{\Xi}_i \circ \boldsymbol{\phi}_i(\boldsymbol{X}_\mathrm{p}, \boldsymbol{U}_\mathrm{p}, t). \tag{7.3b}$$

Here, $\circ$ is the Hadamard product, $\boldsymbol{Z}_i \in \mathbb{R}^d$ and $\boldsymbol{\Xi}_i \in \mathbb{R}^d$ are the vectors of random coefficients in the $N$th-order polynomials with orthogonal bases $\boldsymbol{\varphi}_i \in \mathbb{R}^d$ and $\boldsymbol{\phi}_i \in \mathbb{R}^d$ respectively, defined deterministically. While the Wiener process, $\boldsymbol{W}_x(t)$ or $\boldsymbol{W}_u(t)$ in (7.1), is a random *function*, an infinite-dimensional object that necessitates the use of stochastic calculus, the parameters $\boldsymbol{Z}_i$ and $\boldsymbol{\Xi}_i$ are random *variables*; hence, for any realization $\boldsymbol{z}_i$ and $\boldsymbol{\xi}_i$ of $\boldsymbol{Z}_i$ and $\boldsymbol{\Xi}_i$, (7.3) are deterministic differential equations amenable to a standard numerical or analytical treatment. Moreover, the joint PDF of the random inputs and

outputs in (7.3) defined in an *augmented phase space* that includes the random coefficients, $f_{\boldsymbol{XU\Xi Z}}(\boldsymbol{x}_\mathrm{p}, \boldsymbol{u}_\mathrm{p}, \boldsymbol{\xi}, \boldsymbol{z}; t)$, satisfies the Liouville equation

$$\begin{aligned}&\frac{\partial f_{\boldsymbol{XU\Xi Z}}}{\partial t} + \nabla_{\boldsymbol{x}_\mathrm{p}} \cdot [(\boldsymbol{u}_\mathrm{p} + \sum_{i=1}^{N} \boldsymbol{z}_i \circ \boldsymbol{\varphi}_i(\boldsymbol{x}_\mathrm{p}, \boldsymbol{u}_\mathrm{p}, t)) f_{\boldsymbol{XU\Xi Z}}] \\ &+ \nabla_{\boldsymbol{u}_\mathrm{p}} \cdot [(\boldsymbol{\mu}_a(\boldsymbol{x}_\mathrm{p}, \boldsymbol{u}_\mathrm{p}, t) + \sum_{i=1}^{N} \boldsymbol{\xi}_i \circ \boldsymbol{\phi}_i(\boldsymbol{x}_\mathrm{p}, \boldsymbol{u}_\mathrm{p}, t)) f_{\boldsymbol{XU\Xi Z}}] = 0,\end{aligned} \tag{7.4}$$

a hyperbolic partial-differential equation that admits a solution via the method of characteristics (MoC) [5]. This solution might or might not be Gaussian, depending on, e.g., the PDF of the initial data or the random coefficients. Alternatively, (7.3)–(7.4) can be used to learn the series in (7.3) from data, making the Liouville approach adequate for developing stochastic models using data assimilation techniques [6]. We point out that the functions $\boldsymbol{\varphi}_i$ and $\boldsymbol{\phi}_i$ do not need to act as basis functions necessarily for the formulation to be valid.

Our analysis pursues two goals. The first is to elucidate that the Liouville model of particle-laden flows, i.e., Eq. (7.4), amounts to a generalization of the Langevin approach. We show it in two canonical examples in which the former reduces to the latter when the random variables $\boldsymbol{Z}_i$ and $\boldsymbol{\Xi}_i$ are Gaussian and the source terms are found to fit the solution of the Fokker-Planck equivalent model. An analytical generalization for non-Gaussian systems is provided with the Liouville model. The second goal is to show the potential of the Liouville approach for developing stochastic models of the particle phase. By adjusting the random coefficients to fit data, the Liouville approach can be framed in a data-driven manner. We propose an analytical model for fluidized homogeneous heating systems (FHHS) based on the Liouville approach. The accuracy of this model is established via comparison with the predictions of both particle-resolved direct numerical simulations (PR-DNS) and previous models proposed in the literature [261, 1, 141, 144, 143].

## 7.2 Stochastic Models of Particle Dynamics

If (the sum of) forces $\boldsymbol{g}(\boldsymbol{x}_\mathrm{p}, \boldsymbol{u}_\mathrm{p}, t)$ acting on a particle were known with certainty, then its trajectory $\boldsymbol{x}_\mathrm{p}(t)$ and velocity $\boldsymbol{u}_\mathrm{p}(t)$ would be deterministic and computable from Newton's second law,

$$\frac{\mathrm{d}\boldsymbol{x}_\mathrm{p}}{\mathrm{d}t} = \boldsymbol{u}_\mathrm{p}, \qquad \frac{\mathrm{d}\boldsymbol{u}_\mathrm{p}}{\mathrm{d}t} = \boldsymbol{g}. \tag{7.5}$$

In particle-laden flows, these forces are unresolved/uncertain, e.g., due to multi-particle interactions or drag on particles of non-canonical shapes. When treated probabilistically, this uncertainty gives rise to stochastic dynamics, such that the deterministic functions $\boldsymbol{x}_\mathrm{p}(t)$ and velocity $\boldsymbol{u}_\mathrm{p}(t)$ are replaced with the random processes $\boldsymbol{X}_\mathrm{p}(t)$ and velocity $\boldsymbol{U}_\mathrm{p}(t)$.

### 7.2.1 Particle trajectory

A reduced-complexity model of particle dynamics superimposes stochastic fluctuations onto a given deterministic drift velocity $\boldsymbol{u}_\mathrm{p}(t)$. This model is used for example in the literature to compute Lagrangian Coherent Structures (LCS) of fluid particles for uncertain fluid velocity field [262], also denoted particle Langevin model [141] for inertial particles with unresolved drag.

#### Langevin approach

For deterministic drift velocity $\boldsymbol{u}_\mathrm{p}(t)$ and dispersion tensor $\boldsymbol{b}_x$, the Langevin approach is to replace (7.5) with stochastic ODEs [262, 141]

$$\mathrm{d}\boldsymbol{X}_\mathrm{p} = \boldsymbol{u}_\mathrm{p}\mathrm{d}t + \boldsymbol{b}_x(\boldsymbol{X}_\mathrm{p}, t)\mathrm{d}\boldsymbol{W}_x. \tag{7.6}$$

A single-point PDF of the stochastic trajectory $\boldsymbol{X}_{\mathrm{p}}(t)$ in the Langevin equation (7.6), $f_{\boldsymbol{X}}(\boldsymbol{x}_{\mathrm{p}};t)$, satisfies the Fokker-Planck equation [263],

$$\frac{\partial f_{\boldsymbol{X}}}{\partial t}+\nabla_{\boldsymbol{x}_{\mathrm{p}}}\cdot(\boldsymbol{u}_{\mathrm{p}}f_{\boldsymbol{X}})=\nabla_{\boldsymbol{x}_{\mathrm{p}}}\cdot(\boldsymbol{\mathcal{D}}\nabla_{\boldsymbol{x}_{\mathrm{p}}}f_{\boldsymbol{X}}),\quad \boldsymbol{\mathcal{D}}=\frac{\boldsymbol{b}_x\,\boldsymbol{b}_x^{\top}}{2}. \tag{7.7}$$

**Liouville approach**

Instead of using the Wiener process $\boldsymbol{W}_x(t)$, the Liouville approach accounts for stochasticity of the particle dynamics using time-invariant random variables $\boldsymbol{Z}_i$, characterized by the joint PDF $f_{\boldsymbol{Z}}(\boldsymbol{z})$. Specifically, the stochastic ODE (7.6) is replaced with an ODE with random coefficients,

$$\frac{\mathrm{d}\boldsymbol{X}_{\mathrm{p}}}{\mathrm{d}t}=\boldsymbol{u}_{\mathrm{p}}+\sum_{i=1}^{N}\boldsymbol{Z}_i\circ\boldsymbol{\varphi}_i(\boldsymbol{X}_{\mathrm{p}},t), \tag{7.8}$$

where $\boldsymbol{\varphi}_i(\boldsymbol{X}_{\mathrm{p}},t)$ is a prescribed vector function conforming a basis, for example Chebyshev polynomials. While the derivation of the PDF equation for $f_{\boldsymbol{X}}(\boldsymbol{x}_{\mathrm{p}};t)$ requires a closure approximation [227], the equation for the joint PDF $f_{\boldsymbol{XZ}}(\boldsymbol{x}_{\mathrm{p}},\boldsymbol{z};t)$ of the model input $\boldsymbol{Z}_i$ and output $\boldsymbol{X}_{\mathrm{p}}(t)$ is exact:

$$\frac{\partial f_{\boldsymbol{XZ}}}{\partial t}+\nabla_{\boldsymbol{x}_{\mathrm{p}}}\cdot\left[\left(\boldsymbol{u}_{\mathrm{p}}+\sum_{i=1}^{N}\boldsymbol{z}_i\circ\boldsymbol{\varphi}_i(\boldsymbol{x}_{\mathrm{p}},t)\right)f_{\boldsymbol{XZ}}\right]=0. \tag{7.9}$$

This result can be derived via either the Liouville theorem [264, 265] or the method of distributions [227, 2, 5].

Since $f_{\boldsymbol{X}}(\boldsymbol{x}_{\mathrm{p}};t)$ is the marginal of $f_{\boldsymbol{XZ}}(\boldsymbol{x}_{\mathrm{p}},\boldsymbol{z};t)$, i.e.,

$$f_{\boldsymbol{X}}(\boldsymbol{x}_{\mathrm{p}};t)=\int f_{\boldsymbol{XZ}}(\boldsymbol{x}_{\mathrm{p}},\boldsymbol{z};t)\mathrm{d}\boldsymbol{z},$$

the integration of (7.9) yields

$$\frac{\partial f_{\boldsymbol{X}}}{\partial t} + \nabla_{\boldsymbol{x}_\mathrm{p}} \cdot (\boldsymbol{u}_\mathrm{p} f_{\boldsymbol{X}}) = -\nabla_{\boldsymbol{x}_\mathrm{p}} \cdot \left( \int \sum_{i=1}^{N} \boldsymbol{z}_i \circ \boldsymbol{\varphi}_i f_{\boldsymbol{X}\boldsymbol{Z}} \, \mathrm{d}\boldsymbol{z} \right). \tag{7.10}$$

As mentioned above, the derivation of a PDF equation for $f_{\boldsymbol{X}}$ requires a closure to approximate the right hand side term. Comparison of (7.10) and (7.7) indicates that the Langevin and Liouville approaches yield the identical predictions of the PDF $f_{\boldsymbol{X}}(\boldsymbol{x}_\mathrm{p}; t)$ if

$$\nabla_{\boldsymbol{x}_\mathrm{p}} \cdot \left( \boldsymbol{\mathcal{D}} \nabla_{\boldsymbol{x}_\mathrm{p}} f_{\boldsymbol{X}} + \int \sum_{i=1}^{N} \boldsymbol{z}_i \circ \boldsymbol{\varphi}_i f_{\boldsymbol{X}\boldsymbol{Z}} \, \mathrm{d}\boldsymbol{z} \right) = 0. \tag{7.11}$$

If a solution of a Fokker-Planck equation is known, the above identity may be used to develop an equivalent Liouville model. Taking moments of (7.7) and (7.9), similar relations can be found for each moment, adding constrains to the Liouville approach to match an equivalent Langevin model. A moment model based on the Liouville approach is provided in Appendix J.

### 7.2.2 Particle velocity

A class of models of particle-laden flows takes $\mathbf{g}$ in (7.5) to represent the drag force acting on a particle (see Ref. [104] and references therein). This force is proportional to the difference between the carrier flow velocity at the point $\boldsymbol{x}_\mathrm{p}$ occupied by the particle, $\boldsymbol{u}(\boldsymbol{x}_\mathrm{p}, t)$, and the particle velocity, $\boldsymbol{u}_\mathrm{p}(t)$, so that (7.5) is replaced with

$$\frac{\mathrm{d}\boldsymbol{x}_\mathrm{p}}{\mathrm{d}t} = \boldsymbol{u}_\mathrm{p}, \qquad \frac{\mathrm{d}\boldsymbol{u}_\mathrm{p}}{\mathrm{d}t} = \frac{\mathcal{F}}{\tau_\mathrm{p}} (\boldsymbol{u} - \boldsymbol{u}_\mathrm{p}). \tag{7.12}$$

The coefficient of proportionality comprises the correction factor $\mathcal{F}$, which accounts for a possible deviation from the Stokes drag (due to, e.g., finite particle-Reynolds number, particle Mach number, volume fraction of the particles), and the particle's response time $\tau_\mathrm{p}$.

**Langevin approach**

A probabilistic treatment of (7.12), which is referred to velocity Langevin model [141], uses Wiener increments to account for velocity fluctuations

$$\mathrm{d}\boldsymbol{X}_\mathrm{p} = \boldsymbol{U}_\mathrm{p}\mathrm{d}t, \tag{7.13a}$$

$$\mathrm{d}\boldsymbol{U}_\mathrm{p} = \frac{\mathcal{F}}{\tau_\mathrm{p}}\left[\boldsymbol{u}(\boldsymbol{X}_\mathrm{p}, t) - \boldsymbol{U}_\mathrm{p}\right]\mathrm{d}t + \boldsymbol{b}_u(\boldsymbol{X}_\mathrm{p}, \boldsymbol{U}_\mathrm{p}, t)\,\mathrm{d}\boldsymbol{W}_u. \tag{7.13b}$$

The Fokker-Planck equation for the joint PDF $f_{\boldsymbol{XU}}\left(\boldsymbol{x}_\mathrm{p}, \boldsymbol{u}_\mathrm{p}; t\right)$ is given by

$$\frac{\partial f_{\boldsymbol{XU}}}{\partial t} + \nabla_{\boldsymbol{x}_\mathrm{p}} \cdot (\boldsymbol{u}_\mathrm{p} f_{\boldsymbol{XU}}) + \nabla_{\boldsymbol{u}_\mathrm{p}} \cdot \left[\frac{\mathcal{F}}{\tau_\mathrm{p}}(\boldsymbol{u} - \boldsymbol{u}_\mathrm{p}) f_{\boldsymbol{XU}}\right] = \nabla_{\boldsymbol{u}_\mathrm{p}} \cdot (\boldsymbol{\mathcal{D}} \nabla_{\boldsymbol{u}_\mathrm{p}} f_{\boldsymbol{XU}}), \tag{7.14}$$

with prescribed functions $\boldsymbol{u} = \boldsymbol{u}(\boldsymbol{x}_\mathrm{p}, t)$ and $\boldsymbol{\mathcal{D}}(\boldsymbol{x}_\mathrm{p}, \boldsymbol{u}_\mathrm{p}, t) = \boldsymbol{b}_u \boldsymbol{b}_u^\top / 2$.

**Liouville approach**

Our Liouville model relies on random variables $\boldsymbol{Z}_i$ and $\boldsymbol{\Xi}_i$, with PDFs $f_{\boldsymbol{Z}}(\boldsymbol{z})$ and $f_{\boldsymbol{\Xi}}(\boldsymbol{\xi})$, and basis functions given by $\boldsymbol{\phi}_i(\boldsymbol{X}_\mathrm{p}, \boldsymbol{U}_\mathrm{p}, t)$ and $\boldsymbol{\varphi}_i(\boldsymbol{X}_\mathrm{p}, \boldsymbol{U}_\mathrm{p}, t)$ to represent the stochastic particle dynamics

$$\frac{\mathrm{d}\boldsymbol{X}_\mathrm{p}}{\mathrm{d}t} = \boldsymbol{U}_\mathrm{p} + \sum_{i=1}^{N} \boldsymbol{Z}_i \circ \boldsymbol{\varphi}_i(\boldsymbol{X}_\mathrm{p}, \boldsymbol{U}_\mathrm{p}, t), \tag{7.15a}$$

$$\frac{\mathrm{d}\boldsymbol{U}_\mathrm{p}}{\mathrm{d}t} = \frac{\mathcal{F}}{\tau_\mathrm{p}}\left[\boldsymbol{u}(\boldsymbol{X}_\mathrm{p}, t) - \boldsymbol{U}_\mathrm{p}\right] + \sum_{i=1}^{N} \boldsymbol{\Xi}_i \circ \boldsymbol{\phi}_i(\boldsymbol{X}_\mathrm{p}, \boldsymbol{U}_\mathrm{p}, t). \tag{7.15b}$$

The corresponding Liouville equation for the joint PDF $f_{\boldsymbol{XUZ\Xi}}(\boldsymbol{x}_\mathrm{p}, \boldsymbol{u}_\mathrm{p}, \boldsymbol{z}, \boldsymbol{\xi}; t)$ is

$$\begin{aligned}\frac{\partial f_{\boldsymbol{XUZ\Xi}}}{\partial t} &+ \nabla_{\boldsymbol{x}_\mathrm{p}} \cdot \left[\left(\boldsymbol{u}_\mathrm{p} + \sum_{i=1}^{N} \boldsymbol{z}_i \circ \boldsymbol{\varphi}_i(\boldsymbol{x}_\mathrm{p}, \boldsymbol{u}_\mathrm{p}, t)\right) f_{\boldsymbol{XUZ\Xi}}\right] \\ &+ \nabla_{\boldsymbol{u}_\mathrm{p}} \cdot \left[\left(\frac{\mathcal{F}}{\tau_\mathrm{p}}\left(\boldsymbol{u}(\boldsymbol{x}_\mathrm{p}, t) - \boldsymbol{u}_\mathrm{p}\right) + \sum_{i=1}^{N} \boldsymbol{\xi}_i \circ \boldsymbol{\phi}_i(\boldsymbol{x}_\mathrm{p}, \boldsymbol{u}_\mathrm{p}, t)\right) f_{\boldsymbol{XUZ\Xi}}\right] = 0.\end{aligned} \tag{7.16}$$

Since $f_{\boldsymbol{XU}}$ is the marginal of $f_{\boldsymbol{XUZ\Xi}}$, the integration of (7.16) over the coefficients yields an unclosed PDF equation for $f_{\boldsymbol{XU}}$. Comparing that equation with the Fokker-Planck equation (7.14) yields a compatibility condition,

$$\begin{aligned}
&\nabla_{\boldsymbol{x}_\mathrm{p}} \cdot \left[ \int \sum_{i=1}^{N} \boldsymbol{z}_i \circ \boldsymbol{\varphi}_i \left( \int f_{\boldsymbol{XUZ\Xi}} \, \mathrm{d}\boldsymbol{\xi} \right) \mathrm{d}\boldsymbol{z} \right] + \\
&\nabla_{\boldsymbol{u}_\mathrm{p}} \cdot \left[ \boldsymbol{\mathcal{D}} \nabla_{\boldsymbol{u}_\mathrm{p}} f_{\boldsymbol{XU}} + \int \sum_{i=1}^{N} \boldsymbol{\xi}_i \circ \boldsymbol{\phi}_i \left( \int f_{\boldsymbol{XUZ\Xi}} \, \mathrm{d}\boldsymbol{z} \right) \mathrm{d}\boldsymbol{\xi} \right] = 0,
\end{aligned} \tag{7.17}$$

for the Langevin and Liouville approaches. Relation (7.17) can be used to compare both Fokker-Planck and Liouville approaches. We note that the Liouville approach has additional degrees as compared to the Fokker-Planck approach. By comparing moments of both approaches, additional relations can be found.

## 7.3 Analytical solutions to Liouville models

### 7.3.1 Particle trajectory

Lattanzi *et al.* [141] considered a one-dimensional version of the Fokker-Planck equation (7.7) with constant velocity $u_\mathrm{p}$ and diffusion tensor $b_{xij} = \sqrt{2D}\delta_{ij}$,

$$\frac{\partial f_X}{\partial t} + u_\mathrm{p} \frac{\partial f_X}{\partial x_\mathrm{p}} = D \frac{\partial^2 f_X}{\partial x_\mathrm{p}^2}, \tag{7.18}$$

subject to the deterministic initial condition, $f_X(x_\mathrm{p}; 0) = \delta(x_\mathrm{p})$. Its solution,

$$f_X(x_\mathrm{p}; t) = \frac{1}{\sqrt{4\pi D t}} \exp\left( -\frac{(x_\mathrm{p} - u_\mathrm{p} t)^2}{4Dt} \right), \tag{7.19}$$

provides a probabilistic prediction of the particle trajectory, $X_\mathrm{p}(t)$, within the Langevin framework. As expected, this solution is Gaussian.

In the corresponding one-dimensional Liouville approach, we search for relations

to define the random forcings such that the solution of the Fokker-Planck equation and the Liouville equation coincide. Starting from (7.18) and (7.19), we take the first moment of the Fokker-Plank solution and compare that with the first moment of the Liouville approach. In particular, if we employ the law of the unconscious statistician (LOTUS) [266] to the characteristics of the Liouville equation (7.9),

$$\frac{\mathrm{d}\hat{x}_{\mathrm{p}}}{\mathrm{d}t} = u_{\mathrm{p}} + \sum_{i=1}^{N} z_i \varphi_i(t), \tag{7.20}$$

to find the first moment of the particle position which according to (7.19) is $\bar{X}_{\mathrm{p}} = u_{\mathrm{p}} t$, we find

$$\bar{X}_{\mathrm{p}} = u_{\mathrm{p}} t + \int \left( \sum_{i=1}^{N} z_i \int_0^t \varphi_i(t') \mathrm{d}t' \right) f_{\boldsymbol{Z}}(\boldsymbol{z}) \mathrm{d}\boldsymbol{z}, \tag{7.21}$$

where we have applied the deterministic initial condition $X_{\mathrm{p}}(0) = 0$, according to the heat kernel solution (7.19). The second term in the right hand side of (7.21) must be zero to match the solution of the Fokker-Planck equation. We therefore find a condition to match the first moment

$$\int \left( \sum_{i=1}^{N} z_i \int_0^t \varphi_i(t') \mathrm{d}t' \right) f_{\boldsymbol{Z}}(\boldsymbol{z}) \mathrm{d}\boldsymbol{z} = 0. \tag{7.22}$$

Then, looking at the second moment of the solution (7.19), $\overline{X'^2_{\mathrm{p}}} = 2Dt$, using the same procedure we find the condition

$$\int [u_{\mathrm{p}} t + \sum_{i=1}^{N} z_i \int_0^t \varphi_i(t') \mathrm{d}t' - \bar{X}_{\mathrm{p}}]^2 f_{\boldsymbol{Z}}(\boldsymbol{z}) \mathrm{d}\boldsymbol{z} = 2Dt. \tag{7.23}$$

Conditions (7.22) and (7.23) can be fulfilled by considering a single random coefficient

$\Xi \equiv Z_i$, for $i = 1, \ldots, N$, which when used in (7.22) leads to

$$\bar{\Xi} \sum_{i=1}^{N} \int_0^t \varphi_i(t') \mathrm{d}t' = 0, \qquad \bar{\Xi} = 0. \tag{7.24}$$

Then, applying this to also (7.23) gives

$$\sigma_\Xi \sum_{i=1}^{N} \int_0^t \varphi_i(t') \mathrm{d}t' = \sqrt{2Dt}, \tag{7.25}$$

that can be fulfilled by considering a single function $\varphi \equiv \varphi_i$ such that

$$\varphi = \sqrt{\frac{D}{2t}}, \qquad \sigma_\Xi = 1. \tag{7.26}$$

Note that in general, basis function may be used to approximate the source by a finite number of terms $\sum_{i=1}^{N} \varphi_i(t) \approx \sqrt{D/(2t)}$. The random source term can be simply described by a single term $\Xi\, \varphi(t)$ such that (7.9) reduces to

$$\frac{\partial f_{X\Xi}}{\partial t} + \left( u_\mathrm{p} + \xi \sqrt{\frac{D}{2t}} \right) \frac{\partial f_{X\Xi}}{\partial x_\mathrm{p}} = 0. \tag{7.27}$$

Since the initial position of the particle, $X_p(0) = 0$ is known with certainty, i.e., deterministic, this Liouville equation is subject to the initial condition $f_{X\Xi}(x_\mathrm{p}, \xi; 0) = f_\Xi(\xi)\delta(x_\mathrm{p})$. Its solution, obtained via the method of characteristics in Appendix L, is

$$f_{X\Xi}(x_\mathrm{p}, \xi; t) = f_\Xi(\xi)\delta(x_\mathrm{p} - u_\mathrm{p} t - \xi\sqrt{2Dt}). \tag{7.28}$$

The PDF of the particle position, $f_X(x_\mathrm{p}; t)$, is the marginal of $f_{X\Xi}$ computed by integrating (7.28) over $\xi$, while accounting for the properties of the the Dirac delta function

$\delta(-x) = \delta(x)$ and $|\gamma|\delta(\gamma x) = \delta(x)$ for a given scalar $\gamma$,

$$f_X(x_\mathrm{p}; t) = \frac{1}{\sqrt{2Dt}} f_\Xi \left( \frac{x_\mathrm{p} - u_\mathrm{p} t}{\sqrt{2Dt}} \right). \tag{7.29}$$

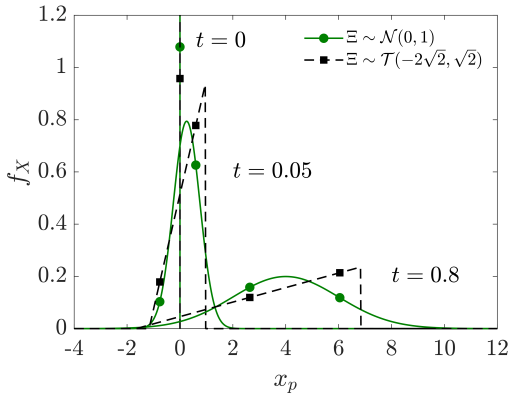


**Figure 7.1.** Particle position PDF $f_X$ at times $t = [0,\ 0.05,\ 0.8]$ given by (7.29) with $D = 2.5$ and $u_\mathrm{p} = 5$ for normal and triangular distributions of the parameter $\Xi$. The uniform distribution has been omitted for clarity (see Fig. 7.2b).

If $f_\Xi(\xi)$ is standard normal, $\Xi \sim \mathcal{N}(0, 1)$, then the Liouville solution (7.29) reduces to the Gaussian solution (7.19) predicted by the Langevin approach. Otherwise, the PDF $f_X$ in (7.29) is non-Gaussian (Fig. 7.1). The temporal evolution of the particle-trajectory PDF $f_X(x_\mathrm{p}; t)$ is depicted in Figure 7.2 for the normal, $\mathcal{N}(0, 1)$; uniform, $\mathcal{U}(-\sqrt{3}, \sqrt{3})$; and triangular, $\mathcal{T}(-2\sqrt{2}, \sqrt{2})$; distributions of the parameter $\Xi$. These three distributions have the same mean, 0, and variance, 1, but different higher moments. The normal distribution gives rise to the Gaussian $f_X(x_\mathrm{p}; t)$, associated with the Wiener process. On the other hand, the triangular distribution translates into a skewed (non-Gaussian) PDF of the particle trajectory. The uniform distribution provides the same statistics than the normal up to the second moments, despite both PDFs differ at any given time (Figs. 7.2a and 7.2b).

The compatibility condition (7.11) may be employed to obtain the diffusion tensor $\mathcal{D}$ for the Fokker-Planck equation from the results obtained with the Liouville approach.

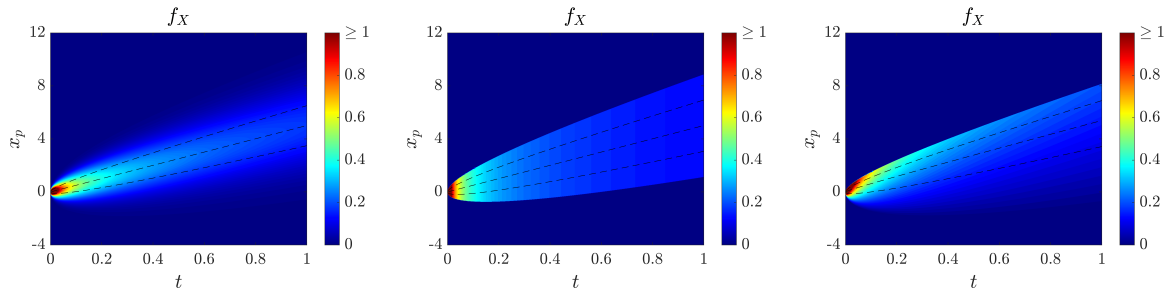


**Figure 7.2.** Temporal evolution of $f_X(x_\mathrm{p};t)$, PDF of the particle trajectory $X_\mathrm{p}(t)$, predicted by the Liouville solution (7.29) for (a) normal, (b) uniform and (c) triangular distributions of the parameter $\Xi$. The deterministic parameters are set to $D = 2.5$ and $u_\mathrm{p} = 5$.

In fact, the substitution of (7.28) and (7.29) into (7.18) proves the identity, showing consistency between the Langevin and Liouville approaches.

### 7.3.2 Particle velocity

The so-called velocity Langevin model [141] deals with a one-dimensional version of (7.13),

$$\mathrm{d}X_\mathrm{p} = \tau_\mathrm{p} U_\mathrm{p} \mathrm{d}t, \qquad \mathrm{d}U_\mathrm{p} = -U_\mathrm{p}\mathrm{d}t + \sqrt{2D}\mathrm{d}W, \tag{7.30}$$

in a reference frame moving at the average particle velocity [141]. The corresponding Fokker-Planck equation for the joint PDF $f_{XU}(x_\mathrm{p}, u_\mathrm{p}; t)$ of the particle trajectory $X_\mathrm{p}(t)$ and velocity $U_\mathrm{p}(t)$ is

$$\frac{\partial f_{XU}}{\partial t} + \tau_\mathrm{p} u_\mathrm{p} \frac{\partial f_{XU}}{\partial x_\mathrm{p}} - \frac{\partial}{\partial u_\mathrm{p}}\left(u_\mathrm{p} f_{XU}\right) = D \frac{\partial^2 f_{XU}}{\partial u_\mathrm{p}^2}. \tag{7.31}$$

If the initial particle position and velocity are known with certainty, $X_\mathrm{p}(0) = 0$ and $U_\mathrm{p}(0) = v_0$, then (7.31) is subject to the initial condition $f_{XU}(x_\mathrm{p}, u_\mathrm{p}; 0) = \delta(x_\mathrm{p})\delta(u_\mathrm{p} - v_0)$. Integration of this equation over $x_\mathrm{p}$ yields the Fokker-Planck equation for the marginal

$f_U(u_\mathrm{p};t)$.

$$\frac{\partial f_U}{\partial t} - \frac{\partial}{\partial u_\mathrm{p}}\left(u_\mathrm{p} f_U\right) = D\frac{\partial^2 f_U}{\partial u_\mathrm{p}^2}, \tag{7.32}$$

subject to the initial condition $f_U(u_\mathrm{p};0) = \delta(u_\mathrm{p} - v_0)$. This problem admits the Gaussian solution [263, 202, 267, 141]

$$f_U(u_\mathrm{p};t) = \frac{1}{\sqrt{2\pi D(1-\mathrm{e}^{-2t})}}\exp\left[-\frac{(u_\mathrm{p} - v_0\mathrm{e}^{-t})^2}{2D(1-\mathrm{e}^{-2t})}\right]. \tag{7.33}$$

Our Liouville approach replaces the Langevin model (7.30) with the one-dimensional version of (7.15). To find the random forcings that make coincide both approaches, we proceed similar as in the previous case (see Section 7.3.1). Equivalently to the use of the LOTUS with the characteristics of the Liouville equation to obtain moments, the model developed in Appendix J, can also be used to find expressions for the moments using the Liouville approach. In essence, we compare the moments of the solution of the Fokker-Planck equation (7.31) to find the random forcings in the Liouville approach. As in the previous example, we assume a single random coefficient can be used $\Xi \equiv \Xi_i = Z_i$ and the basis functions reduce to a deterministic function of time, $\varphi(t)$ and $\phi(t)$ for the position and velocity equations respectively. Then, using the moment equations (K.2.5) derived in Appendix K.2, one can find the closed-form functions

$$\varphi = \frac{\mathrm{d}\sigma_X}{\mathrm{d}t} - \tau_p\sigma_U = \tau_\mathrm{p}\sqrt{D}\left(\frac{1-2\mathrm{e}^{-t}+\mathrm{e}^{-2t}}{\sqrt{2t-3+4\mathrm{e}^{-t}-\mathrm{e}^{-2t}}} - \sqrt{1-\mathrm{e}^{-2t}}\right), \tag{7.34a}$$

$$\phi = \frac{\mathrm{d}\sigma_U}{\mathrm{d}t} + \sigma_U = \sqrt{\frac{D}{1-\mathrm{e}^{-2t}}}, \tag{7.34b}$$

where we have taken as in the previous example, $\bar{\Xi} = 0$, and $\sigma_\Xi = 1$. The functions $\sigma_X(t)$ and $\sigma_U(t)$ are the standard deviations of $X_\mathrm{p}(t)$ and $U_\mathrm{p}(t)$ according to the Fokker-Planck

equation (7.31), given by [141]

$$\sigma_X = \sqrt{\tau_{\mathrm{p}}^2 D\left(2t - 3 + 4\mathrm{e}^{-t} - \mathrm{e}^{-2t}\right)}, \tag{7.35a}$$

$$\sigma_U = \sqrt{D\left(1 - \mathrm{e}^{-2t}\right)}. \tag{7.35b}$$

In general, data-driven techniques can be used to adjust the random forcings in (7.3) by defining an optimization problem. See for example Ref. [6] where the PDF of the random coefficients are learned from DNS with an adjoint-based data assimilation procedure using Fourier series as basis functions.

With the random forcings defined by the random coefficient $\Xi$ and the functions in (7.34), our Liouville approach replaces the Langevin model (7.30) with

$$\frac{\mathrm{d}X_{\mathrm{p}}}{\mathrm{d}t} = \tau_{\mathrm{p}} U_{\mathrm{p}} + \Xi\varphi, \qquad \frac{\mathrm{d}U_{\mathrm{p}}}{\mathrm{d}t} = -U_{\mathrm{p}} + \Xi\phi, \tag{7.36}$$

The Liouville equation for the joint PDF $f_{XU\Xi}(x_{\mathrm{p}}, u_{\mathrm{p}}, \xi; t)$ is

$$\frac{\partial f_{XU\Xi}}{\partial t} + \frac{\partial}{\partial x_{\mathrm{p}}}\left[\left(\tau_{\mathrm{p}} u_{\mathrm{p}} + \xi\varphi\right) f_{XU\Xi}\right] + \frac{\partial}{\partial u_{\mathrm{p}}}\left[\left(-u_{\mathrm{p}} + \xi\phi\right) f_{XU\Xi}\right] = 0, \tag{7.37}$$

subject to the initial condition $f_{XU\Xi}(x_{\mathrm{p}}, u_{\mathrm{p}}, \xi; 0) = \delta(x_{\mathrm{p}})\delta(u_{\mathrm{p}} - v_0) f_{\Xi}(\xi)$, which gives rise to the solution (Appendix L)

$$f_{XU\Xi} = \mathrm{e}^t f_{\Xi}(\xi)\delta[x_{\mathrm{p}} - \tau_{\mathrm{p}} v_0(1 - \mathrm{e}^{-t}) - \xi\sigma_X]\,\delta[\mathrm{e}^t(u_{\mathrm{p}} - \xi\sigma_U) - v_0]. \tag{7.38}$$

The marginals of (7.38) are the PDFs of the particle position and velocity,

$$f_X(x_{\mathrm{p}}; t) = \frac{1}{\sigma_X} f_{\Xi}\left(\frac{x_{\mathrm{p}} - \bar{X}_{\mathrm{p}}}{\sigma_X}\right), \tag{7.39}$$

and

$$f_U(u_\mathrm{p};t) = \frac{1}{\sigma_U} f_\Xi\left(\frac{u_\mathrm{p} - \bar{U}_\mathrm{p}}{\sigma_U}\right), \tag{7.40}$$

where $\bar{X}_\mathrm{p}(t)$ and $\bar{U}_\mathrm{p}(t)$ are the means of $X_\mathrm{p}(t)$ and $U_\mathrm{p}(t)$, respectively (given in (K.2.6)). Solutions (7.39) and (7.40) are generalizations of the velocity Langevin model [141], with (7.40) reducing to (7.33) when the random variable $\Xi$ is standard normal, $\Xi \sim \mathcal{N}(0,1)$. The temporal evolution of the PDFs $f_X(x_\mathrm{p};t)$ and $f_U(u_\mathrm{p};t)$ is depicted in Figure 7.3, for the normal, uniform and triangular distributions of $\Xi$. The spatial variations of the PDFs of particle positions and velocity related to non-Gaussian effects (Figs. 7.3b– 7.3c and 7.3e– 7.3f) can not be represented by the Fokker-Plank model (7.31) (Figs. 7.3a and 7.3d). The Liouville approach may be used then to formulate non-Gaussian stochastic models.

When applied to (7.37), the method of characteristics provides a geometric interpretation of the dynamics of the joint PDF $f_{XU\Xi}(x_\mathrm{p}, u_\mathrm{p}, \xi; t)$ and its marginals. The joint PDF $f_{XU\Xi}$ is transported along the characteristics $\boldsymbol{y}(t) = [\hat{x}_\mathrm{p}(t), \hat{u}_\mathrm{p}(t), \xi]^\top$, defined by (L.0.4). This process defines a flow map [5] and is akin to mapping the initial state $f_{XU\Xi}(x_\mathrm{p}, u_\mathrm{p}, \xi; 0)$ onto its counterpart at time $t$ via the method of transformations [265]

$$f_{XU\Xi}(x_\mathrm{p}, u_\mathrm{p}, \xi; 0) = J(t) f_{XU\Xi}(x_\mathrm{p}, u_\mathrm{p}, \xi; t), \quad J = \left|\frac{\partial\, \boldsymbol{y}(t)}{\partial\, \boldsymbol{y}(0)}\right|, \tag{7.41}$$

where $J(t)$ the determinant of the transformation Jacobian. Its direct evaluation from the characteristics equation (L.0.4a) yields $J(t) = \exp(-t)$, which is consistent with (7.38) and (L.0.4b). Numerical evaluation of the Jacobian and the use of the method of transformations, i.e., using (7.41), provides an alternative to computing the solution of (L.0.4b).

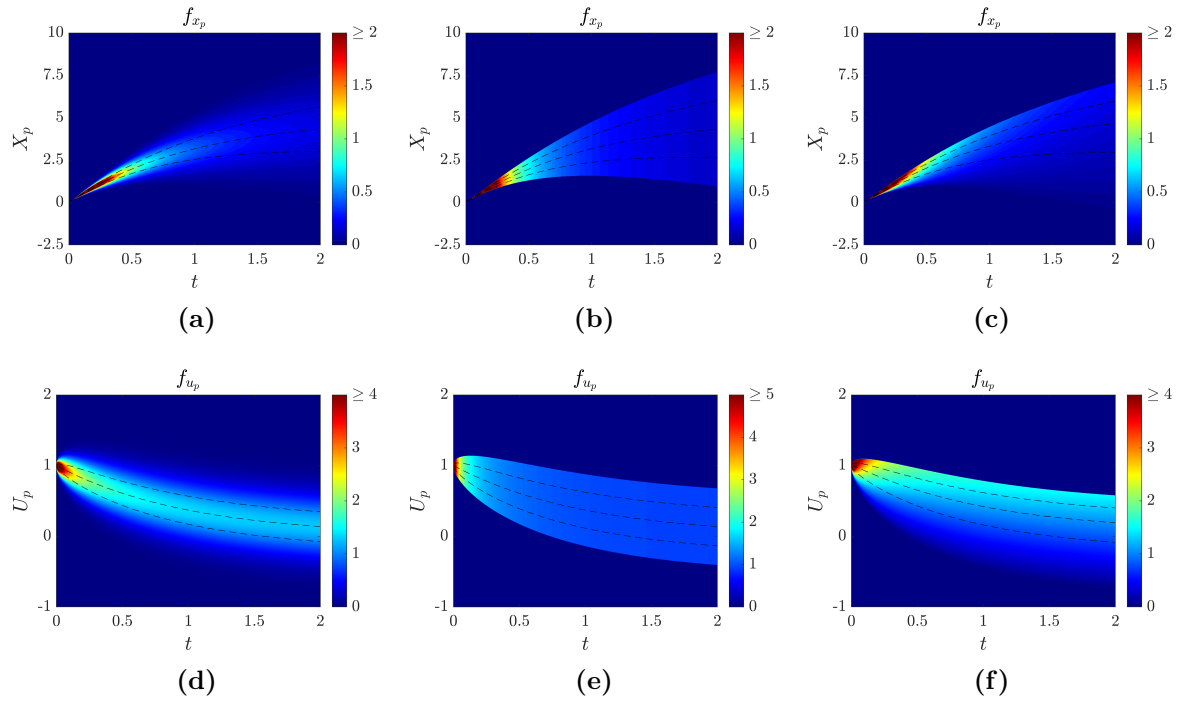


**Figure 7.3.** Temporal evolution of $f_X(x_\mathrm{p};t)$ and $f_U(u_\mathrm{p};t)$, PDFs of the particle trajectory $X_\mathrm{p}(t)$ and velocity $U_\mathrm{p}(t)$, predicted by the Liouville solutions (7.39) and (7.40) for normal (left column), uniform (middle column) and triangular (right column) distributions of the parameter $\Xi$. The deterministic parameters are set to $\tau_\mathrm{p} = 10$, $v_0 = 1$ and $D = 1/50$.

## 7.4 A Liouville model for fluidized homogeneous heating systems

In a fluidized homogeneous heating system (FHHS), particles with diameter $d_\mathrm{p}$ are released into a current of carrier-fluid (with density $\rho_\mathrm{f}$ and viscosity $\mu_\mathrm{f}$). As time increases, the particle velocity $\boldsymbol{U}_\mathrm{p}(t)$ deviates from the fluid velocity in such a way that the variances of the particle velocity along each component reach a steady value. The quantities

$$T = \frac{1}{3}\overline{\boldsymbol{U}'_\mathrm{p}\cdot\boldsymbol{U}'_\mathrm{p}} \quad \text{and} \quad \mathrm{Re}_T = \frac{\rho_\mathrm{f}\, d_\mathrm{p}}{\mu_\mathrm{f}}\sqrt{T} \tag{7.42}$$

are referred to as the granular temperature and the thermal Reynolds number, respectively [143]. Notice that a Reynolds decomposition is used for $\boldsymbol{U}_\mathrm{p} = \bar{\boldsymbol{U}}_\mathrm{p} + \boldsymbol{U}'_\mathrm{p}$. They

have been studied analytically via kinetic theory [261] or empirical treatment of Langevin models [144] and numerically via PR-DNS [1] or Langevin equations [143]. We use these results to ascertain the veracity of a new model based on our Liouville approach.

In a reference frame moving with the average particle velocity [141, 143], a one-dimensional Liouville model of the random particle velocity $U_\mathrm{p}(t)$ is

$$\frac{\mathrm{d}U_\mathrm{p}}{\mathrm{d}t} = -\frac{1}{\tau_\mathrm{p}}U_\mathrm{p} + \Xi\phi, \tag{7.43}$$

such that $T = \sigma_U^2/3$. The random variable $\Xi$ has zero mean, $\bar{\Xi} = 0$, and standard deviation $\sigma_\Xi = \sigma_\Xi(\mathrm{Re_m})$, which depends on the mean Reynolds number in the PR-DNS [143],

$$\mathrm{Re_m} = (1-\omega)\frac{\rho_\mathrm{f} d_\mathrm{p}}{\mu_\mathrm{f}}|\boldsymbol{V}|,$$

where $\boldsymbol{V}$ is the average relative velocity, and $\omega$ is the average particle solid volume fraction. The deterministic function,

$$\phi = \frac{1}{\tau_\mathrm{p}}\left(1-\mathrm{e}^{-\mathcal{C}_1 t/\tau_\mathrm{p}}\right)^{\mathcal{C}_2-1}\left[1+(\mathcal{C}_1\mathcal{C}_2-1)\,\mathrm{e}^{-\mathcal{C}_1 t/\tau_\mathrm{p}}\right] \tag{7.44}$$

is chosen phenomenologically, with the constants $\mathcal{C}_1$ and $\mathcal{C}_2$ characterizing the behavior of the granular temperature $T$ at early and late times, respectively. Both constants depend on $\mathrm{Re_m}$, $\rho_\mathrm{p}/\rho_\mathrm{f}$ and $\omega$, and are adjusted to match the PR-DNS results [1, 144, 143].

The Liouville equation for the joint PDF $f_{U\Xi}(u_\mathrm{p}, \xi; t)$ is

$$\frac{\partial f_{U\Xi}}{\partial t} + \frac{\partial}{\partial u_\mathrm{p}}\left[\left(-\frac{1}{\tau_\mathrm{p}}u_\mathrm{p} + \xi\phi\right) f_{U\Xi}\right] = 0. \tag{7.45}$$

Its solution is (Appendix L)

$$f_{U\Xi} = f^0_{U\Xi}\mathrm{e}^{t/\tau_\mathrm{p}} = \mathrm{e}^{t/\tau_\mathrm{p}} f_\Xi(\xi)\delta[(u_\mathrm{p} - \xi\eta)\mathrm{e}^{t/\tau_\mathrm{p}}] = \frac{1}{\eta} f_\Xi(\xi)\delta\left(\frac{u_\mathrm{p}}{\eta} - \xi\right), \tag{7.46a}$$

where

$$\eta(t) = (1 - \mathrm{e}^{-\mathcal{C}_1 t/\tau_\mathrm{p}})^{\mathcal{C}_2}. \tag{7.46b}$$

The marginalization along $\xi$ gives the PDF of the particle velocity $U_\mathrm{p}(t)$ in FHHS,

$$f_U(u_\mathrm{p}; t) = \int \frac{1}{\eta} f_\Xi(\xi) \delta\left(\frac{u_\mathrm{p}}{\eta} - \xi\right) \mathrm{d}\xi = \frac{1}{\eta} f_\Xi\left(\frac{u_\mathrm{p}}{\eta}\right). \tag{7.47}$$

In accordance with (7.42), the variance of this PDF, $\sigma_U^2(t)$, is proportional to granular temperature $T(t)$. If $\Xi$ were Gaussian, $f_\Xi \sim \mathcal{N}(0, \sigma_\Xi^2)$, then

$$\bar{U}_\mathrm{p}(t) = \bar{U}_\mathrm{p}(0)\mathrm{e}^{-t/\tau_\mathrm{p}} \quad \text{and} \quad \sigma_U^2(t) = \sigma_\Xi^2(1 - \mathrm{e}^{-\mathcal{C}_1 t/\tau_\mathrm{p}})^{2\mathcal{C}_2}. \tag{7.48}$$

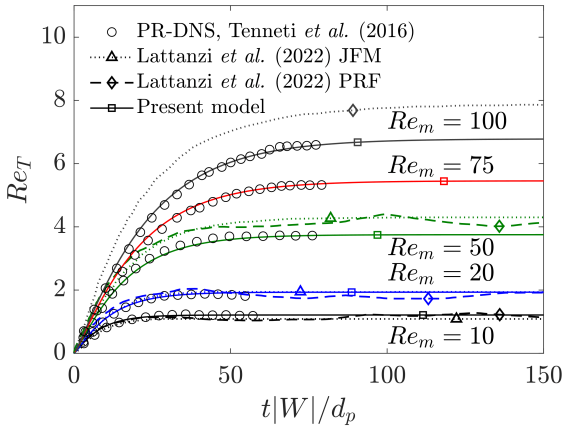


**Figure 7.4.** Temporal evolution of the thermal Reynolds number $Re_T(t)$ alternatively predicted with our model (7.48) (solid lines with square symbol), the model of Ref. [144] (dotted lines with triangle symbol) and the Langevin approach of Ref. [143] (dashed lines with diamond symbol), for several values of the mean Reynolds number $\mathrm{Re_m}$. The open circles indicate the PR-DNS data [1, 143], to which $\sigma_\Xi = \sigma_\Xi(\mathrm{Re_m})$ and $\mathcal{C}_1 = \mathcal{C}_1(\mathrm{Re_m})$ are fitted (Fig. 7.5). The average volume fraction and density ratio are $\omega = 0.1$ and $\rho_\mathrm{p}/\rho_\mathrm{f} = 100$ respectively. For all cases $\mathcal{C}_2 = 1.2$ and $\tau_\mathrm{p} = 0.14$.

Figure 7.4 exhibits the granular temperature predicted with this solution, $T(t) = \sigma_U^2/3$, for $\tau_\mathrm{p} = 0.14$, $\rho_\mathrm{p}/\rho_\mathrm{f} = 100$ and $\omega = 0.1$ [143]. The functional dependencies

$\sigma_\Xi = \sigma_\Xi(\mathrm{Re_m})$ and $\mathcal{C}_1 = \mathcal{C}_1(\mathrm{Re_m})$ are obtained by fitting the predictions of $T(t)$ from (7.48) to the PR-DNS data from Ref. [1] This fitting reveals that both $\sigma_\Xi$ and $\mathcal{C}_1$ depend linearly in a log-log scale on $\mathrm{Re_m}$ (Fig. 7.5), whereas $\mathcal{C}_2$ is constant ($\mathcal{C}_2 = 1.2$). Our model matches the PR-DNS data better than its Langevin alternatives [143, 144]. It captures both the early growth and asymptotic values of $T(t)$, while the models of Refs. [144, 143] underestimate the steady values of $T(t)$ and predict the unphysical/unobserved long-term fluctuations in $T(t)$, respectively.

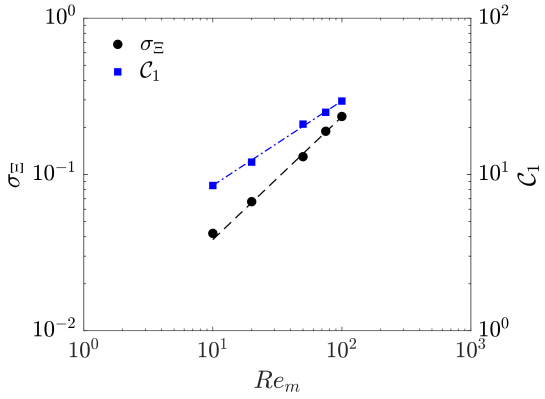


**Figure 7.5.** Functional dependencies of the model parameters $\sigma_\Xi$ and $\mathcal{C}_1$ on the mean Reynolds number $\mathrm{Re_m}$. The squares and circles indicate the values of $\sigma_\Xi$ and $\mathcal{C}_1$ obtained via fitting (7.48) to the PR-DNS data [1] for $\rho_\mathrm{p}/\rho_\mathrm{f} = 100$ and $\omega = 0.1$. These data are represented by $\log(\sigma_\Xi) = 0.06258\log(\mathrm{Re_m}) + \log(0.7866)$ and $\log(\mathcal{C}_1) = 2.446\log(\mathrm{Re_m}) + \log(0.5411)$, with the coefficient of determination $R^2 = 0.998$.

### 7.4.1 Phenomenology of granular-temperature dynamics

It has been argued that granular temperature in a FHHS, $T(t)$, exhibits the source-and-sink dynamics [261, 1, 144],

$$\frac{\mathrm{d}T}{\mathrm{d}t} = S(T) - \Gamma(T). \tag{7.49}$$

In Ref. [261], the source is taken to be $S \sim T^{-1/2}$, which is singular at $T = 0$, i.e., at initial time $t = 0$. In contrast, the ensemble averaging of our Liouville model (7.43) gives

rise to the source $S(T)$ and sink $\Gamma(T)$ (see Appendix J for detail),

$$S = \frac{2}{\sqrt{3}}\sigma_{\Xi}\phi T^{1/2} \quad \text{and} \quad \Gamma = \frac{2}{\tau_{\mathrm{p}}}T, \tag{7.50}$$

that behave well at $T = 0$. Figure 7.6 exhibits the curves $S(T)$ and $\Gamma(T)$ given by (7.50) and by the model in Ref. [261]] in comparison with PR-DNS data [1]. While the mismatch between both models and the data is noticeable, our model exhibit the correct qualitative behavior, while the model in Ref. [261] does not.

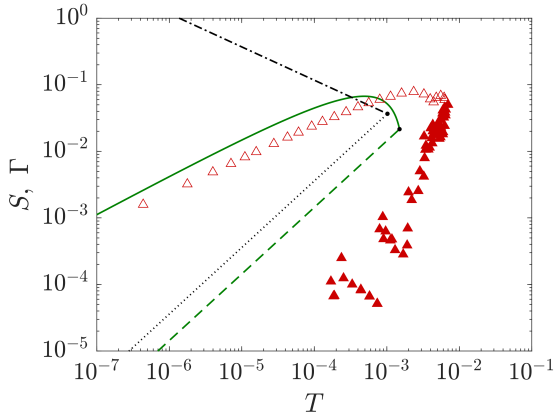


**Figure 7.6.** The source, $S(T)$, and sink, $\Gamma(T)$, terms in the granular-temperature model (7.49). Our model (7.50) yields the solid and dashed green lines for $S(T)$ and $\Gamma(T)$, respectively. The model of Ref. [261] has $S(T)$ and $\Gamma(T)$ depicted by the dash-dotted and dotted black lines, respectively. The PR-DNS estimates of $S(T)$ and $\Gamma(T)$[1] are represented by the non-filled and filled red triangles, respectively. The parameter values are $\mathrm{Re_m} = 20$, $\rho_{\mathrm{p}}/\rho_{\mathrm{f}} = 100$ and $\omega = 0.1$.

### 7.4.2 Particle-velocity distributions

A Langevin counterpart to our Liouville model (7.43) is a stochastic ODE $\mathrm{d}U_{\mathrm{p}} = -(1/\tau_{\mathrm{p}})U_{\mathrm{p}}\mathrm{d}t + \sqrt{2D}\mathrm{d}W$, which gives rise to the Fokker-Planck equation for the particle velocity PDF, $f_U(u_{\mathrm{p}}; t)$,

$$\frac{\partial f_U}{\partial t} - \frac{\partial}{\partial u_{\mathrm{p}}}\left(\frac{1}{\tau_{\mathrm{p}}}u_{\mathrm{p}}f_U\right) = \frac{\partial}{\partial u_{\mathrm{p}}}\left(D\frac{\partial f_U}{\partial u_{\mathrm{p}}}\right). \tag{7.51}$$

Many studies focus on the numerical determination of the diffusion coefficient $D(u_\mathrm{p}, t)$ using the standard deviation of particle acceleration and its integral time scale [143] or directly fitting a correlation from PR-DNS data [1]. Our Liouville approach provides an alternative means to accomplish this task analytically. Substituting $f_U(u_\mathrm{p}; t)$ from (7.47) into (7.51) yields a second-order ODE for $D(u_\mathrm{p}, \cdot)$, whose solution is

$$D = \eta\phi\sigma_\Xi^2 + \frac{K}{u_\mathrm{p}} \exp\left(\frac{u_\mathrm{p}^2}{2\eta^2\sigma_\Xi^2}\right), \tag{7.52}$$

with $K$ an integration constant whose value is not constrain by the compatibility condition (see (7.11) and (7.17)), and it is an extra degree of freedom of the model. Here we choose $K = 0$, such that the diffusion coefficient is simply $D = \eta\phi\sigma_\Xi^2$. Using the analytical relations derived previously, the diffusion tensor can be expressed in terms of the granular temperature as

$$D = \frac{3}{\tau_\mathrm{p}} \left[ (1 - \mathcal{C}_1\mathcal{C}_2)\, T + \frac{\mathcal{C}_1\mathcal{C}_2\sigma_\Xi^{1/\mathcal{C}_2}}{3^{1/(2\mathcal{C}_2)}} T^{1-1/(2\mathcal{C}_2)} \right]. \tag{7.53}$$

Models in the literature [1, 143] and, in general, numerical approximations of the diffusion coefficient in the Langevin approach are not consistently linked to Fokker-Planck equations and an equivalent PDF formulation is seldom investigated. Moreover, the full statistical description is provided by a PDF description (7.46a). The model presented here with the Liouville approach leads to equivalent Langevin and Fokker-Planck formulations. In Fig 7.7 we compare the derived diffusion coefficient (7.53) with the model proposed in Ref. [1], showing agreement at lower values of the granular temperature, linked to the evolution at the early times of the FHHS. The model in Ref. [1] is based on a correlation that contains 8 constants fitted from PR-DNS data.

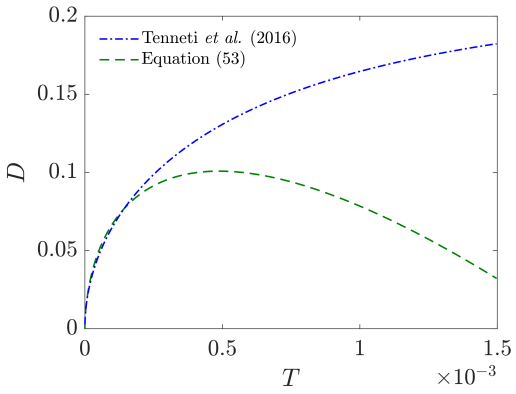


**Figure 7.7.** Diffusion coefficient in terms of the granular temperature in the model presented in Ref. [1] and the one developed here, equation (7.53), for $\mathrm{Re}_m = 20$, $\omega = 0.1$, $\rho_\mathrm{p}/\rho_\mathrm{f} = 100$ and $\tau_\mathrm{p} = 0.14$.

## 7.5 Discussion

The advantage of the Liouville approach is obvious, the source and sink terms for the evolution of the granular temperature can be proposed starting from defining the standard deviations of the particle velocity (7.48) based on phenomenology. Then, we proceed to find the source term $\phi$ going back to the characteristics that can be analytically described. The model also leads a diffusion coefficient that can be computed accordingly by comparing the Fokker-Planck equation with the marginalized Liouville equation. Trying to formulate the problem from the Langevin perspective without previous knowledge of the diffusion coefficient and arrive at the expression in (7.52) is a hard task. The procedure can be used to develop a model based on the time evolution of $T$ reported in PR-DNS results by adjusting the parameters $\sigma_\Xi$, $\mathcal{C}_1$ and $\mathcal{C}_2$.

The temporal evolution of the granular temperature in FHHS is characterized by a source and sink behavior [1] stabilizing at a constant value after an initial growth. To this purpose, the parameter $\sigma_\Xi$ is responsible for the steady value, and the coefficients $\mathcal{C}_1$ and $\mathcal{C}_2$ characterize the growth of the granular temperature at two distinguished time scales, at early and later times respectively. The Langevin models in Ref. [141] correspond

to ODE systems with a random coefficient in the Liouville approach with source terms not defined at the initial time, making the solution singular at $t = 0$, corresponding to an initial infinite impulse of the particles (events moving in phase space). See the previous Sections 7.3.1 and 7.3.2 that reproduce results reported in Ref. [141]. Another model where the solution is not defined at the initial time is the one presented in Ref. [261], where the granular temperature grows infinitely at the initial time. In our model, the initial impulse in the granular temperature is bounded and governed by the parameter $\mathcal{C}_2$, leading to an ODE system whose solution is bounded at $t = 0$.

## 7.6 Summary of results

A framework to formulate stochastic descriptions of particle-laden flows based on a Liouville PDF governing equation introduced. A connection between Langevin dynamical systems and the new Liouville approach allows to analytically treat the solution with the method of characteristics and circumvent numerical difficulties related to Itô calculus and the numerical resolution of the Fokker-Planck equation. The Liouville approach is based on expressing stochastic processes with random coefficients constants in time and additional source terms. The problem is then governed by the Liouville equation that can be derived with the method of distributions in an augmented dimensionality that includes the added random coefficients, the particle position and particle velocity. With proper selection of the random coefficients and source terms, both Langevin and Liouville approaches coincide. This implies that the Liouville equation marginalized along the extra dimension of the random coefficients leads to the Fokker-Planck equation of an equivalent Langevin system.

The Liouville approach is compared with canonical Eulerian-Lagrangian models of particle-laden flows formulated with Langevin equations used to obtain the time evolution of particle dispersion and granular temperature in the literature. We develop a full

description of the statistics with the Liouville approach, that analytically describes exact results of the PDFs of the particle position and velocity as well as their moments.

The potential of the Liouville approach to develop modeling of particle statistics is assessed by proposing a phenomenological model to FHHS. Based on the analytical character of the Liouville approach, the sink and source terms that govern the time evolution of the granular temperature can be represented in the Liouville approach by selecting a source term that depends on the non-dimensional parameters of the problem. This leads to matching of PR-DNS results more accurately than previous proposed numerical and analytical models based on the Langevin approach. The FHHS model presented here also eliminates the singularity at the initial time in the granular temperature equation, that leads to an ill-posed problem that contains an initial infinite impulse. Previous models in the literature did not offer descriptions of the granular temperature without such singularity. This singularity at the initial time can be interpreted as an initial infinite impulse by virtue of the Liouville approach that links events with possible particles. Such events are associated with deterministic characteristic equations that are derived from the Liouville equation with the method of characteristics. The hyperbolicity of the Liouville equation is therefore advantageous as opposed to the advection-diffusion character of the Fokker-Planck equation. The model presented here is well posed at the initial time and describes the early evolution of the granular temperature accurately as compared with PR-DNS. Additionally, the Liouville approach may be used to find the diffusion coefficient and with it other descriptions of the same problem based on the Fokker-Planck or Langevin equations.

The Liouville approach may be used to describe other Langevin dynamical systems in general, making its numerical treatment simpler. It is not bounded by Gaussianity and does not rely on sampling nor requires closure. It opens new possibilities in proposing reduced models that capture statistics obtained with PR-DNS. Moreover, because events and their probability to occur are traced deterministically, each event has a deterministic

equation given by the characteristics that can be physically interpreted as a possible particle in the system. Then each event is associated with a physical particle and how likely to occur is that particle in the system. Therefore it provides a connection between the statistics and the particle physics.

Additionally, moment equations provide a reduced description, which may lead to closure challenges depending on the non-linearity of the particle equations. In the results presented here, the moment equations are found in closed form.

## 7.7 Acknowledgments

Sections 7.1 through 7.6 are a reprint of the material as it appears in Ref. [7], "Liouville models of particle-laden flow", D. Domínguez-Vázquez, G. B. Jacobs and D. M. Tartakovsky. D. Domínguez-Vázquez: conceptualization, investigation, methodology, visualization, original draft preparation. G. B. Jacobs: conceptualization, supervision, review & editing. D. M. Tartakovsky: conceptualization, supervision, review & editing.

# Chapter 8

# Concluding remarks

## 8.1 Conclusions

The influence of randomness in a point-particle forcing on the statistical description of particle-laden flow is modeled with Monte Carlo methods, a method of moments, and a method of distributions. The PDF and a cloud perspective provide confidence intervals in the solution over finite times.

A center piece of the formulations is the random forcing model that relies on series expansions to express uncertainty in the particle forcing, as a result of deviations of the physical conditions from a Stokes flow over a spherical particle. By assuming a random forcing law, both the effect of epistemic and aleatoric uncertainty can be modeled. Stochastic models should therefor be considered a subset of the random models, which do not account for incomplete descriptions of the particle dynamics not based on first principles, as it is the case of empirical forcing laws.

As compared to Monte Carlo, the cloud model offers computational efficiency in computing a reduced statistical description such as the first two moments of the particle phase variables. We build upon the previously presented SPARSE description in Davis *et al.* (2017) by including second moments of the particle variables in the cloud region; including a closure model; including the consideration of randomness in the forcing in its extended SPARSE-R version; and approximating moments higher than second and

PDFs of the particle phase variables. A third order convergence rate with the standard deviations of the initial condition is shown, ensuring computational savings as compared to Monte Carlo simulations by splitting the initial condition. The SPARSE-R model then propagates the confidence intervals in the forcing function into quantifiable measures of uncertainty of the particle phase variables (second moments) in closed-form. It provides a scalable method suitable for complex three-dimensional flows, shown to compute accurately the first two moments by a fraction of the computational cost of Monte Carlo.

Using the method of distributions, a deterministic Eulerian (hyperbolic) PDF model is derived that provides a complete statistical description of the randomly forced particle phase. It does not use truncation or closure approximations as it was done in SPARSE and SPARSE-R. This model accounts for both, aleatoric and epistemic uncertainties in the forcing. The Eulerian PDF solution computed with a high-order spectral method preserves moment accuracy of the PDFs, which lower-order finite difference methods do not. The description of deterministic initial conditions in the Eulerian formulation numerically, requires the use of regularized Dirac delta functions, originally developed to approximate singular source terms in EL systems. The vanishing moment condition of such approximations conditions the accuracy of the Eulerian model regardless of the discretization scheme in space and time. This PDF model requires more computational resources than SPARSE and SPARSE-R methods, as it involves the solution of a high-dimensional hyperbolic PDE with high-order methods instead of ODE systems. However, it offers full a statistical description.

Exploiting the hyperbolic character of the developed Eulerian PDF model, a deterministic Lagrangian PDF framework for its accurate numerical resolution is proposed, based on the application of the method of characteristics to the governing PDF equation. This novel framework provided an alternative to traditional Eulerian models, offering analytical tractability and a deeper understanding of particle dynamics in fluid flows. Isolated (rare) events in the parameter space can be traced independently. Moreover,

sampling techniques are not required and yet, the Lagrangian character of the model is preserved, as opposed to Langevin methods. The curse of dimensionality is alleviated by the use of flow maps which trace only the surroundings of groups of particles in Lagrangian form, reducing the computational domain of consideration as compared to the Eulerian counterpart. Several orders of magnitudes in computational savings have been reported in this work for canonical examples. Additionally, only the domain of influence of the initial conditions has to be prescribed at the initial time, which will evolve in time in a Lagrangian sense. On the contrary, the Eulerian model requires to prescribe the full domain that the particle phase in position and velocity space will occupy at any later time. This might not be known a priori, which becomes a difficulty to provide initial conditions to the Eulerian model.

A method of inference of a particle forcing law from sparse, noisy measurements is also introduced that uses the adjoint equations to a randomly forced particle model. By integrating adjoint particle dynamics with Hamiltonian Markov Chain methods, we demonstrated the framework's effectiveness in accurately identifying forcing functions and quantifying uncertainty. This data-driven approach represented a significant advancement in our ability to infer particle behavior from limited observational data, opening new avenues for predictive modeling and analysis.

Finally, a Liouville PDF approach is introduced, offering an alternative to Langevin dynamical systems and Eulerian PDF models such as the Fokker-Planck model. This approach, characterized by its simplicity and analytical tractability, holds promise for advancing modeling capabilities and understanding particle-laden flows. Most notably, it allows the use of the method of characteristics, offering a geometrical interpretation of the statistical description of particle systems. Generalization for non-Gaussian systems become natural to this description, where non-Gaussian analytical solutions to particle models based on Wiener increments are extended for non-Gaussianity *analytically*. The development of reduced stochastic models from limited data may benefit from the mathematical properties

of this approach, as demonstrated by proposing a stochastic model for FHHS from reported statistics in the literature.

## 8.2 Future work

Future works include extension of the methods here developed to two-way coupling regime. In ongoing work, a two-way coupled PDF framework is developed that quantifies uncertainty related to the use of non-deterministic point-particle models. Different dependencies of the random particle forcing, not based on the relative velocity, such as particle shapes, may also be an avenue of future research.

Extension of SPARSE and SPARSE-R to account for higher order statistics in each kernel (subcloud) are also future research work. In ongoing efforts, the adjoint formulation is derived for both PDF and moment descriptions of the particle statistics.

# Appendix A

# Derivation of the PDF equation using the method of distributions

Here, a PDF equation is developed to solve the stochastic system defined by (2.1) with the so-called method of distributions. Firstly, we define the fine-grained JPDF $\Pi$ as

$$\Pi(A, a; X_p, x_p; U_p, u_p; t) = \delta(A - a)\delta(X_p - x_p(t))\delta\left(U_p - u_p(t)\right), \tag{A.1}$$

where $A$, $X_p$ and $U_p$ are deterministic magnitudes and $\delta(\cdot)$ is the Dirac delta function. Taking the derivative of $\Pi$ with respect to time and using the chain rule and the Dirac delta properties we find

$$\frac{\partial \Pi}{\partial t} = \frac{dx_p}{dt}\frac{\partial \Pi}{\partial x_p} + \frac{du_p}{dt}\frac{\partial \Pi}{\partial u_p} = -\frac{dx_p}{dt}\frac{\partial \Pi}{\partial X_p} - \frac{du_p}{dt}\frac{\partial \Pi}{\partial U_p}, \tag{A.2}$$

where we can make use of (2.1) for writing

$$\frac{\partial \Pi}{\partial t} + u_p\frac{\partial \Pi}{\partial X_p} + \frac{ag\left(u - u_p\right)}{\tau_p}(u - u_p)\frac{\partial \Pi}{\partial U_p} = 0, \tag{A.3}$$

that in conservative form is

$$\frac{\partial \Pi}{\partial t} + \frac{\partial}{\partial X_p}\left(u_p\Pi\right) + \frac{\partial}{\partial U_p}\left[\frac{ag(u - u_p)}{\tau_p}(u - u_p)\Pi\right] = 0. \tag{A.4}$$

Defining the ensemble mean of an integrable function $h(a, x_p, u_p)$ with the joint PDF $f_{ax_pu_p}$ as

$$E[h(a, x_p, u_p)] = \iiint_{-\infty}^{\infty} h(A', X'_p, U_p) f_{ax_pu_p}(A', X'_p, U'_p; t) \mathrm{d}A' \mathrm{d}X'_p \mathrm{d}U'_p, \tag{A.5}$$

the ensemble of the function $\Pi$ for a particular set of the deterministic variables is obtained as

$$\begin{aligned} E[\Pi] &= \iiint_{-\infty}^{\infty} \Pi(A, A'; X_p, X'_p, U_p, U'_p; t) f_{ax_pu_p}(A', X'_p, U'_p; t) dA' dX'_p dU'_p \\ &= \iiint_{-\infty}^{\infty} \delta(A - A') \delta(X_p - X'_p) \delta(U_p - U'_p) f_{ax_pu_p}(A', X'_p, U'_p; t) dA' dX'_p dU'_p \\ &= f_{ax_pu_p}(A, X_p, U_p; t). \end{aligned} \tag{A.6}$$

This procedure suggests how to obtain a partial differential equation for $f_{ax_pu_p}$ from (A.4) taking the ensemble mean each term. To do so, we need to use the property that allows us to exchange expectation with derivatives respect to deterministic variables. For example, for the deterministic variable time, one has

$$E\left[\frac{\partial h(a, x_p, u_p)}{\partial t}\right] = \frac{\partial E[h(a, x_p, u_p)]}{\partial t}. \tag{A.7}$$

Using this property, the ensemble mean of the first term in (A.4) is trivial

$$E\left[\frac{\partial \Pi}{\partial t}\right] = \frac{\partial f_{ax_pu_p}}{\partial t}. \tag{A.8}$$

The second is calculated as

$$
\begin{aligned}
E\left[\frac{\partial\left(u_p\Pi\right)}{\partial X_p}\right] &= \frac{\partial}{\partial X_p}E\left[u_p\Pi\right] \\
&= \frac{\partial}{\partial X_p}\left[\iiint_{-\infty}^{\infty} U_p'\Pi(A,A';X_p,X_p';U_p,U_p';t)f_{ax_pu_p}(A',X_p',U_p';t)dA'dX_p'dU_p'\right] \\
&= \frac{\partial}{\partial X_p}\left[\iiint_{-\infty}^{\infty} U_p'\delta(A-A')\delta(X_p-X_p')\delta(U_p-U_p')f_{ax_pu_p}(A',X_p',U_p';t)dA'dX_p'dU_p\right] \\
&= \frac{\partial}{\partial X_p}\left(U_pf_{ax_pu_p}\right).
\end{aligned}
\tag{A.9}
$$

In the same way, the third term is

$$
E\left[\frac{\partial}{\partial U_p}\left(\frac{ag\left(u-u_p\right)}{\tau_p}(u-u_p)\Pi\right)\right] = \frac{\partial}{\partial U_p}\left(\frac{Ag\left(U-U_p\right)}{\tau_p}(U-U_p)f_{ax_pu_p}\right), \tag{A.10}
$$

where for coherence we make use of $U$ as the deterministic value of the carrier flow. In this study, the carrier flow is considered deterministic and therefore $u = U$.

Finally, the deterministic equation that governs the joint probability density function of the solution is

$$
\frac{\partial f_{ax_pu_p}}{\partial t} + \frac{\partial}{\partial X_p}\left(U_pf_{ax_pu_p}\right) + \frac{\partial}{\partial U_p}\left(\frac{Ag(U-U_p)}{\tau_p}(U-U_p)f_{ax_pu_p}\right) = 0. \tag{A.11}
$$

This equation has to be solved with deterministic or stochastic initial conditions defined by (2.7) or (2.6), and also be marginalized according to

$$
f_{x_pu_p}(X_p,U_p;t) = \int_{-\infty}^{\infty} f_{ax_pu_p}(A,X_p,U_p;t)dA, \tag{A.12}
$$

$$
f_{x_p}(X_p;t) = \int_{-\infty}^{\infty} f_{x_pu_p}(X_p,U_p;t)dU_p, \tag{A.13}
$$

$$
f_{u_p}(U_p;t) = \int_{-\infty}^{\infty} f_{x_pu_p}(X_p,U_p;t)dX_p. \tag{A.14}
$$

We also define here the $n^{th}$ moment about $c$ of a continuum random variable $x$ with PDF $f_x(x)$ as

$$\mu_n = \int_{-\infty}^{\infty} (x-c)^n f_x(x) dx, \tag{A.15}$$

where if $n = 1$ and $c = 0$ we obtain the mean $\mu_x$, and if $c$ is selected to be the mean, we find the $n^{th}$ central moment of $f_x$.

# Appendix B

# Deterministic analytical solution of the test cases

## B.1 Uniform flow

For the uniform flow where $u$ is constant, the system of equations (2.1) can be expressed as a first order ODE system with constant coefficients for $x_p(t)$ and $u_p(t)$

$$\frac{d}{dt}\begin{bmatrix} x_p \\ u_p \end{bmatrix} = \begin{bmatrix} 0 & 1 \\ 0 & -b \end{bmatrix}\begin{bmatrix} x_p \\ u_p \end{bmatrix} + \begin{bmatrix} 0 \\ bu \end{bmatrix}, \tag{B.1}$$

a second order ODE for $x_p(t)$

$$\frac{d^2x_p}{dt^2} + b\frac{dx_p}{dt} = bu, \tag{B.2}$$

a first order ODE for $u_p(t)$

$$\frac{du_p}{dt} + bu_p = bu, \tag{B.3}$$

or as a differential equation of separable variables for the phase space $u_p(x_p)$ as the system (2.1) becomes autonomous

$$\frac{du_p}{dx_p} = \frac{b\,(u - u_p)}{u_p}. \tag{B.4}$$

The analytical solution of $x_p(t)$ and $u_p(t)$ is trivially obtained solving any of the above options as

$$x_p(t) = x_{p_0} + ut + \frac{1}{b}(u - u_{p_0})\left(e^{-bt} - 1\right), \tag{B.5}$$

$$u_p(t) = u + (u_{p_0} - u)e^{-bt}. \tag{B.6}$$

The time can be removed combining the last two equations to find the solution in the particle phase as $u_p(x_p)$.

## B.2 Stagnation flow

For the center line of the stagnation flow $y = 0$, the carrier flow is $u = -kx = -kx_p$ after interpolating at the particle location according to Hiemenz solution [176]. The system (2.1) can be described as a first ODE system of constant coefficients

$$\frac{d}{dt}\begin{bmatrix} x_p \\ u_p \end{bmatrix} = \begin{bmatrix} 0 & 1 \\ -kb & -b \end{bmatrix}\begin{bmatrix} x_p \\ u_p \end{bmatrix}, \tag{B.7}$$

a second order ODE for $x_p(t)$

$$\frac{d^2x_p}{dt^2} + b\frac{dx_p}{dt} + kbx_p = 0, \tag{B.8}$$

or an integrable equation for the particle phase $u_p(x_p)$

$$\frac{du_p}{dx_p} = -\frac{b\,(kx_p + u_p)}{u_p}. \tag{B.9}$$

Writing the system (B.7) as $\mathbf{z}'(t) = B\mathbf{z(t)}$, with the initial condition $\mathbf{z}(0) = \mathbf{z}_0$, where

$$\mathbf{z}'(t) = \begin{bmatrix} x_p(t) \\ u_p(t) \end{bmatrix}, \quad \mathbf{z}_0 = \begin{bmatrix} x_{p_0} \\ u_{p_0} \end{bmatrix}, \quad B = \begin{bmatrix} 0 & 1 \\ -bk & -b \end{bmatrix}, \tag{B.10}$$

the analytical solution is given by

$$\mathbf{z}(t) = e^{Bt}\mathbf{z}_0. \tag{B.11}$$

Using the eigen decomposition $B = S\Lambda S^{-1}$, the exponential matrix can be obtained as

$$e^{Bt} = Se^{\Lambda t}S^{-1}, \tag{B.12}$$

with

$$S = \begin{bmatrix} \frac{-1+\sqrt{b-4k}}{2k\sqrt{b}} & \frac{-1-\sqrt{b-4k}}{2k\sqrt{b}} \\ 1 & 1 \end{bmatrix}, \quad \Lambda = \begin{bmatrix} \lambda_1 & 0 \\ 0 & \lambda_2 \end{bmatrix}, \tag{B.13}$$

and

$$\lambda_1 = \frac{-b - \sqrt{b\,(b-4k)}}{2}, \quad \lambda_2 = \frac{-b + \sqrt{b\,(b-4k)}}{2}. \tag{B.14}$$

Finally, the exponential matrix is

$$e^{\Lambda t} = \begin{bmatrix} e^{\lambda_1 t} & 0 \\ 0 & e^{\lambda_2 t} \end{bmatrix}, \tag{B.15}$$

and the analytical solution can be expressed as

$$x_p(t) = e^{-\frac{bt}{2}} \left[ \frac{b x_{p_0} + 2u_{p_0}}{\gamma} \sinh\left(\frac{t\gamma}{2}\right) + x_{p_0} \cosh\left(\frac{t\gamma}{2}\right) \right], \tag{B.16}$$

and

$$u_p(t) = \frac{1}{2\gamma} e^{-\frac{t(\gamma+b)}{2}} \left[ u_{p_0}\gamma \left(e^{\gamma t} + 1\right) - b\left(e^{\gamma t} - 1\right)\left(2k x_{p_0} + u_{p_0}\right) \right], \tag{B.17}$$

where $\gamma = \sqrt{b}\sqrt{b - 4k}$.

Just for completion, in the case $b = 4k$, the matrix $S$ is singular, and the Jordan decomposition $B = MJM^{-1}$ is required [268] to find the exponential matrix defined as $e^{Bt} = Me^{Jt}M^{-1}$ with

$$M = \begin{bmatrix} -1/(2k) & -1/(4k^2) \\ 1 & 0 \end{bmatrix}, \quad J = \begin{bmatrix} -2k & 1 \\ 0 & -2k \end{bmatrix}, \tag{B.18}$$

so that one has

$$e^{Jt} = \begin{bmatrix} e^{-2kt} & e^{-2kt}t \\ 0 & e^{-2kt} \end{bmatrix}, \tag{B.19}$$

and the analytical solution changes to

$$x_p(t) = e^{-2kt}\left[x_{p_0} + t\left(2kx_{p_0} + u_{p_0}\right)\right], \tag{B.20}$$

$$u_p(t) = e^{-2kt}\left[u_{p_0} - 2kt\left(2kx_{p_0} + u_{p_0}\right)\right]. \tag{B.21}$$

# Appendix C

# Expected convergence of SPARSE-R

Here, the expected convergence rate of the SPARSE–R formulation with respect to the size of the initial cloud is derived. Consider the Taylor expansion of the forcing function $f_1$ around the average values of the particle cloud in a one–dimensional setting, we can find the next term omitted in the SPARSE–R method by tracking the leading order term of the Taylor series that were neglected previously in the SPARSE formulation (4.6) and (4.11)–(4.18). Looking at the approximation of the average forcing $f_1$ given in (4.14) and retaining terms on the order to fluctuations to the third power one has

$$\begin{aligned}\overline{f_1(\alpha,a)} &\approx \overline{A_{00}+A_{10}\alpha'+A_{01}a'+A_{20}\alpha'^2+A_{11}\alpha'a'+A_{02}a'^2+A_{30}\alpha'^3+A_{21}\alpha'^2a'+A_{12}\alpha'a'^2+A_{03}\alpha'^3}\\ &= A_{00}+A_{11}\overline{\alpha'a'}+A_{02}\overline{a'^2}+A_{12}\overline{\alpha'a'^2}+A_{03}\overline{a'^3}\end{aligned} \tag{C.1}$$

where we have considered that $\partial^2 f_1/\partial\alpha^2 = \partial^3 f_1/\partial\alpha^3 = 0$ and the constants $A_{ij}$ are defined by

$$A_{ij} = \left.\frac{\partial^{(i+j)} f_1}{\partial\alpha^{(i)}\partial a^{(j)}}\right|_{\overline{\alpha},\overline{a}}, \tag{C.2}$$

where the superscript in parenthesis indicates the order of the partial derivative.

Then, using the definition of the relative velocity $\boldsymbol{a} = \boldsymbol{u} - \boldsymbol{u}_p$ we arrive to

$$\begin{aligned}\overline{f(\alpha,a)} \approx A_{00} &+ A_{11}\left(\overline{\alpha' u'} - \overline{\alpha' u'_p}\right) + A_{02}\left(\overline{u'^2} - 2\overline{u' u'_p} + \overline{u'^2_p}\right) \\ &+ A_{12}\left(\overline{\alpha' u'^2} - 2\overline{\alpha' u' u'_p} + \overline{\alpha' u'^2_p}\right) + A_{03}\left(\overline{u'^3} + 3\overline{u' u'^2_p} - 3\overline{u'^2 u'_p} - \overline{u'^3_p}\right),\end{aligned} \tag{C.3}$$

that can be related to variables of the particle phase using the closure (4.11)–(4.18)

$$\begin{aligned}\overline{f(\alpha,a)} \approx A_{00} &+ A_{11}\left[\left(B_1\overline{\alpha' x'_p} + B_2\overline{\alpha' x'^2_p}\right) - \overline{\alpha' u'_p}\right] \\ &+ A_{02}\left[\left(B_1^2\overline{x'^2_p} + 2B_1B_2\overline{x'^3_p}\right) - 2\left(B_1\overline{x'_p u'_p} + B_2\overline{x'_p u'^2_p}\right) + \overline{u'^2_p}\right] \\ &+ A_{12}\left[B_1^2\overline{\alpha' x'^2_p} - 2B_1\overline{\alpha' x'_p u'_p} + \overline{\alpha' u'^2_p}\right] \\ &+ A_{03}\left(B_1^3\overline{x'^3_p} + 3B_1\overline{x'_p u'^2_p} - 3B_1^2\overline{x'^2_p u'_p} - \overline{u'^3_p}\right),\end{aligned} \tag{C.4}$$

where the constants are $B_1$ and $B_2$ are defined as

$$B_1 = \left.\frac{\partial u}{\partial x}\right|_{\overline{x}_p}, \qquad B_2 = \left.\frac{\partial^2 u}{\partial x^2}\right|_{\overline{x}_p}, \tag{C.5}$$

and reordering one has

$$\begin{aligned}\overline{f(\alpha,a)} \approx \overbrace{A_{00} + A_{11}\left(B_1\overline{\alpha' x'_p} - \overline{\alpha' u'_p}\right) + A_{02}\left(B_1^2\overline{x'^2_p} - 2B_1\overline{x'_p u'_p} + \overline{u'^2_p}\right)}^{\text{Terms included in SPARSE}} &+ A_{11}B_2\overline{\alpha' x'^2_p} \\ &+ 2A_{02}\left(B_1B_2\overline{x'^3_p} - B_2\overline{x'_p u'^2_p}\right) + A_{12}\left(B_1^2\overline{\alpha' x'^2_p} - 2B_1\overline{\alpha' x'_p u'_p} + \overline{\alpha' u'^2_p}\right) \\ &+ A_{03}\left(B_1^3\overline{x'^3_p} + 3B_1\overline{x'_p u'^2_p} - 3B_1^2\overline{x'^2_p u'_p} - \overline{u'^3_p}\right).\end{aligned} \tag{C.6}$$

The leading order term of the error is proportional to third order moments of the particle phase that can be related to the standard deviations of the particle phase variables by making use of the coefficient of skewness $\gamma$ of a given third order central moment. Additionally, the terms included in the SPARSE–R formulation (up to second moments) can be also related to the standard deviation of the particle phase variables by the use of

the Pearson's coefficient $\rho$ of two given magnitudes. In this way, one can write the average forcing as

$$\begin{aligned}\overline{f_1(\alpha,a)} \approx \overbrace{A_{00} + A_{02}B_1^2\sigma_{x_p}^2 + A_{02}\sigma_{u_p}^2 - 2A_{02}B_1\rho_{x_pu_p}\sigma_{x_p}\sigma_{u_p} + A_{11}B_1\rho_{\alpha x_p}\sigma_\alpha\sigma_{x_p} - A_{11}\rho_{\alpha u_p}\sigma_\alpha\sigma_{u_p}}^{\text{Terms included in SPARSE–R}} \\ + 2A_{02}B_1B_2\gamma_{x_p^3}\sigma_{x_p}^3 - A_{03}\gamma_{u_p^3}\sigma_{u_p}^3 + \left(3A_{03}B_1 - 2A_{02}B_2\right)\gamma_{x_pu_p^2}\sigma_{x_p}\sigma_{u_p}^2 - 3A_{03}B_1^2\gamma_{x_p^2u_p}\sigma_{x_p}^2\sigma_{u_p} \\ + \left(A_{11}B_2 + A_{12}B_1^2\right)\gamma_{\alpha x_p^2}\sigma_\alpha\sigma_{x_p}^2 + A_{12}\gamma_{\alpha u_p^2}\sigma_\alpha\sigma_{u_p}^2 - 2A_{12}B_1\gamma_{\alpha x_pu_p}\sigma_\alpha\sigma_{x_p}\sigma_{u_p},\end{aligned} \tag{C.7}$$

where we can see that the leading order term of the error is proportional to the standard deviations of the particle phase variables $\alpha$, $x_p$ and $u_p$ in combinations of order three with the form $\sigma_\alpha^{n_\alpha}\sigma_{x_p}^{n_{x_p}}\sigma_{u_p}^{n_{u_p}}$ where the integer exponents are $n_\alpha + n_{x_p} + n_{u_p} = 3$ with $0 \leq n_\alpha \leq 3$, $0 \leq n_{x_p} \leq 3$ and $0 \leq n_{u_p} \leq 3$. Then, when using splitting, i.e., dividing the domain of the cloud in uniform sets that define subclouds, the number of divisions can be expressed as $M_p = M_p^\alpha M_p^{x_p} M_p^{u_p} = M^3$ for a one–dimensional case where the same number of divisions $M$ per dimension ($\alpha$, $x_p$ and $u_p$) is considered. Every subcloud $k$, with $k = 1, \ldots, M^3$ is solved with the SPARSE–R equations (4.6) jointly with the closure (4.11)–(4.19). Each subcloud has a reduced standard deviation in the particle phase magnitudes such that for the $k$-th subcloud $\sigma_{x_pk} \sim \sigma_{x_p}/M$ and similarly for $\alpha$ and $u_p$. Also, the constants $A_{ij}$ and $B_i$ in (C.2) and (C.5) for each subcloud differ for the ones of the cloud without splitting in that they are evaluated at average locations of the different subclouds, for example $B_{1k} = \frac{\partial u}{\partial x}\big|_{\overline{x}_{p_k}}$, is evaluated at $\overline{x}_{pk}$ instead of the average location of the total cloud with no splitting $\overline{x}_p$. However, because the cloud has to be small enough for the Taylor series to be consider accurate, we can assume that the constants remain on the same order of magnitude $A_{ijk} \sim A_{ij}$ and $B_{ik} \sim B_i$ as a result of assuming $\overline{x}_{pk} \simeq \overline{x}_p$. Additionally, and also based on the same assumption of having a small enough cloud, i.e., having smooth gradients within the cloud, the average coefficient of skewness of the different subclouds remains on the same order of magnitude that the one of the cloud without splitting. This is $\sum_{k=1}^{M_p} w_k\gamma_{x_pk^3} \sim \gamma_{x_p^3}$ and similarly for other third moments, where $w_k$ is the weight of

the $k$-th subcloud.

With these considerations, the average forcing when using splitting can be written as

$$\overline{f_1(\alpha,a)} = \sum_{k=1}^{M^3} w_k \overline{f_1(\alpha,a)}_k, \tag{C.8}$$

where the leading order terms of the error are

$$2\sum_{k=1}^{M^3} w_k A_{02k} B_{1k} B_{2k} \gamma_{x_p^3 k} \sigma_{x_p k}^3 \sim 2A_{02} B_1 B_2 \gamma_{x_p^3} \left(\frac{\sigma_{x_p}}{M}\right)^3, \tag{C.9a}$$

$$\sum_{k=1}^{M^3} w_k A_{03k} \gamma_{u_p^3 k} \sigma_{u_p k}^3 \sim A_{03} \gamma_{u_p^3} \left(\frac{\sigma_{u_p}}{M}\right)^3, \tag{C.9b}$$

$$\sum_{k=1}^{M^3} w_k \left(3A_{03k} B_{1k} - 2A_{02k} B_{2k}\right) \gamma_{x_p u_p^2 k} \sigma_{x_p k} \sigma_{u_p k}^2 \sim \left(3A_{03} B_1 - 2A_{02} B_2\right) \gamma_{x_p u_p^2} \left(\frac{\sigma_{x_p}}{M}\right) \left(\frac{\sigma_{u_p}}{M}\right)^2, \tag{C.9c}$$

$$3\sum_{k=1}^{M^3} w_k A_{03k} B_{1k}^2 \gamma_{x_p^2 u_p k} \sigma_{x_p k}^2 \sigma_{u_p k} \sim 3A_{03} B_1^2 \gamma_{x_p^2 u_p} \left(\frac{\sigma_{x_p}}{M}\right)^2 \left(\frac{\sigma_{u_p}}{M}\right), \tag{C.9d}$$

$$\sum_{k=1}^{M^3} w_k \left(A_{11k} B_{2k} + A_{12k} B_{1k}^2\right) \gamma_{\alpha x_p^2 k} \sigma_{\alpha k} \sigma_{x_p k}^2 \sim \left(A_{11} B_2 + A_{12} B_1^2\right) \gamma_{\alpha x_p^2} \left(\frac{\sigma_\alpha}{M}\right) \left(\frac{\sigma_{x_p}}{M}\right)^2, \tag{C.9e}$$

$$\sum_{k=1}^{M^3} w_k A_{12k} \gamma_{\alpha u_p^2 k} \sigma_{\alpha k} \sigma_{u_p k}^2 \sim A_{12} \gamma_{\alpha u_p^2} \left(\frac{\sigma_\alpha}{M}\right) \left(\frac{\sigma_{u_p}}{M}\right)^2, \tag{C.9f}$$

$$\sum_{k=1}^{M^3} w_k A_{12k} B_{1k} \gamma_{\alpha x_p u_p k} \sigma_{\alpha k} \sigma_{x_p k} \sigma_{u_p k} \sim A_{12} B_1 \gamma_{\alpha x_p u_p} \left(\frac{\sigma_\alpha}{M}\right) \left(\frac{\sigma_{x_p}}{M}\right) \left(\frac{\sigma_{u_p}}{M}\right) \tag{C.9g}$$

that shows the proportionality of the errors with $M^{-3}$. The SPARSE–R method is therefore expected to converge with a third order rate with the number of divisions per dimension $M$ or level of splitting. Note that the analysis performed for the term $\overline{f_1(\alpha,a)}$ can be extended to all the terms included in the closure (4.11)–(4.19). We refer the reader to [3] where a similar derivation was performed for other terms in the closure (4.11)–(4.19).

# Appendix D

# SPARSE–R equations for the SF test case

The closed SPARSE–R equations for the stagnation flow (4.33) when the Stokes' law is considered ($f_1 = \alpha$ and $g_1 = 1$) are presented here. The interpolation of the flow velocity at the average particle location is simplified to $\overline{u} = -k\overline{x}_p$ and $\overline{v} = k\overline{v}_p$. The SPARSE–R equations for $x-$direction read as

$$\frac{\mathrm{d}\overline{x}_p}{\mathrm{d}t} = \overline{u}_p, \tag{D.1a}$$

$$St\frac{\mathrm{d}\overline{u}_p}{\mathrm{d}t} = \overline{\alpha}\left(-k\overline{x}_p - \overline{u}_p\right) - k\overline{\alpha' x'_p} - \overline{\alpha' u'_p}, \tag{D.1b}$$

$$\frac{\mathrm{d}\overline{x'^2_p}}{\mathrm{d}t} = 2\overline{x'_p u'_p}, \tag{D.1c}$$

$$St\frac{\mathrm{d}\overline{u'^2_p}}{\mathrm{d}t} = 2\overline{\alpha}\left(-k\overline{x'_p u'_p} - \overline{u'^2_p}\right) + 2\overline{\alpha' u'_p}\left(-k\overline{x}_p - \overline{u}_p\right), \tag{D.1d}$$

$$\frac{\mathrm{d}}{\mathrm{d}t}\left(\overline{x'_p u'_p}\right) = \overline{u'^2_p} + \frac{1}{St}\left[\overline{\alpha}\left(-k\overline{x'^2_p} - \overline{x'_p u'_p}\right) + \overline{\alpha' x'_p}\left(-k\overline{x}_p - \overline{u}_p\right)\right], \tag{D.1e}$$

$$\frac{\mathrm{d}}{\mathrm{d}t}\left(\overline{\alpha' x'_p}\right) = \overline{\alpha' u'_p}, \tag{D.1f}$$

$$St\frac{\mathrm{d}}{\mathrm{d}t}\left(\overline{\alpha' u'_p}\right) = \overline{\alpha}\left(-k\overline{\alpha' x'_p} - \overline{\alpha' u'_p}\right) + \overline{\alpha'^2}\left(-k\overline{x}_p - \overline{u}_p\right), \tag{D.1g}$$

for the $y-$direction

$$\frac{\mathrm{d}\overline{y}_p}{\mathrm{d}t} = \overline{v}_p, \tag{D.2a}$$

$$St\frac{\mathrm{d}\overline{v}_p}{\mathrm{d}t} = \overline{\alpha}\left(k\overline{y}_p - \overline{v}_p\right) + k\overline{\alpha' y'_p} - \overline{\alpha' v'_p}, \tag{D.2b}$$

$$\frac{\mathrm{d}\overline{y'^2_p}}{\mathrm{d}t} = 2\overline{y'_p v'_p}, \tag{D.2c}$$

$$St\frac{\mathrm{d}\overline{v'^2_p}}{\mathrm{d}t} = 2\overline{\alpha}\left(k\overline{y'_p v'_p} - \overline{v'^2_p}\right) + 2\overline{\alpha' v'_p}\left(k\overline{y}_p - \overline{v}_p\right), \tag{D.2d}$$

$$\frac{\mathrm{d}}{\mathrm{d}t}\left(\overline{y'_p v'_p}\right) = \overline{v'^2_p} + \frac{1}{St}\left[\overline{\alpha}\left(k\overline{y'^2_p} - \overline{y'_p v'_p}\right) + \overline{\alpha' y'_p}\left(k\overline{y}_p - \overline{v}_p\right)\right], \tag{D.2e}$$

$$\frac{\mathrm{d}}{\mathrm{d}t}\left(\overline{\alpha' y'_p}\right) = \overline{\alpha' v'_p}, \tag{D.2f}$$

$$St\frac{\mathrm{d}}{\mathrm{d}t}\left(\overline{\alpha' v'_p}\right) = \overline{\alpha}\left(k\overline{\alpha' y'_p} - \overline{\alpha' v'_p}\right) + \overline{\alpha'^2}\left(k\overline{y}_p - \overline{v}_p\right), \tag{D.2g}$$

and for the variables that combine directions one has

$$\frac{\mathrm{d}}{\mathrm{d}t}\left(\overline{x'_p y'_p}\right) = \overline{x'_p v'_p} + \overline{y'_p u'_p} \tag{D.3a}$$

$$\frac{\mathrm{d}}{\mathrm{d}t}\left(\overline{x'_p v'_p}\right) = \overline{u'_p v'_p} + \frac{1}{St}\left[\overline{\alpha}\left(k\overline{x'_p y'_p} - \overline{x'_p v'_p}\right) + \overline{\alpha' x'_p}\left(k\overline{y}_p - \overline{v}_p\right)\right], \tag{D.3b}$$

$$\frac{\mathrm{d}}{\mathrm{d}t}\left(\overline{y'_p u'_p}\right) = \overline{u'_p v'_p} - \frac{1}{St}\left[\overline{\alpha}\left(k\overline{x'_p y'_p} + \overline{y'_p u'_p}\right) + \overline{\alpha' y'_p}\left(k\overline{x}_p + \overline{u}_p\right)\right], \tag{D.3c}$$

$$St\frac{\mathrm{d}}{\mathrm{d}t}\left(\overline{u'_p v'_p}\right) = \overline{\alpha}\left(-k\overline{x'_p v'_p} + k\overline{y'_p u'_p} - 2\overline{u'_p v'_p}\right) + \overline{\alpha' u'_p}\left(-k\overline{x}_p - \overline{u}_p\right) + \overline{\alpha' v'_p}\left(k\overline{y}_p - \overline{v}_p\right), \tag{D.3d}$$

where the directions are decouple and the horizontal magnitudes can be computed independently of the vertical ones and vice versa. The moments that combine magnitudes of different directions (equations in (D.3)) can be solved after system (D.1) and (D.2).

Considering that the variables $\boldsymbol{x}_p$, $\boldsymbol{u}_p$ and $\alpha$ are uncorrelated at the initial time $t = 0$, for infinite samples $N_p \to \infty$, the initial conditions (4.34) set all moments of the particle variables to be zero initially but the initial average location $\overline{x}_p = -1$ and standard deviations of the particle location $\sigma_{x_p} = \sigma_{y_p} = 0.3$ as described in Section 4.3.2. This means

that the only average relative velocity different from zero at the initial time $t = 0$ is on the horizontal direction $\overline{a}_x = \overline{u} - \overline{u}_p = k$ with zero in the vertical direction $\overline{a}_y = \overline{v} - \overline{v}_p = 0$. Note that under this circumstance, the input of uncertainty in the vertical equations (D.2) occurs in the term $\overline{\alpha'^2}\left(k\overline{y}_p - \overline{v}_p\right)$ that is zero because the relative velocity initially is set to zero $\overline{a}_y = 0$. Taking into account this initial condition, some moments remain zero for the entire simulation since the right hand side terms of its corresponding equations are all zero for any later time. In particular, the SPARSE–R equations in the horizontal components are the same as in (D.1). However, in the vertical component the system (D.2) simplifies to

$$\frac{\mathrm{d}\overline{y_p'^2}}{\mathrm{d}t} = 2\overline{y_p'v_p'}, \tag{D.4a}$$

$$\frac{\mathrm{d}\overline{v_p'^2}}{\mathrm{d}t} = \frac{2\overline{\alpha}}{St}\left(k\overline{y_p'v_p'} - \overline{v_p'^2}\right), \tag{D.4b}$$

$$\frac{\mathrm{d}}{\mathrm{d}t}\left(\overline{y_p'v_p'}\right) = \overline{v_p'^2} + \frac{\overline{\alpha}}{St}\left(k\overline{y_p'^2} - \overline{y_p'v_p'}\right), \tag{D.4c}$$

$$\overline{y}_p = \overline{v}_p = \overline{\alpha' y_p'} = \overline{\alpha' v_p'} = 0, \tag{D.4d}$$

and the equations for the moments combining directions (D.3) simplify to

$$\frac{\mathrm{d}}{\mathrm{d}t}\left(\overline{x_p'y_p'}\right) = \overline{x_p'v_p'} + \overline{y_p'u_p'} \tag{D.5a}$$

$$\frac{\mathrm{d}}{\mathrm{d}t}\left(\overline{x_p'v_p'}\right) = \overline{u_p'v_p'} + \frac{2\overline{\alpha}}{St}\overline{x_p'y_p'}, \tag{D.5b}$$

$$\frac{\mathrm{d}}{\mathrm{d}t}\left(\overline{y_p'u_p'}\right) = \overline{u_p'v_p'} - \frac{2\overline{\alpha}}{St}\overline{x_p'y_p'}, \tag{D.5c}$$

$$St\frac{\mathrm{d}}{\mathrm{d}t}\left(\overline{u_p'v_p'}\right) = \overline{\alpha}\left(-k\overline{x_p'v_p'} + k\overline{y_p'u_p'} - 2\overline{u_p'v_p'}\right) + \overline{\alpha' u_p'}\left(-k\overline{x}_p - \overline{u}_p\right). \tag{D.5d}$$

It is important to notice that the solution of the moments in the vertical component (D.4) when the average relative velocity is zero $\overline{a}_y = 0$ and the variables are uncorrelated between them initially $\overline{\alpha' y_p'} = \overline{\alpha' v_p'} = 0$, that the solution simplifies to the deterministic case, i.e., the deterministic SPARSE equations considering $\alpha = \overline{\alpha}$, with

$\alpha' = 0$. This can be seen in Figures 4.10c, 4.10d and 4.10e where the moments $\overline{y_p'^2}$, $\overline{v_p'^2}$ and $\overline{y_p' v_p'}$ are plotted for the rF and dF coinciding for the computed time interval.

# Appendix E

# Flow map representation of the Liouville equation

For a time interval between the initial time $t_0$ and a later time $t$, we define the flow map of the augmented particle phase space $\mathcal{F}_{t_0}^{t}$ by considering the $N$–dimensional smooth function $\boldsymbol{g}(\boldsymbol{x}, t)$ on a $N$–dimensional domain $\Omega$ that satisfies

$$\frac{\mathrm{d}\boldsymbol{y}}{\mathrm{d}t} = \boldsymbol{g}\left(\boldsymbol{y}, t\right), \quad \boldsymbol{g} = \left(\boldsymbol{u}_{\mathrm{p}},\ \boldsymbol{h}(\boldsymbol{x}_{\mathrm{p}}, \boldsymbol{u}_{\mathrm{p}}),\ \boldsymbol{0}\right)^{\top}, \quad \boldsymbol{y} = \left(\boldsymbol{x}_{\mathrm{p}},\ \boldsymbol{u}_{\mathrm{p}},\ \boldsymbol{\xi}\right)^{\top} \in \Omega \subset \mathbb{R}^{N}, \quad \boldsymbol{y}(t_0) = \boldsymbol{y}_0, \tag{E.0.1}$$

with $\boldsymbol{0}$ a $N_{\xi}$–dimensional vector of zeros. The function $\boldsymbol{g}$ is defined by the right hand side of equations (5.11a) and (5.11b). Notice that the last $N_{\xi}$ components of $\boldsymbol{g}$ are zero because the random coefficients are constant in time. Trajectories $\boldsymbol{y}(t; \boldsymbol{y}_0, t_0)$ in phase space of the dynamical system (E.0.1) define the flow map $\mathcal{F}_{t_0}^{t}$ that is computed as

$$\mathcal{F}_{t_0}^{t} : \ \boldsymbol{y}_0 \longmapsto \boldsymbol{y}(t; \boldsymbol{y}_0, t_0) = \boldsymbol{y}_0 + \int_{t_0}^{t} \boldsymbol{g}(\boldsymbol{y}(\tau; \boldsymbol{y}_0, t_0), \tau) d\tau. \tag{E.0.2}$$

According to (E.0.2), $\mathcal{F}_{t_0}^{t}$ maps an initial condition $\boldsymbol{y}_0$ of the augmented particle phase space vector at time $t_0$ to its position $\boldsymbol{y}$ at a later time $t$.

Accordingly, we also define a flow map $\mathcal{Z}_{t_0}^{t}$ for the joint PDF $f_{\boldsymbol{XU\Xi}}$. We rewrite

equation (5.11c) as

$$\frac{\mathrm{d}f_{\boldsymbol{XU\Xi}}}{\mathrm{d}t} = q(f_{\boldsymbol{XU\Xi}}, \boldsymbol{y}, t), \quad f_{\boldsymbol{XU\Xi}}(t_0) = f_{\boldsymbol{XU\Xi}_0}. \tag{E.0.3}$$

We therefore define equivalently the flow map for the joint PDF as

$$\mathcal{Z}_{t_0}^t : \ f_{\boldsymbol{XU\Xi}_0} \longmapsto f_{\boldsymbol{XU\Xi}}(t; f_{\boldsymbol{XU\Xi}_0}, t_0) = f_{\boldsymbol{XU\Xi}_0} + \int_{t_0}^{t} q(f_{\boldsymbol{XU\Xi}}(\tau; f_{\boldsymbol{XU\Xi}_0}, t_0), \ \mathcal{F}_{t_0}^{\tau}, \tau) d\tau. \tag{E.0.4}$$

The function $q$ is defined by the right hand side of equation (5.11c). Then, $\mathcal{Z}_{t_0}^t$ maps an initial condition $f_{\boldsymbol{XU\Xi}_0}$ of the joint PDF at time $t_0$ defined with support $\boldsymbol{y}_0$, to its later value $f_{\boldsymbol{XU\Xi}}$ defined on $\boldsymbol{y}$. Therefore, the flow map $\mathcal{Z}_{t_0}^t$ is a function of the flow map $\mathcal{F}_{t_0}^t$. Notice that according to the description in Section 5.3, we have that $\boldsymbol{y}_0 = (\boldsymbol{\eta}_x, \boldsymbol{\eta}_u, \boldsymbol{\xi})^\top$. Also, $f_{\boldsymbol{XU\Xi}_0} = f_{\boldsymbol{XU}}^{\text{in}}(\boldsymbol{\eta}_x, \boldsymbol{\eta}_u) f_{\boldsymbol{\Xi}}(\boldsymbol{\xi})$.

# Appendix F

# Isoparametric maps in the augmented phase space

Following [229, 233], we present here the isoparametric mapping given by $\boldsymbol{y} = \boldsymbol{\Theta}(\boldsymbol{\zeta})$ for $N = 2$, that is given by

$$\begin{aligned}\boldsymbol{y} = &(1-\zeta_2)\Gamma_1(\zeta_1) + \zeta_2\Gamma_3(\zeta_1) + (1-\zeta_1)\Gamma_4(\zeta_2) + \zeta_1\Gamma_2(\zeta_2) \\ &- (1-\zeta_1)(1-\zeta_2)\boldsymbol{y}_1 - \zeta_1(1-\zeta_2)\boldsymbol{y}_2 - \zeta_1\zeta_2\boldsymbol{y}_3 - (1-\zeta_1)\zeta_2\boldsymbol{y}_4,\end{aligned} \tag{F.0.1}$$

and for $N = 3$ by

$$\begin{aligned}\boldsymbol{y} = &-(1-\zeta_2)\Sigma_1(\zeta_1,\zeta_3) - \zeta_2\Sigma_2(\zeta_1,\zeta_3)\Sigma_3(\zeta_1,\zeta_2) - \zeta_1\Sigma_4(\zeta_2,\zeta_3) - \zeta_3\Sigma_5(\zeta_1,\zeta_2) - (1-\zeta_1)\Sigma_6(\zeta_2,\zeta_3) \\ &+ (1-\zeta_2)(1-\zeta_3)\Gamma_1(\zeta_1) + \zeta_1(1-\zeta_2)\Gamma_2(\zeta_3) + (1-\zeta_2)\zeta_3\Gamma_3(\zeta_1) + (1-\zeta_1)(1-\zeta_2)\Gamma_4(\zeta_3) \\ &+ \zeta_2(1-\zeta_3)\Gamma_5(\zeta_1) + \zeta_1\zeta_2\Gamma_6(\zeta_3) + \zeta_2\zeta_3\Gamma_7(\zeta_1) + (1-\zeta_1)\zeta_2\Gamma_8(\zeta_3) + (1-\zeta_1)(1-\zeta_3)\Gamma_9(\zeta_2) \\ &+ \zeta_1(1-\zeta_3)\Gamma_{10}(\zeta_2) + \zeta_1\zeta_3\Gamma_{11}(\zeta_2) + (1-\zeta_1)\zeta_3\Gamma_{12}(\zeta_2) - \boldsymbol{y}_1(1-\zeta_1)(1-\zeta_2)(1-\zeta_3) \\ &- \boldsymbol{y}_2\zeta_1(1-\zeta_2)(1-\zeta_3) - \boldsymbol{y}_3\zeta_1\zeta_2(1-\zeta_3) - \boldsymbol{y}_4(1-\zeta_1)\zeta_2(1-\zeta_3) - \boldsymbol{y}_5(1-\zeta_1)(1-\zeta_2)\zeta_3 \\ &- \boldsymbol{y}_6\zeta_1(1-\zeta_2)\zeta_3 - \boldsymbol{y}_7\zeta_1\zeta_2\zeta_3 - \boldsymbol{y}_8(1-\zeta_1)\zeta_2\zeta_3.\end{aligned} \tag{F.0.2}$$

The representation in computational space of the mappings are shown in Fig F.1. In (F.0.1), the corners are defined by $\boldsymbol{y}_r$, with $r = 1, \ldots, 4$. The edges are represented by $\Gamma_r$, which

is its polynomial approximation given by

$$\Gamma_r(s) = \sum_{j=1}^{M} \boldsymbol{y}_j^r l_j(s), \tag{F.0.3}$$

that applied to the different boundaries gives $\Gamma_r$ with $r = 1, \ldots, N$. Notice that $\Gamma_r$ represents a vector with the coordinates of points along the boundary despite it is not represented with a bold symbol. In (F.0.3), $\boldsymbol{y}_j^r$, with $j = 1, \ldots, M$ are the points along the boundary labeled $r$, and $s$ is changed to $\zeta_1$ for $r = 1, 3$ and $\zeta_2$ for $r = 2, 4$. For the case $N = 3$ in (F.0.2), the corners are $\boldsymbol{y}_r$ with $r = 1, \ldots, 8$, and the edges are also computed with (F.0.3) accordingly. The faces $\Sigma_r$ are defined by also a polynomial approximation using the points in each face by

$$\Sigma_r(s_1, s_2) = \sum_{i=1}^{M} \sum_{j=1}^{M} \boldsymbol{y}_{ij}^r l_i(s_1) l_j(s_2), \tag{F.0.4}$$

with $\boldsymbol{y}_{ij}^r$, the coordinates of the points composing the face $r$. Then, the variables in computational space $\zeta_1$, $\zeta_2$ or $\zeta_3$ are substituted in (F.0.4) by $s_1$ and $s_2$ accordingly to the corresponding face. In concordance with the definition of the edges, $\Sigma_r$ evaluated gives a vector with the coordinates of points contained in the face, despite it is not represented by a bold symbol.

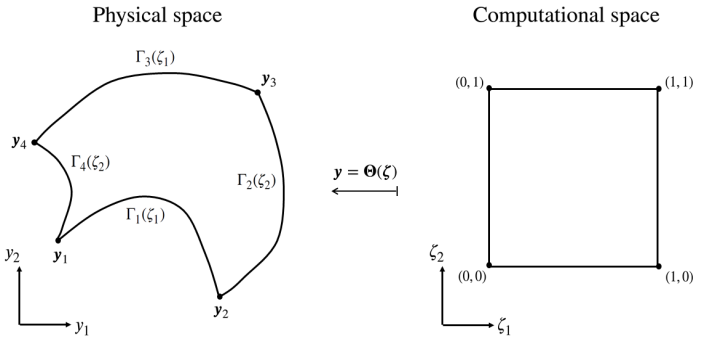


**(a)**

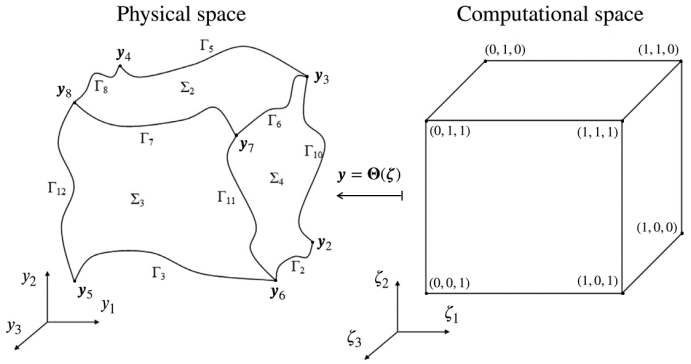


**(b)**

**Figure F.1.** Mapping from the physical space to the computational space for (a) $N = 2$ and (b) $N = 3$ following [229, 233].

# Appendix G

# High-order computation of moments and marginals

The computation of moments is performed via integration of the mapped solution along the parameters using the Jacobian in the $N$-dimensional domain $\Omega_\epsilon$. The computation of the average particle position and velocity computed in Lagrangian form for $N = 3$ using the spectral approach described in Section 5.4.3 are as follows

$$\bar{X}_{\mathrm{p}}(t) = \int_{\Omega_\epsilon} x_{\mathrm{p}} f_{XU\Xi}(\boldsymbol{y}; t)\mathcal{J}\mathrm{d}\boldsymbol{\zeta} \approx \sum_{i=1}^{M}\sum_{j=1}^{M}\sum_{k=1}^{M} w_i w_j w_k y^n_{1ijk}\mathcal{J}^n_{ijk} f^n_{XU\Xi ijk}, \tag{G.0.1a}$$

$$\bar{U}_{\mathrm{p}}(t) = \int_{\Omega_\epsilon} u_{\mathrm{p}} f_{XU\Xi}(\boldsymbol{y}; t)\mathcal{J}\mathrm{d}\boldsymbol{\zeta} \approx \sum_{i=1}^{M}\sum_{j=1}^{M}\sum_{k=1}^{M} w_i w_j w_k y^n_{2ijk}\mathcal{J}^n_{ijk} f^n_{XU\Xi ijk}. \tag{G.0.1b}$$

The numerical quadratures in (G.0.1) involve the nodal values of the mapped solution $\boldsymbol{y}$ and $f_{XU\Xi}$, which are distinguished with the superscript prime $()'$ in Section 5.4.3. These primes are dropped here for readability. The weights $w_i$ correspond to the $M$-point Clenshaw-Curtis (CC) quadrature rule that takes advantage of the nodes distribution used and it is exact for polynomials of order equal or less than $Q = M - 1$. The weights can be computed with the fast Fourier transform [269, 270].

To compute the marginals of the joint PDF with the high-order technique, we will follow the next procedure at any given time, where the joint PDF has been already computed with the flow maps $\mathcal{F}^t_0$ and $\mathcal{Z}^t_0$,

1. Compute Cartesian-aligned container element in the phase space, $\boldsymbol{y}_C$.

2. Interpolate the function $f_{XU\Xi}(\boldsymbol{y}; t)$ to $\mathrm{f}_{XU\Xi}(\boldsymbol{y}_C; t)$, where the subscript $C$ stands for container.

3. Compute the integrals using Clenshaw–Curtis quadrature on every tensorial line of the container element $\boldsymbol{y}_C$.

For simplicity, we describe the procedure for $N = 2$, with $\boldsymbol{y} = (x_\mathrm{p}, u_\mathrm{p})$. Take the two–dimensional flow map $\boldsymbol{y} = \mathcal{F}_{t_0}^{t}(\boldsymbol{y}_0)$ to be the spectral element defined by discrete points $\boldsymbol{y}_{ij}$ in the phase space (physical space in Fig. G.1), with edges $\Gamma_r$ and corners $\boldsymbol{y}_r$, with $r = 1, \ldots, 4$. The computational space is defined with the conformal map in (F.0.1). The corners of the unitary square map to $\boldsymbol{y}_r$, and points along its edges map to $\Gamma_r$, via $\boldsymbol{y} = \boldsymbol{\Theta}(\boldsymbol{\zeta})$. The unitary local spectral element with a nodal distribution given by $\boldsymbol{\zeta}_{ij}$ (black box in computational space, Fig. G.1).

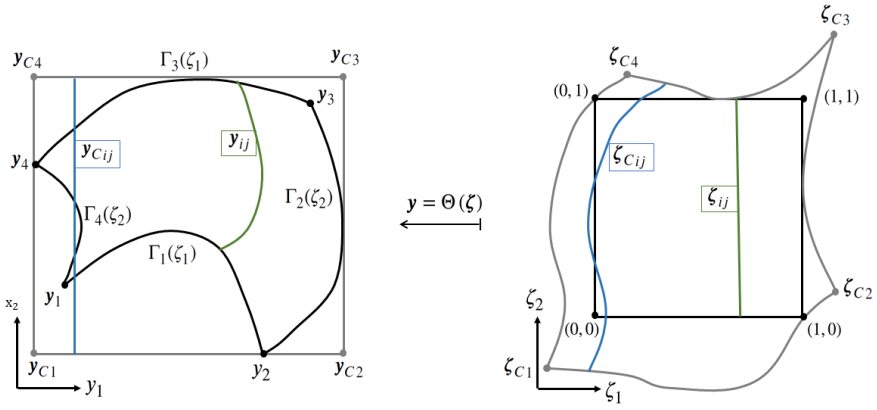


**Figure G.1.** Conformal mapping $\boldsymbol{y} = \Theta(\boldsymbol{\zeta})$ applied to the single element and the container element for the computation of marginals.

The container element, composed by discrete points $\boldsymbol{y}_{Cij}$, is defined as the axis-aligned element, that strictly contains $\boldsymbol{y}_{ij}$ in the physical space (red box), and which

corners are defined by the points $\boldsymbol{y}_{Cr}$, with $r = 1, \ldots, 4$. To find the locations of these corners, the global minima and maxima of points along the edges given by $\Gamma_r$ should be found using a optimization technique, e.g., the Newton-Raphson method, together with (F.0.1), so that

$$\begin{aligned} \boldsymbol{y}_{C1} &= [\min(\Gamma_r)(1),\ \min(\Gamma_r)(2)], \quad \boldsymbol{x}_{C2} = [\max(\Gamma_r)(1),\ \min(\Gamma_r)(2)], \\ \boldsymbol{y}_{C3} &= [\max(\Gamma_r)(1),\ \max(\Gamma_r)(2)], \quad \boldsymbol{x}_{C4} = [\min(\Gamma_r)(1),\ \max(\Gamma_r)(2)]. \end{aligned} \tag{G.0.2}$$

The size of the the container element per component is the vector

$$\mathcal{S}_C = \max(\Gamma_r) - \min(\Gamma_r), \tag{G.0.3}$$

so that the container element discrete representation is found by scaling the computational space

$$\boldsymbol{y}_{Cij} = \min(\Gamma_r) + \mathcal{S}_C \odot \boldsymbol{\zeta}_{ij}, \tag{G.0.4}$$

with $\odot$ defining a pointwise operation.

Now, to perform the interpolation of the joint PDF evaluated on $\boldsymbol{y}_{ij}$ to the discrete points of the container element $\boldsymbol{y}_{Cij}$, we use the following

$$\mathrm{f}_{XUlm} = \sum_{i=1}^{M} \sum_{j=1}^{M} f_{XU_{ij}} l_i(\zeta_{C1lm}) l_j(\zeta_{C2lm}), \tag{G.0.5}$$

with $l, m = 1, \ldots, M$. Lastly, if $\boldsymbol{\zeta}_{Cij}$ is outside the unitary box, i.e., if

$$\left(1 \leq \zeta_{C1ij} \vee 0\zeta_{C1ij}\right) \wedge \left(1 \leq \zeta_{C2ij} \vee 0 \leq \zeta_{C2ij}\right), \tag{G.0.6}$$

then

$$\mathrm{f}_{XUlm} = 0, \tag{G.0.7}$$

because it lies outside of the compact support (5.9). Then, with the interpolated values to the container element, the maginalization along the velocity dimension for example, can be performed by simply

$$f^n_{X\,i} \approx \int_{\min(y^n_{2\,ij})}^{\max(y^n_{2\,ij})} \mathrm{f}_{XU}(\boldsymbol{y}; t) dy_2 \approx \mathcal{J}_C \sum_{j=1}^{M} w_j \mathrm{f}^n_{XU\,ij}, \tag{G.0.8}$$

with $i = 1, \ldots, M$ and $w_j$ being the weights of the Clenshaw–Curtis quadrature and $\mathcal{J}_C$ being the Jacobian of the container element mapped to computational space which is simply

$$\mathcal{J}_C = \begin{vmatrix} \mathcal{S}_{C1} & 0 \\ 0 & \mathcal{S}_{C2} \end{vmatrix},$$

because the element is aligned with the axis.

# Appendix H

# Analytical solution for stagnation flow

In the stagnation flow, the particles in the center line $y = 0$ see the carrier flow field velocity $u = -\kappa x$, that when interpolating at the particle location simply becomes $u = -\kappa x_p$. If we consider the Stokes drag, the correction function becomes unity for deterministically forced particles $\phi(Re_p) = 1$. Therefore, the basis functions $\psi_i$ with $i = 1, \ldots, N_\xi$ are zero, with the exception of the first one which is unity $\psi_1 = 1$ and therefore only the first stochastic mode has influence in the solution such that one has for randomly forced particles $\phi = \Xi$. This is the forcing model in Figure 5.10 depicted in black if $\Xi$ follows a Gaussian distribution. The system of equations according to the MoC is given by

$$\frac{\mathrm{d}x_\mathrm{p}}{\mathrm{d}t} = u_\mathrm{p}, \tag{H.0.1a}$$

$$\frac{\mathrm{d}u_\mathrm{p}}{\mathrm{d}t} = -\frac{\xi}{\mathrm{St}}\left(\kappa x_\mathrm{p} + u_\mathrm{p}\right), \tag{H.0.1b}$$

$$\frac{\mathrm{d}f_{XU\Xi}}{\mathrm{d}t} = \frac{\xi}{\mathrm{St}} f_{XU\Xi}, \tag{H.0.1c}$$

whose analytical solution is given by

$$x_{\mathrm{p}} = e^{-\frac{\xi}{2\mathrm{St}}t}\left[\frac{\xi\eta_x + 2\mathrm{St}\eta_u}{\gamma}\sinh\left(\frac{\gamma}{2\mathrm{St}}t\right) + \eta_x\cosh\left(\frac{\gamma}{2\mathrm{St}}t\right)\right], \tag{H.0.2a}$$

$$u_{\mathrm{p}} = \frac{1}{2\gamma}e^{-\frac{\xi+\gamma}{2\mathrm{St}}t}\left[\gamma\eta_u\left(e^{\frac{\gamma}{\mathrm{St}}t}+1\right) - \xi\left(2\kappa\eta_x + \eta_u\right)\left(e^{\frac{\gamma}{\mathrm{St}}t}-1\right)\right], \tag{H.0.2b}$$

$$f_{XU\Xi} = f^{\mathrm{in}}_{XU}(\eta_x,\eta_u)f_{\Xi}(\xi)e^{\frac{\xi}{\mathrm{St}}t}, \tag{H.0.2c}$$

with $\gamma = \sqrt{\xi\left(\xi - 4\kappa\mathrm{St}\right)}$.

# Appendix I

# Non-periodic functions

The Trapezoidal rule exhibits exponential convergence for periodic functions, where its convergence is determined by the Fourier approximation of the function to integrate. This special case is not necessarily the most common in PDF descriptions of the particle phase. The PDF solution of a particle cloud may be arbitrary, including non-periodic functions. We dedicate this test to a non-symmetric, non-periodic definition of an initial condition which serves to analyze non-periodic solutions. In particular, the initial state of the particles is governed by a Beta distribution such that the different numerical schemes can be analyzed. The Beta distribution has a sharp gradient in one side, and a smooth tail in the opposite side. The initial condition is then selected such that $X_{\mathrm{p}_0} \sim \mathcal{B}(2,3) + 0.6$ and $U_{\mathrm{p}_0} \sim \mathcal{B}(2,3) - 1.5$ such that $(\bar{X}_{\mathrm{p}_0},\ \bar{U}_{\mathrm{p}_0}) = (-1,\ 1)$ and $\sigma_{X_{\mathrm{p}0}} = \sigma_{U_{\mathrm{p}0}} = 0.2$. The initial condition then is defined with compact support in the intervals $[-1.4,\ -0.4]$ along $x_{\mathrm{p}}$ and $[0.6,\ 1.6]$ along $u_{\mathrm{p}}$ without clipping of the joint PDF.

The interpolation errors in this case are significantly different between the linear and spectral interpolants when using the Lagrangian approach. The spectral scheme exhibits machine precision for a very low number of points $M = 5$ (see Fig. I.1). For the computation of marginals however, the convergence is affected by the integration step between the deformed element to the one aligned with the axis in phase space. In this case, because the Beta distribution has high gradients in one of the limits of its support,

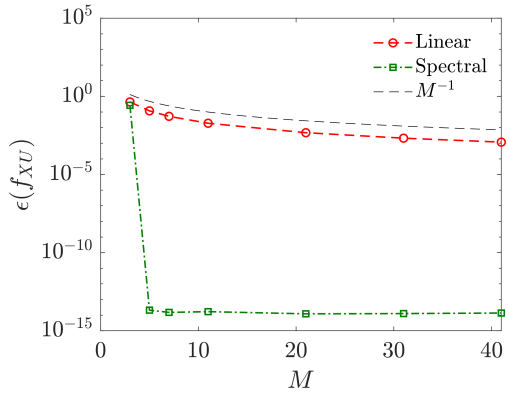


**Figure I.1.** Convergence of the interpolant of the joint PDF for the Lagrangian approach with a linear and spectral scheme.

the integral performed along lines in the marginalization step contains sharp gradients. Despite initially the support is defined such that this gradient is not part of the grid because the support is defined in a compact form, the deformation of the element in time and its interpolation to the aligned element eventually results in the inclusion of gradients in the domain. This can be seen in Figure I.2, where the error distribution as well as both grids (the aligned and the non-aligned) are shown. The convergence of the marginals is then affected by such gradients and when integrating along lines, some of them would lead to integrations limited by the first order convergence as in the case of non-smooth functions, whereas some others not containing such gradients will converge with either second order (for linear interpolant and Trapezoidal Rule) or exponentially (for spectral interpolant and Clenshaw Curtis quadrature). The convergence of the marginals is shown in Figures I.3a and I.3b with convergence rates ranging from $N^{-1}$ to $N^{-2}$. For the initial condition however, where there are no discontinuities in the interpolated element as both are aligned initially, the convergence rates are as expected, second order for the linear interpolant combined with Trapezoidal rule and exponential for the spectral interpolant combined with Clenshaw Curtis (Fig. I.3a).

When computing the moments of the joint PDF, the deformed element is integrated without the use of a container element where an interpolation has been carried out. Because

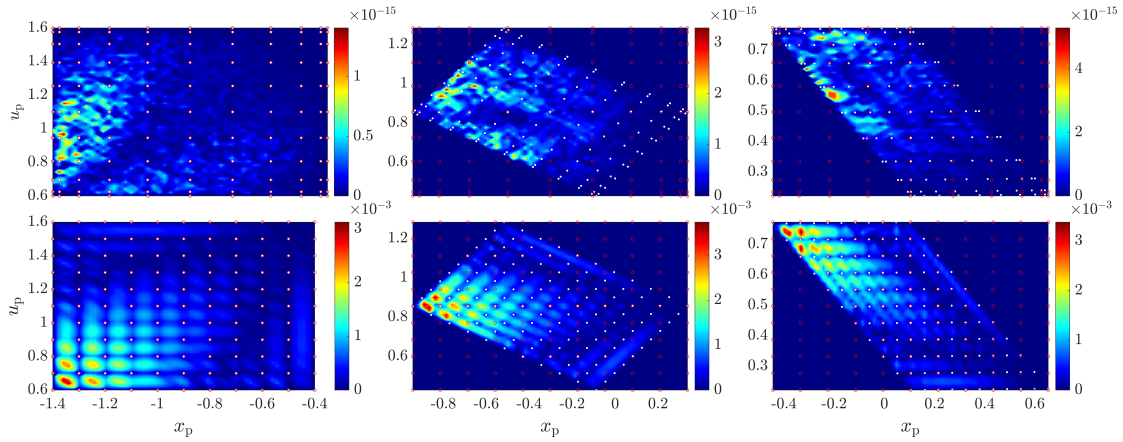


**Figure I.2.** Errors of test case for deterministic forcing and non-periodic functions for the Lagrangian approach using a spectral interpolant (a)–(c) and linear interpolant (d)–(f) for times $t = [0\ 0.6\ 1.2]$. The red dots represent the grid aligned with the axis used for the marginalization step where the solution is interpolated from the non-aligned grid (white dots).

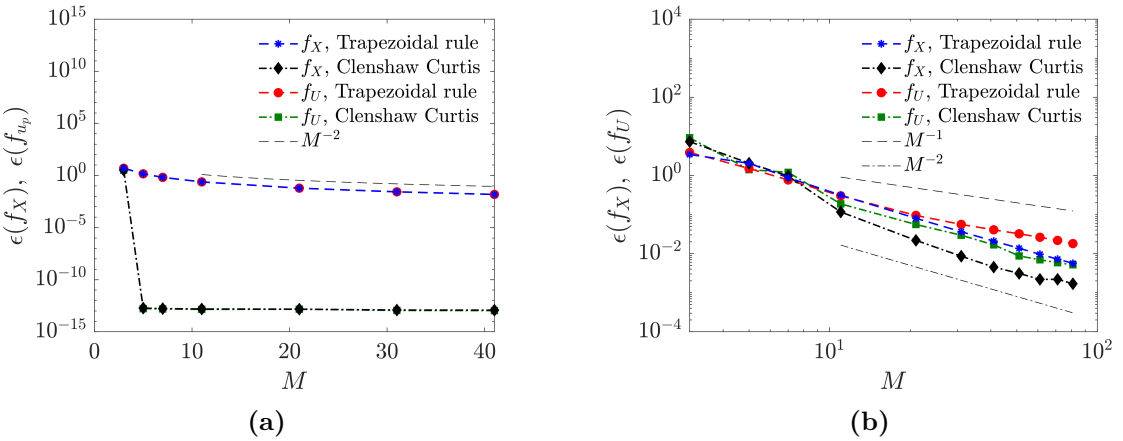


**Figure I.3.** Convergence rates of the marginals for the deterministically forced test case with non–periodic functions. Marginals computed with the linear interpolant combined with the Trapezoidal rule and spectral interpolant combined with the Clenshaw Curtis quadrature for (a) the initial time and (b) the final time.

of this, discontinuities in the element are not present and the integration is not limited by a first order convergence rate. In fact, the spectral scheme combined with Clenshaw Curtis quadrature converges to machine precision with low number of nodes and the linear scheme

combined with Trapezoidal rule shows second order convergence as expected (Fig. I.4).

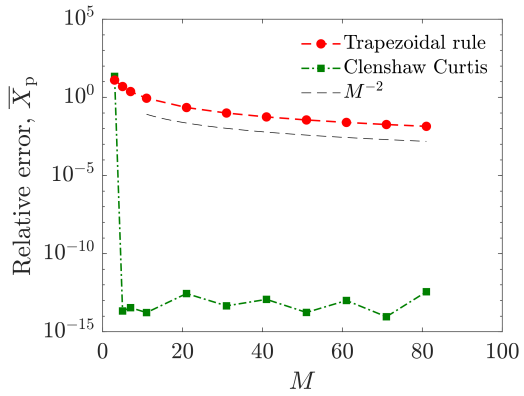


**Figure I.4.** Convergence of the moments with the number of nodes for the deterministically forced case for non–periodic functions computed with the MoC with linear and spectral schemes combined with the Trapezoidal Rule and Clenshaw Curtis respectively.

# Appendix J

# Moment Models

With the Liouville approach, descriptions of moments of the particle phase variables may also be derived using the systems (7.8) or (7.15). These include the variance of particle positions (particle dispersion), the variance of particle velocity (granular temperature) and higher moments as the third and fourth moment of the particle position less reported in the literature. To write a general moment model based on the systems of ODEs with a random coefficient described previously, we first rewrite the ODE systems in terms of the vector of state variables $\boldsymbol{q}$. Then, both systems (7.8) and (7.15) can be written as

$$\frac{\mathrm{d}\boldsymbol{q}}{\mathrm{d}t} = \boldsymbol{g}(\boldsymbol{q}), \tag{J.0.1}$$

where $\boldsymbol{q} = (\boldsymbol{x}_\mathrm{p},\ \Xi) \in \mathbb{R}^4$ for the model in (7.8) and $\boldsymbol{q} = (\boldsymbol{x}_\mathrm{p},\ \boldsymbol{u}_\mathrm{p},\ \Xi) \in \mathbb{R}^7$ for (7.15) with the corresponding function with right hand side terms here taken as $\boldsymbol{g}$, and considering a single random coefficient $\Xi$. Then, we employ a Reynolds decomposition of the random variables $(\cdot) = \overline{(\cdot)} + (\cdot)'$. Substituting in (J.0.1) and averaging, we arrive to the first two moment equations

$$\frac{\mathrm{d}\overline{q}_i}{\mathrm{d}t} = \overline{g}_i, \tag{J.0.2a}$$

$$\frac{\mathrm{d}\overline{q_i' q_j'}}{\mathrm{d}t} = \overline{q_j' g_i'} + \overline{q_i' g_j'}, \tag{J.0.2b}$$

where unclosed terms appear as the average of the non-linear function $\boldsymbol{g}$ is in principle unknown, as well as second order moments involving it. Closures for such terms may be based on *a priori* computations [57] or expansions [3, 4]. If the right hand side of the ODE system is composed by a product of non-linear functions of the state variables, $\boldsymbol{q}$, statistical moments of order higher appear in each moment equation, defining a classic closure problem. Take for exmaple $\boldsymbol{g}(\boldsymbol{q}) = \boldsymbol{r}(\boldsymbol{q}) \circ \boldsymbol{h}(\boldsymbol{q})$, then the system (J.0.2) is rewritten as

$$\frac{\mathrm{d}\overline{q}_i}{\mathrm{d}t} = \overline{r}_i \overline{h}_i + \overline{r'_i h'_i}, \tag{J.0.3a}$$

$$\frac{\mathrm{d}\overline{q'_i q'_j}}{\mathrm{d}t} = \overline{q'_j h'_i}\overline{r}_i + \overline{q'_j r'_i}\ \overline{h}_i + \overline{q'_i h'_j}\overline{r}_j + \overline{q'_i r'_j}\ \overline{h}_j + \overline{q'_j h'_i r'_i} + \overline{q'_i h'_j r'_j}, \tag{J.0.3b}$$

with $\boldsymbol{r}$ and $\boldsymbol{h}$ two non-linear functions. This is for example is the case if a correction of the Stokes drag $\mathcal{F}$ based on the relative velocity is used in (7.15). By combining closures based on expansions with truncation of higher order terms and a splitting algorithm, in Ref. [4], the first two moments were computed in closed form.

When applied to (7.43), the method of moments yields

$$\frac{\mathrm{d}T}{\mathrm{d}t} = -\frac{2}{\tau_\mathrm{p}} T + \frac{2}{3}\overline{\Xi' U'_\mathrm{p}}\phi, \tag{J.0.4a}$$

$$\frac{\mathrm{d}\overline{\Xi' U'_\mathrm{p}}}{\mathrm{d}t} = -\frac{1}{\tau_\mathrm{p}}\overline{\Xi' U'_\mathrm{p}} + \sigma^2_\Xi \phi. \tag{J.0.4b}$$

The solution of the second ODE is

$$\overline{\Xi' U'_\mathrm{p}} = \sigma^2_\Xi (1 - \mathrm{e}^{-\mathcal{C}_1 t/\tau_\mathrm{p}})^{\mathcal{C}_2}. \tag{J.0.5a}$$

Since $T = \sigma_U^2/3$, with $\sigma_U^2$ given by (7.48), substituting this result into (J.0.4a), yields the source $S$ and sink $\Gamma$ terms in (7.50).

# Appendix K

# Analytical solutions based on the moment model

## K.1 Particle trajectory

The moment equations of the one-dimensional version of (7.8) with a single random variable $Z = \Xi$ read as

$$\frac{\mathrm{d}\overline{X}_\mathrm{p}}{\mathrm{d}t} = \ u_\mathrm{p} + \overline{\Xi}\varphi, \tag{K.1.1a}$$

$$\frac{\mathrm{d}\overline{X_\mathrm{p}'^2}}{\mathrm{d}t} = 2\overline{X_\mathrm{p}' U_\mathrm{p}'} + 2\overline{\Xi' X_\mathrm{p}'}\varphi, \tag{K.1.1b}$$

$$\frac{\mathrm{d}\overline{\Xi' X_\mathrm{p}'}}{\mathrm{d}t} = \overline{\Xi'^2}\varphi. \tag{K.1.1c}$$

Considering constant and deterministic velocity $u_\mathrm{p}$, one has $u_\mathrm{p} = \overline{u}_\mathrm{p}$ and $u_\mathrm{p}' = 0$. The impulse initial condition, given by a Dirac delta function located at zero, gives $\overline{X}_{\mathrm{p}_0} = \overline{X_{\mathrm{p}0}'^2} = 0$. Also, initially the random coefficient and the particle locations are statistically independent such that $\overline{\Xi' X_{\mathrm{p}0}'} = \sigma_\Xi \sigma_{X_{\mathrm{p}_0}} = 0$. With this initial condition, the system (K.1.1)

leads to the following solution

$$\overline{X}_{\mathrm{p}} = u_{\mathrm{p}} t + \overline{\Xi}\sqrt{2Dt}, \tag{K.1.2a}$$

$$\overline{X_{\mathrm{p}}'^{2}} = 2\overline{\Xi'^{2}} Dt, \tag{K.1.2b}$$

$$\overline{\Xi' X_{\mathrm{p}}'} = \overline{\Xi'^{2}}\sqrt{2Dt}, \tag{K.1.2c}$$

where if $\overline{\Xi} = 0$ and $\overline{\Xi'^{2}} = 1$, in concordance with the classic heat kernel solution where $\Xi \sim \mathcal{N}(0,1)$, the solution (K.1.2) leads to the classic result for the particle dispersion $\overline{X_{\mathrm{p}}'^{2}} = 2Dt$. The average position grows linear in time $\overline{X}_{\mathrm{p}} = u_{\mathrm{p}} t$, and the correlation of position with the random coefficient is $\overline{\Xi' X_{\mathrm{p}}'} = \sigma_{X_{\mathrm{p}}}$. The characteristic in equation (L.0.2a) can be recasted in the form $\hat{x}_{\mathrm{p}} = \overline{X}_{\mathrm{p}} + \xi\sigma_{X_{\mathrm{p}}}$ according to (K.1.2). This linear relation indicates that for each value of $\xi$, a quantity $\xi\sigma_{X_{\mathrm{p}}}$ is added to the average path and causes that corresponding trajectory to deviate from the average.

The general expression for the average particle position can be also obtained by averaging of the characteristic equation $\hat{x}_{\mathrm{p}}(\xi, t)$ with respect to $\xi$, which corresponds to the application of the law of the unconscious statistician (LOTUS) [266]. Making use of (L.0.2a), with the impulse located at zero $\hat{x}_{\mathrm{p}}^{0} = 0$, one has

$$\overline{X}_{\mathrm{p}} = \int \hat{x}_{\mathrm{p}}(\xi, t) f_{\Xi}(\xi) d\xi = \int \left(\hat{x}_{\mathrm{p}}^{0} + u_{\mathrm{p}} t + \xi\sqrt{2Dt}\right) f_{\Xi}(\xi) d\xi = u_{\mathrm{p}} t + \overline{\Xi}\sqrt{2Dt} \tag{K.1.3}$$

and for the $n$-th central moment

$$\overline{X_{\mathrm{p}}'^{n}} = \int (\hat{x}_{\mathrm{p}}(\xi, t) - \overline{X}_{\mathrm{p}})^{n} f_{\Xi}(\xi) d\xi = \overline{\Xi'^{n}} \left(2Dt\right)^{n/2}, \tag{K.1.4}$$

for $n \geq 2$. Notice that the even moments are non-zero for any of the chosen distributions for $\Xi$ ($\mathcal{N}$, $\mathcal{U}$ or $\mathcal{T}$) whereas the odds moments are zero for symmetric distributions. These result generalize those reported in Ref. [141] for non-Gaussian white noise.

## K.2 Particle velocity

The moment equations of the system (7.36) read as

$$\frac{\mathrm{d}\overline{X}_\mathrm{p}}{\mathrm{d}t} = \tau_\mathrm{p}\overline{U}_\mathrm{p} + \overline{\Xi}\varphi, \tag{K.2.5a}$$

$$\frac{\mathrm{d}\overline{U}_\mathrm{p}}{\mathrm{d}t} = -\overline{U}_\mathrm{p} + \overline{\Xi}\phi, \tag{K.2.5b}$$

$$\frac{\mathrm{d}\overline{X_\mathrm{p}'^2}}{\mathrm{d}t} = 2\tau_\mathrm{p}\overline{X_\mathrm{p}'U_\mathrm{p}'} + 2\varphi\overline{\Xi' X_\mathrm{p}'}, \tag{K.2.5c}$$

$$\frac{\mathrm{d}\overline{X_\mathrm{p}'U_\mathrm{p}'}}{\mathrm{d}t} = \tau_\mathrm{p}\overline{U_\mathrm{p}'^2} - \overline{X_\mathrm{p}'U_\mathrm{p}'} + \varphi\overline{\Xi' U_\mathrm{p}'} + \phi\overline{\Xi' X_\mathrm{p}'}, \tag{K.2.5d}$$

$$\frac{\mathrm{d}\overline{U_\mathrm{p}'^2}}{\mathrm{d}t} = -2\overline{U_\mathrm{p}'^2} + 2\phi\overline{\Xi' U_\mathrm{p}'}, \tag{K.2.5e}$$

$$\frac{\mathrm{d}\overline{\Xi' X_\mathrm{p}'}}{\mathrm{d}t} = \tau_\mathrm{p}\overline{\Xi' U_\mathrm{p}'} + \overline{\Xi'^2}\varphi, \tag{K.2.5f}$$

$$\frac{\mathrm{d}\overline{\Xi' U_\mathrm{p}'}}{\mathrm{d}t} = -\overline{\Xi' U_\mathrm{p}'} + \overline{\Xi'^2}\phi, \tag{K.2.5g}$$

where the equations are closed because in this reference frame the flow velocity does not appear in the average velocity equation and the Stokes drag has been assumed, $\mathcal{F} = 1$. The solution to the system (K.2.5) considering $\overline{\Xi} = 0$ and $\sigma_\Xi = 1$, according to $\Xi \sim \mathcal{N}(0, 1)$, and all other first and second moments zero at the initial time except $\overline{U}_{\mathrm{p}0} = v_0$, as well as

statistical independence of the variables initially, is given by

$$\overline{X}_{\mathrm{p}} = \tau_{\mathrm{p}} v_0 \left(1 - e^{-t}\right), \tag{K.2.6a}$$

$$\overline{U}_{\mathrm{p}} = v_0 e^{-t} \tag{K.2.6b}$$

$$\overline{X_{\mathrm{p}}'^2} = \tau_{\mathrm{p}}^2 D \left(2t - 3 + 4e^{-t} - e^{-2t}\right), \tag{K.2.6c}$$

$$\overline{X_{\mathrm{p}}' U_{\mathrm{p}}'} = \tau_{\mathrm{p}} D \sqrt{\left(1 - e^{-2t}\right)\left(2t - 3 + 4e^{-t} - e^{-2t}\right)}, \tag{K.2.6d}$$

$$\overline{U_{\mathrm{p}}'^2} = D \left(1 - e^{-2t}\right), \tag{K.2.6e}$$

$$\overline{\Xi' X_{\mathrm{p}}'} = \sqrt{\tau_{\mathrm{p}}^2 D \left(2t - 3 + 4e^{-t} - e^{-2t}\right)}, \tag{K.2.6f}$$

$$\overline{\Xi' U_{\mathrm{p}}'} = \sqrt{D \left(1 - e^{-2t}\right)}. \tag{K.2.6g}$$

The averages particle position and velocity as well as the variances of particle positions $\overline{X_{\mathrm{p}}'^2}$ and velocities $\overline{U_{\mathrm{p}}'^2}$ is exact to the results reported in Ref. [141] for the velocity Langevin model (see Figure K.1a). In addition, the solution (K.2.6) includes the second moments of variables combined such as the correlation of particle positions and velocities, $\overline{X_{\mathrm{p}}' U_{\mathrm{p}}'}$, which have not been previously reported in the literature for this particular model. For completeness, we show in Figure K.1b the rest of the second moments of the particle phase which are related to the standard deviation of the particle position and velocity by $\overline{X_{\mathrm{p}}' U_{\mathrm{p}}'} = \sigma_X \sigma_U$, $\overline{\Xi' X_{\mathrm{p}}'} = \sigma_\Xi \sigma_X$ and $\overline{\Xi' U_{\mathrm{p}}'} = \sigma_\Xi \sigma_U$.

The general system (K.2.5), may be used for any other initial conditions or correlations of the fluctuations by selecting $\overline{\Xi}$ and $\overline{\Xi'^2}$ differently. For example, if the particle velocity is initialized with a Maxwellian distribution $\mathcal{N}(0, D)$, such that $\overline{U_{\mathrm{p}0}'^2} = D$, the system (K.2.5) reproduces the classic ballistic–diffusive result of Taylor [271] where $\overline{X_{\mathrm{p}}'^2} = 2\tau_{\mathrm{p}}^2 D \left(t - 1 + e^{-t}\right)$. This is also for $\overline{\Xi} = 0$ and $\overline{\Xi'^2} = 1$.

Higher moments are also found with this moment model. Using the characteristics equations (L.0.4a) and applying the LOTUS, one may find the following general expressions

for the $n$-th central moments

$$\overline{X_{\mathrm{p}}'^{n}} = \overline{\Xi'^{n}} \left[\tau_{\mathrm{p}}^2 D \left(2t - 3 + 4e^{-t} + e^{-2t}\right)\right]^{n/2}, \tag{K.2.7a}$$

$$\overline{U_{\mathrm{p}}'^{n}} = \overline{\Xi'^{n}} \left[D \left(1 - e^{-2t}\right)\right]^{n/2}. \tag{K.2.7b}$$

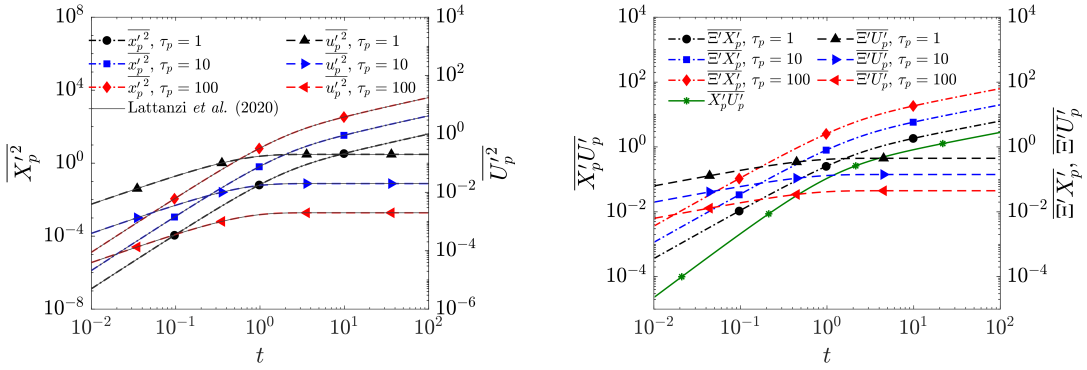


**Figure K.1.** Moments of the particle position and velocities according to the solutions (K.2.6). In (a) solutions of the particle position and velocity variance which coincides with solutions reported in Ref. [141] and (b) additional moments correlating particle positions with velocities and the random coefficient with particle variables. The cases correspond to particle time constants $\tau_{\mathrm{p}} = [1,\ 10,\ 100]$ and $(\tau_p D)^{-1} = 5$.

# Appendix L

# Derivation of analytical solutions

The method of characteristics, i.e., the mapping of the fixed (Eulerian) coordinate system in the phase space, $x_\mathrm{p}$, onto the moving (Lagrangian) coordinate system in the phase space, $\hat{x}_\mathrm{p}(t)$, transforms the PDE (7.27) into a system of ODEs

$$\frac{\mathrm{d}\hat{x}_\mathrm{p}}{\mathrm{d}t} = u_\mathrm{p} + \xi\sqrt{\frac{D}{2t}}, \qquad \hat{x}_\mathrm{p}(0) = \hat{x}_\mathrm{p}^0; \tag{L.0.1a}$$

$$\frac{\mathrm{d}f_{X\Xi}}{\mathrm{d}t} = 0, \qquad f_{X\Xi}(\hat{x}_\mathrm{p}(0), \xi; 0) = f_\Xi(\xi)\delta(\hat{x}_\mathrm{p}^0). \tag{L.0.1b}$$

The solution to the characteristics (L.0.1) is

$$\hat{x}_\mathrm{p} = \hat{x}_\mathrm{p}^0 + u_\mathrm{p}t + \xi\sqrt{2Dt}, \tag{L.0.2a}$$

$$f_{X\Xi} = f_{X\Xi}^0. \tag{L.0.2b}$$

After substituting $\hat{x}_\mathrm{p}^0$ from (L.0.2a) we arrive to (7.28).

The characteristics of the Liouville equation (7.37) are given by

$$\frac{\mathrm{d}\hat{x}_\mathrm{p}}{\mathrm{d}t} = \tau_\mathrm{p}\hat{u}_\mathrm{p} + \xi\varphi, \quad \hat{x}_\mathrm{p}(0) = \hat{x}_\mathrm{p}^0; \tag{L.0.3a}$$

$$\frac{\mathrm{d}\hat{u}_\mathrm{p}}{\mathrm{d}t} = -\hat{u}_\mathrm{p} + \xi\phi, \quad \hat{u}_\mathrm{p}(0) = \hat{u}_\mathrm{p}^0; \tag{L.0.3b}$$

and

$$\begin{aligned} &\frac{\mathrm{d}f_{XU\Xi}}{\mathrm{d}t} = f_{XU\Xi}, \\ &f_{XU\Xi}(\hat{x}_\mathrm{p}(0), \hat{u}_\mathrm{p}(0), \xi; 0) = \delta(\hat{x}_\mathrm{p}^0)\delta(\hat{u}_\mathrm{p}^0 - v_0)f_\Xi(\xi). \end{aligned} \tag{L.0.3c}$$

The joint PDF changes along time because the non-conservative version of the equation (7.37) is non-homogeneous. This occurs because the third term in (7.37) has an explicit dependency with the particle velocity which leads to a non zero right hand side in the ODE for the joint PDF (L.0.3c). The solution to (L.0.3) is

$$\hat{x}_\mathrm{p}(t) = \hat{x}_\mathrm{p}^0 + \tau_\mathrm{p}\hat{u}_\mathrm{p}^0(1 - \mathrm{e}^{-t}) + \xi\sigma_X, \quad \hat{u}_\mathrm{p}(t) = \hat{u}_\mathrm{p}^0\mathrm{e}^{-t} + \xi\sigma_U, \tag{L.0.4a}$$

$$f_{XU\Xi} = f_{XU\Xi}^0\mathrm{e}^t. \tag{L.0.4b}$$

where $\sigma_X$ and $\sigma_U$ are defined by (7.35). They are derived with the moment model (J.0.2). The general expression for the joint PDF $f_{XU\Xi}(x_\mathrm{p}, u_\mathrm{p}, \xi; t)$ is found by obtaining $\hat{x}_\mathrm{p}^0$ and $\hat{u}_\mathrm{p}^0$ from the characteristics (L.0.4a) and substituting them into (L.0.4b):

$$f_{XU\Xi} = e^t f_\Xi(\xi)\delta(\hat{x}_\mathrm{p}^0)\delta(\hat{u}_\mathrm{p}^0 - v_0), \tag{L.0.5}$$

which leads to (7.38).

The characteristics of (7.45) are

$$\frac{\mathrm{d}\hat{u}_\mathrm{p}}{\mathrm{d}t} = -\frac{1}{\tau_\mathrm{p}}\hat{u}_\mathrm{p} + \xi\phi, \tag{L.0.6}$$

$$\frac{\mathrm{d}f_{U\Xi}}{\mathrm{d}t} = \frac{1}{\tau_\mathrm{p}}f_{U\Xi}, \tag{L.0.7}$$

that one can be solve analytically, obtaining

$$\hat{u}_\mathrm{p} = \hat{u}_\mathrm{p}^0 \mathrm{e}^{-t/\tau_\mathrm{p}} + \xi(1 - \mathrm{e}^{-\mathcal{C}_1 t/\tau_\mathrm{p}})^{\mathcal{C}_2}, \tag{L.0.8a}$$

$$f_{U\Xi} = f_{U\Xi}^0 \, \mathrm{e}^{t/\tau_\mathrm{p}}, \tag{L.0.8b}$$

which leads to (7.46).

# Bibliography


[1] S. Tenneti, M. Mehrabadi, and S. Subramaniam. Stochastic Lagrangian model for hydrodynamic acceleration of inertial particles in gas–solid suspensions. *Journal of Fluid Mechanics*, 788:695–729, 2016.

[2] D. Domínguez-Vázquez, G. B. Jacobs, and D. M. Tartakovsky. Lagrangian models of particle-laden flows with stochastic forcing: Monte Carlo, moment equations, and method of distributions analyses. *Physics of Fluids*, 33(3):033326, 2021.

[3] D. Domínguez-Vázquez, B. F. Klose, and G. B. Jacobs. Closed SPARSE—A predictive particle cloud tracer. *International Journal of Multiphase Flow*, 161:104375, 2023.

[4] D. Domínguez-Vázquez and G. B. Jacobs. SPARSE–R: A point-cloud tracer with random forcing. *International Journal of Multiphase Flow*, 170:104653, 2024.

[5] D. Dominguez-Vazquez, S. A. Castiblanco-Ballesteros, G. B. Jacobs, and D. M. Tartakovsky. Lagrangian Liouville models of multiphase flows with randomly forced inertial particles. *arXiv preprint arXiv:2312.07713*, 2023.

[6] D. Domínguez-Vázquez, Q. Wang, and G. B. Jacobs. Adjoint-based particle forcing reconstruction and uncertainty quantification. *arXiv preprint arXiv:2211.10849*, 2022.

[7] D. Domínguez-Vázquez, G. B. Jacobs, and D. M. Tartakovsky. Liouville models of particle-laden flow. *arXiv preprint arXiv:2403.04913*, 2024.

[8] N. G. Deen, M. V. S. Annaland, M. A. Van der Hoef, and J. A. M. Kuipers. Review of discrete particle modeling of fluidized beds. *Chemical engineering science*, 62(1-2):28–44, 2007.

[9] P. Sippola, J. Kolehmainen, A. Ozel, X. Liu, P. Saarenrinne, and S. Sundaresan. Experimental and numerical study of wall layer development in a tribocharged fluidized bed. *Journal of Fluid Mechanics*, 849:860–884, 2018.

[10] Z. Ren, B. Wang, G. Xiang, D. Zhao, and L. Zheng. Supersonic spray combustion subject to scramjets: Progress and challenges. *Progress in Aerospace Sciences*, 105:40–59, 2019.

[11] P. Jenny, D. Roekaerts, and N. Beishuizen. Modeling of turbulent dilute spray combustion. *Progress in Energy and Combustion Science*, 38(6):846–887, 2012.

[12] S. Kumar and H. P. Lee. The perspective of fluid flow behavior of respiratory droplets and aerosols through the facemasks in context of SARS-CoV-2. *Physics of Fluids*, 32(11):111301, 2020.

[13] A. Nemes, T. Dasari, J. Hong, M. Guala, and F. Coletti. Snowflakes in the atmospheric surface layer: observation of particle–turbulence dynamics. *Journal of Fluid Mechanics*, 814:592–613, 2017.

[14] S. V. Prants. Chaotic Lagrangian transport and mixing in the ocean. *The European Physical Journal Special Topics*, 223(13):2723–2743, 2014.

[15] M. Serra, P. Sathe, I. Rypina, A. Kirincich, S. D. Ross, P. Lermusiaux, A. Allen, T. Peacock, and G. Haller. Search and rescue at sea aided by hidden flow structures. *Nature communications*, 11(1):1–7, 2020.

[16] T. E. Ongaro, C. Cavazzoni, G. Erbacci, A. Neri, and M. Salvetti. A parallel multiphase flow code for the 3d simulation of explosive volcanic eruptions. *Parallel Computing*, 33(7-8):541–560, 2007.

[17] J. Dufek, M. Manga, and A. Patel. Granular disruption during explosive volcanic eruptions. *Nature Geoscience*, 5(8):561–564, 2012.

[18] R. Delannay, A. Valance, A. Mangeney, O. Roche, and P. Richard. Granular and particle-laden flows: from laboratory experiments to field observations. *Journal of Physics D: Applied Physics*, 50(5):053001, 2017.

[19] S. H. Bryngelson, K. Schmidmayer, and T. Colonius. A quantitative comparison of phase-averaged models for bubbly, cavitating flows. *International Journal of Multiphase Flow*, 115:137–143, 2019.

[20] A. R. Jamaluddin, G. J. Ball, C. K. Turangan, and T. G. Leighton. The collapse of single bubbles and approximation of the far-field acoustic emissions for cavitation induced by shock wave lithotripsy. *Journal of Fluid Mechanics*, 677:305–341, 2011.

[21] L. Guo and J. Capecelatro. The role of clusters on heat transfer in sedimenting gas-solid flows. *International Journal of Heat and Mass Transfer*, 132:1217–1230, 2019.

[22] N. Takashi and T. J. R. Hughes. An arbitrary Lagrangian–Eulerian finite element method for interaction of fluid and a rigid body. *Computer methods in applied mechanics and engineering*, 95(1):115–138, 1992.

[23] H. H. Hu, N. A. Patankar, and M. Zhu. Direct numerical simulations of fluid–solid systems using the arbitrary Lagrangian–Eulerian technique. *Journal of Computational Physics*, 169(2):427–462, 2001.

[24] A. A. Johnson and T. E. Tezduyar. Advanced mesh generation and update methods for 3D flow simulations. *Computational Mechanics*, 23(2):130–143, 1999.

[25] T. M. Burton and J. K. Eaton. Fully resolved simulations of particle-turbulence interaction. *Journal of Fluid Mechanics*, 545:67–111, 2005.

[26] T. Yabe, F. Xiao, and T. Utsumi. The constrained interpolation profile method for multiphase analysis. *Journal of Computational physics*, 169(2):556–593, 2001.

[27] J. Lu, X. Xu, S. Zhong, R. Ni, and G. Tryggvason. The dynamics of suspensions of prolate spheroidal particles—Effects of volume fraction. *International Journal of Multiphase Flow*, page 104469, 2023.

[28] M. Uhlmann. An immersed boundary method with direct forcing for the simulation of particulate flows. *Journal of computational physics*, 209(2):448–476, 2005.

[29] F. Lucci, A. Ferrante, and S. Elghobashi. Modulation of isotropic turbulence by particles of taylor length-scale size. *Journal of Fluid Mechanics*, 650:5–55, 2010.

[30] G. Akiki and S. Balachandar. Immersed boundary method with non-uniform distribution of Lagrangian markers for a non-uniform Eulerian mesh. *Journal of Computational Physics*, 307:34–59, 2016.

[31] Y. Yao, E. Biegert, B. Vowinckel, T. Köllner, E. Meiburg, S. Balachandar, C. S. Criddle, and O. B. Fringer. Particle-resolved simulations of four-way coupled, polydispersed, particle-laden flows. *International Journal for Numerical Methods in Fluids*, 94(11):1810–1840, 2022.

[32] E. Biegert, B. Vowinckel, and E. Meiburg. A collision model for grain-resolving simulations of flows over dense, mobile, polydisperse granular sediment beds. *Journal of Computational Physics*, 340:105–127, 2017.

[33] A. T. Cate, J. J. Derksen, L. M. Portela, and H. E. A. Van Den Akker. Fully resolved simulations of colliding monodisperse spheres in forced isotropic turbulence. *Journal of Fluid Mechanics*, 519:233–271, 2004.

[34] H. Gao, H. Li, and L. P. Wang. Lattice Boltzmann simulation of turbulent flow laden with finite-size particles. *Computers & Mathematics with Applications*, 65(2):194–210, 2013.

[35] X. Luo, M. R. Maxey, and G. E. Karniadakis. Smoothed profile method for particulate flows: Error analysis and simulations. *Journal of Computational Physics*, 228(5):1750–1769, 2009.

[36] K. Sengupta, B. Shotorban, G. B. Jacobs, and F. Mashayek. Spectral–based simulations of particle–laden turbulent flows. *International Journal of Multiphase Flow*, 35(9):811–826, 2009.

[37] P. G. Saffman. On the settling speed of free and fixed suspensions. *Studies in Applied Mathematics*, 52(2):115–127, 1973.

[38] C. T. Crowe, M. P. Sharma, and D. E. Stock. The particle-source-in cell (PSI-CELL) model for gas-droplet flows. *Journal of Fluids Engineering-transactions of The Asme*, 99:325–332, 1977.

[39] G. G. Stokes. *On the effect of the internal friction of fluids on the motion of pendulums*, volume 9. Pitt Press Cambridge, 1851.

[40] J. Boussinesq. Sur la resistance qu'oppose un fluide indefini en repos. *CR Acad. Sc. Paris*, 100:935–937, 1885.

[41] A. B. Basset. *A treatise on hydrodynamics*. Deighton, Bell and Company, 1888.

[42] C. W. Oseen. *Hydrodynamik*. Akademische Verlagsgesellschaft, 1927.

[43] R. Gatignol. The Faxén formulae for a rigid particle in an unsteady non-uniform Stokes flow. *J. Méc Théor. Appl.*, 2(2):143–160, 1983.

[44] M. R. Maxey and J. J. Riley. Equation of motion for a small rigid sphere in a nonuniform flow. *The Physics of Fluids*, 26(4):883–889, 1983.

[45] M. Parmar, A. Haselbacher, and S. Balachandar. Equation of motion for a sphere in non–uniform compressible flows. *Journal of fluid mechanics*, 699:352–375, 2012.

[46] S. Annamalai and S. Balachandar. Faxén form of time-domain force on a sphere in unsteady spatially varying viscous compressible flows. *Journal of Fluid Mechanics*, 816:381–411, 2017.

[47] M. Parmar, A. Haselbacher, and S. Balachandar. Generalized Basset-Boussinesq-Oseen equation for unsteady forces on a sphere in a compressible flow. *Physical*

*review letters*, 106(8):084501, 2011.

[48] V. M. Boiko, V. P. Kiselev, S. P. Kiselev, A. N. Papyrin, S. V. Poplavsky, and V. M. Fomin. Shock wave interaction with a cloud of particles. *Shock Waves*, 7(5):275–285, 1997.

[49] V. M. Boiko and S. V. Poplavskii. Drag of nonspherical particles in a flow behind a shock wave. *Combustion, Explosion and Shock Waves*, 41(1):71–77, 2005.

[50] E. Loth. Compressibility and rarefaction effects on drag of a spherical particle. *AIAA journal*, 46(9):2219–2228, 2008.

[51] M. Parmar, A. Haselbacher, and S. Balachandar. Improved drag correlation for spheres and application to shock-tube experiments. *Aiaa Journal*, 48(6):1273–1276, 2010.

[52] G. Tedeschi, H. Gouin, and M. Elena. Motion of tracer particles in supersonic flows. *Experiments in Fluids*, 26(4):288–296, 1999.

[53] Z. G. Feng, E. Michaelides, and S. Mao. On the drag force of a viscous sphere with interfacial slip at small but finite reynolds numbers. *Fluid Dynamics Research*, 44(2):025502, 2012.

[54] L. Zhao, X. Chen, and Q. Zhou. Inhomogeneous drag models for gas-solid suspensions based on sub-grid quantities. *Powder Technology*, 385:170–184, 2021.

[55] C. K. Birdsall and D. Fuss. Clouds-in-clouds, clouds-in-cells physics for many-body plasma simulation. *Journal of Computational Physics*, 3(4):494–511, 1969.

[56] E. J. Ching, S. R Brill, M. Barnhardt, and M. Ihme. A two-way coupled Euler-Lagrange method for simulating multiphase flows with discontinuous Galerkin schemes on arbitrary curved elements. *Journal of Computational Physics*, 405:109096, 2020.

[57] S. L. Davis, G. B. Jacobs, O. Sen, and H. S. Udaykumar. SPARSE – A subgrid particle averaged Reynolds stress equivalent model: testing with a priori closure. *Proceedings of the Royal Society A: Mathematical, Physical and Engineering Sciences*, 473(2199):20160769, 2017.

[58] S. Taverniers, H. S. Udaykumar, and G. B. Jacobs. Two-way coupled cloud-in-cell modeling of non-isothermal particle-laden flows: A subgrid particle-averaged Reynolds stress-equivalent (SPARSE) formulation. *Journal of Computational Physics*, 390:595–618, 2019.

[59] O. Sen, N. J. Gaul, S. Davis, K. K. Choi, G. B. Jacobs, and H. S. Udaykumar. Role of pseudo-turbulent stresses in shocked particle clouds and construction of surrogate models for closure. *Shock Waves*, 28(3):579–597, 2018.

[60] M. Mehrabadi, S. Tenneti, R. Garg, and S. Subramaniam. Pseudo-turbulent gas-phase velocity fluctuations in homogeneous gas–solid flow: fixed particle assemblies and freely evolving suspensions. *Journal of Fluid Mechanics*, 770:210–246, 2015.

[61] B. Sun, S. Tenneti, S. Subramaniam, and D. L. Koch. Pseudo-turbulent heat flux and average gas–phase conduction during gas–solid heat transfer: flow past random fixed particle assemblies. *Journal of Fluid Mechanics*, 798:299–349, 2016.

[62] M. C. Baker, R. O. Fox, B. Kong, J. Capecelatro, and O. Desjardins. Reynolds-stress modeling of cluster-induced turbulence in particle-laden vertical channel flow. *Physical Review Fluids*, 5(7):074304, 2020.

[63] S. Balachandar and J. K. Eaton. Turbulent dispersed multiphase flow. *Annual review of fluid mechanics*, 42:111–133, 2010.

[64] R. O. Fox. Large-eddy-simulation tools for multiphase flows. *Annual Review of Fluid Mechanics*, 44:47–76, 2012.

[65] M. Maxey. Simulation methods for particulate flows and concentrated suspensions. *Annual Review of Fluid Mechanics*, 49:171–193, 2017.

[66] S. Elghobashi. Direct numerical simulation of turbulent flows laden with droplets or bubbles. *Annual Review of Fluid Mechanics*, 51:217–244, 2019.

[67] L. Brandt and F. Coletti. Particle-laden turbulence: Progress and perspectives. *Annual Review of Fluid Mechanics*, 54:159–189, 2022.

[68] J. Bec, K. Gustavsson, and B. Mehlig. Statistical models for the dynamics of heavy particles in turbulence. *arXiv preprint arXiv:2304.01312*, 2023.

[69] P. K. Yeung and S. B. Pope. An algorithm for tracking fluid particles in numerical simulations of homogeneous turbulence. *Journal of computational physics*, 79(2):373–416, 1988.

[70] S. Balachandar and M. R. Maxey. Methods for evaluating fluid velocities in spectral simulations of turbulence. *Journal of Computational Physics*, 83(1):96–125, 1989.

[71] G. B. Jacobs, D. A. Kopriva, and F. Mashayek. Towards efficient tracking of inertial particles with high-order multidomain methods. *Journal of computational and applied mathematics*, 206(1):392–408, 2007.

[72] R. Cortez. The method of regularized Stokeslets. *SIAM Journal on Scientific Computing*, 23(4):1204–1225, 2001.

[73] J. P. Suarez, G. B. Jacobs, and W. S. Don. A high–order Dirac–delta regularization with optimal scaling in the spectral solution of one–dimensional singular hyperbolic conservation laws. *SIAM Journal on Scientific Computing*, 36(4):A1831–A1849, 2014.

[74] J. P. Suarez and G. B. Jacobs. Regularization of singularities in the weighted summation of Dirac–delta functions for the spectral solution of hyperbolic conservation laws. *Journal of Scientific Computing*, 72(3):1080–1092, 2017.

[75] F. Evrard, F. Denner, and B. Wachem. Euler-Lagrange modelling of dilute particle-laden flows with arbitrary particle-size to mesh-spacing ratio. *Journal of Computational Physics: X*, 8:100078, 2020.

[76] P. Gualtieri, F. Picano, G. Sardina, and C. M. Casciola. Exact regularized point particle method for multiphase flows in the two-way coupling regime. *Journal of Fluid Mechanics*, 773:520–561, 2015.

[77] J. A. K. Horwitz, G. Iaccarino, J. K. Eaton, and A. Mani. The discrete Green's function paradigm for two-way coupled Euler–Lagrange simulation. *Journal of Fluid Mechanics*, 931, 2022.

[78] J. F. Poustis, J. M. Senoner, D. Zuzio, and P. Villedieu. Regularization of the Lagrangian point force approximation for deterministic discrete particle simulations. *International Journal of Multiphase Flow*, 117:138–152, 2019.

[79] S. Lomholt and M. R. Maxey. Force-coupling method for particulate two-phase flow: Stokes flow. *Journal of Computational Physics*, 184(2):381–405, 2003.

[80] M. R. Maxey and B. K. Patel. Localized force representations for particles sedimenting in Stokes flow. *International journal of multiphase flow*, 27(9):1603–1626, 2001.

[81] S. L. Dance and M. R. Maxey. Incorporation of lubrication effects into the force-coupling method for particulate two-phase flow. *Journal of computational Physics*, 189(1):212–238, 2003.

[82] J. A. K. Horwitz and A. Mani. Correction scheme for point-particle models applied to a nonlinear drag law in simulations of particle-fluid interaction. *International Journal of Multiphase Flow*, 101:74–84, 2018.

[83] S. Balachandar and K. Liu. A correction procedure for self-induced velocity of a finite-sized particle in two-way coupled euler–lagrange simulations. *International*

*Journal of Multiphase Flow*, 159:104316, 2023.

[84] P. Koumoutsakos. Multiscale flow simulations using particles. *Annu. Rev. Fluid Mech.*, 37:457–487, 2005.

[85] J. Capecelatro and O. Desjardins. An euler–lagrange strategy for simulating particle-laden flows. *Journal of Computational Physics*, 238:1–31, 2013.

[86] P. J. Ireland and O. Desjardins. Improving particle drag predictions in euler–Lagrange simulations with two-way coupling. *Journal of Computational Physics*, 338:405–430, 2017.

[87] G. S. Shallcross, R. O. Fox, and J. Capecelatro. A volume-filtered description of compressible particle-laden flows. *International Journal of Multiphase Flow*, 122:103138, 2020.

[88] D. Fuster, J. M. Conoir, and T. Colonius. Effect of direct bubble-bubble interactions on linear-wave propagation in bubbly liquids. *Physical Review E*, 90(6):063010, 2014.

[89] C. T. Hsiao, J. Ma, and G. L. Chahine. Multiscale tow-phase flow modeling of sheet and cloud cavitation. *International Journal of Multiphase Flow*, 90:102–117, 2017.

[90] G. Akiki, T. L. Jackson, and S. Balachandar. Pairwise interaction extended point-particle model for a random array of monodisperse spheres. *Journal of Fluid Mechanics*, 813:882–928, 2017.

[91] G. Akiki, W. C. Moore, and S. Balachandar. Pairwise-interaction extended point-particle model for particle-laden flows. *Journal of Computational Physics*, 351:329–357, 2017.

[92] W. C. Moore, S. Balachandar, and G. Akiki. A hybrid point–particle force model that combines physical and data–driven approaches. *Journal of Computational Physics*, 385:187–208, 2019.

[93] S. Balachandar, W. C. Moore, G. Akiki, and K. Liu. Toward particle-resolved accuracy in Euler–Lagrange simulations of multiphase flow using machine learning and pairwise interaction extended point-particle (PIEP) approximation. *Theoretical and Computational Fluid Dynamics*, 34(4):401–428, 2020.

[94] A. Seyed-Ahmadi and A. Wachs. Microstructure-informed probability-driven point-particle model for hydrodynamic forces and torques in particle-laden flows. *Journal of Fluid Mechanics*, 900, 2020.

[95] F. Battista, P. Gualtieri, J.-P. Mollicone, and C. M. Casciola. Application of the

exact regularized point particle method (ERPP) to particle laden turbulent shear flows in the two-way coupling regime. *International Journal of Multiphase Flow*, 101:113–124, 2018.

[96] L. He and Danesh K. Tafti. A supervised machine learning approach for predicting variable drag forces on spherical particles in suspension. *Powder technology*, 345:379–389, 2019.

[97] A. Seyed-Ahmadi and A. Wachs. Physics–inspired architecture for neural network modeling of forces and torques in particle–laden flows. *Computers & Fluids*, 238:105379, 2022.

[98] G. B. Jacobs and H. S. Udaykumar. Uncertainty quantification in Eulerian–Lagrangian simulations of (point-) particle-laden flows with data-driven and empirical forcing models. *International Journal of Multiphase Flow*, 121:103114, 2019.

[99] R. J. L. Rutjens, G. B. Jacobs, and D. M. Tartakovsky. Method of distributions for systems with stochastic forcing. *International Journal for Uncertainty Quantification*, 11(2), 2021.

[100] O. Sen, S. Davis, G. B. Jacobs, and H. S. Udaykumar. Evaluation of convergence behavior of metamodeling techniques for bridging scales in multi-scale multimaterial simulation. *Journal of Computational Physics*, 294:585–604, 2015.

[101] O. Sen, N. J. Gaul, K. K. Choi, G. B. Jacobs, and H. S. Udaykumar. Evaluation of kriging based surrogate models constructed from mesoscale computations of shock interaction with particles. *Journal of Computational Physics*, 336:235–260, 2017.

[102] O. Sen, N. J. Gaul, K. K. Choi, G. B. Jacobs, and H. S. Udaykumar. Evaluation of multifidelity surrogate modeling techniques to construct closure laws for drag in shock–particle interactions. *Journal of Computational Physics*, 371:434–451, 2018.

[103] R. V. R. Pandya and F. Mashayek. Non-isothermal dispersed phase of particles in turbulent flow. *Journal of Fluid Mechanics*, 475:205–245, 2003.

[104] F. Mashayek and R. V. R. Pandya. Analytical description of particle/droplet-laden turbulent flows. *Progress in energy and combustion science*, 29(4):329–378, 2003.

[105] Y. A. Buyevich. Statistical hydromechanics of disperse systems Part 1. Physical background and general equations. *Journal of Fluid Mechanics*, 49(3):489–507, 1971.

[106] Y. A. Buyevich. Statistical hydromechanics of disperse systems. Part 2. Solution of the kinetic equation for suspended particles. *Journal of Fluid Mechanics*, 52(2):345–355, 1972.

[107] Y. A. Buyevich. Statistical hydromechanics of disperse systems. Part 3. Pseudo-turbulent structure of homogeneous suspensions. *Journal of Fluid Mechanics*, 56(2):313–336, 1972.

[108] M. W. Reeks. Eulerian direct interaction applied to the statistical motion of particles in a turbulent fluid. *Journal of Fluid Mechanics*, 97(3):569–590, 1980.

[109] M. W. Reeks. The transport of discrete particles in inhomogeneous turbulence. *Journal of aerosol science*, 14(6):729–739, 1983.

[110] M. W. Reeks. On a kinetic equation for the transport of particles in turbulent flows. *Physics of Fluids A: Fluid Dynamics*, 3(3):446–456, 1991.

[111] M. W. Reeks. On the continuum equations for dispersed particles in nonuniform flows. *Physics of Fluids A: Fluid Dynamics*, 4(6):1290–1303, 1992.

[112] D. C. Swailes and K. F. F. Darbyshire. A generalized Fokker-Planck equation for particle transport in random media. *Physica A: Statistical Mechanics and its Applications*, 242(1-2):38–48, 1997.

[113] A. Bragg, D. C. Swailes, and R. Skartlien. Drift-free kinetic equations for turbulent dispersion. *Physical Review E*, 86(5):056306, 2012.

[114] D. C. Swailes, Y. A. Sergeev, and A. Parker. Chapman–enskog closure approximation in the kinetic theory of dilute turbulent gas-particulate suspensions. *Physica A: Statistical Mechanics and its Applications*, 254(3-4):517–547, 1998.

[115] L. I. Zaichik and V. M. Alipchenkov. Refinement of the probability density function model for preferential concentration of aerosol particles in isotropic turbulence. *Physics of Fluids*, 19(11):113308, 2007.

[116] V. M. Alipchenkov and L. I. Zaichik. Dispersion and clustering of bidisperse particles in isotropic turbulence. *Fluid Dynamics*, 40(1):83–94, 2005.

[117] R. V. R. Pandya and F. Mashayek. Probability density function modeling of evaporating droplets dispersed in isotropic turbulence. *AIAA journal*, 39(10):1909–1915, 2001.

[118] R. V. R. Pandya and F. Mashayek. Turbulent thermal diffusion and barodiffusion of passive scalar and dispersed phase of particles in turbulent flows. *Physical review letters*, 88(4):044501, 2002.

[119] M. W. Reeks. The Development and Application of a Kinetic Theory for Modeling Dispersed Particle Flows. *Journal of Fluids Engineering*, 143(8), 2021.

[120] D. Marchisio, A. Barresi, G. Baldi, and R. O. Fox. Comparison between the Classes Method and the Quadrature Method of Moments for multiphase systems. In *Proceedings 8th International Conference on Multiphase Flows in Industrial Plants*, pages 283–300. ANIMP Servizi srl, 2002.

[121] D. L. Marchisio, J. Pikturna, L. Wang, R. D. Vigil, and R. O. Fox. Quadratic method of moments for population balances in CFD applications: Comparison with experimental data. *Chem. Engg. Trans*, 1:305–310, 2002.

[122] V. Raman, H. Pitsch, and R. O. Fox. Quadrature moments method for the simulation of turbulent reactive flows. *Center for Turbulence Research Annual Research Briefs 2003*, 2003.

[123] D. L. Marchisio, R. D. Vigil, and R. O. Fox. Quadrature method of moments for aggregation–breakage processes. *Journal of colloid and interface science*, 258(2):322–334, 2003.

[124] D. L. Marchisio, J. T. Pikturna, R. O. Fox, R. D. Vigil, and A. A. Barresi. Quadrature method of moments for population-balance equations. *AIChE Journal*, 49(5):1266–1276, 2003.

[125] J. C. Heylmun, B. Kong, A. Passalacqua, and R. O. Fox. A quadrature-based moment method for polydisperse bubbly flows. *Computer Physics Communications*, 244:187–204, 2019.

[126] S. H. Bryngelson, A. Charalampopoulos, T. P. Sapsis, and T. Colonius. A Gaussian moment method and its augmentation via LSTM recurrent neural networks for the statistics of cavitating bubble populations. *International Journal of Multiphase Flow*, 127:103262, 2020.

[127] A. Charalampopoulos, S. H. Bryngelson, T. Colonius, and T. P. Sapsis. Hybrid quadrature moment method for accurate and stable representation of non-Gaussian processes applied to bubble dynamics. *Philosophical Transactions of the Royal Society A*, 380(2229):20210209, 2022.

[128] S. H. Bryngelson, R. O. Fox, and T. Colonius. Conditional moment methods for polydisperse cavitating flows. *Journal of Computational Physics*, page 111917, 2023.

[129] S. B. Pope. PDF methods for turbulent reactive flows. *Progress in energy and combustion science*, 11(2):119–192, 1985.

[130] D. C. Haworth and S. B. Pope. A generalized Langevin model for turbulent flows. *The Physics of fluids*, 29(2):387–405, 1986.

[131] I. Iliopoulos, Y. Mito, and T. J. Hanratty. A stochastic model for solid particle dispersion in a nonhomogeneous turbulent field. *International journal of multiphase flow*, 29(3):375–394, 2003.

[132] Z. Gao and F. Mashayek. Stochastic modeling of evaporating droplets polydispered in turbulent flows. *International journal of heat and mass transfer*, 47(19-20):4339–4348, 2004.

[133] Z. Gao and F. Mashayek. Stochastic model for nonisothermal droplet-laden turbulent flows. *AIAA journal*, 42(2):255–260, 2004.

[134] Z. Gao and F. Mashayek. A stochastic model for gravity effects in particle-laden turbulent flows. *J. Fluids Eng.*, 126(4):620–625, 2004.

[135] B. Shotorban and F. Mashayek. Modeling subgrid–scale effects on particles by approximate deconvolution. *Physics of Fluids*, 17(8):081701, 2005.

[136] B. Shotorban and F. Mashayek. A stochastic model for particle motion in large-eddy simulation. *Journal of Turbulence*, 7:N18, 2006.

[137] B. Shotorban and F. Mashayek. On stochastic modeling of heavy particle dispersion in large-eddy simulation of two-phase turbulent flow. In *IUTAM Symposium on Computational Approaches to Multiphase Flow: Proceedings of an IUTAM Symposium held at Argonne National Laboratory, October 4–7, 2004*, pages 373–380. Springer, 2006.

[138] J. Pozorski and S. V. Apte. Filtered particle tracking in isotropic turbulence and stochastic modeling of subgrid-scale dispersion. *International Journal of Multiphase Flow*, 35(2):118–128, 2009.

[139] M. G. Pai and S. Subramaniam. Two-way coupled stochastic model for dispersion of inertial particles in turbulence. *Journal of Fluid Mechanics*, 700:29–62, 2012.

[140] A. Esteghamatian, F. Euzenat, A. H., M. Lance, and A. Wachs. A stochastic formulation for the drag force based on multiscale numerical simulation of fluidized beds. *International Journal of Multiphase Flow*, 99:363–382, 2018.

[141] A. M. Lattanzi, V. Tavanashad, S. Subramaniam, and J. Capecelatro. Stochastic models for capturing dispersion in particle-laden flows. *Journal of Fluid Mechanics*, 903, 2020.

[142] M. Knorps and J. Pozorski. Stochastic modeling for subgrid–scale particle dispersion in large–eddy simulation of inhomogeneous turbulence. *Physics of Fluids*, 33(4):043323, 2021.

[143] A. M. Lattanzi, V. Tavanashad, S. Subramaniam, and J. Capecelatro. Stochastic model for the hydrodynamic force in Euler–Lagrange simulations of particle–laden flows. *Physical Review Fluids*, 7(1):014301, 2022.

[144] A. M. Lattanzi, V. Tavanashad, S. Subramaniam, and J. Capecelatro. Fluid-mediated sources of granular temperature at finite Reynolds numbers. *Journal of Fluid Mechanics*, 942:A7, 2022.

[145] J. Friedrich, B. Viggiano, M. Bourgoin, R. B. Cal, and L. Chevillard. Single inertial particle statistics in turbulent flows from Lagrangian velocity models. *Physical Review Fluids*, 7(1):014303, 2022.

[146] K. Pietrzyk, J. A. K. Horwitz, F. M. Najjar, and R. W. Minich. On analysis and stochastic modeling of the particle kinetic energy equation in particle-laden isotropic turbulent flows. *Physics of Fluids*, 34(1):013316, 2022.

[147] V. Holubec, K. Kroy, and S. Steffenoni. Physically consistent numerical solver for time-dependent Fokker-Planck equations. *Physical Review E*, 99(3):032117, 2019.

[148] A. Tabandeh, N. Sharma, L. Iannacone, and P. Gardoni. Numerical solution of the Fokker–Planck equation using physics-based mixture models. *Computer Methods in Applied Mechanics and Engineering*, 399:115424, 2022.

[149] D. Venturi, D. M. Tartakovsky, A. M. Tartakovsky, and G. E. Karniadakis. Exact PDF equations and closure approximations for advective-reactive transport. *Journal of Computational Physics*, 243:323–343, 2013.

[150] H. Cho, D. Venturi, and G. E. Karniadakis. Statistical analysis and simulation of random shocks in stochastic Burgers equation. *Proceedings of the Royal Society A: Mathematical, Physical and Engineering Sciences*, 470(2171):20140080, 2014.

[151] S. Taverniers and D. M. Tartakovsky. Estimation of distributions via multilevel monte carlo with stratified sampling. *J. Comput. Phys.*, 419:109572, 2020.

[152] S. Taverniers, S. B. M. Bosma, and D. M. Tartakovsky. Accelerated multilevel Monte Carlo with kernel-based smoothing and Latinized stratification. *Water Resour. Res.*, 56(9):e2019WR026984, 2020.

[153] X. Ma and N. Zabaras. An adaptive hierarchical sparse grid collocation algorithm for the solution of stochastic differential equations. *Journal of Computational Physics*, 228(8):3084–3113, 2009.

[154] D. A. Barajas-Solano and D. M. Tartakovsky. Stochastic collocation methods for nonlinear parabolic equations with random coefficients. *SIAM/ASA Journal on*

*Uncertainty Quantification*, 4(1):475–494, 2016.

[155] X. Wan and G. E. Karniadakis. An adaptive multi-element generalized polynomial chaos method for stochastic differential equations. *Journal of Computational Physics*, 209(2):617–642, 2005.

[156] X. Wan and G. E. Karniadakis. Multi-element generalized polynomial chaos for arbitrary probability measures. *SIAM Journal on Scientific Computing*, 28(3):901–928, 2006.

[157] Daniele Venturi, Xiaoliang Wan, and George Em Karniadakis. Stochastic bifurcation analysis of rayleigh–bénard convection. *Journal of fluid mechanics*, 650:391–413, 2010.

[158] B. Debusschere. *Intrusive Polynomial Chaos Methods for Forward Uncertainty Propagation*, pages 617–636. Springer International Publishing, Cham, 2017.

[159] M. Ye, S. P. Neuman, Alberto Guadagnini, and D. M. Tartakovsky. Nonlocal and localized analyses of conditional mean transient flow in bounded, randomly heterogeneous porous media. *Water Resour. Res.*, 40:W05104, 2004.

[160] T. Maltba, P. Gremaud, and D. M. Tartakovsky. Nonlocal pdf methods for langevin equations with colored noise. *J. Comput. Phys.*, 367:87–101, 2018.

[161] T. S. Lundgren. Distribution functions in the statistical theory of turbulence. *Phys. Fluids*, 10(5):969–975, 1967.

[162] D. M. Tartakovsky and P. A. Gremaud. Method of distributions for uncertainty quantification. In R. Ghanem, D. Higdon, and H. Owhadi, editors, *Handbook of Uncertainty Quantification*, pages 763–783. Springer, New York, 2015.

[163] P. Wang and D. M. Tartakovsky. Uncertainty quantification in kinematic-wave models. *J. Comput. Phys.*, 231(23):7868–7880, 2012.

[164] P. Wang, D. M. Tartakovsky, Jr. K. D. Jarman, and A. M. Tartakovsky. CDF solutions of Buckley-Leverett equation with uncertain parameters. *Multiscale Model. Simul.*, 11(1):118–133, 2013.

[165] A. Alawadhi, F. Boso, and D. M. Tartakovsky. Method of distributions for water-hammer equations with uncertain parameters. *Water Resour. Res.*, 54(11):9398–9411, 2018.

[166] F. Boso and D. M. Tartakovsky. Data-informed method of distributions for hyperbolic conservation laws. *SIAM J. Sci. Comput.*, 42(1), 2020.

[167] H.-J. Yang, F. Boso, H. A. Tchelepi, and D. M. Tartakovsky. Probabilistic forecast of single-phase flow in porous media with uncertain properties. *Water Resour. Res.*, 55(11):8631–8645, 2019.

[168] G. Haller. Lagrangian coherent structures. *Annual Review of Fluid Mechanics*, 47:137–162, 2015.

[169] B. W. Wissink, G. B. Jacobs, J. K. Ryan, W. S. Don, and E. T. A. van der Weide. Shock regularization with smoothness-increasing accuracy-conserving dirac-delta polynomial kernels. *Journal of scientific computing*, 77(1):579–596, 2018.

[170] G. B. Jacobs and W. S. Don. A high-order WENO-Z finite difference based particle-source-in-cell method for computation of particle-laden flows with shocks. *Journal of Computational Physics*, 228(5):1365–1379, 2009.

[171] B. Shotorban, G. B. Jacobs, O. Ortiz, and Q. Truong. An eulerian model for particles nonisothermally carried by a compressible fluid. *International Journal of Heat and Mass Transfer*, 65:845–854, 2013.

[172] R. G. Patel, O. Desjardins, and R. O. Fox. Three-dimensional conditional hyperbolic quadrature method of moments. *Journal of Computational Physics: X*, 1:100006, 2019.

[173] D. Gottlieb and J. S. Hesthaven. Spectral methods for hyperbolic problems. *Journal of Computational and Applied Mathematics*, 128(1-2):83–131, 2001.

[174] J. S. Hesthaven, S. Gottlieb, and D. Gottlieb. *Spectral methods for time-dependent problems*, volume 21. Cambridge University Press, 2007.

[175] S. Gottlieb and C. W. Shu. Total variation diminishing Runge-Kutta schemes. *Mathematics of Computation*, 67(221):73–85, 1998.

[176] K. Hiemenz. Die Grenzschicht an einem in den gleichformigen Flussigkeitsstrom eingetauchten geraden Kreiszylinder. *Dinglers Polytech. J.*, 326:321–324, 1911.

[177] L. Rosenhead. *Laminar boundary layers: an account of the development, structure, and stability of laminar boundary layers in incompressible fluids, together with a description of the associated experimental techniques*. Dover Publications, 1988.

[178] C. T. Crowe, M. Sommerfeld, and Y. Tsuji. *Multiphase Flows with Droplets and Particles*. CRC Press LLC, Boca Raton, Fl, 1998.

[179] S. Balachandar, K. Liu, and M. Lakhote. Self-induced velocity correction for improved drag estimation in euler–lagrange point-particle simulations. *Journal of*

*Computational Physics*, 376:160–185, 2019.

[180] S. Balachandar. A scaling analysis for point–particle approaches to turbulent multiphase flows. *International Journal of Multiphase Flow*, 35(9):801 – 810, 2009. Special Issue: Point-Particle Model for Disperse Turbulent Flows.

[181] J. Capecelatro. Modeling high-speed gas-particle flows relevant to spacecraft landings: A review and perspectives. *arXiv preprint arXiv:2109.02523*, 2021.

[182] J. Capecelatro, O. Desjardins, and R. O. Fox. On fluid–particle dynamics in fully developed cluster-induced turbulence. *Journal of Fluid Mechanics*, 780:578–635, 2015.

[183] G. B. Jacobs and J. S. Hesthaven. High-order nodal discontinuous galerkin particle-in-cell method on unstructured grids. *Journal of Computational Physics*, 214(1):96–121, 2006.

[184] E. J. Ching and M. Ihme. Efficient projection kernels for discontinuous Galerkin simulations of disperse multiphase flows on arbitrary curved elements. *Journal of Computational Physics*, 435:110266, 2021.

[185] JAK Horwitz and A Mani. Two-way coupled particle-turbulence interaction: effect of numerics and resolution on fluid and particle statistics. *Physical Review Fluids*, 5(10):104302, 2020.

[186] O. Desjardins, R. O. Fox, and P. Villedieu. A quadrature-based moment method for dilute fluid-particle flows. *Journal of Computational Physics*, 227(4):2514–2539, 2008.

[187] A. Buffo, M. Vanni, D. L. Marchisio, and R. O. Fox. Multivariate quadrature-based moments methods for turbulent polydisperse gas–liquid systems. *International Journal of Multiphase Flow*, 50:41–57, 2013.

[188] E. Michaelides, C. T. Crowe, and J. D. Schwarzkopf. *Multiphase flow handbook*. CRC Press, 2016.

[189] G. B. Jacobs, W. S. Don, and T. Dittmann. High-order resolution eulerian–lagrangian simulations of particle dispersion in the accelerated flow behind a moving shock. *Theoretical and Computational Fluid Dynamics*, 26(1-4):37–50, 2012.

[190] S. Davis, O. Sen, G. B. Jacobs, and H. S. Udaykumar. Coupling of micro-scale and macro-scale Eulerian-Lagrangian models for the computation of shocked particle-laden flows. In *ASME International Mechanical Engineering Congress and Exposition*, volume 56314, page V07AT08A011. American Society of Mechanical Engineers, 2013.

[191] R. B. Bird, W. E. Stewart, and E. N. Lightfoot. *Transport phenomena*, volume 1. John Wiley & Sons, 2006.

[192] V. I. Arnold. Sur la topologie des écoulements stationnaires des fluides parfaits. In *Vladimir I. Arnold-Collected Works*, pages 15–18. Springer, 1965.

[193] S. Olivieri, A. Akoush, L. Brandt, M. E. Rosti, and A. Mazzino. Turbulence in a network of rigid fibers. *Physical Review Fluids*, 5(7):074502, 2020.

[194] C. Rorai, D. Rosenberg, A. Pouquet, and P. D. Mininni. Helicity dynamics in stratified turbulence in the absence of forcing. *Physical Review E*, 87(6):063007, 2013.

[195] G. Haller. Distinguished material surfaces and coherent structures in three-dimensional fluid flows. *Physica D: Nonlinear Phenomena*, 149(4):248–277, 2001.

[196] G. Froyland and K. Padberg-Gehle. Finite-time entropy: A probabilistic approach for measuring nonlinear stretching. *Physica D: Nonlinear Phenomena*, 241(19):1612–1628, 2012.

[197] S. Mowlavi, M. Serra, E. Maiorino, and L. Mahadevan. Detecting Lagrangian coherent structures from sparse and noisy trajectory data. *Journal of Fluid Mechanics*, 948:A4, 2022.

[198] G. A. Blaisdell, N. N. Mansour, and W. C. Reynolds. Compressibility effects on the growth and structure of homogeneous turbulent shear flow. *Journal of Fluid Mechanics*, 256:443–485, 1993.

[199] J. R. Ristorcelli and G. A. Blaisdell. Consistent initial conditions for the DNS of compressible turbulence. *Physics of Fluids*, 9(1):4–6, 1997.

[200] B. F. Klose, G. B. Jacobs, and D. A. Kopriva. Assessing standard and kinetic energy conserving volume fluxes in discontinuous galerkin formulations for marginally resolved navier-stokes flows. *Computers & Fluids*, 205:104557, 2020.

[201] G. B. Jacobs, D. A. Kopriva, and F. Mashayek. Validation study of a multidomain spectral code for simulation of turbulent flows. *AIAA journal*, 43(6):1256–1264, 2005.

[202] S. B. Pope. *Turbulent flows*. Cambridge University Press, 2000.

[203] L. Schiller and A. Naumann. Über die grundlegenden berechnungen bei der schwerkraftaufbereitung. *Aiaa Journal*, 77:318–321, 1933.

[204] E. Loth. Drag of non-spherical solid particles of regular and irregular shape. *Powder Technology*, 182(3):342–353, 2008.

[205] F. Mashayek. Droplet–turbulence interactions in low-Mach-number homogeneous shear two-phase flows. *Journal of Fluid Mechanics*, 367:163–203, 1998.

[206] M. Mehrabadi and S. Subramaniam. Mechanism of kinetic energy transfer in homogeneous bidisperse gas-solid flow and its implications for segregation. *Physics of Fluids*, 29(2):020714, 2017.

[207] A. Esteghamatian, M. Bernard, M. Lance, A. Hammouti, and A. Wachs. Micro/meso simulation of a fluidized bed in a homogeneous bubbling regime. *International Journal of Multiphase Flow*, 92:93–111, 2017.

[208] L. T. Zhu and A. Wachs. Interpolation of probability–driven model to predict hydrodynamic forces and torques in particle–laden flows. *AIChE Journal*, page e18209, 2023.

[209] G Akiki and S Balachandar. Shear-induced lift force on spheres in a viscous linear shear flow at finite volume fractions. *Physics of Fluids*, 32(11):113306, 2020.

[210] S. Chen, P. Chen, and J. Fu. Drag and lift forces acting on linear and irregular agglomerates formed by spherical particles. *Physics of Fluids*, 34(2):023307, 2022.

[211] A. N. Osnes, M. Vartdal, M. Khalloufi, J. Capecelatro, and S. Balachandar. Comprehensive quasi-steady force correlations for compressible flow through random particle suspensions. *International Journal of Multiphase Flow*, page 104485, 2023.

[212] V. Chéron, F. Evrard, and B. van Wachem. Drag, lift and torque correlations for axi-symmetric non-spherical particles in locally non-uniform flows. *arXiv preprint arXiv:2304.10357*, 2023.

[213] L. Jbara, A. Ghigo, and A. Wachs. Steady three–dimensional unbounded flow past an obstacle continuously deviating from a sphere to a cube. *Physics of Fluids*, 35(1):013343, 2023.

[214] B. Siddani and S. Balachandar. Point-particle drag, lift, and torque closure models using machine learning: Hierarchical approach and interpretability. *Physical Review Fluids*, 8(1):014303, 2023.

[215] S. Tenneti and S. Subramaniam. Particle–resolved direct numerical simulation for gas-solid flow model development. *Annual review of fluid mechanics*, 46:199–230, 2014.

[216] M. Mehrabadi, J. A. K. Horwitz, S. Subramaniam, and A. Mani. A direct comparison of particle–resolved and point–particle methods in decaying turbulence. *Journal of Fluid Mechanics*, 850:336–369, 2018.

[217] J. Capecelatro and O. Desjardins. Volume-filtered Euler-Lagrange method for strongly coupled fluid-particle flows. In *Modeling Approaches and Computational Methods for Particle-Laden Turbulent Flows*, pages 383–417. Elsevier, 2023.

[218] P. Wang, A. M. Tartakovsky, and D. M. Tartakovsky. Probability density function method for Langevin equations with colored noise. *Phys. Rev. Lett.*, 110(14):140602, 2013.

[219] M. Delgado. Classroom note: The Lagrange-Charpit method. *SIAM Review*, 39(2):298–304, 1997.

[220] H. Miyagi and T. Taniguchi. Application of the lagrange-charpit method to analyse the power system's stability. *International Journal of Control*, 32(2):371–379, 1980.

[221] H. Miyagi and T. Taniguchi. Lagrange-Charpit method and stability problem of power systems. *IEEE Proceedings D (Control Theory and Applications)*, 128(3):117–122, 1981.

[222] A. Halder and R. Bhattacharya. Dispersion analysis in hypersonic flight during planetary entry using stochastic Liouville equation. *Journal of Guidance, Control, and Dynamics*, 34(2):459–474, 2011.

[223] B. Kruglikov and V. Lychagin. A compatibility criterion for systems of PDEs and generalized Lagrange-Charpit method. *AIP Conference Proceedings*, 729(1):39–53, 2004.

[224] K. Kanazawa and D. Sornette. Field master equation theory of the self–excited hawkes process. *Physical Review Research*, 2(3):033442, 2020.

[225] V. G. Rau and N. Krishnamoorthy. Construction of improved Lyapunov functions and extension of transient stability regions for power systems. *International Journal of Electrical Power & Energy Systems*, 11(1):65–69, 1989.

[226] D. Sels, F. Brosens, and W. Magnus. Classical trajectories: A powerful tool for solving tunneling problems. *Physica A: Statistical Mechanics and its Applications*, 391(1-2):78–81, 2012.

[227] D. M. Tartakovsky and P. A. Gremaud. Method of distributions for uncertainty quantification. In R. Ghanem, D. Higdon, and H. Owhadi, editors, *Handbook of Uncertainty Quantification*. Springer, Cham., 2016.

[228] D. A. Nelson and G. B. Jacobs. Computation of Forward–Time Finite–Time Lyapunov Exponents Using Discontinuous–Galerkin Spectral Element Methods. In *ASME International Mechanical Engineering Congress and Exposition*, volume 56444, page V015T16A015. American Society of Mechanical Engineers, 2013.

[229] D. A. Nelson and G. B. Jacobs. DG–FTLE: Lagrangian coherent structures with high–order discontinuous–Galerkin methods. *Journal of Computational Physics*, 295:65–86, 2015.

[230] T. E. Maltba, H. Zhao, and D. M. Tartakovsky. Autonomous learning of nonlocal stochastic neuron dynamics. *J. Cogn. Neurodyn.*, 16:683–705, 2022.

[231] K. D. Squires and J. K. Eaton. Preferential concentration of particles by turbulence. *Physics of Fluids A: Fluid Dynamics*, 3(5):1169–1178, 1991.

[232] M. Sudharsan, S. L. Brunton, and J. J. Riley. Lagrangian coherent structures and inertial particle dynamics. *Physical Review E*, 93(3):033108, 2016.

[233] D. A. Nelson and G. B. Jacobs. High–order visualization of three–dimensional lagrangian coherent structures with DG–FTLE. *Computers & Fluids*, 139:197–215, 2016.

[234] P. D. Hill. Kernel estimation of a distribution function. *Communications in Statistics-Theory and Methods*, 14(3):605–620, 1985.

[235] A. W. Bowman and A. Azzalini. *Applied smoothing techniques for data analysis: the kernel approach with S-Plus illustrations*, volume 18. OUP Oxford, 1997.

[236] L. N. Trefethen and J. A. C. Weideman. The exponentially convergent trapezoidal rule. *SIAM Review*, 56(3):385–458, 2014.

[237] C. Jung, T. Tél, and E. Ziemniak. Application of scattering chaos to particle transport in a hydrodynamical flow. *Chaos: An Interdisciplinary Journal of Nonlinear Science*, 3(4):555–568, 1993.

[238] G. Haller and T. Sapsis. Where do inertial particles go in fluid flows? *Physica D: Nonlinear Phenomena*, 237(5):573–583, 2008.

[239] T. Sapsis and G. Haller. Instabilities in the dynamics of neutrally buoyant particles. *Physics of fluids*, 20(1), 2008.

[240] G. Haller and T. Sapsis. Localized instability and attraction along invariant manifolds. *SIAM Journal on Applied Dynamical Systems*, 9(2):611–633, 2010.

[241] M. Serra, J. Vétel, and G. Haller. Exact theory of material spike formation in flow separation. *Journal of Fluid Mechanics*, 845:51–92, 2018.

[242] D. L. Marchisio and R. O. Fox. *Multiphase reacting flows: modelling and simulation*, volume 492. Springer, 2007.

[243] M. Ishii. *Thermo-Fluid Dynamic Theory of Two-phase Flow*. Eyrolles, France, 1975.

[244] O. Sen, S. Taverniers, P. Das, G. Jacobs, and H. S. Udaykumar. Machine-learning based multi-scale model for shock-particle interactions. *Bulletin of the American Physical Society*, 64, 2019.

[245] M. Parmar, A. Haselbacher, and S. Balachandar. Modeling of the unsteady force for shock–particle interaction. *Shock Waves*, 19(4):317–329, 2009.

[246] J. Regele, J. Rabinovitch, T. Colonius, and G. Blanquart. Numerical modeling and analysis of early shock wave interactions with a dense particle cloud. In *42nd AIAA Fluid Dynamics Conference and Exhibit*, page 3161, 2012.

[247] A. Blanco-Casares and G. B. Jacobs. Wall roughness effects on the supersonic flow over a circular cylinder. *Shock Waves*, pages 1–21, 2022.

[248] Y. Wang, X. Shi, L. Lei, and J. C. H. Fung. Deep learning augmented data assimilation: Reconstructing missing information with convolutional autoencoders. *Monthly Weather Review*, 2022.

[249] Z. Y. Wan and T. P. Sapsis. Machine learning the kinematics of spherical particles in fluid flows. *Journal of Fluid Mechanics*, 857, 2018.

[250] Q. Wang, Y. Hasegawa, and T. A. Zaki. Spatial reconstruction of steady scalar sources from remote measurements in turbulent flow. *Journal of Fluid Mechanics*, 870:316–352, 2019.

[251] M. Wang, Q. Wang, and T. A. Zaki. Discrete adjoint of fractional-step incompressible navier-stokes solver in curvilinear coordinates and application to data assimilation. *Journal of Computational Physics*, 396:427–450, 2019.

[252] Q. Wang, M. Wang, and T. A. Zaki. What is observable from wall data in turbulent channel flow? *Journal of Fluid Mechanics*, 941:A48, 2022.

[253] L. Yang, X. Meng, and G. E. Karniadakis. B-pinns: Bayesian physics-informed neural networks for forward and inverse pde problems with noisy data. *Journal of Computational Physics*, 425:109913, 2021.

[254] S. Chib and E. Greenberg. Understanding the metropolis-hastings algorithm. *The american statistician*, 49(4):327–335, 1995.

[255] V. Garzó and J. W. Dufty. Dense fluid transport for inelastic hard spheres. *Physical Review E*, 59(5):5895, 1999.

[256] V. Garzó, S. Tenneti, S. Subramaniam, and C. M. Hrenya. Enskog kinetic theory for monodisperse gas–solid flows. *Journal of Fluid Mechanics*, 712:129–168, 2012.

[257] M. R. H. Sheikhi, P. Givi, and S. B. Pope. Velocity-scalar filtered mass density function for large eddy simulation of turbulent reacting flows. *Physics of fluids*, 19(9), 2007.

[258] S. Gheorghiu, J. R. Van Ommen, and M.O. Coppens. Power-law distribution of pressure fluctuations in multiphase flow. *Physical Review E*, 67(4):041305, 2003.

[259] L Biferale, P Perlekar, M Sbragaglia, and FJPRL Toschi. Convection in multiphase fluid flows using lattice boltzmann methods. *Physical Review Letters*, 108(10):104502, 2012.

[260] F. Forgues, L. Ivan, A. Trottier, and J. G. McDonald. A gaussian moment method for polydisperse multiphase flow modelling. *Journal of Computational Physics*, 398:108839, 2019.

[261] D. L. Koch and A. S. Sangani. Particle pressure and marginal stability limits for a homogeneous monodisperse gas-fluidized bed: kinetic theory and numerical simulations. *Journal of Fluid Mechanics*, 400:229–263, 1999.

[262] D. Schneider, J. Fuhrmann, W. Reich, and G. Scheuermann. A variance based FTLE-like method for unsteady uncertain vector fields. In *Topological Methods in Data Analysis and Visualization II: Theory, Algorithms, and Applications*, pages 255–268. Springer, 2011.

[263] H. Risken and T. Frank. *The Fokker-Planck Equation: Methods of Solution and Applications*. Springer, Berlin, 1996.

[264] J. E. Moyal. Stochastic processes and statistical physics. *Journal of the Royal Statistical Society. Series B (Methodological)*, 11(2):150–210, 1949.

[265] T. T. Soong and J. L. Bogdanoff. *Random Differential Equations in Science and Engineering*. Academic Press, New York, 1974.

[266] B. Flury. *A first course in multivariate statistics*. Springer Science & Business Media, 2013.

[267] C. Gardiner. *Stochastic methods*. Springer, Berlin, 2009.

[268] B. Noble, J. W. Daniel, et al. *Applied linear algebra*, volume 3. Prentice-Hall Englewood Cliffs, NJ, 1977.

[269] H. O'hara and F. J. Smith. Error estimation in the Clenshaw–Curtis quadrature formula. *The Computer Journal*, 11(2):213–219, 1968.

[270] L. N. Trefethen. Is Gauss quadrature better than Clenshaw–Curtis? *SIAM review*, 50(1):67–87, 2008.

[271] G. I. Taylor. Diffusion by continuous movements. *Proceedings of the London Mathematical Society*, 2(1):196–212, 1922.